An Investigation into Microstructure and Microstructural Control of Additive Layer Manufactured Ti-6Al-4V by Electron Beam Melting

Sinan Saadi Al-Bermani

Thesis submitted for the degree of Doctor of Philosophy

Department of Engineering Materials
The University of Sheffield

January 2011

I. SUMMARY

An additive layer manufacturing (ALM) technique, electron beam melting, has been used for the production of simple geometries, from pre-alloyed Ti-6Al-4V powder. Microstructure, texture and mechanical properties achieved under standard conditions have been investigated, alongside numerical modelling of the electron beam and attempts to modify solidification through the addition of boron.

Experimentation reveals an asymmetric electron beam which can be manipulated to produce different material responses. The electron beam has been used in this work, at its least powerful, as a means of preheating powder particles and, at its most powerful; to produce what is effectively a macro-scale electron beam weld. Numerical modelling and extraction of solidification parameters reveal that solidification occurs in the columnar region – columnar grains are observed experimentally and are a feature of the process.

Observed microstructures indicate a complicated thermal history that is capable of producing diffusion-less and diffusional transformation products. Electron backscatter diffraction (EBSD) and prior β grain reconstruction reveal a strong texture perpendicular to the *build* axis. Mechanical properties, tested over a range of *build temperatures*, are sensitive to temperature over the tested range of 625 – 700 °C.

Attempts to disrupt columnar solidification via the addition of boron to Ti-6Al-4V, before subsequent EBM processing, were unsuccessful. Solidification remained in the columnar regime with no refinement in grain morphology observed.

II. CONTENTS

III. NOMENCLATURE

Terminology	Description
ALM	Additive Layer Manufacture
BCC	Body centre cubic
CAD	Computer aided design
CP	Commercial purity
CV-EBM	Controlled vacuum electron beam melting
DMLS	Direct metal laser sintering
EBM	Electron Beam Melting
EBSD	Electron back scatter diffraction
EBSP	Electron back scatter patterns
ELI	Extra low interstitial
FFF	Freeform fabrication
FO	*Focus offset*
GA	Gas atomised
HAGB	High angle grain boundary
HCF	High cycle fatigue
HCP	Hexagonal close packed
HIP	Hot isostatic pressing
IPF	Inverse pole figure
JMAK	Johnson-Mehl-Avrami-Kolomogorov
LAGB	Low angle grain boundary
LAM	Layer additive manufacture
LCF	Low cycle fatigue
MUD	Multiples of uniform density
PREP	Plasma rotating electrode process
PRS	Powder recovery system
RM	Rapid manufacturing
RP	Rapid prototyping
RT	Rapid tooling
SEM	Scanning electron microscope
SF	*Speed function*
SLA	Stereolithography
SLS	Selective laser sintering
STL	Standard triangulation language
TMP	Thermo-mechanical processing
XRD	X-ray diffraction

Terminology	Description	Units
R_p	Electron penetration range	µm
V_f	Volume fraction	
C_C	crystal coordinate system	
C_S	sample coordinate system	
g	orientation	
YS	Yield strength	MPa
q	Power	W
R	$\sqrt{(x^2 + y^2 + z^2)}$	m
R	Solidification velocity	cms^{-1}
P	Power	W
M_s	Martensite start temperature	K , °C
M_f	Martensite finish temperature	K , °C
I	Current	mA
V	Voltage	V
v	Velocity	ms^{-1}
x, y, z	Orthogonal coordinates	
η	Efficiency parameter	
ΔG	Free energy	
ΔG_v	Volume free energy	
G	Thermal gradient	Kcm^{-1}
V	Solidification velocity	cms^{-1}
θ	Melt pool angle	°
λ_2	Secondary dendrite arm spacing	
k	Thermal conductivity	$Wm^{-1}K^{-1}$
$C\rho$	Specific heat capacity	$Jg^{-1}K^{-1}$
ρ	Density	gcm^{-3}
α	Thermal diffusivity	m^2s^{-1}
σ_y	Yield strength	MPa
α	HCP alpha phase	
α_p	Primary alpha phase	
α_{GB}	Grain boundary alpha phase	
α'	Martensitic alpha phase	
R_a	Surface roughness	µm
β	BCC beta phase	
T_β	Beta transus temperature	K , °C
T	Temperature	K , °C

T_e	Equilibrium temperature	K , °C
T_L	Liquidus temperature	K , °C
T_{mp}	Melting point	K , °C
$\dot{T}$	Cooling rate	Ks^{-1}
Q	Growth restriction factor	K
m_0	Liquidus slope	$°Cwt\%^{-1}$
C_0	Solute concentration	wt%
k	Partition coefficient	
N_0	nuclei density	cm^{-3}
ΔT_n	nucleation undercooling	K , °C
ΔT_c	solutal undercooling	K , °C
D_L	diffusivity of solute in liquid metal	m^2s^{-1}
k_{TD}	Thermal conductivity at theoretical density	$Wm^{-1}K^{-1}$
k_{eff}	Effective thermal conductivity	$Wm^{-1}K^{-1}$
k_g	Thermal conductivity of pore medium	$Wm^{-1}K^{-1}$
φ	Void fraction	

IV. GLOSSARY OF TERMS

The field of additive layer manufacture (ALM) uses terminology that is perhaps ambiguous to those not directly involved with the processes. Terminology can be specific to a particular ALM system although there are common, shared terms across the field. This glossary defines all terminology used in this thesis for ALM in general and for the process under investigation in this work, electron beam melting.

When the intended meaning of a term is the one given in this glossary, the term shall be italicised in the text.

Term	Meaning
Contour	The perimeter of a 3D component when sliced into layers, for example, the *contour* of a cylinder is a circle.
Hatching	Melting of material within the confines of the *contours* by moving the electron beam back and forth in a linear raster pattern.
Auto Power Calc	A calculation performed in the Arcam EBM software to determine the energy input required to maintain a constant *build temperature*.
Layer	A nominally two-dimensional shape that forms a portion of a three dimensional component. By melting layers, 100 μm in thickness, on top of each other a three dimensional object is produced.
Rake	A mechanical arm within the Arcam S12 machine used to collect and apply powder layers.
Speed function	The relationship between beam speed and current are determined by using *speed functions*. The degree to which the beam speed is increased as a result of increasing the beam current is given by the *speed function*.
Focus offset	The value of current, in mA, applied to the focussing coils of the gun column.
Mean current	The current used during the pre-heating stage that sinters powder layers together prior to melting.
Line offset	The distance between beam scan lines during *hatching*.
Line order	The order in which the beam travels along scan lines during *hatching*. A *line order* of 1 means that adjacent scan lines are melted.

Build	The term given to describe a production run in ALM systems because parts are built up incrementally.
Multi-beam	Rapid deflection of the electron beam makes it possible to maintain multiple simultaneous molten pools within the same layer. To the eye it appears as though multiple electron beams are being used.
Theme	A collection of electron beam control parameters used for a specific purpose e.g. a melt *theme* contains all of the necessary parameters (current, speed, *focus offset* etc.) used for melting. Other *themes* include preheating and supports.
Beam current	The current, in mA, of the electron beam.
Beam speed	The traverse speed of the electron beam.
Build assembler	A piece of Arcam software used to slice components within a *build* into layers of user specified thickness. In this work layer thickness was 100 μm.
Build direction	The direction in which components are incrementally produced i.e. the direction perpendicular to the plane of each layer. In general ALM coordinate systems, this is typically the *z*-axis.
Build file	A *.abf file type that contains the layer information generated in the *build assembler*. This file is the data input for the EBM process.
Build temperature	For small *builds* this temperature is the near constant temperature maintained during processing. For larger *builds* the thermocouple moves increasingly further away from the deposition surface and so specifying *build temperature* is ambiguous.
Bed temperature	See *build temperature*.
Materialise Magics	Software from Belgian company *Materialise*, used for placing and orientating components in a virtual ALM machine prior to slicing in the *build assembler* software.
Self-supporting	A geometry which does not require any support structures i.e. there are no over-hanging surfaces.

V. ACKNOWLEDGEMENTS

It would not have been possible to complete this project without the help and support of many people within the Department of Engineering Materials, especially those within the Innovative Metals Research Centre (IMPC) and Institute of Microstructural and Mechanical Process Engineering: The University of Sheffield (IMMPETUS). This work is testament to the generosity of the people I have worked with in terms of both their time and expertise.

My initial thanks go to my supervisor, Dr Iain Todd, who made my transition back to the department seamless and supplied me with more ideas in three years than I will ever have. I shall always be grateful for his advice, support and meetings in 'the Hoi'.

I am also especially grateful for the help and friendship of Dr Michael Blackmore, who taught me all I know about 'Betsy'.

I would like to thank Dr Bradley Wynne for his help and discussions about all things titanium and EBSD, and apologise for regularly hijacking his time. My gratitude also goes to Dr Peter Davies for allowing me to use his invaluable reconstruction program. Special thanks also go to Dr Krzysztof Muszka for all of the hours spent toiling and never giving up hope. I also wish to thank Dr Ignacio Figueroa Vargas for his 'fantastic ideas' and help with the arc melter and Dr Magda Lopez-Pedrosa for EBSD training.

I would like to acknowledge the financial support given by the Engineering and Physical Sciences Research Council (EPSRC) and Renault Formula 1 that made this work possible. Special thanks go to Pat Warner of Renault F1 for his help and for making my day by giving me a tour of a Formula 1 factory, twice.

I would like to thank the technical staff in the Quarrel Laboratory, namely Mr Stuart Bater, Mr Dean Haylock, Mr Phil Staton, Mr Ian Watts, and those at the Sorby Centre of Electron Microscopy, for their training, technical assistance and entertainment.

My thanks also go to my D1, IMPC and IMMPETUS colleagues, past and present, for their friendship and for making my time such an enjoyable experience.

Finally I would like to say a special thank you to my close friends and family, who provided me with much needed support, help and distraction. I would like to dedicate this thesis to my parents: Olwen and Walid, brother: Sami and partner: Amy. Their help, support and confidence in me has made this possible and for that I shall always be in their debt.

To,

Boulton, Sherlock, Baba and Mum.

And in loving memory of,

John Robert Williams (Uncle John)

1. INTRODUCTION

1.1. Additive Manufacturing

Traditional manufacturing techniques, used to produce metallic engineering components, are well understood both in terms of process control and material performance. Generally speaking, wrought material is considered superior to cast material in terms of properties with this enhanced performance coming at an extra cost. Relatively recent advances in layer-based manufacturing technology, originating approximately 25 years ago, means that today it is possible to produce highly complex metallic components directly from 3D CAD models.

This avenue of manufacturing is referred to as additive layer manufacturing (ALM); several methodologies are available to convert 3D CAD data into a physical component. The powder-bed technique of electron beam melting (EBM) will be investigated in this thesis. The alloy system under investigation will be the $\alpha + \beta$ titanium alloy Ti-6Al-4V, the most widely used of all titanium alloys. The EBM system, at the time of writing, is the only commercially available system capable of producing titanium components as a result of its vacuum environment.

The production of highly complex titanium components is of great interest for automotive and aerospace applications as are the potential financial benefits associated with near-net shape processes. However, the potential gains have been advertised for a number of years, without a vast uptake of the technology. Beyond reports of an $\alpha + \beta$ microstructure, limited information is available regarding the metallurgical aspects of the EBM process.

Nonetheless, the potential for the production of structural Ti-6Al-4V components via the EBM method presents exciting opportunities in terms of design. A major strength of the technology lies in the ability to produce novel, light-weight structures from a low density alloy.

The work presented in this thesis has been part-funded by the Renault Formula 1 racing team. The motorsport environment may prove to be ideal for metallic ALM systems – polymer systems are already heavily used for prototypes, packaging of electrical components and casting blanks. The use of metallic ALM components in this sector would help to pave the way for use in commercial automotive and aviation applications. However, this route is far from straightforward and requires a sound understanding of the process. The first milestone is determining the process capabilities and the resulting material behaviour; this is the focus of the work in this thesis.

1.2. Project Aims

The aim of this work is to investigate EBM processing of Ti-6Al-4V to gain a better understanding of both the process and the material produced. The effect of changing some of the key, standard processing variables on the material will be investigated and numerical modelling will be used to predict the field of influence of the electron beam. The potential to modify the 'default' microstructure via chemical means will also be investigated.

1.3. Thesis Outline

Chapter 2 is a review of the literature discussing the general metallurgy of titanium, its alloys and the field of ALM. The history of production of metallic ALM components is discussed alongside the relevant and recent literature available on the EBM process.

Chapter 3 documents the experimental procedures used to carry out all of the investigations in this work. It describes the metallographic methods used to characterise the Ti-6Al-4V samples produced as well as describing how they were produced using an Arcam S12 EBM machine.

Chapter 4 discusses the experimental characterisation and numerical modelling performed to characterise the electron beam. Tests on solid substrate material were used to determine how variation of the input parameters affected the electron beam. Rosenthal's equation has been used as a means of reproducing the thermal effect of the electron beam.

Chapter 5 describes the metallographic work carried out to quantify the microstructures produced during EBM. Microstructure, texture, phase constitution, transformation mechanisms and mechanical properties are all discussed.

Chapter 6 discusses how the addition of boron to Ti-6Al-4V affects solidification, grain morphology and texture prior to- and post- EBM.

Chapter 7 documents the key conclusions from this work.

Chapter 8 suggests avenues for further work which are discussed as a result of the investigations in the previous chapters.

2. LITERATURE REVIEW

This chapter begins with an introduction to titanium and its alloys, specifically the α + β alloy Ti-6Al-4V, that has been the subject of this work. After discussing the material of interest, the second section discusses additive layer manufacture (ALM) of metallic components with specific emphasis on electron beam melting (EBM) commercialised by Swedish company Arcam AB.

2.1. Titanium and Titanium Alloys

2.1.1. History

The occurrence of titanium was first noted at the end of the 18th century by an English clergyman, William Gregor. In 1791, Gregor published the results into his investigations of a black magnetic sand containing an oxide of an unknown element. Gregor concluded that the sand contained "*iron in a magnetic state, united to the calx of a new metallic substance*" [1]. Gregor found this sand in the parish of Menaccan in Cornwall, England and suggested that the new-found element be called menaccanite, after the mineral in which it was found [1,2].

Simultaneously, a German chemist, M. H. Klaproth, was investigating minerals among which was the mineral now known as rutile. Klaproth carried out investigations into the properties of rutile and concluded that it was the oxide of a new element; he named this element titanium after the mythological Greek Titans. Later, Klaproth investigated the mineral ilmenite (Gregor's menaccanite), and found the menaccanite it contained was identical to titanium [1,2].

2.1.2. Extraction

Although discovered in 1791, extraction of elemental titanium did not occur until 1910 when Wilhelm Justin Kroll reduced titanium tetrachloride ($TiCl_4$) with magnesium. This batch process is known as the Kroll Process and remains to be the main method by which titanium is produced commercially. The product of the Kroll process is titanium sponge which requires further processes to remove contamination and consolidate the material [3]. As such, titanium is an expensive metal relative to alternatives such as steel and aluminium alloys.

In 2000, a means of producing cheaper titanium was reported; the Fray-Farthing-Chen (FFC) Cambridge process [4] uses direct electrochemical reduction of TiO_2 in a molten bath of $CaCl_2$. This method is currently being developed into a commercial process with the aim of producing cheap titanium powder.

2.1.3. General Metallurgy

Titanium is a transition metal with an atomic number of 22; it is a highly reactive element and this reactivity, combined with the relatively high melting point, makes the melting of titanium and its alloys difficult. As well as this, at temperatures above a few hundred degrees centigrade, titanium readily absorbs oxygen, nitrogen and hydrogen from the atmosphere; all of which are deleterious to mechanical properties. Unlike hydrogen, oxygen and nitrogen cannot be removed, once absorbed, by any commercially viable process – their presence causes a severe reduction in ductility. The melting of titanium must therefore be carried out under vacuum or in an atmosphere of high purity inert gas [2].

The initial drive for the production and development of titanium and its alloys came from the aerospace industry because of titanium's high strength: weight ratio at elevated temperatures. With a melting point of 1678°C it was initially thought that titanium could be utilised over a wide temperature range; although the useful temperature range was found to be smaller than expected, titanium is of great importance to the aerospace industry with around 80% of all titanium being used in this sector [5].

Figure 2.1 shows the comparatively high specific 0.2% proof stress of titanium with temperature and highlights why titanium alloys are important in aerospace applications. As well as aerospace, titanium is found in automotive, sports, chemical and medical applications as a consequence of their high strength, low density, good resistance to corrosion and biocompatibility inside the human body.

2.1.4. Crystallography

Titanium is an allotropic element existing as two different crystal structures dependant on temperature. Below 883 °C, pure titanium has a hexagonal close packed (HCP) structure and is referred to as alpha phase, denoted α. Above 883 °C the structure transforms to a body centre cubic (BCC) structure and is referred to as beta phase, denoted β [5]. The temperature at which the α↔β transition occurs is known as the beta transus.

The hexagonal unit cell of α titanium has a c/a ratio of 1.587; the ideal c/a ratio for close packed spheres is 1.633. Figure 2.2 (a) highlights the closest packed planes in the hexagonal unit cell. The (0001) plane is referred to as the basal plane, the $(10\bar{1}0)$ plane is one of six prismatic planes and the $(10\bar{1}\bar{1})$ plane is one of three pyramidal planes. Figure 2.2 (b) shows the BCC unit cell of β-titanium and highlights the (110) close-packed plane.

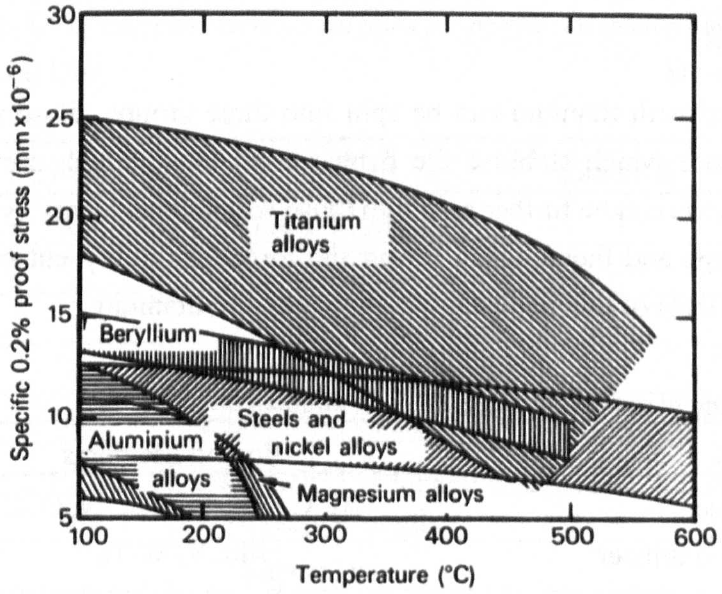

Figure 2.1 : Relationship of specific 0.2% proof stress (ratio of proof stress to relative density) with temperature for light alloys, steels and nickel alloys [5].

The planes shown in the hexagonal unit cell are described by the Miller-Bravais four index notation (*hkil*) whilst planes in the cubic system are described by the three index Miller notation (*hkl*). The Miller-Bravais notation requires that $h + k + i = 0$ and this allows the notation to be abbreviated to (*hk.l*) where . represents *i*. Directions in Miller-Bravais notation are given by [*uvtw*] where $u + v + t = 0$ and again, *t* may be replaced by a dot for abbreviation.

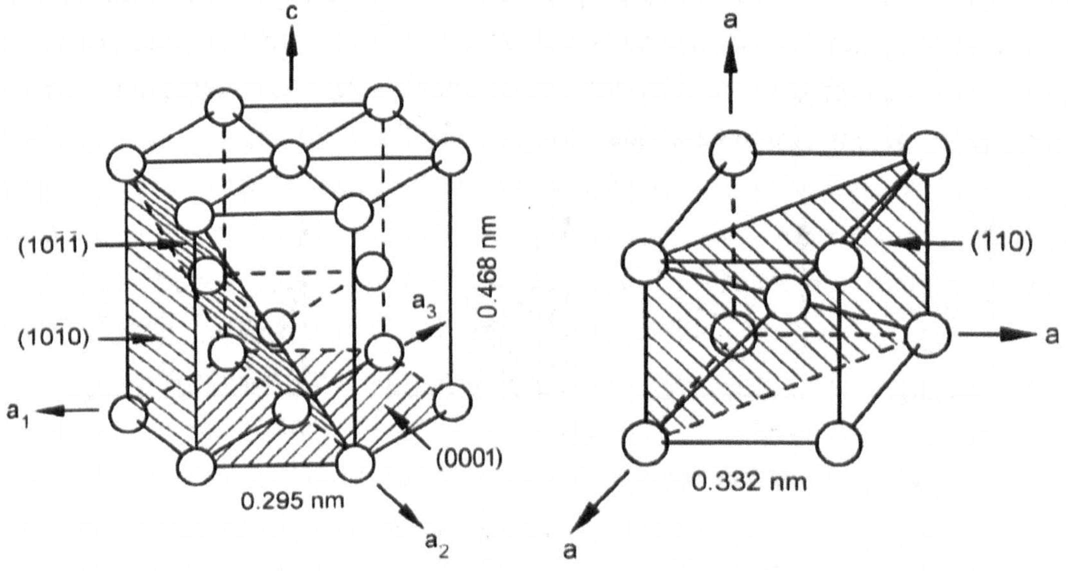

(a) (b)

Figure 2.2 : HCP and BCC unit cells of α-titanium (a) and β-titanium (b) [6].

2.1.5. Alloying

Elements alloyed with titanium can be split into three groups, those which stabilise the α phase, those which stabilise the β phase and those which are neutral. Beta-stabilising elements can be further split into those which form binary systems of the β-isomorphous[1] type and those which favour the formation of a β-eutectoid [5]. Table 2.1 shows the effects of the major alloying elements on titanium.

Table 2.1 : Alloying elements and their effect on titanium alloys [5, 7].

Effect	Alloying Elements
α-stabiliser	Al, Ga; interstitial: N, O, C
β-isomorphous stabiliser	Mo, V, W Ta
β-eutectoid stabiliser	Cu, Mn, Cr, Fe, Ni, Co, Si; interstitial: H
Strengthening elements	Sn, Zr (extensive solid solubility in α and β)

The effects of the above elements on the titanium-rich portion of a pseudobinary system can be seen in Figure 2.3. The dotted phase boundaries show the martensite start (M_s) temperatures. For alloys quenched from the β or α + β phase fields, β transforms to the martensitic form of the α phase, denoted α'. Unlike ferrous materials, the formation of martensite within titanium alloys has a much less pronounced strengthening effect [5].

As well as single phase α and β alloys, three other alloy groups exist which are a mixture of both α and β in differing proportions; these classifications are near-α, α + β and near-β. Changes in crystal structure from α to β and back play a major role in defining titanium properties. The effects of grain size and morphology can be generalised to give trends of behaviour, as shown in Table 2.2.

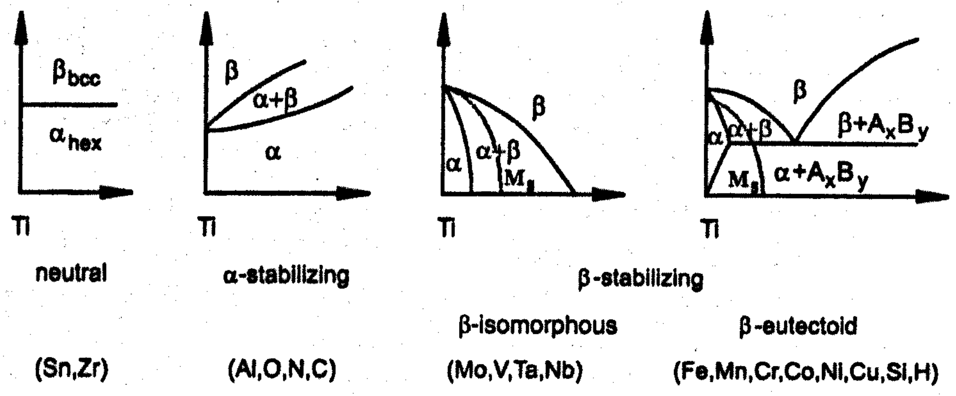

Figure 2.3 : Basic types of phase diagram for titanium alloys [8].

---

[1] β-isomorphs have a similar structure to bcc titanium and do not form intermetallics

Table 2.2 : Influence of microstructure on titanium properties, adapted from [8].

Microstructural Unit Size			Morphology	
Fine	Coarse	Property	Lamellar	Equiaxed
0	0	Elastic Modulus	0	+/- (texture)
+	-	Strength	-	+
+	-	Ductility	-	+
-	+	Fracture Toughness	+	-
+	-	Fatigue Crack Initiation	-	+
-	+	Fatigue Crack Propagation	+	-
-	+	Creep Strength	+	-
+	-	Superplasticity	-	+
+	-	Oxidation Behaviour	+	-

Key : 0 = no effect, + = increase in property, - = decrease in property

2.1.6. Alpha Alloys

Alpha alloys can be split into fully-α and near-α alloys. There are few commonly used fully-α alloys which include commercial purity (CP) alloys (Ti-O alloys) and the ternary Ti-5Al-2.5Sn system. These single phase alloys have relatively low tensile strengths but reasonable creep strength owing to high thermal stability. Ductility is good, even at very low temperatures, and such alloys are easily welded. Formability of fully-α alloys is limited because of the hexagonal crystal structure (fewer slip planes than a cubic structure) and a high rate of strain hardening [5].

Mechanical properties of fully-α alloys exhibit relative insensitivity to microstructure, however, three different α morphologies can be formed. Working and annealing in the α phase field produces equiaxed α grains with relatively small grain sizes. Quenching from the β phase field results in the formation of martensite, α', and slow cooling from the β phase field forms Widmanstätten α plates [5].

Near-α alloys are forging alloys developed to meet increased temperature demands in the compressor sections of gas turbine engines. In comparison to fully-α alloys, near-α alloys have increased room temperature tensile strength and, above 400°C, show the greatest creep resistance of all titanium alloys.

2.1.7. Alpha + Beta Alloys

To improve upon strength and formability issues associated with fully-α alloys, investigations were made into alloys containing both α and β phases. The result affords relatively high tensile strength, improved formability, with a sacrifice in creep strength above 400°C and reduced weldability. The main use of these alloys is in forged components such as fan blades in jet engines. Alpha plus beta alloys contain α-stabilising elements alongside 4 – 6% of β-stabilising elements; these allow the retention of β phase on cooling [5]. Enhancements in strength can be achieved by heat treatments with a wide range of microstructures, and therefore properties, achievable.

2.1.8. Beta Alloys

Beta alloys are formed by additions of β-stabilising elements such that a fully β structure is retained at room temperature. These alloys provide high strength, good formability and high hardenability when compared to the other classes of titanium alloys. The increased formability arises because of the BCC structure of the β phase. As previously mentioned, molybdenum is a β-stabiliser and β alloys are defined as having a molybdenum equivalent of ≥ 10; Mo equivalent = 1.0(% Mo) + 0.67(% V) + 0.444(% W) + 0.28(% Nb) + 0.22(% Ta) + 2.9(% Fe) + 1.6(% Cr) – 1.0(% Al). The β alloy Ti-10V-2Fe-3Al (Ti 10-2-3) has been used as a replacement for steel on landing gear components as it has a combination of high strength and good formability.

The schematic phase diagram, Figure 2.4 (a), highlights the regions over which the titanium alloy classifications exist. The martensitic start (M_s) and finish (M_f) lines are represented by the dashed line in the figure; Flower [9] states that typically, the M_s and M_f temperature are very close together in titanium alloys. A very similar phase diagram shown in Figure 2.4 (b) indicates some engineering alloys and their positions in the classification system. It is interesting to note that in this diagram the M_s and M_f temperatures are separate in contrast to that reported by Flower [9].

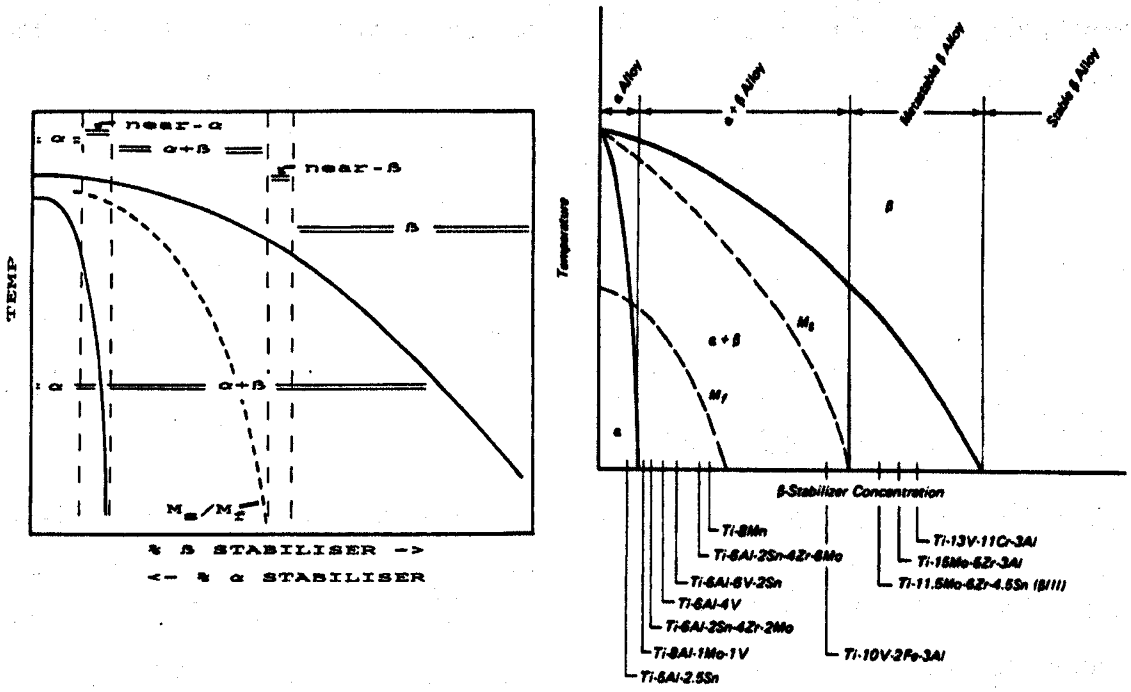

(a) (b)

Figure 2.4 : (a) Schematic section of a phase diagram for ternary titanium alloys containing α and β stabilising elements [9] and (b) composition of some engineering titanium alloys mapped onto a pseudo binary phase diagram [10].

2.2. Phase Transformation and Microstructure in α + β Alloys

The final microstructure of α + β titanium alloys depends on the transformation of the high temperature β phase. Very slow cooling allows α to form continuous layers on prior β grain boundaries with solute rich, retained β separating lamellar α plates (Figure 2.5 A). At faster cooling rates, α forms lamellar colonies (Figure 2.5 B); when these colonies are regular and interleaved, the famous basket weave α structure is produced (Figure 2.5 C). Increased cooling rates nucleate more α variants, with finer precipitates, and a true Widmanstätten structure with a reduced microstructural unit size (Figure 2.5 D). Quenching titanium alloys from the β phase field prevents diffusional change; a diffusion-less transformation to martensite occurs (Figure 2.5 E). All of these microstructures result from heat treating in the β phase field, heat treatment in the α + β phase field allows primary α to be retained on cooling, surrounded by a fine transformed structure (Figure 2.5 F) [9].

On cooling from the β phase field, α forms with an orientation relationship with the β phase from which it transforms. Below the β transus, α grains form with their $\{0001\}$basal, close-packed planes parallel to the $\{110\}$close-packed planes in the β phase. The distance between basal planes in α is slightly larger than the distance between the $\{110\}$ planes causing an atomic distortion upon transformation from β to α. The relationship between the planes and crystallographic directions upon transformation from β to α is given below and is referred to as the Burgers relationship after the investigations made by Burgers on zirconium [11].

$$\{0001\}\alpha \parallel \{110\}\beta \quad \text{(parallel planes)}$$
$$\langle 1120\rangle \alpha \parallel \langle 111\rangle\ \beta \quad \text{(parallel directions)}$$

Figure 2.6 shows the mechanism for the Burgers relationship in zirconium; the same relationship applies to titanium. Within the BCC β phase there are six close packed (slip) planes and two close packed (slip) directions – this leads to the α grains having twelve possible orientations upon formation. These twelve possible orientations are referred to as variants and α grains nucleate and grow preferentially along the variant planes; thus plates of α are developed. It is multiple repetitions of the twelve orientations formed upon transformation that form the basket weave microstructure [5, 8].

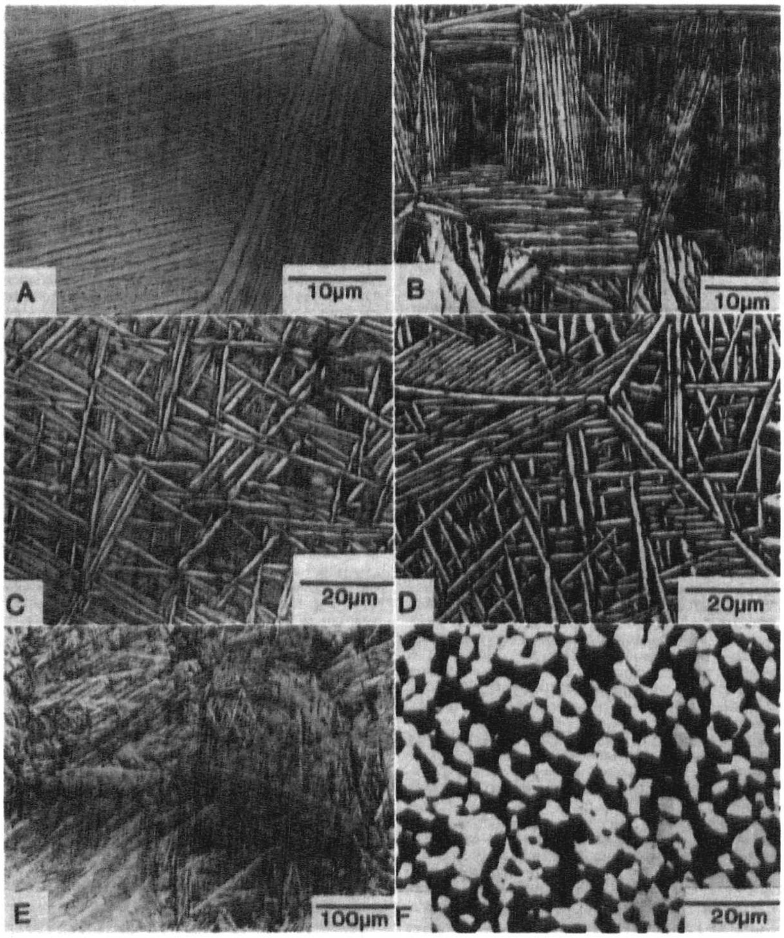

Figure 2.5 : A range of titanium microstructures after transformation of the β phase. A. Ti-1Mo furnace cooled, B. Ti-1Mo slow air cooled, C. IMI 550 air cooled, D. IMI 550 forged above transus and air cooled, E. IMI 829 WQ and F. IMI 550 forged, annealed and air cooled [9].

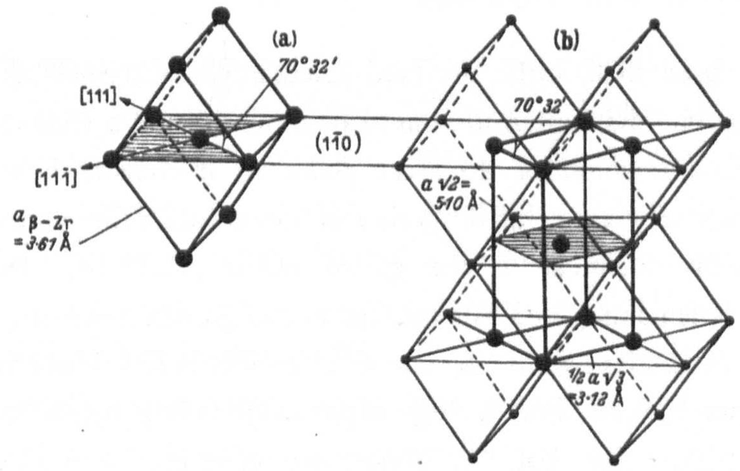

Figure 2.6 : Mechanism for the Burgers relationship in zirconium [2].

The formation of Widmanstätten (basket weave) α plates is shown schematically for Ti-6Al-4V in Figure 2.7 as a result of relatively slow cooling from the β phase. Slower cooling rates would result in the formation of α phase along prior β grain boundaries, referred to as grain boundary α or α_{GB}.

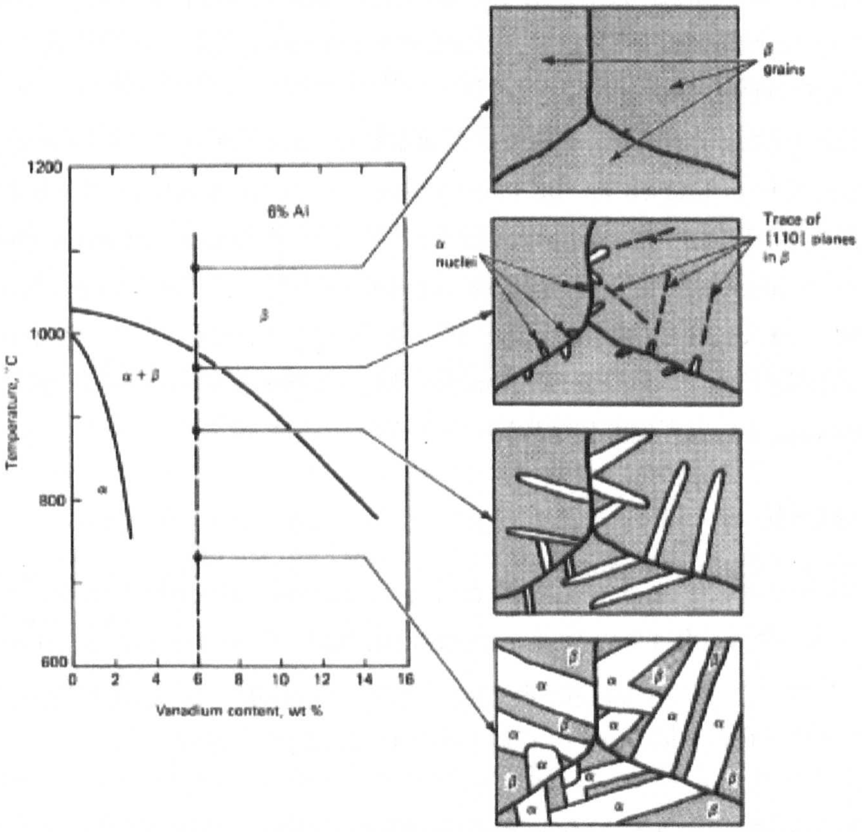

Figure 2.7 : Formation of Widmanstätten α laths in Ti-6Al-4V as a result of slow cooling from the β phase field. The α laths form with the Burgers orientation relationship with the β phase, some of which is retained at room temperature [7].

2.2.1. *The Martensitic Transformation*

Whilst initially used to describe the hard acicular phase formed upon quenching steels, martensite and the martensitic transformation occur in a wide range of metals and alloys. Transformation of a parent phase to martensite is a diffusionless transformation whereby cooperative motion of atoms forms the martensite structure that is chemically identical to the parent phase [12,13,14]. The martensitic transformation, when considered as a nucleation and growth processes, posses a very large barrier to nucleation; whilst the barrier to growth is practically zero. The large nucleation barrier thus requires a very large undercooling below the equilibrium transformation temperature. The low, almost negligible barrier to growth, results in martensite grain growth at speeds approaching the speed of sound [14].

The cooperative motion of atoms in the martensitic transformation results in the transformation being halted by grain boundaries; transformation across grain boundaries can not occur and a fine initial grain size stabilises the parent phase hindering transformation to martensite [12]. The atomic motion during transformation is restricted by the surrounding matrix, resulting in plastic deformation. The deformation occurs more easily in the transforming martensite [12]. Owing to the nature of the transformation, an orientation relationship always exists between the martensitic and parent phase.

Martensite plates formed in a parent grain lie parallel to a certain plane in the parent phase; this is known as the habit plane. In titanium alloys, the habit plane is close to $\{334\}_\beta$ [15]. As well as the $\beta \rightarrow \alpha + \beta$ transformation, the $\beta \rightarrow \alpha'$ transformation also obeys the Burgers relationship [2, 6]. In some alloys, the M_s temperature is affected by the cooling rate. In binary titanium alloys quenched from the β phase field it has been shown that the M_s temperature is unaffected by cooling rates in the range 10 – 10 000 K/s [2].

2.3. Ti–6Al–4V

The alloy Ti-6Al-4V is an α + β alloy and is commonly described as the '*workhorse*' of the titanium alloys. It accounts for more than half of the sales of all titanium alloys [7,16] and contains an α stabiliser (6 wt% aluminium) and a β stabiliser (4 wt% vanadium) with small additions of other elements, as per Table 2.3.

Table 2.3 : ASTM B348 Ti-6Al-4V composition specification.

Element	Al	V	Fe	O	N	H	C	Ti
ASTM B348, wt%	5.5 – 6.75	3.5 – 4.5	< 0.40	< 0.20	< 0.05	< 0.015	< 0.08	Bal.

2.3.1. Applications of Ti-6Al-4V for Aerospace

Ti-6Al-4V components are widely used in structural components for aircraft. Even on a density normalised comparison, Ti-6Al-4V possesses higher yield strength and fatigue strength as well as better corrosion resistance, higher modulus of elasticity and higher temperature capability in contrast to competing metals. In large structural components, the most important mechanical property is fatigue crack propagation resistance – inspection times are based on this property and significant disassembly is required in order to perform inspections [6].

Forging Ti-6Al-4V components via the most economical route (forge in α + β phase field and mill anneal) results in a nominally equiaxed α structure with some degree of recrystallisation. A fully lamellar microstructure can be achieved by annealing in the β phase field (β annealing) but this adds expense to the component. This expense, however, is generally compensated for by the enhancement in crack propagation resistance. As-cast Ti-6Al-4V exhibits the fully lamellar microstructure required for crack resistance but maximum component size is limited by furnace and hot isostatic press (HIP) facilities [6].

Titanium α + β alloys are also used in aero-engines as both rotating and non-rotating components. Ti-6Al-4V is limited to the fan, low pressure (LP) compressor and front stages in the high pressure (HP) compressor region of a gas turbine engine. This limitation arises because Ti-6Al-4V becomes unusable at temperatures in excess of 300°C.

Fan and compressor blades require resistance to crack nucleation (HCF resistance) as service produces large oscillating stresses. Good LCF resistance is also required in the regions where blades are attached to the disk. For this purpose, forged components are usually recrystallised to produce a bi-modal microstructure that has an increased HCF strength over equiaxed and mill-annealed microstructures [6].

Ti-6Al-4V is the most common disk material where good LCF life is essential alongside resistance to crack nucleation. Again, use is made of the bi-modal microstructure. Non-rotating Ti-6Al-4V engine components include castings, ducts, stators and manifolds [6].

2.3.2. Wrought Ti-6Al-4V Microstructures and Mechanical Properties

The properties of Ti-6Al-4V are developed by cooling from the β or α + β regions and subsequent low temperature ageing to decompose martensite formed on quenching. Table 2.4 shows some typical properties for wrought Ti-6Al-4V in two conditions of heat treatment.

The two most important microstructures in titanium alloys are fully lamellar and bi-modal [17], see Figure 2.8. Bi-modal microstructures consist of equiaxed primary alpha grains (α_p) surrounded by an $\alpha + \beta$ lamellar structure. The bimodal structure arises as a result of thermo-mechanical processing (TMP); Figure 2.8 (b) shows a schematic production route for the bi-modal structure. The homogenisation step, step I, results in a fully lamellar structure on cooling from above the β transus. The cooling rate is a critical parameter as the width of the α lamellae, and the amount of grain boundary α formed on prior β grain boundaries, increases with decreasing cooling rate.

Table 2.4 : Typical properties of wrought Ti-6Al-4V after heat treatment [5].

Condition	0.2% Proof Stress /MPa	Tensile Strength /MPa	Elongation /%
Annealed, (700°C)	925	990	14
Solution Treated (α+β phase field) and Aged (500°C)	1100	1170	10

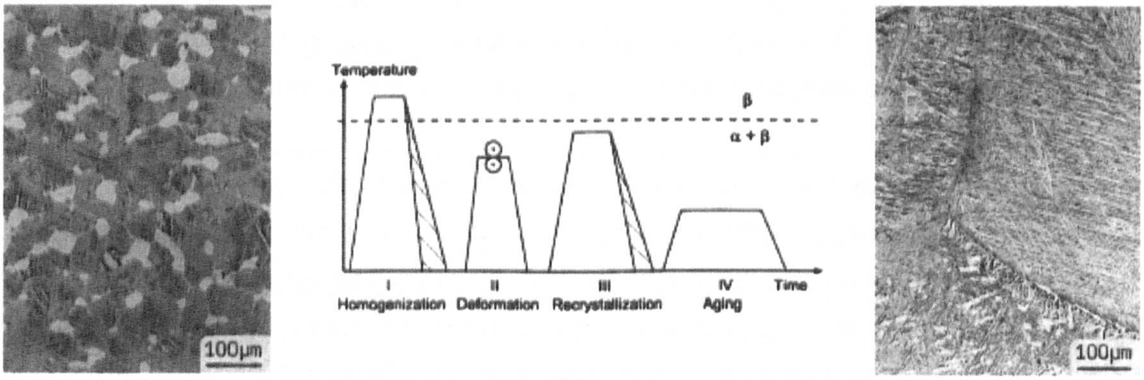

(a) (b) (c)

Microstructure	Tensile Strength (MPa)	Yield Strength (MPa)	Elongation (%)	Reduction of Area (%)
Bimodal (a)	967	930	13.5	50.6
Basket Weave (c)	970	907	7.3	17.1

Figure 2.8 : (a) Bi-modal Ti-6Al-4V microstructure, (b) schematic production route for the bimodal structure and (c) fully lamellar microstructure and below the effect of microstructure on Ti-6Al-4V on mechanical properties [17,18].

Deformation in the $\alpha + \beta$ phase field plastically deforms the lamellar structure; the recrystallisation step results in the formation of equiaxed α_p. Equiaxed α_p and β grains are formed during recrystallisation as a result of the recrystallised β phase penetrating along α/α grain boundaries; individual α_p grains result [17]. During the recrystallisation step, temperature is a critical parameter - it controls the volume fraction of α_p produced. The cooling rate determines the width of α lamellae and colony size of the lamellar structure. It is possible to form a structure of solely α_p grains, with no α lamellae within β grains, if a slow enough cooling rate is achieved. The resulting structure is termed 'globular' and the β grains are located at triple points of the α_p grains [17].

2.3.3. *Heat Treatment of Ti-6Al-4V*

Heat treatments of forged Ti-6Al-4V and the resulting microstructures are discussed by Qazi and Rack [19]. The lamellar, bimodal and equiaxed microstructures discussed above are reported to form as a result of the following heat treatments:

(i) solution treatment > β transus, air cool → age 700 – 800°C → lamellar
(ii) solution treatment < β transus (900 – 950°C) → age 700°C → bimodal
(iii) solution treatment < β transus (800 – 925°C) → equiaxed [19]

General heat treatments for wrought α + β alloys are summarised in Table 2.5.

Table 2.5 : Heat treatments for α + β titanium alloys [7].

Heat Treatment	Heat Treatment Cycle	Microstructure
Duplex anneal	Solution treat at 50 – 75 °C below T_β, air cool and age for 2 – 8 hrs at 540 – 675 °C	Primary α, plus Widmanstätten α + β regions
Solution treat and age	Solution treat at ~40 °C below T_β, water quench and age for 2 – 8hrs at 535 – 675 °C	Primary α, plus tempered α' or α + β mixture
Beta anneal	Solution treat at ~15 °C above T_β, air cool and stabilise at 650 – 760 °C for 2hrs	Widmanstätten α + β colony
Beta quench	Solution treat at ~15 °C above T_β, water quench and temper at 650 – 760 °C for 2hrs	Tempered α'
Recrystallisation anneal	925 °C for 4hrs, cool at 50 °C/hr to 760 °C, air cool	Equiaxed α with β at grain boundary triple points
Mill anneal	α + β hot work plus anneal at 705 °C for 30 mins to several hours and air cool	Incompletely recrystallised α with a small volume fraction of β particles

2.3.4. Martensite in Ti-6Al-4V

It is well documented that quenching Ti-6Al-4V from above the β transus to below the M_s temperature results in a martensitic microstructure. However, figures given in literature for the required cooling rate and M_s temperature vary. Ahmed and Rack [20] report that: cooling rates above 410 K/s produce a fully martensitic structure, cooling rates between 410 K/s and 20 K/s result in the formation of α by a massive transformation and, at cooling rates lower that 20 K/s, α formation is diffusion controlled resulting in a Widmanstätten α structure. Table 2.6 compares M_s temperatures, cooling rates and compositions for some Ti-6Al-4V alloys reported in the literature.

Table 2.6 : Ms temperatures, cooling rates and compositions from literature.

Ms °C	$\frac{dT}{dt}$ K/s	Ref.	Year	Composition wt%							
				Ti	Al	V	Fe	O	C	N	H
~750	-	[2]	1956	Ti-4.25V binary							
625	-	[21]	1959	bal	6.0	4.0	-	-	-	-	-
800	-	[10]	1994	Ti-6Al-4V							
800	-	[22]	1995	Ti-6Al-4V							
575	>410	[20]	1998	bal	6.04	4.03	0.12	0.09	0.03	0.009	23 ppm
775	-	[8]	2003	Ti-6Al-4V							
-	>16.7	[6]	2003	Ti-6Al-4V							
-	48	[23]	2003	bal	6.1	4.3	0.16	0.12	0.01	0.06	0.015
> β transus (100% α') 900 – 750 (α' +α)	WQ	[19]	2003	Ti-6Al-4V							

M_s temperature is a function of chemistry and as such, variations in the literature may be, in part, attributable to compositional differences. Figure 2.9 shows the variation of M_s temperatures with additions of V and Fe to pure titanium. Variation in vanadium content within the limits of ASTM B348 (3.5 – 4.5 wt% V) causes a ~30 °C decrease in the M_s temperature. Whilst over the allowable range for Fe content in ASTM B348 (0 – 0.4 wt% Fe), a ~25 °C decrease in M_s is observed in the binary system. If the effect of alloying elements on the M_s temperature is assumed to be additive, as assumed by Neelakantan *et al.* [24] for a β alloy, the M_s temperature of Ti-6Al-4V may thus vary by approximately 55 °C based purely on vanadium and iron concentrations alone. As well as chemistry, Leyens and Peters [8] state that the M_s

temperature is also a function of starting microstructure and microstructural homogeneity.

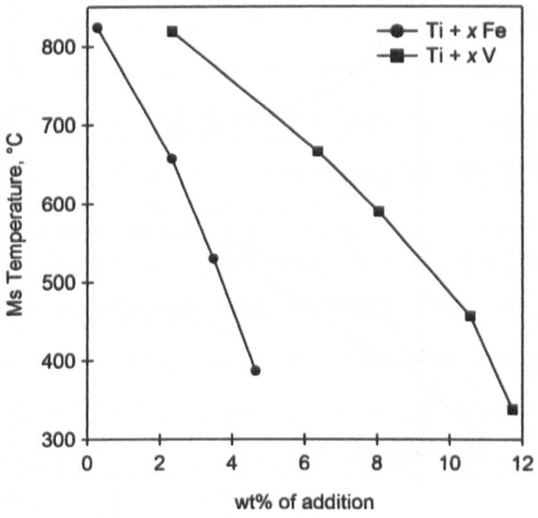

Figure 2.9 : Variation in M_s for Ti-Fe and Ti-V binary alloys, adapted from [2].

It is evident from searching literature that data regarding the M_s temperature for titanium alloys is somewhat limited and, as shown in Table 2.6, can vary quite significantly. To the author's knowledge, the variations presented in Table 2.6 have not been investigated; this may be a consequence of titanium martensite being a non-engineering material. As highlighted in Figure 2.4, literature is also inconsistent regarding the separation, if any, between the M_s and M_f temperatures.

From the data available for binary titanium systems, it is possible to produce an approximation for the M_s temperature in β titanium alloys by assuming each element in an alloy contributes to the M_s of the alloy via an additive process, neglecting interactions between elements and grain size dependence [24].

2.4. Boron Additions to Titanium Alloys

2.4.1. *Introduction to Constitutional Supercooling*

Solidification of alloys is controlled by the diffusion of solute into the liquid (analogous to the removal of latent heat in pure metals) and the temperature gradient in the solidifying liquid [25]. A variation in solute content of the liquid exists ahead of the solidification front (Figure 2.10 (a)) and as such, the equilibrium solidification temperature (T_e) also varies with distance from solidification front (Figure 2.10 (b)). The temperature of the liquid (T_L) also varies with distance and thus a temperature gradient exists in the liquid; solidification behaviour is determined by comparison of T_L with T_e.

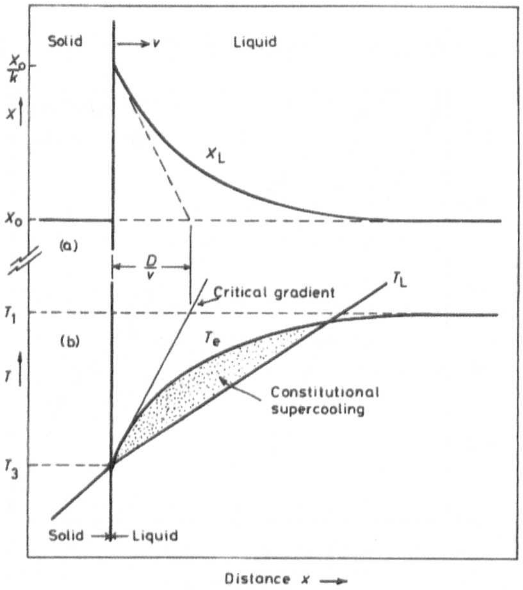

Figure 2.10 : Constitutional supercooling ahead of a planar solidification front showing (a) composition profile and (b) temperature profile. T_e = equilibrium solidification temperature, T_L = liquid temperature [25].

If T_L is less than T_e, the liquid temperature lies below the equilibrium temperature and the liquid is supercooled. This phenomenon is a result of compositional (or constitutional) effects and is known as constitutional supercooling; stable protuberances, i.e. non-planar growth, can only exist under these conditions. From Figure 2.10, the tip of any protuberance that forms will be at a higher temperature than the planar front. However, as long as the temperature of the tip is less than T_e, solidification can occur and the tip may grow in a cellular/dendritic manner.

If T_L is greater than T_e, any protuberances formed are at a higher temperature than the planar front and are also above the equilibrium solidification temperature. The temperature of the tip is raised above the liquidus temperature and melts back thus, planar growth is stable.

2.4.2. Boron Additions to Titanium Alloys

In 2003, Zhu *et al.* [26] reported the effect of additions of boron to dental cast titanium alloys. Samples were produced with boron contents ranging from 0 to 1.02 wt %. Increasing boron content was found to significantly refine the as-cast grain size. However, in Ti-6Al-4V + *x*B alloys, grain size refinement was coupled with a decreased tensile elongation and only a modest increase in tensile strength, with increasing boron content. Refinement was attributed to the precipitation of TiB particles and the decrease in elongation attributed to the brittle nature of TiB. For other titanium alloy systems, an initial increase in elongation (due to grain refinement) was counteracted by increasing amounts of brittle TiB at higher boron contents.

In 2005, Tamirisakandala *et al.* [27], making reference to the Ti-B binary phase diagram, argued that precipitation of TiB occurs after the formation of primary β grains. TiB particles are thus not present to act as an inoculant and promote refinement as suggested by Zhu *et al.* [26]. The suggested mechanism of refinement is via solute partitioning and associated constitutional supercooling ahead of the solidification front.

The low solubility of boron in titanium (<0.02 wt%) results in the rejection of boron into the liquid surrounding primary β grains. The solute enrichment of this liquid causes a variation in the liquidus temperature and, the resulting constitutional supercooling, causes an instability at the liquid/solid interface. This is thought to provide an additional driving force for the nucleation of finer primary β grains ahead of the solid/liquid interface [27].

The relative contribution of a solute to constitutional supercooling can be predicted by use of the growth restriction factor Q [27, 28]:

$$Q = m_l C_o(k-1) \qquad (2.1)$$

where m_l is the slope of the liquidus, C_o is the solute concentration and k is the partition coefficient. Solutes with a high growth restriction factor partition strongly ahead of the solid/liquid interface resulting in a high degree of constitutional supercooling [28].

Sen *et al.* [29] discuss the effects of boron additions to the mechanical behaviour of Ti-6Al-4V. Whilst modest increases in yield and tensile strength were in agreement with the work of Zhu *et al.* [26], a small increase in elongation was observed at 0.05 wt% boron. This is shown in Figure 2.11 alongside the effect on tensile strength. Increasing boron content was also found to decrease fracture toughness. Despite the deleterious effects of boron additions, the authors emphasise the fact that trace amounts of boron refine as-cast microstructures to those resembling heavily thermo-mechanically processed material.

Boron additions of ≤ 1 wt% have also been shown to improve elevated temperature fatigue behaviour compared to standard Ti-6Al-4V. Although an increase is observed at 1 wt% B, the addition of 0.1 wt% B yields the largest improvement. Enhanced fatigue behaviour is attributed to the refinement in grain size and the presence of TiB whiskers, decreasing slip length and impeding dislocation motion [30]. On slow cooling from above the β transus, boron additions to Ti-6Al-4V have also been observed to produce equiaxed (or globular) α grains that nucleate and grow from TiB precipitates [28, 31]. Boron is also known to raise the β transus of titanium alloys, an increase of ~60 °C has been reported for a Ti-6Al-4V-1.7B weight percent alloy [32].

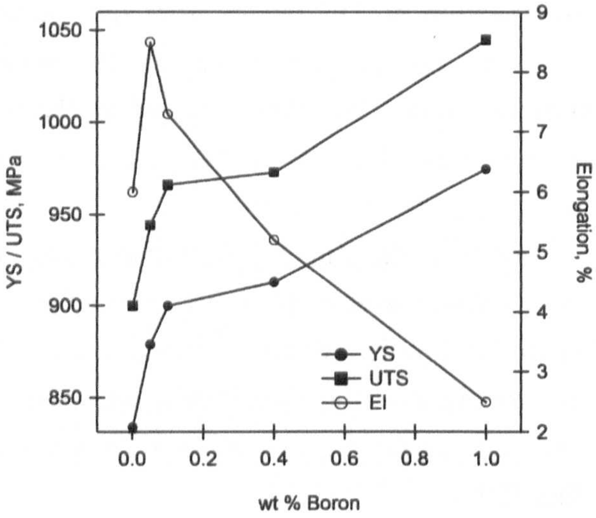

Figure 2.11 : Yield strength, ultimate tensile strength and elongation versus boron content of Ti-6Al-4V-xB alloys, adapted from [27, 30].

2.5. Texture

Titanium is used in polycrystalline form and, like most other materials, crystallographic orientation is usually non-random [33]. A non-random orientation suggests that certain orientations exist with higher probability; these orientations are the preferred orientations of the crystal structure. Certain material properties (Young's modulus, ductility, toughness and strength [34]) are dependant on texture and, as such, textured materials exhibit anisotropy. This is especially true of titanium alloys containing large volume fractions of HCP α phase. The HCP structure has an inherent anisotropy and a textured HCP structure may show significant elastic and plastic anisotropy [5]. Figure 2.12 highlights the ~45 GPa difference in Young's Modulus depending on HCP unit cell orientation.

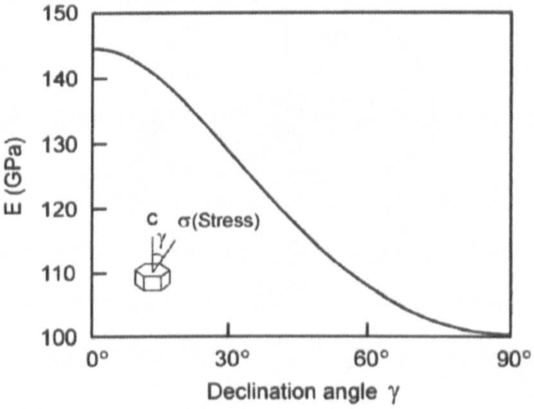

Figure 2.12 : The effect of HCP unit cell orientation on Young's Modulus [6].

2.5.1. Texture Representations

Quantitative texture analysis requires the relation of the sample coordinate system to that of individual crystals. This can be done using Euler angles or an angle-axis pair [35]. Euler angles relate two orthogonal right-handed coordinate systems (sample: *a*, *b*, *c*; crystal: *x*, *y*, *z*) through three rotations. In Bunge convention the three rotations are denoted φ_1, Φ and φ_2. An angle-axis pair brings two coordinate systems to coincidence via a single rotation about an axis [35]. Sample coordinate systems are usually defined by the manufacturing process; rolled material is defined by the rolling direction (RD), transverse direction (TD) and normal direction (ND).

Texture is commonly presented by the use of pole figures. Pole figures are stereographic projections produced by projecting a set of crystallographic directions/planes onto a sphere and then onto a circle, as per Figure 2.13 (a). The sample coordinate system, as described above, needs to be present on the pole figure in order to relate crystal orientations to the coordinate system. Individual grain orientations can be discerned by, as an example, plotting the position of the three $\{100\}$ poles relative to the coordinate system. A (100) pole figure is the result which can be plotted for individual grains, Figure 2.13 (b), or all of the grains in a polycrystalline sample, Figure 2.13 (c).

Plotting pole density, relative to that expected for a sample with random texture, allows for clear visualisation and quantification of preferred orientations, Figure 2.13 (d) and (e).

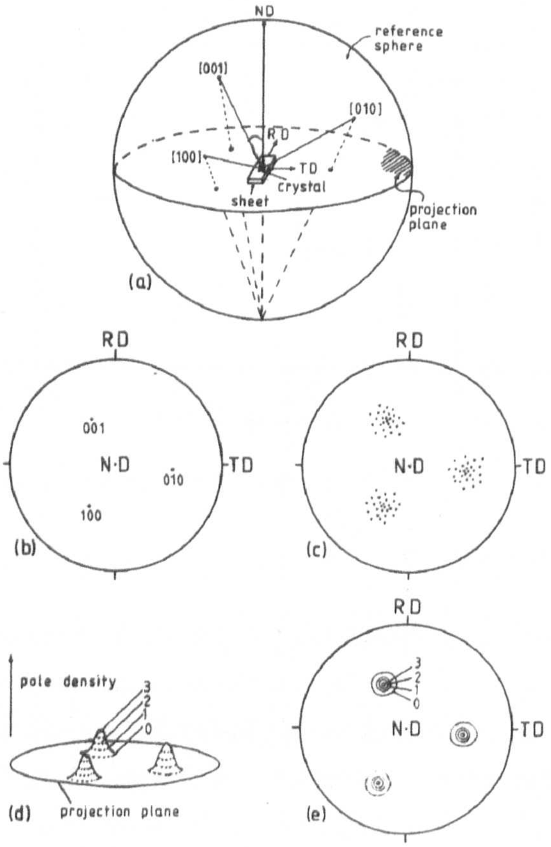

Figure 2.13 : (a) Projection of $\{100\}$ *poles onto a reference sphere and then onto a projection plane, (b) projected poles of a single grain, (c) projected poles of textured grains, (d) pole density distribution and (e) a contour map of the pole density [36].*

2.5.2. Electron Back Scatter Diffraction (EBSD)

Diffraction techniques are most widely used to measure crystallographic orientation; x-ray diffraction (with a pole-figure goniometer), electron diffraction using transmission electron microscopy (TEM) or scanning electron microscopy (SEM) and neutron diffraction are all suitable methods. The use of a SEM is a highly popular technique as it does not require a substantial background in texture theory from the user [34] and can be performed on bulk samples (where information is gained from the uppermost layer). Interaction of electrons with the uppermost layer produces electron back-scatter diffraction patterns (EBSP) analogous to Kikuchi patterns in TEM [35].

Automation of EBSP indexing and specimen scanning allow users to set up and leave the instrument to acquire data; relatively large orientation maps can therefore be produced. This technique, however, is only applicable to crystals with fairly low dislocation densities, good surface preparation of the sample is essential and automatic indexing can produce errors. These errors are either from non-indexing or mis-indexing; both of which are orientation dependant and can lead to texture artefacts.

2.5.3. *Fibre and Cube Textures*

Two commonly observed textures in processed metals are the fibre and cube textures. Fibre textures have a uniaxial (fibre) symmetry that can result from a process such as the drawing of wire [35]. The drawing process causes individual crystals to align a certain crystallographic direction parallel to the wire axis and is observed in artificial and natural fibres.

Cube texture is usually observed in rolled sheet and results from a certain crystallographic plane, within the rolled grains, being nominally parallel to the sheet surface. A certain direction on the plane is also nominally parallel to the rolling direction.

2.6. Summary

Ti-6Al-4V is a common, widely used titanium alloy. Microstructure is strongly influenced by processing and post-processing heat treatments; this allows a wide variety of microstructures to be produced as evident in Figure 2.5. Conventional manufacturing techniques (wrought, cast etc) are well established and the manipulation of microstructure via processing or heat treatment is well documented.

The phase transformations observed in Ti-6Al-4V are also well documented although there is some discrepancy in the literature regarding the start temperature for the formation of martensite (M_s), the required cooling rate and the temperature difference between M_s and M_f temperatures. A widely referenced paper by Ahmed and Rack [20] suggests a cooling rate of 410 Ks^{-1} is necessary for the formation of martensite.

The addition of boron to Ti-6Al-4V has been found to refine both prior β grains size and α lath width. Although the presence of brittle TiB particles can be deleterious to elongation and fracture toughness, additions of boron of the order of 0.1 wt% have potential to increase yield strength, ultimate tensile strength, elongation and high temperature fatigue performance.

2.7. Additive Layer Manufacture

2.7.1. *Introduction*

Additive processing, as the name suggests, involves the addition of material, in layers, to produce a component. Such processes have been given many names; the field itself has been referred to as rapid prototyping (RP), rapid tooling (RT), rapid manufacturing (RM), freeform fabrication (FFF), solid freeform fabrication (SFF), layer additive manufacture (LAM) and additive layer manufacture (ALM), amongst others. Unless otherwise appropriate, ALM will be used for the remainder of this work to describe the aforementioned processes. Acronyms are also rife for the commercial systems available which will be discussed shortly.

2.7.2. *Stereolithography (SLA)*

The very first ALM process is considered to be stereolithography (SLA); a commercial patent in 1986 was followed by a working machine in 1987. The process uses an ultra-violet (UV) laser to cure photocurable resin in layers, derived from a computer aided design (CAD) model. The production of a 3D CAD model that is then '*sliced*' into nominally 2D layers is the ethos behind all ALM processes – variation arises from the means in which the 2D layers are recombined to '*build*' the 3D object.

In 1988 the standard triangulation language (STL) file was chosen as a neutral format between CAD packages and stereolithography systems. A *.stl file is a conversion of a CAD geometry into an approximation using triangles [37]. It is the *.stl file that is sliced into layers; in SLA layer thickness is approximately 100 μm. Figure 2.14 shows schematically (a) CAD model → *.stl file → sliced layers and (b) the SLA process.

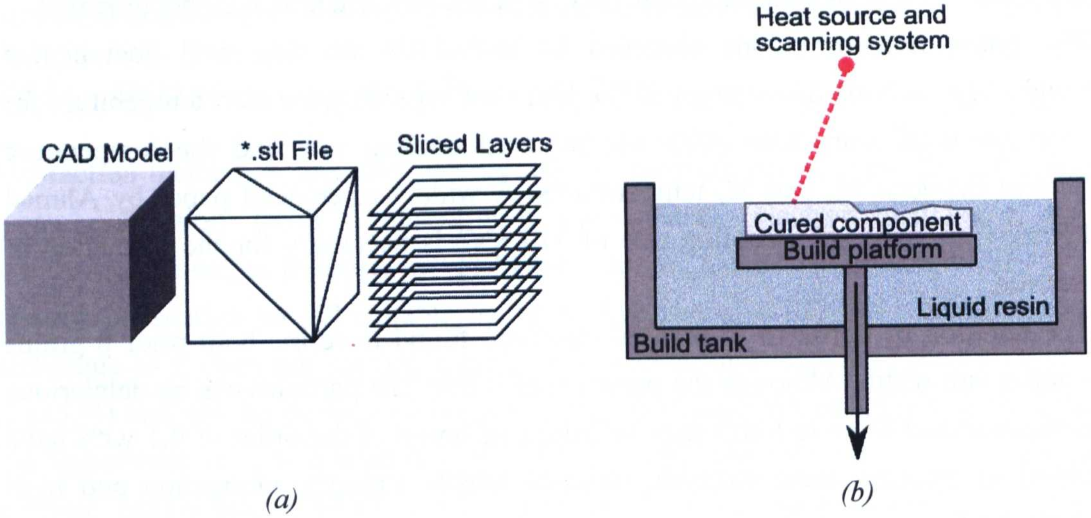

(a) *(b)*

*Figure 2.14 : Schematic of (a) generation of sliced layers from a CAD model via a *.stl file and (b) the stereolithography (SLA) process.*

2.7.3. *ALM Hardware*

ALM processes have been described with the prefix *rapid* (as in RP, RT and RM) arising from the lack of typical constraints associated with conventional processing. Components are made without the need for tooling which allows for both a cost and time saving. The lack of tooling also allows many variations of a design to be produced with no cost penalties. Names such as freeform fabrication (FFF) [38] were used to describe the processes because of the perceived design freedom tool-less production allowed.

ALM hardware is currently available from a variety of original equipment manufacturers although systems and processes differ depending on material and the methods by which layers are deposited. Table 2.7 lists some of the many different methods that are currently used in ALM.

In the above SLA schematic, the arrow indicates the direction of motion of the build table; the table moves down by one layer thickness after the completion of each layer. It is convention in ALM to refer to this axis, perpendicular to the layers, as either the *build axis* or the *z*-axis.

Table 2.7 : ALM processes and equipment manufacturers, adapted from [39].

Process	Shorthand	OEM
3D Keltool	-	3D Systems
Electron beam melting	EBM	Arcam AB
Direct laser forming	DLF	Trumpf
Direct metal deposition	DMD	POM Group
Direct metal laser sintering	DMLS	EOS
Laser additive manufacture	LAM	Aeromet
LaserCusing	-	concept laser
Laser consolidation	-	Accufusion
Laser engineered net shaping	LENS	Optomec
Direct metal printing	DMP	ProMetal RCT
Selective laser melting	SLM	MTT Group
Selective laser sintering	SLS	3D Systems
Shaped metal deposition	SMD	Rolls Royce
Ultrasonic Consolidation	UC	Solidica
Electron beam freeform fabrication	EBF^3	NASA [40]

2.7.4. *Advantages and disadvantages of ALM*

Layer-based production techniques are credited with many advantages that differentiate them from the conventional forming, moulding or machining (subtractive) processes. The most celebrated advantages can be divided into those that affect design and those that affect production.

In 1995, an editorial comment on the thoughts of Hull *et al.* [38] described a '*cautious optimism*' towards rapid prototyping and the requirement to '*convince many* *sceptics*'. Whilst many ALM processes are in use today, their uptake is not quite the new '*Industrial Revolution*' predicted by some [37] and, from an engineering materials perspective, a cautious optimism and many sceptics are, in the view of this author, still present. Somewhat over-exaggerated claims about the capability of the technology have also acted to hinder its usage.

The design freedom and tool-less manufacture of ALM processes allows a potential reduction in design considerations, foe example cost (no tooling) and lead time (no design and manufacture of tooling). However, it has been commented by Hague *et al.* [41] that ALM can produce '*any*' shape. This is not quite the case as considerations still need to be made regarding component orientation and supports need to be generated for overhanging surfaces. Part distortion, accuracy [42] and resolution are also limitations and fine features may be destroyed during the application of subsequent layers.

The near-net shape nature of ALM brings both cost (buy-to-fly ratio) and environmental advantages; recycling of unused feedstock results in limited waste. Conversely the handling of feedstock (fine powders) and its containment and disposal can have negative effects on the environment and adds cost. The grading of materials in ALM can be achieved by changing structure, changing material or both. An example of this is given in Figure 2.15. Part consolidation and mass customisation [37] are also noted advantages of the ALM processes.

One potential drawback of ALM systems is surface finish, arising from the layer-by-layer fabrication process. Deposition of thick layers gives poor resolution whilst using very thin layers increases production time.

(a) *(b)*

Figure 2.15 : Examples of graded ALM structures (a) Ti-6Al-4V acetabular cup graded by changing structure from fully dense to a porous outer mesh [43] and (b) a cheese and jam hors d'oeuvre showing how multiple materials can be used to grade structures and the potential for multiple materials per layer in ALM [44].

2.7.5. Early ALM of Metals and Alloys

Materials available to use in early commercial RP machines included photopolymers, polymers, paper, wax and rubber [45]. Whilst these materials produced acceptable prototypes, they had limited functional use. The natural progression from RP was to actual component production whereby form and functionality were both essential. In order to make the transition away from prototyping, the technology needed to be applied to more traditional engineering materials. In 1995 Agarwala *et al.* [46] commented that '*one ultimate aim in rapid prototyping is to fabricate...fully functional parts directly from metals and ceramic materials without the use of intermediate binders...*'.

Two of the most promising additive layer methodologies for producing metal components involve powder feedstock. The methodologies differ in the way in which powder is delivered to form layers; Figure 2.16 shows schematically the (a) blown powder and (b) powder bed systems. Blown powder techniques deliver powder to the focal point of a heat source, e.g. laser beam, where it is melted/sintered and deposited onto a substrate. Powder bed systems cover a platform with a powder layer before selectively sintering/melting with a scanning heat source.

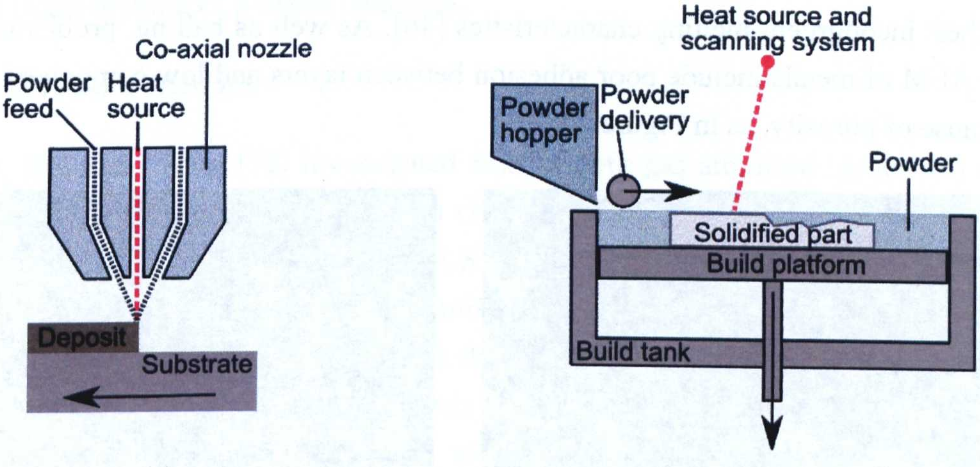

(a) (b)

Figure 2.16 : Schematics of ALM of metals using (a) blown powder and (b) powder bed methodologies.

Current ALM systems that process metals are capable of fully melting the feedstock material. Earlier systems were not always capable of this and relied on both solid phase and liquid phase sintering as a means of consolidation. Porous components could then be further sintered to higher density or infiltrated with liquid metal to produce a fully dense component [47]. The use of the word *sintering* is thus common in ALM terminology and is remnant from early systems. For example EOS' direct metal laser sintering (DMLS) process is capable of full melting; the use of the word sintering in this case is thus somewhat misleading.

2.7.6. Selective Laser Sintering (SLS)

The powder bed, selective laser sintering (SLS) process was identified as a method by which metals could be successfully processed in layers, although initial attempts to process single phase metals such as Ni, Cu, Pb, Sn and Zn by SLS were unsuccessful [46, 48]; the lack of success was a result of 'balling'. Balling results from the surface tension of the molten material forming spheres (minimising surface energy) rather than producing a flat layer. The problem of balling was attributed the congruent melting temperature of pure metal powders. To overcome balling phenomenon multi-component systems or pre-alloyed powders were used [45, 46].

Multi-component systems are made up of a high melting point and low melting point (binder) material; melting and solidification of the binder material entraps the un-melted, high melting point component. When metal powders with polymer binders were used, removal of the binder left a porous framework that could be infiltrated with metal. Pre-alloyed powders were also found to be less prone to balling because of their incongruent melting characteristics [46]. As well as balling, problems during the ALM of metals include poor adhesion between layers and low component density because of porosity, as in Figure 2.17.

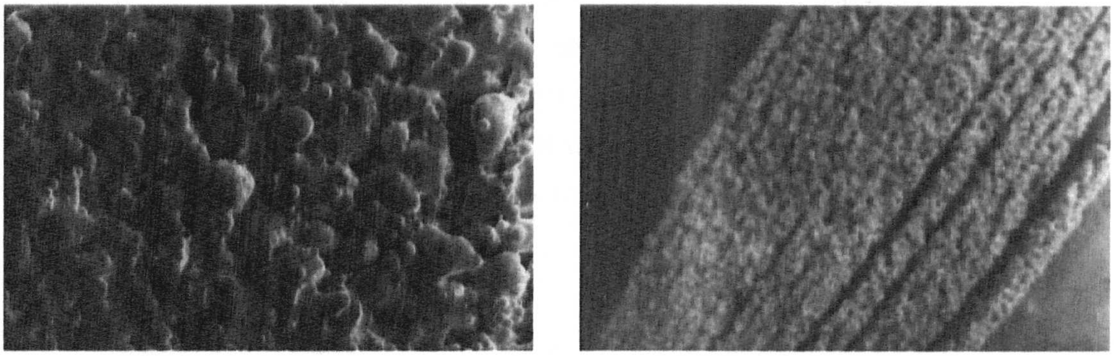

(a) *(b)*

Figure 2.17 : Examples of (a) balling and (b) poor layer adhesion in SLS of pre-alloyed bronze [46].

Powder systems are not the only means of producing metal ALM components; consolidation of metal foils and the melting of wire feedstock are also used. Solidica's Formation^{TM} Machine (www.solidica.com) uses a combination of ultrasonic welding, to consolidate metal foil, and machining to remove excess foil. The shaped metal deposition (SMD) process uses metal wire as a consumable electrode to deposit multi-pass welds using a robot controlled, inert gas, welding torch [49]. Table 2.8 gives a selection of heat source and feedstock combinations for metal ALM processes.

Table 2.8 : Heat source and feedstock combinations for a selection of metal ALM processes.

Heat Source	Feedstock	Process (*Company*)
Laser	Powder	DMLS (*EOS*), LaserCusing (*concept laser*), SLM (*MTT Group*), DLF (*Trumpf*), DMD (*POM Group*), LENS (*Optomec*), DMP (*ProMetal RCT*)
Electron beam	Powder	EBM (*Arcam*)
Electron beam	Wire	EBF^3 (*NASA*)
TIG/MIG weld torch	Wire	SMD (*Rolls Royce*)
Ultra-sonic	Foil	UC (*Solidica*)

It can be seen from Table 2.8 that the combination of a laser heat source and powder feedstock is a popular processing method. In this research, the powder bed, EBM system developed by Arcam was used. As such, emphasis will be placed on electron beam melting of powder feedstock.

2.7.7. *Powder Feedstock*

In 1999, Niu and Chang [50] investigated SLS of both gas atomised (spherical) and water atomised (jagged) high speed steel (HSS) powders. The two different powder morphologies reacted differently to the SLS process in which laser power was varied between 2.5 W and 30 W. The gas atomised (GA) powder was found to produce relatively homogeneous structures whilst the water atomised (WA) powder formed either agglomerates or segregated towards the centre of the laser beam [50]. The behavioural differences were attributed to both shape and compositional affects. Increasing laser power was also observed to change the densification mechanism from solid phase sintering (SPS) at 2.5 W, to liquid phase sintering (LPS) and finally complete melting at 30 W; Figure 2.18.

Metal ALM systems, that use powder feedstock, generally require powder with spherical morphology. Whilst blown powder systems may use other morphologies, powder bed systems utilise spherical powders for their rheological behaviour. Application of a layer of powder necessitates good flow that is not achievable using non-spherical morphologies. The two main production routes for spherical powder are gas atomisation (GA) and the plasma rotating electrode process (PREP); Figure 2.19 shows SEM images of commercial purity (CP) titanium powder that has been produced by (a) GA and (b) PREP.

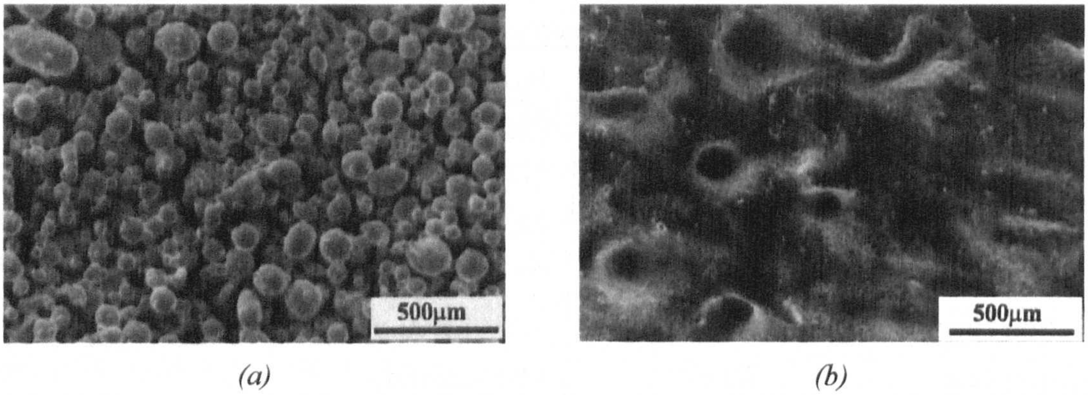

Figure 2.18 : The effect of laser power on densification mechanism during SLS of gas atomised, HSS powder; (a) solid phase sintering at 2.5 W and (b) complete melting at 30 W [50].

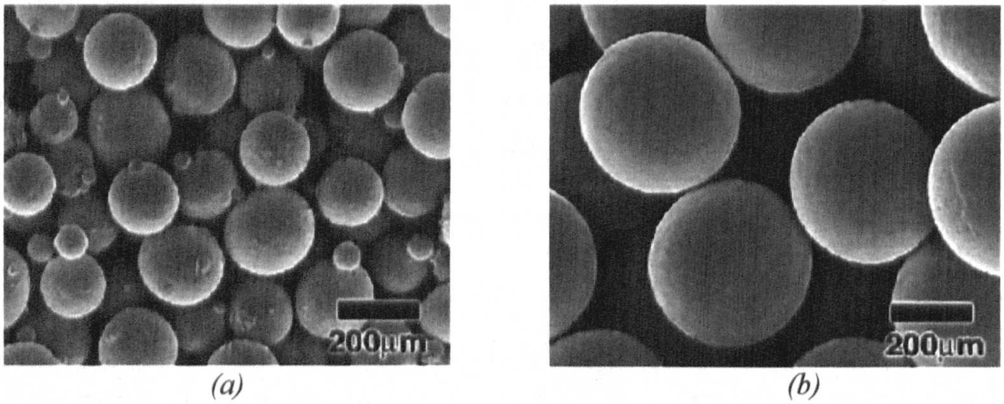

Figure 2.19 : SEM images of commercial purity titanium powder (a) produced by gas atomisation (GA) and (b) produced by the plasma rotating electrode process (PREP) [51].

GA powders are produced by feeding liquid metal through a central tube, surrounded by a co-axial gas nozzle; the nozzle directs high velocity gas towards the stream of liquid metal. The metal stream is disintegrated into droplets that freeze in-flight (in an inert atmosphere), producing spherical powder particles with a typical size range of 1 – 250 μm [52].

PREP powder is produced by using high temperature plasma to melt a rotating ingot (electrode). The centrifugal force causes liquid metal to be ejected from the electrode; the molten droplets enter into a gas jet, arranged around the perimeter of the electrode. Aerodynamic drag causes the particles to shatter, further refining their size [53]. Antony and Reddy [53] give a fairly recent overview of production processes for high-purity metal powders including GA and PREP with schematics of each of the processes.

The use of GA and PREP powder is a trade-off between economy and quality. It can be seen from Figure 2.19 that GA powder contains satellites (small powder particles attached to larger ones) and it is well known that hollow powder particles exist from entrapped inert gas, e.g. argon, from the atomisation process [54]. It is possible for such gas porosity to remain present in an ALM component. The advantage of using GA powder is its lower cost when compared to PREP powder. Although more expensive, PREP powder is highly spherical and powder size fraction is less variable than GA powder.

2.7.8. Powder Size and Packing Density

Powder morphology and, in the case of SLS - laser power, have both been observed to affect the resultant structures. Packing density of the powder bed is also a variable that influences ALM processing. For mono-sized spheres, the maximum theoretical packing density achievable is 74% – this can be enhanced by using powders of different sizes. Theoretically, packing density of a mixture of powders can be as high as 98% [55]. Figure 2.20 shows schematically how using powder mixtures can increase packing density.

A tri-modal powder distribution is, theoretically, capable of producing a powder bed with a packing density of 95.7%, if the ratio of the diameters of the large (D_L), medium (D_M) and small (D_S) powders are 9.23:3.83:1 and they are present in the proportions 1:1:4, respectively [55].

As well as increasing packing density, the presence of smaller particles increases sintering/melting kinetics arising from the increased surface area available to absorb energy from the heat source [50]. However, the use of very fine powders can have detrimental effects; (i) fine powders can agglomerate easily, reducing their effect and (ii) fine powders are more hazardous to health (increased risk of entering the body), carry a higher risk of explosion [55] and require specialist disposal.

Zhu *et al.* [55] report a direct link between the packing density of a powder bed and the final density of SLS parts, produced from various copper powders and a copper-phosphor binder. An upper packing density limit was found, above which there was no improvement in part density.

One reason given for the upper limit was that the flow of liquid was restricted by the dense powder bed. In multi-component systems this could be viewed as a disadvantage because of the impediment of the liquid binder. However, in systems where complete melting occurs, restriction of liquid flow into the surrounding powder bed is advantageous. Unwanted fluid flow into the powder bed can have an adverse effect on part geometry and surface finish.

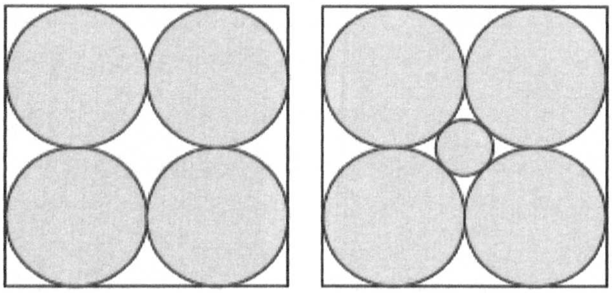

(a) monosized (b) bimodal $D_L >> D_S$

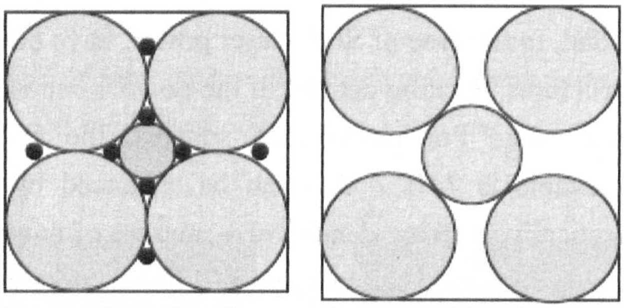

(c) trimodal $D_L >> D_M >> D_S$ (d) bimodal $D_L \sim D_S$

Figure 2.20 : Effect of powder size on packing density of spherical powders [55].

2.7.9. Electron Beam Processing

Electron beams have been used to process materials since the 19th century; Table 2.9 gives a timeline of some significant developments. The projection of electrons onto solid materials results in some reflection (via elastic and inelastic collisions) and, for the majority of electrons, penetration into the solid. Interactions between the electrons and the solid produce X-rays, fluorescence, secondary (reflected) electrons and the generation of heat.

Heat is generated by the transfer of energy from the incident electron beam to the electrons in the outer shells of the target material. This transfer of energy increases the thermal vibration of the atoms in the target material and thus generates the necessary heat required for processing [56]. It has been shown experimentally that electron penetration range R_p (m) is dependent on the electron acceleration voltage V and density ρ (kgm^{-3}) of the target material; the relationship is given in the Equation (2.2) [56].

$$R_p = \frac{2.2 \times 10^{-11} \cdot V^2}{\rho} \qquad (2.2)$$

Incident electrons of high energy are able to penetrate into the target, through the lattice, owing to the diameter of the electrons being very small when compared with the lattice spacing. Electrons dissipate their energy randomly along the penetration path and stop at random positions below the surface of the material; as shown in Figure 2.21.

Table 2.9 : Timeline of electron beam processing developments, adapted from [56].

Date	Occurrence
1879	Sir William Crookes discovers that a platinum anode is melted by cathode ray bombardment
1897	Thompson shows that cathode rays are streams of electrons
1907	Pirani obtains U.S. patent for electron beam melting
1938	Ardenne indicates the possibility of using the corpuscular beam as a processing tool
1950s	Charlesby investigates electron beam polymerisation
1953	Steigerwald points out the ability to perform machining using an electron beam
1957 & 1958	Stohr (1957) and Wyman (1958) report on electron beam welding
1959	Electron beam heating used in the sintering of metal powders by Candidus, Hablanian and Steinherz [57]

The paths of several electrons into the incident material can be seen in Figure 2.21. The depth of maximum absorption rate is indicated as X_e and the largest proportion of electrons are absorbed at X_d. As a consequence of this, atoms at the surface of a material are not heated directly by an electron beam; they are heated by conduction from sub-surface atoms [56]. The reflected/backscattered electrons shown in the figure may carry away a significant fraction of the incident beam energy; this fraction is dependant on the material and accelerating voltage [58].

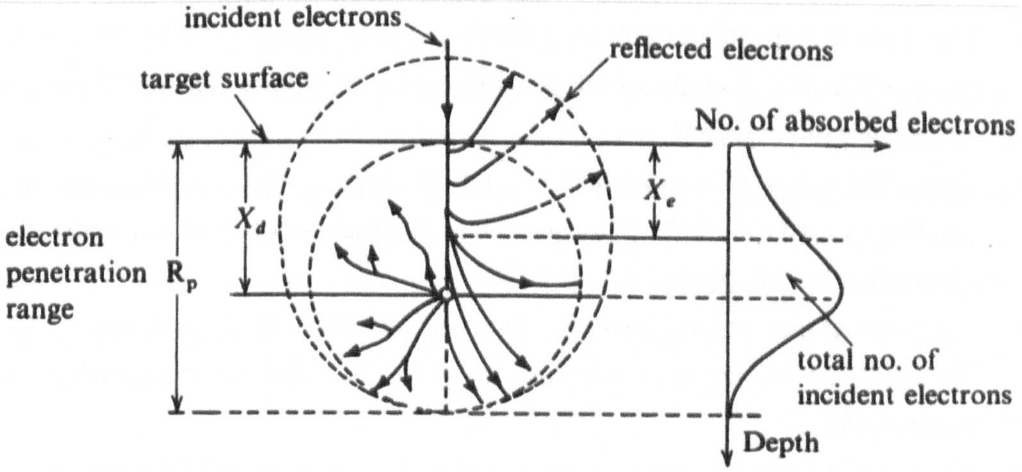

Figure 2.21 : Electron penetration range [56].

The use of an electron beam as a heat source for ALM hardware is perhaps a shrewd choice given the advantages over a laser-based system:

- Vacuum – the vacuum environment necessary for the use of an electron beam ensures that the process is clean and an inert shroud gas is not required [40].
- Electron coupling – the penetration of electrons into a target material and subsequent heat generation means that electron beams couple well with all electrically conductive, non-magnetic material. This is true even for highly reflective materials, such as aluminium [40], which laser systems can struggle to melt because of excessive reflection.
- Cost – although initial electron beam system costs are higher than laser-based systems because of the vacuum system, replacement filaments for electron beam systems are relatively cheap. This in stark contrast with replacement lasers which can be very expensive.
- Power – electron beam systems are capable of melting tungsten; they have high power compared with laser systems.
- Deposition rate – the high power of electron beams also means that deposition rates are high.

2.7.10. Electron Beam ALM Literature

Available literature on the use of electron beams, to process metals by ALM, is limited. Table 2.10 gives a selection of journal articles detailing research in this field. Of the few alloy systems investigated, titanium alloy Ti-6Al-4V has been the most heavily researched and has been of specific interest in the field of biomedical science [61, 62, 64, 67] for its biocompatibility. Some key points discussed in the listed literature include:

- The substantial refinement in primary carbide size in EBM 718 material compared to that found in bulk solidification and the deleterious clustering of oxides and nitrides [58].
- The consistency of mechanical properties over a wide range of processing conditions for EBF^3 2219 aluminium and mechanical properties comparable to conventionally processed material [40].
- The martensitic microstructure observed in EBM H13 tool steel and the identification of possible alloying element loss due to vaporisation under vacuum [59].
- The potential promise for custom orthopaedic implants with tailored properties [61] and the ability of human foetal cell to proliferate on EBM Ti-6Al-4V [62].

- The improved performance of a H13 injection moulding tool, with integral conformal cooling channels, produced by EBM [63].

Table 2.10 : A selection of available literature concerning the ALM of metals using electron beams.

Authors	Material	Process (*Company*)	Year	Ref.
Matz and Eagar	718 wire	EBSFFF	2002	[58]
Taminger and Hafley	2219 aluminium	EBF^3 (*NASA*)	2003	[40]
Cormier *et al.*	H13 steel	EBM (*Arcam*)	2004	[59]
Dalgarno and Goodridge	H13 steel	EBM (*Arcam*)	2004	[60]
Harrysson *et al.*	Ti-6Al-4V	EBM (*Arcam*)	2007	[61]
Ponader *et al.*	Ti-6Al-4V	EBM (*Arcam*)	2007	[62]
Rännar *et al.*	H13 steel	EBM (*Arcam*)	2007	[63]
Murr *et al.*	Ti-6Al-4V	EBM (*Arcam*)	2008	[64]
Cansizoglu *et al.*	Ti-6Al-4V	EBM (*Arcam*)	2008	[65]
Murr *et al.*	Ti-6Al-4V	EBM (*Arcam*)	2009	[66]
Li *et al.*	Ti-6Al-4V	EBM (*Arcam*)	2009	[67]
Facchini *et al.*	Ti-6Al-4V	EBM (*Arcam*)	2010	[68]

2.7.11. ALM Microstructures

ALM processes provide thermal energy to melt feedstock material and, as such, solidification is a fundamental issue. During processing, solidification times are short and steep thermal gradients may exist. Previously deposited material is also thermally affected by the deposition of subsequent layers, resulting in complex thermal histories. Such thermal histories make the prediction of precise microstructures difficult [69] in alloy systems that have multiple phase transformations.

Whether blown powder or powder bed systems are used, a significant microstructural morphology identified by many authors [70, 71, 72] is the columnar microstructure. Columnar grains originate as a result of directional cooling through the deposit/substrate where grains are aligned nominally parallel to the thermal gradient. An example of a columnar microstructure in laser deposited Ti-6Al-4V can be seen in Figure 2.22 in which the *z*-axis runs from top to bottom of the page.

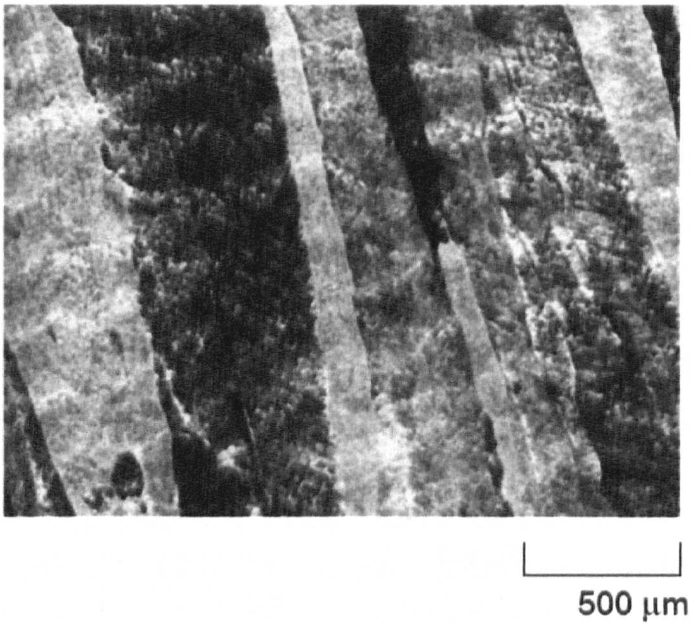

Figure 2.22 : Columnar grain structure in laser deposited Ti-6Al-4V [71].

Columnar microstructures are, generally, undesirable because of the reduction in mechanical properties with increasing grain size as per the Hall-Petch equation. However, in applications where creep resistance is required, a columnar structure (and highly oriented grains) may be advantageous [73]. The severity of the reduction in properties for columnar microstructures is dependant on the alloy system; Moat *et al.* [73] comment on the fact that, unlike ferritic steels and titanium, nickel superalloys do not undergo a grain refining phase transformation. There is therefore, a significant difference in the ALM processing of transforming and non-transforming alloy systems.

In both laser and electron beam ALM systems, used to deposit H13 tool steel, regions of martensite have been identified [59, 70]. The presence of martensite gives an indication of how solidification in ALM processes occurs. Mazumder *et al.* [70] investigated this further by measuring secondary dendrite arm spacing (SDAS), denoted λ_2, and calculating cooling rate during the direct metal deposition (DMD) process. Cooling rates were calculated to be of the order of 10^5 Ks^{-1}. A cooling rate of ~ 10^5 Ks^{-1} has also been reported by Qian *et al.* [69] in the direct laser fabrication (DLF) process of Ti-6Al-4V.

Microstructures observed in ALM processing of Ti-6Al-4V are similar although slight differences are observed depending on the process involved; Table 2.11 gives a brief summary of some of these microstructures.

Table 2.11 : Ti-6Al-4V ALM microstructures.

Heat Source	Prior β Structure	Transformed $\alpha + \beta$ Structure	Ref.
Laser	Columnar	Fine Widmanstätten, very fine α particles within grains and along grain boundaries, some α_{GB}. Some macroscopic banding due to sudden change in number of equiaxed α particles.	[71]
Laser	-	α' at top and bottom of sample (high cooling rates), basket weave $\alpha + \beta$ in between.	[69]
Laser	Columnar	Widmanstätten α laths outlined in retained β, continuous α_{GB}, colonies of acicular α.	[74]
Laser	Columnar	Fine Widmanstätten, small amount of α'	[72]
EBM	-	Uniform acicular α phase with β along the phase boundaries.	[64]

2.7.12. *Solidification during ALM*

The presence of columnar grains in ALM microstructures is a result of incremental epitaxial growth [73, 78] and high thermal gradients. High thermal gradients, relative to solidification rates, prevent nucleation ahead of the solid-liquid interface [71]. Solidification of molten alloys can be characterised by consideration of the temperature distribution and speed of solidification alongside diffusion of solute, alloy freezing range and undercooling. Thermal gradient, G (Km^{-1}), and solidification velocity, R (ms^{-1}), can be used to predict solidification microstructures [75] based upon both morphology and cooling rate.

Porter and Easterling [76] define the solidification velocity during welding as described by Equation (2.3), where v = welding velocity and θ = the angle between the normal to the solidification front and the welding direction. ALM produces, in effect; multiple welds both adjacent to and on top of one another.

$$R = v \cos \theta \qquad (2.3)$$

In 2001, Gäumann *et al.* [77] discussed the microstructural control of nickel based superalloy CMSX-4, deposited by the laser metal forming (LMF) blown powder technique. Control of the deposited microstructure (single crystal or polycrystalline) was demonstrated, based upon control of solidification parameters G and R. This allowed the production of microstructure-processing maps to determine the deposited microstructure as a function of process parameters.

Such a maturity of understanding is key to the future development and uptake of ALM technology, although the sheer number of variables involved in current powder bed ALM process makes this a challenge. Moat *et al.* [73] comment that the wide scale adoption of ALM will require that processing maps are available; this may be necessary for each alloy system or for individual ALM techniques.

A method adopted by Kobryn and Semaitin [71, 78] is the use of a solidification map which plots *G* against *R* for Ti-6Al-4V, as shown in Figure 2.23. Morphological regions (fully columnar, mixed and fully equiaxed) are defined for appropriate *G* and *R* combinations. This allows microstructural prediction based on the input of process *G* and *R* values. Such a map is ideal because *G* and *R* values for any process may be plotted for comparison.

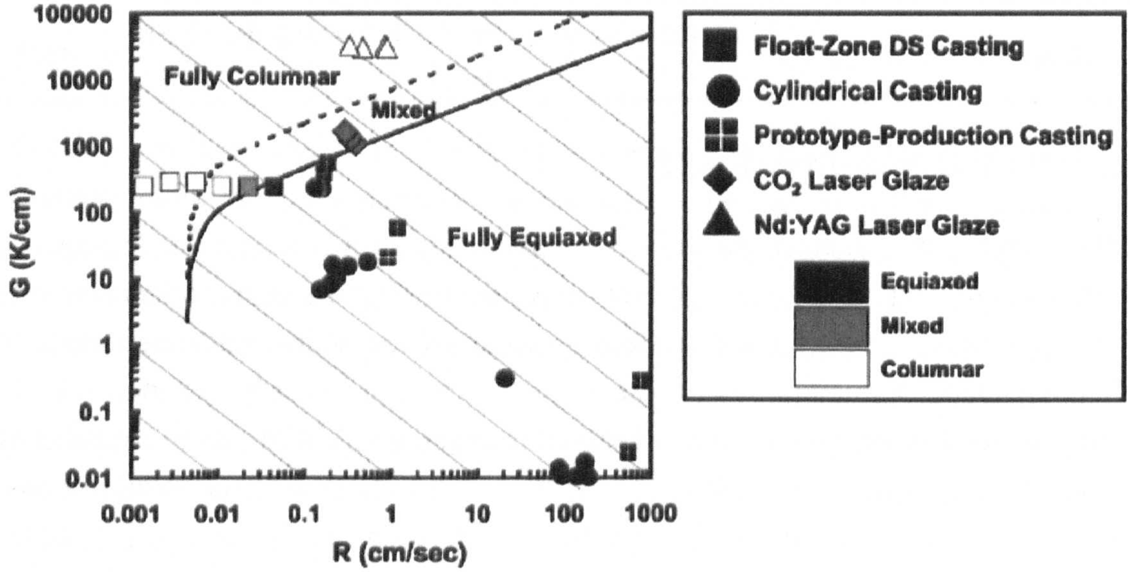

Figure 2.23: Solidification map for Ti-6Al-4V showing measured and predicted values of G vs. R and the observed macrostructures for casting and laser glaze processes [78].

2.7.13. Powder Bed Temperature

Early research into SLS of both polymer and metal systems identified that in situ heating of the powder bed alleviated problems such as wettability and thermal distortion [46]. It was noted that the maximum bed temperature was limited by the sintering temperature of the lowest melting point component (in multi-component systems). At higher temperatures, the entire powder bed sintered together making removal of the component difficult. Current ALM hardware has both heated and non-heated powder beds. The EOS M270 heats base plates to 80 °C prior to processing whilst the Arcam EBM systems are capable of raising base plate temperature to in excess of 1000 °C and maintaining a bed temperature of this order of magnitude.

As well as affecting sintering, powder bed temperature has a strong influence on thermal gradient, cooling rate and internal stress. 'Cold' ALM systems provide no mechanism for the alleviation of thermal stresses, which can cause component distortion and cracking [42], whilst 'hot' systems may allow for a degree of annealing as well as coarsening of the as-solidified structures, depending on temperature.

The presence of internal stress in EBM Ti-6Al-4V has been reported by Murr *et al.* [64], Figure 2.24. Although the deposition process was carried out at a temperature in excess of 600 °C, a dislocation density of 5×10^{-9} cm^{-2} was reported. This compares with a dislocation density of $10^{-9} - 10^{-10}$ cm^{-2} in wrought Ti-6Al-4V (forging reduction and temperature not stated) [64].

Figure 2.24 : Dislocations in an α lath in EBM Ti-6Al-4V [64].

2.7.14. Texture in ALM

The body of work investigating crystallographic texture as a result of ALM is extremely limited. Kobryn and Semiatin [78] discuss observed textures during solidification processing of Ti-6Al-4V. DLF deposits were found to have intensity peaks located very close to an ideal columnar-solidification texture; however, peak broadening indicated potential overlapping of pairs of peaks. The texture of the deposit was also very similar to that of the substrate, making it impossible to separate the two. It was concluded that epitaxial growth from the substrate could have played a significant role in controlling deposit texture.

Moat *et al.* [73] discuss microtexture in pulsed laser-deposited Waspaloy. Preferred orientations were observed ranging from 5.4 × random to 11.1 × random depending on laser pulse length. Pulse length was also found to affect the angle between the (001) plane and the vertical *z*-axis; this was attributed to the shape of the melt pool. The most vertically aligned grains were produced for low melt pool angles; increasing solidification front angle was found to increase (001) pole tilt.

2.7.15. Mechanical properties of ALM Ti-6Al-4V

Mechanical data for EBM Ti-6Al-4V suggests that material performance is good and approaching that of wrought material in terms of static mechanical properties. Murr *et al.* [79] report yield strengths and ultimate tensile strengths in excess of 1.10 GPa and 1.15 GPa respectively, with elongations in excess of 16%. These values seem rather high and the authors do not give a value for the oxygen content of the material. Increasing oxygen content is known to increase the strength of Ti-6Al-4V; this effect can be seen in Table 2.12 for extra low interstitial (ELI) Ti-6Al-4V.

Table 2.12 gives an indication of the effects of sample orientation (XY or Z) and hot isostatic pressing (HIP) on static mechanical properties. Orientating the tensile axis parallel to the *z*-axis is observed to decrease YS, UTS and elongation whilst HIPing can be seen to decrease both YS and UTS with a small increase in elongation.

Table 2.12 : ASTM E8 tensile test data for EBM Ti-6Al-4V ELI showing the effect of orientation and hot isostatic pressing, adapted from [80].

Group	Oxygen, wt%	HIP?	Orientation	YS, MPa	UTS, MPa	El, %
A	0.10	Y	Z	800	876	16
B	0.12	N	Z	856	924	15
C	0.14	Y	XY	841	938	20
ASTM F136-02a	0.13 max	-	-	795	860	10
ASTM F 1108-04	0.20 max	-	-	758	860	8

2.8. Numerical Modelling of ALM Processes

In 1946, Rosenthal [81] solved the heat conduction equation for a moving heat source in the quasi-stationary state. The solution allowed calculation of the temperature distribution during welding processes. Subsequent works [82, 83] have used Rosenthal's solution as a basis for prediction of temperature fields. The major assumptions made by Rosenthal were: (i) the physical characteristics of the metal (i.e. thermal conductivity and diffusivity) are independent of temperature, (ii) the speed, v, and rate of heat input, q, are constant and (iii) convective and radiative heat flows are absent.

Solutions are gained by assuming that the heat source is a point source, with constant strength and velocity, moving along the x-axis. From this, the temperature distribution around the heat source can be determined. Rosenthal showed that the solution to the conduction equation in 3 dimensions is:

$$T\text{-}T_0 = \frac{q}{2\pi kR}\exp\left(\frac{-v(x+R)}{2\alpha}\right) \tag{2.4}$$

where q = heat input, T_0 = initial temperature, $R = \sqrt{(x^2+y^2+z^2)}$, α = thermal diffusivity in m^2s^{-1} and k = thermal conductivity in $Wm^{-1}K^{-1}$.

Comparison of Rosenthal's 2D solution to the heat conduction has been carried out with a finite element model (FEM) [82] to investigate thin wall deposits using the laser engineered net shape (LENS) process. Cooling rates and solidification microstructure in Ti-6Al-4V have been predicted using both methods with good agreement. Rosenthal's solution neglects any temperature dependent properties, and the latent heat of transformation, but the results allow reasonable estimates of grain morphology [82]. As commented by Nguyen *et al.* [84], Rosenthal fails to predict temperature in the vicinity of the heat source; this results in the prediction of an infinite temperature when x, y and $z \rightarrow 0$.

2.9. Literature Review Conclusions

Although ALM has been a technology available for several decades, its use to process metals and alloys is still an emerging field. Research available on ALM is relatively limited and because of the wide range of alloy systems available, literature for each process is somewhat dilute.

It has been well documented that, regardless of alloy system, ALM produces columnar microstructures and this is no exception for Ti-6Al-4V [42, 71]. However, the columnar microstructure in Ti-6Al-4V is applicable to the prior β grains; transformation through the β transus results in fine Widmanstätten α + β and, in some cases α' microstructures. Although ALM microstructures generally exhibit columnar microstructures, there is potential to change microstructural morphology by controlling process conditions [77].

Whilst texture has long been investigated in wrought Ti-6Al-4V microstructures, few researchers have investigated the textures obtained via ALM processing. Given the columnar microstructures and their potential detriment to performance, texture could also be of great significance.

Additions of ≤ 1 wt% B to cast Ti-6Al-4V microstructures have been shown to refine both the prior β and α + β microstructures [26 - 31] and may also present a means of refining Ti-6Al-4V ALM microstructures.

The solidification map of Ti-6Al-4V [71] presents itself as a useful tool for determining microstructural morphology based on solidification conditions. Numerical modelling of ALM processes has been successfully used to determine heat transfer in ALM processes and may be used to extract solidification conditions impossible to measure experimentally.

3. EXPERIMENTAL PROCEDURES

This chapter discusses the experimental techniques used to produce and characterise electron beam melted Ti-6Al-4V. The operation of an Arcam S12 EBM machine will be discussed in detail as this represents the sole piece of hardware used to produce all of the material under investigation. As well as the production of bulk components, EBM was used to melt individual tracks on solid substrates, in order to better understand the thermal influence of the electron beam. Subsequently, the techniques used to analyse the EBM material will be discussed.

3.1. Arcam S12 Processing

This section discusses the use of an Arcam S12 EBM machine. However, before its operation is discussed, the health and safety issues associated with powdered feedstock material shall be considered.

3.1.1. Health and Safety

The feedstock of the EBM process is metal powder; this work focuses solely on the use of Ti-6Al-4V powder. Powdered materials have increased health and safety considerations when compared to their bulk counterparts and thus powder handling and operator safety are two key considerations. Powdered Ti-6Al-4V can, under the right circumstances, ignite and has the potential to explode – great care must be taken during handling. The risk of explosion increases with decreasing powder size, however, the resolution of ALM components increases with decreasing powder size. All powders used in the EBM process are tested by Arcam AB to determine the minimum airborne concentration of powder that may be ignited by a spark of given energy. For this work, powder in the range of 45 – 100 μm in diameter was used. Ti-6Al-4V powder of this size range is considered to have a relatively low risk of explosion when handled correctly.

Unlike the vast majority of metallic powders, Ti-6Al-4V is biocompatible and thus does not represent a hazard from a toxicity point of view. However, inhalation of powdered Ti-6Al-4V can lead to its build up in the lungs. To prevent the inhalation of powdered material, half face mask respirators fitted with a particulate filter were worn at all times when working with the powder; Figure 3.1 shows the respirator mask used. As well as a mask, latex gloves were used to prevent powder entering the body via manual contact and to prevent sensitisation from prolonged exposure.

Figure 3.1 : Sundstrom SR100 half mask respirator worn at all times when in contact with the Ti-6Al-4V powder (particulate filter missing from image). Image from www.arco.co.uk.

Care was taken to ensure powder was never in the vicinity of a naked flame or allowed to ingress into electrical appliances. Any spillages of powder were also immediately cleaned up; spilt powder on hard surfaces is extremely slippery.

3.1.2. Hardware

In order to produce EBM samples, four main pieces of hardware were required, namely:

- An Arcam S12 EBM machine
- Two explosion-proof vacuum cleaners
- A powder recovery system (PRS)
- A compressed air vibrating sieve

The first pieces of equipment for consideration are the two explosion proof vacuum cleaners that provide a means of collecting and transporting powder. The vacuum cleaners were labelled *clean* (used solely for powder within the vacuum chamber) and *dirty* (used for powder outside of the vacuum chamber i.e. non-recyclable powder). Powder from the *dirty* vacuum cleaner was disposed of as necessary, whilst powder in the *clean* vacuum cleaner was recycled. An image of one of the vacuum cleaners used is shown in Figure 3.2 (a). One of the most critical activities during the use of the EBM system was to ensure that the two types of powder, recyclable and contaminated, remained completely separate and were not mixed.

Recycling of powder takes place in the powder recovery system (PRS), the exterior of which is shown in Figure 3.2 (b). The PRS has several functions: (i) to remove sintered powder from the surface/interior of solid components, (ii) to break up sintered blocks of powder into individual powder particles and (iii) to remove any stray magnetic material. Sintered powder blocks are broken up in the PRS by using recycled powder as a blasting medium, carried in a jet of compressed air. Broken up powder and loose powder from the vacuum fall through a grating in the PRS and is carried by compressed air through a coarse sieve (~ 2cm mesh size) before passing over a magnet and into a collection reservoir.

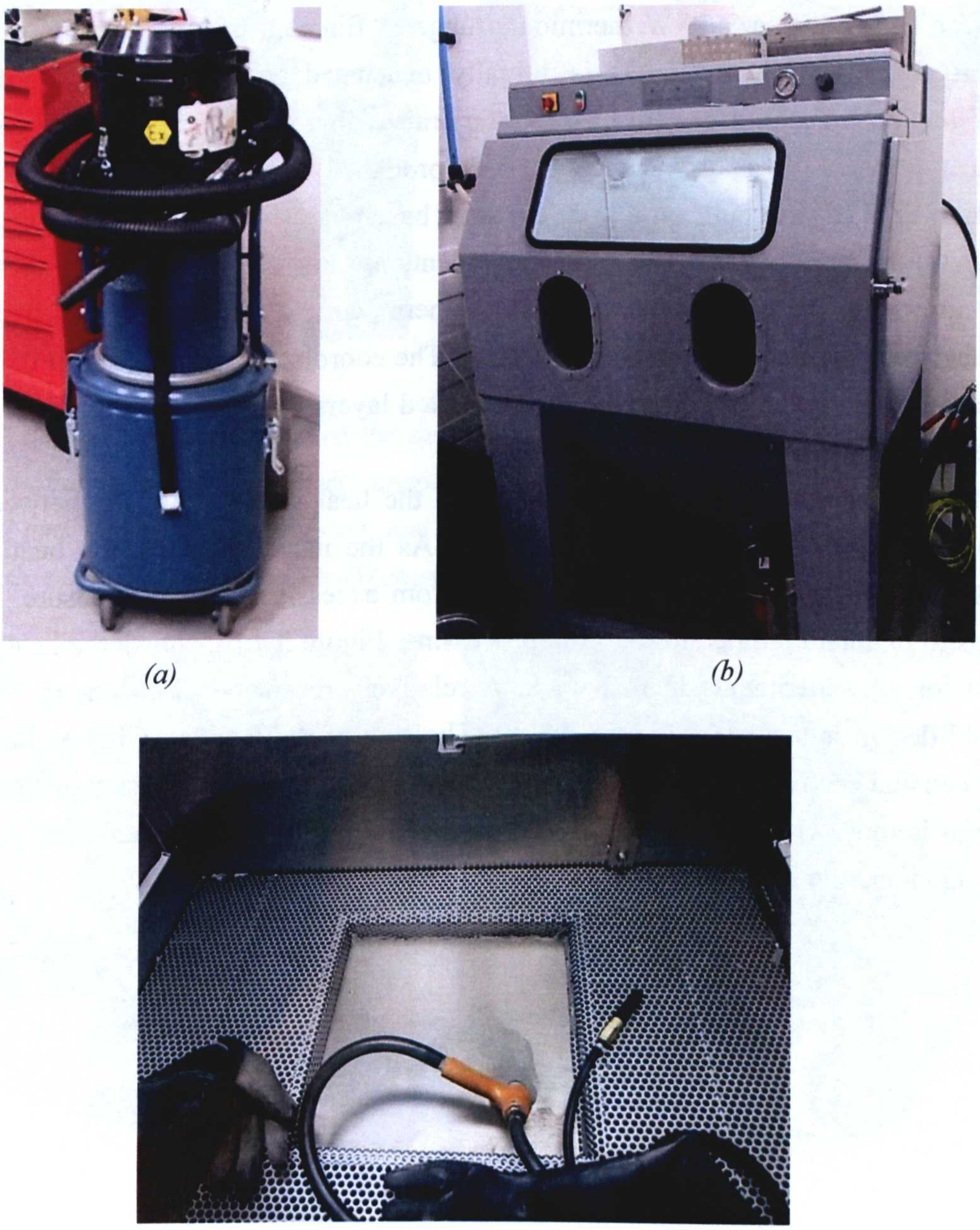
(a) *(b)*

(c)

Figure 3.2 : (a) Explosion proof vacuum cleaner, (b) exterior of the PRS with glove holes on the front for part manipulation during blasting and (c) the interior of the PRS chamber.

The interior of the PRS is shown in Figure 3.2 (c) in which the gloves, blasting nozzle (orange) and compressed air nozzle (black and gold) are resting upon the grating. Powder collected from the PRS is sieved using a vibrating, compressed air sieve (≤150 μm mesh) to remove any large particles. Once in this condition, the sieved powder is fully recycled and ready to use in the EBM process.

3.1.3. S12 Key Components

They key components of the Arcam S12 EBM system are shown in Figure 3.3 in which a schematic, (a), and the actual build chamber, (b), are shown. The electron gun column (A) houses a 3.5 kW thermionic tungsten filament under a vacuum of ~10^{-7} mbar; the build chamber (B) is initially evacuated to ~10^{-4} mbar before the introduction of helium gas (discussed later) raises this to 2×10^{-3} mbar. Powder is held in hoppers (C) and 100 µm layers are produced using the traversing rake (D). Components (E) are built on a stainless steel base plate (F) that sits within the build tank (G). After completing a layer, components are lowered by a layer thickness of 100 µm using the *z*-axis assembly (H). A thermocouple is positioned so that is in contact with the underside of the base plate. The coordinate system used in the EBM process is also given in Figure 3.3 (a), deposited layers lie perpendicular to the *z*-axis (the *build direction*).

A component not shown in Figure 3.3 is the heat shield. This sits between the powder hoppers and above the build table. As the name suggests, the heat shield protects the hoppers and the chamber door from excessive thermal exposure. It also helps to maintain temperature during processing. Figure 3.4 (a) shows the heat shield used for all experiments in this work. A relatively recent development in the heat shield design is shown in Figure 3.4 (b). The size of the viewing window has been reduced and each surface is made of two replaceable sheets of stainless steel. The new design is more effective at maintaining temperature and is also easier to keep clean (by replacing the inner steel sheets).

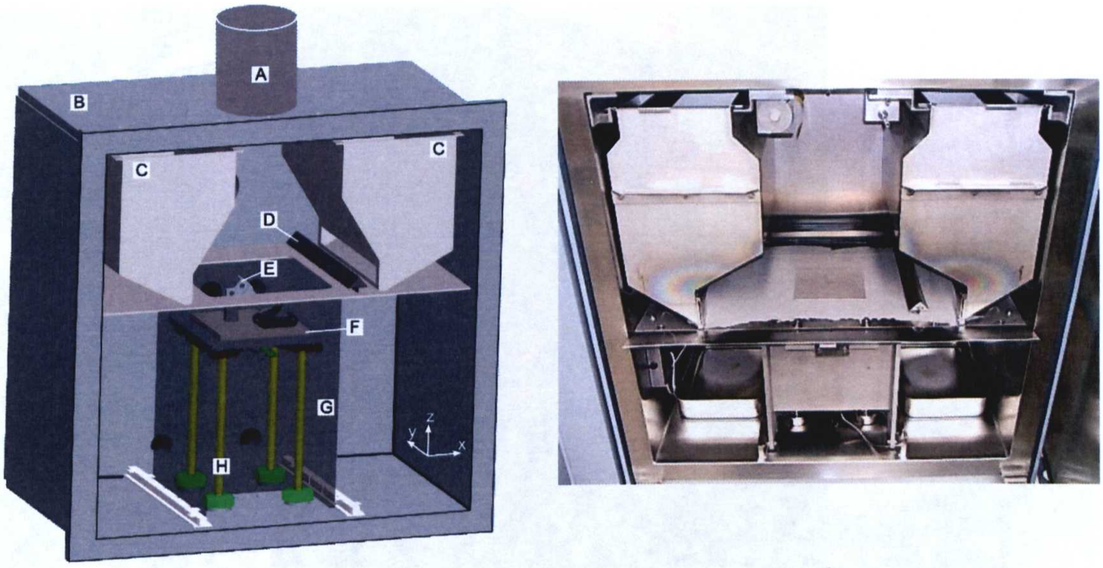

(a) *(b)*

Figure 3.3 : (a) Key components of the Arcam S12 and coordinate system; electron gun column (A), build chamber (B), powder hoppers (C), rake arm (D), component (E), base plate (F), build tank (G), z-axis assembly (H) and coordinate system - Image courtesy Arcam AB, Sweden; (b) photograph of the S12 build chamber.

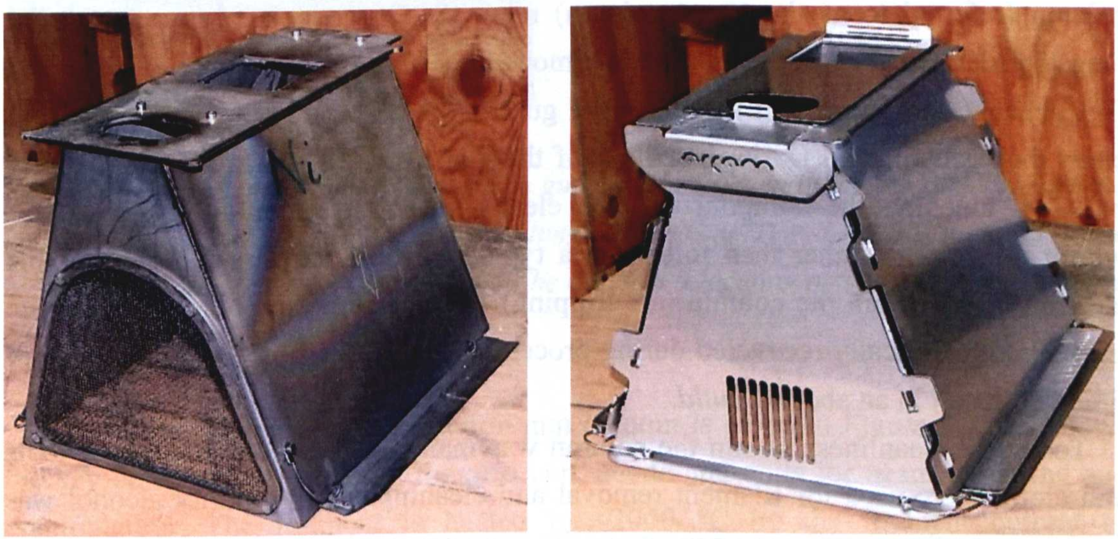

(a) *(b)*

Figure 3.4 : EBM heat shields (a) the initial design used for all experiments in this work and (b) the new Arcam heat shield design. Photographs courtesy of Dr. Michael Blackmore.

The exterior of the Arcam S12 is shown in Figure 3.5 and is made up of 2 units; the right-hand unit houses the build chamber and the electron gun column. The door handle (horizontal red bar) and circular viewing window can be seen on the right-hand side unit.

Figure 3.5 : Exterior of the Arcam S12. The left-hand unit houses the touch screen, computer and control/power units. The right-hand unit houses the build chamber and the electron gun.

A photograph of the electron gun column is shown in Figure 3.6 (a), the top of the column (referred to as the upper column) may be removed to gain access to the tungsten filament. The upper column is removed, generally, for one of three reasons: (i) to change the filament (ii) to clean the gun and remove stray powder and (iii) to clean the vacuum seal. During handling of the gun, care was taken to avoid, where possible, touching the components. The electron beam preferentially arcs to dirt within the column rather than following a typical vertical trajectory. Arcing of the electron beam within the column (arc tripping) can interrupt the process. Whilst arc trips are automatically recovered during processing, multiple trips in a short space of time will result in an aborted *build*.

To ensure cleanliness within the column was maintained, a dedicated set of tools and cloths were used for filament removal and cleaning. A high purity alcohol was used to clean the specific components of the gun such as the anode and the grid cup. Upon reassembly, the upper column was replaced on the main column so that the black marks on each piece were aligned (see Figure 3.6 (a)). This is a relatively crude and subjective method of alignment, future machines would benefit from a mechanical alignment that would be more accurate and easily implemented. A tungsten filament, used as the electron source in the EBM process, is shown in Figure 3.6 (b).

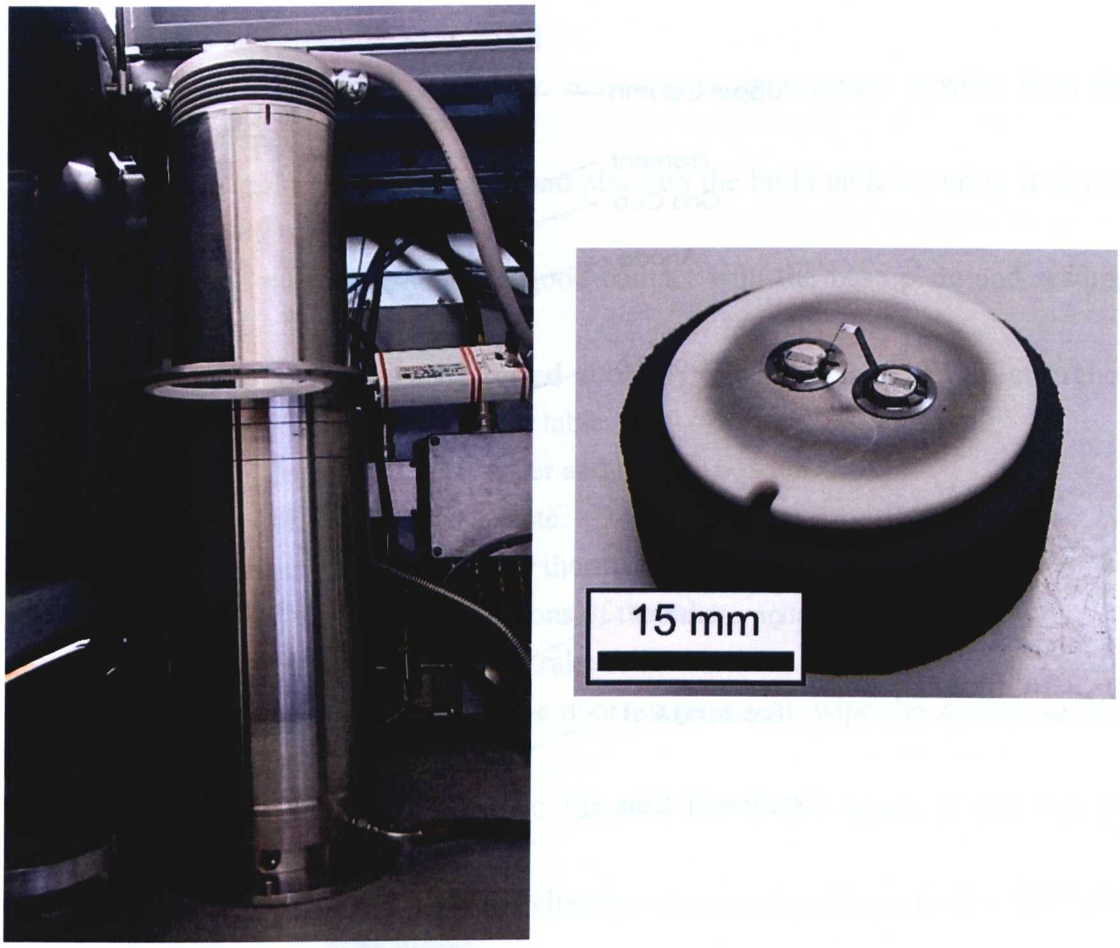

(a) *(b)*

Figure 3.6 : (a) Photograph of the electron gun column situated in the top of the right-hand unit in Figure 3.5 and (b) photograph of a tungsten filament. The filament is attached to two metal contacts that sit on a ceramic disc. The disc has a locating notch to align the filament correctly in the grid cup.

A schematic section of the electron gun column is given in Figure 3.7 and shows the key components including the grid cup, anode and coils for beam focussing and manipulation. The filament is heated to ~2000 °C by the filament current of approximately 10 amperes. Acceleration of the electrons results from the high voltage (60 kV) between the filament and the anode, generating an electric field. The size of the emitting area on the filament is controlled by applying a voltage to the grid cup. The applied voltage produces a magnetic field that may be used to restrict the size of the emitting area and thus control the beam [85, 86].

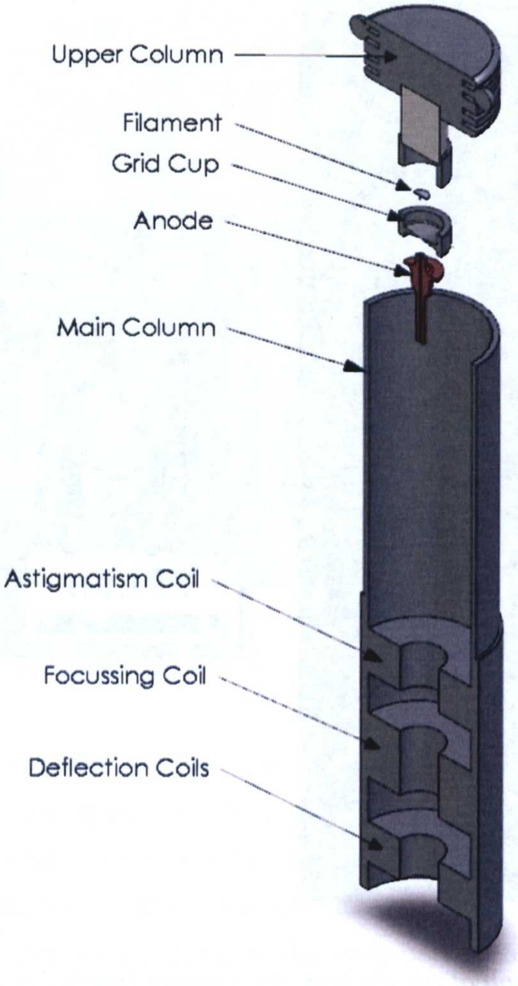

Figure 3.7 : Schematic section of the Arcam electron gun column showing the key components.

3.1.4. Processing Steps

EBM processing is almost fully automatic once the machine has been set up. Assuming that a component has been built in the machine, the following steps describe the processes required to remove the component and set up the machine ready to produce another *build*.

1. Turn off the vacuum pumps and vent the chamber with air only if the thermocouple temperature is below 100°C. If the temperature is in excess of 100 °C, the chamber may be vented with helium. Once below 100 °C, the chamber may be unlocked and opened.
2. Seal off and remove the powder hoppers. Check the powder levels in the hoppers; if insufficient for the next *build*, empty the hoppers into a stainless steel barrel and add new/recycled powder. Thoroughly mix the powder and return to the hoppers.

3. Remove and clean the heat shield.
4. Using the *clean* vacuum cleaner, remove any unnecessary powder from the build chamber.
5. Mark the centre of a base plate and place on the build table ensuring it sits on the levelling screws.
6. Ensure the thermocouple is in good contact with the base plate and reading correctly.
7. Ensure the powder table is seated correctly and there is a 12 mm clearance between the rake and the powder table.
8. Return the hoppers to the chamber and release powder.
9. Using the rake, level the base plate.
10. Lower the base plate to allow for thermal expansion.
11. Calibrate the left and right positions of the rake.
12. Remove excess powder from the rake calibration.
13. Replace the heat shield, clean the door vacuum seal, wipe the sealing surface of the door and close.
14. Observe the filament burn time; filament life is ~60 hours, if this will be exceeded replace the filament.
15. Turn on the vacuum pumps, the chamber vacuum should reach ~5×10^{-6} MPa after ~30 minutes.
16. Turn on the high voltage (HV) units to begin an automatic ramp to 60 kV.
17. Centre the beam on the base plate and perform beam alignments.
18. Load the build file (*.abf) onto S12 and specify the *themes*.
19. Press PLAY to begin base plate heating followed by component production.

Essentially, the steps above require the user to clean the vacuum chamber, replenish powder (as required), insert and level a new stainless steel base plate, calibrate the rake and, if necessary, replace the tungsten filament. These steps are standard EBM practice and information regarding the procedures are documented in the Arcam EBM A2 and S12 User's Manual [85]. Step 18 mentions a *.abf file which stands for *Arcam build file*. This file contains the geometry information of the component being produced and is generated in *Arcam build assembler* software. The required software procedures shall be discussed in the following section. Step 18 also mentions *themes*; *themes* control the electron beam properties and are discussed in Section 3.1.8.

3.1.5. *Software*

All ALM processes are heavily reliant on software; several software packages may be used in order to produce a file that is loaded onto the ALM hardware. Typically, the production of an EBM component requires three pieces of software: (i) 3D CAD software for component design, (ii) Materialise *Magics* RP/RM software for component orientation and support generation and (iii) the Arcam build assembler for layer slicing.

*Figure 3.8 : (a) 3D CAD geometry and (b) *.STL file.*

Figure 3.8 shows in (a) a basic geometry generated in CAD software and (b) the production of a *.STL representation of the CAD geometry. Such CAD geometries are imported into the Materialise *Magics* software; within this software, CAD geometries are oriented in a virtual S12 build chamber and positioned on top of a virtual base plate. If necessary, *Magics* can be used to generate support structures for overhanging surfaces. Support structures are geometry specific and the automatically generated supports can be edited; the geometry in Figure 3.8 does not require any support structures and is termed *self-supporting*.

Once the components have been successfully positioned and supported in *Magics*, the geometries are imported into the *Arcam build assembler* which slices the geometries into 100 μm layers (layer thickness can be changed if necessary). The type of geometry is also assigned in this piece of software i.e. the component is differentiated from the supports so that specific melt *themes* may be applied on the S12. The *build assembler* produces a *.abf file which can be loaded onto the S12 computer.

Software usage can be summarised by the following steps:

1. Produce a 3D model of the component in CAD software.
2. Save in *.STL format.
3. Using Materialise *Magics* software, load the Arcam S-12 build platform.
4. Import *.STL file(s) into Magics and fix the file.
5. Orient the component on a base plate and generate supports, using *Magics*, on overhanging/inclined surfaces.
6. Export the supports and CAD model to the *Arcam build assembler* software.
7. Use *build assembler* to slice the supports and CAD model into 100 μm layers.
8. Save the file in *.abf format in order to load onto the S12 computer.

3.1.6. EBM Control Software

Control of the Arcam S12 system is carried out by using the EBM software. At the very beginning of this work, the S12 was running EBM2.7 control software. This software was not very user-friendly; coupled with this, machine reliability was also an issue. The release of EBM3.0 introduced a more user-friendly interface with a green-light system to direct the user towards any missed operations. This software also incorporated the use of controlled vacuum (CV-EBM) discussed in Section 3.1.7. Figure 3.9 shows a screenshot of the overview page of EBM3.2 (the current EBM software version). The left-hand pane contains the stop, pause and play buttons along with the display of some key processing variables. Navigating away from the overview page gives access to hardware controls, *build* set up controls, process controls and calibration controls.

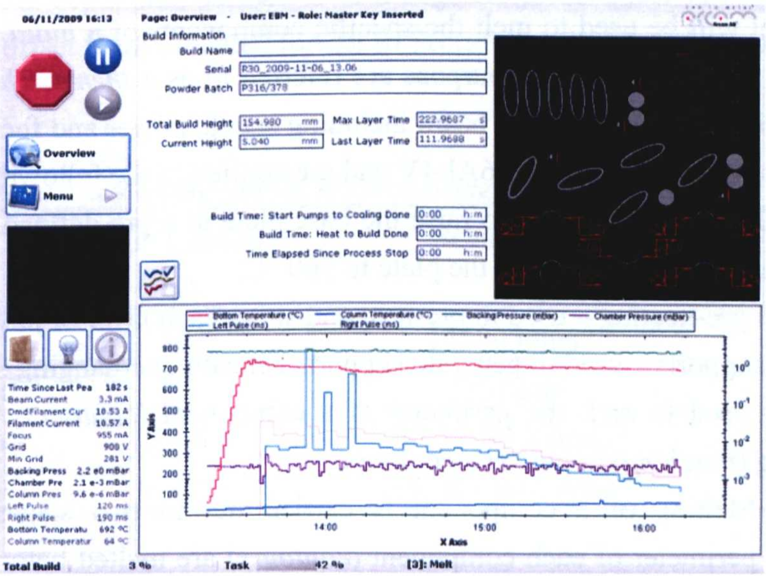

06/11/2009 16:13

Page: Overview - User: EBM - Role: Master Key Inserted

Build Information

Build Name

Serial: R30_2009-11-06_13.06

Powder Batch: P316/378

Total Build Height: 154.980 mm

Current Height: 5.040 mm

Max Layer Time: 222.9687 s

Last Layer Time: 111.9688 s

Build Time: Start Pumps to Cooling Done: 0:00 h:m

Build Time: Heat to Build Done: 0:00 h:m

Time Elapsed Since Process Stop: 0:00 h:m

Time Since Last Pea	182 s
Beam Current	3.3 mA
Dmd Filament Cur	10.53 A
Filament Current	10.57 A
Focus	955 mA
Grid	909 V
Min Grid	281 V
Backing Press	2.2 e0 mBar
Chamber Pre	2.1 e-3 mBar
Column Pres	9.6 e-6 mBar
Left Pulse	120 ms
Right Pulse	190 ms
Bottom Temperatu	692 °C
Column Temperatur	64 °C

Total Build 3 % Task 42 % [3]: Melt

Figure 3.9 : Overview screen from EBM 3.2 control software. Image from www.arcam.com.

3.1.7. Controlled Vacuum

Controlled vacuum EBM (CV-EBM) was introduced into the Arcam system alongside the introduction of the EBM3.0 software. Whilst the software upgrade addressed the issue of being user-friendly, CV-EBM was introduced to enhance process reliability. Although there are several reasons that may cause the process to be aborted, initially a major problem was due to *smoking*. *Smoking* occurs when the electron beam charges powder particles that are not able to dissipate the charge with sufficient speed. The charged powder particles repel each other and are propelled throughout the vacuum chamber. Such an occurrence is sometimes recoverable but, powder can travel into the gun and, in some cases, welds to the hot tungsten filament rendering it unusable. *Smoking* also indicates that the powder is insufficiently sintered. The original system was very sensitive to this phenomenon and *smoked* frequently.

CV-EBM was introduced to combat this problem by allowing helium into the vacuum chamber to raise the pressure to $\sim 2 \times 10^{-3}$ mbar. Helium in the chamber is ionised by the electron beam producing positive ions which are available to carry excess charge away from the powder. The introduction of CV-EBM significantly reduced *smoking* and the sensitivity of the process to this problem. A secondary advantage of using helium is that it can be introduced into the chamber once the process is complete; helium has a high thermal conductivity and does not react with titanium. Thus helium can be used to promote cooling of components and reduce cycle times.

3.1.8. Themes

The process control page of the EBM software is where the user specifies the beam parameters that will be used to melt the specific components of a *build.* A collection of parameters used for a specific purpose are referred to as a *theme*. *Themes* contain all of the properties of the electron beam including speed, power and focus. Typically four themes are used to process Ti-6Al-4V and are applied in the following order:

- Base plate heating – used to raise the base plate to a pre-defined temperature. Standard practice is to raise the plate to 760 °C.
- Powder pre-heating – used to pre-heat and sinter each layer of powder.
- Wafer supports – used to generate supports beneath overhanging surfaces.
- Melt – used to melt the perimeter of a component (*contours*) and for bulk melting (*hatching*) in between contours.
    - Melting of a component is carried out in two stages; firstly the perimeter of each component (*contours*) are melted before the bulk of the component is melted (*hatching*).

Application of three of the key *themes* is shown in Figure 3.10 in which the appearance and motion path of the beam is dependant on the specific operation. In the figure: (a) shows the powder pre-heating stage using and orthogonal raster pattern, (b) shows the melting of component contours using the *multi-beam* contour method and (c) shows hatching using an orthogonal raster pattern. The orthogonal *hatching* raster pattern is rotated by 90° after each layer and thus melting alternates along the *x*- and *y*- axes.


(a) *(b)* *(c)*

Figure 3.10 : Images of the key processing steps (a) powder preheating, (b) melting of contours using multi-beam and (c) hatching. Screenshots taken from a video available at www.arcam.com/technology/ebm-process.aspx.

Some of the key parameters in the aforementioned *themes* are given in Table 3.1. The power of the electron beam is determined by the value of the *beam current*. *Beam speed* is not constant for the melt *theme*; its value depends on a parameter called *speed function*. *Speed function* is discussed in further detail in Section 4.1.2 of the Numerical Modelling Chapter. *Focus offset* is the value of current used by the focussing coils to focus the beam; a positive *focus offset* brings the focal point of the beam above the deposition surface with a negative *focus offset* having the opposite affect. Focus offset is investigated further in Section 4.1.3 of the Numerical Modelling Chapter.

Table 3.1 : Typical beam settings for the key processing themes.

Theme	Beam Current, mA	Beam Speed	Focus Offset, mA
Pre-heat	15	14600 mms^{-1}	45 mA
Wafer support	2.2	275 mms^{-1}	8 mA
Melt (Contour)	5 – 8	40.5 – 93.8 mms^{-1}	22 mA
Melt (Hatch)	6 – 15	187.8 – 802 mms^{-1}	17 mA

Unless otherwise stated, beam parameters given in the above table were used for the production of all EBM samples within this investigation.

3.1.9. Build Temperature and the Auto Power Calculation

It has already been noted that prior to melting powder, the base plate temperature is raised to 760 °C. The temperature of the base plate and the entire *build* is monitored by a single thermocouple, positioned beneath the stainless steel base plate. The thermocouple reading for a 10 mm tall *build* is shown in Figure 3.11. The base plate heating *theme* is used to raise the plate to 760 °C. At this point, a layer of powder is applied and the pre-heat, wafer support and melt *themes* are used to melt the geometry in the layer. An initial drop in temperature is usually followed by a steady temperature; this steady temperature is known as the *build temperature* or *bed temperature*. Upon turning the beam off, the build chamber slowly cools to room temperature.

During the production of Ti-6Al-4V, a target temperature of approximately 650 °C was maintained; this is considered to be standard practice. Excessively high or low temperatures can have detrimental effects on processing. Table 3.2 lists some of the issues that arise from poor control of the *build temperature*.

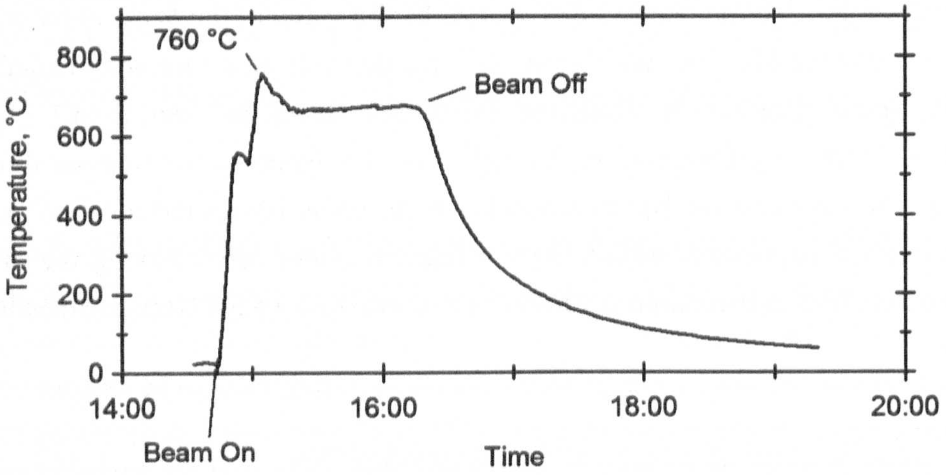

Figure 3.11 : Thermocouple reading for a 10 mm tall EBM build.

The reading given by the thermocouple decreases over time because the distance between the thermocouple and deposition surface increases with the addition of each layer. This is true of a *build* with a constant cross section; however, energy input is also geometry dependent – as the size of the melted area in each layer increases, so does the energy input. For relatively small *builds*, maintaining a constant thermocouple reading is possible (Figure 3.11) by making changes to the pre-heating *theme*. As the height of a component increases, the thermocouple reading becomes less and less meaningful to the user and thus cannot be used as a control parameter.

Table 3.2 : Theme requirements and associated problems during EBM.

Theme	Process Requirement	Problems
Heating base plate	To raise the temperature of the base plate sufficiently to ensure the required build temperature is maintained.	Base plate too cold → poor sintering, potential powder repulsion. Base plate too hot → over sintering can lead to individual layers curling.
Pre-heating (sintering) of powder	To sinter powder sufficiently to prevent repulsion when melting begins.	Insufficient sintering → powder repulsion. Over-sintering → powder difficult/impossible to remove from around component.
Melting	To homogeneously melt pre-sintered powder and produce a smooth layer.	Poor melting → porosity. 'Over melting' → evaporation, potential loss of alloying additions, swelling/distortion of component.
Other Heating	Can be used prior to or post-melting on the entire powder bed, a portion of the bed or on the components only to supply heat to the build.	Too cold → poor sintering, poor melting, potential powder repulsion. Too hot → evaporation, potential loss of alloying additions, swelling/distortion of component.

To combat the variation in energy input, the EBM software performs a calculation referred to as the *Auto Power Calc*. This aims to maintain a constant input of heat into each layer, regardless of the melt volume. The software determines the surface area of each layer and performs calculations (the details of which are unknown) to determine the amount of energy lost as a result of radiation into the vacuum environment and conduction into the sintered powder surrounding a component. Based on these calculations, an *average current* is calculated. The *average current* is the calculated beam melting current required to maintain a constant *build temperature*.

Regardless of this calculated value, the actual current used by the beam can only lie in the range of currents given in Table 3.1. If the calculated current exceeds the maximum current given in this range, the excess is put into a buffer. The deficit in energy is compensated for by using the energy in the buffer to put extra heating operations in between stages e.g. after melting but before the application of the next powder layer.

3.2. EBM Samples

Samples for metallographic analysis were produced on the Arcam S12 by following the methodology outlined in the previous sections. For microstructural analysis, cylindrical and rectangular samples were generally produced. Samples for tensile testing were machined from cylindrical EBM samples. Such samples were used for bulk microstructural analysis and determination of microstructure and texture. Further samples were produced and referred to as *melt tracks*. These samples were used to investigate the effect of processing parameters on the electron beam and substrate material. The production of melt tracks will now be discussed.

3.2.1. Melt Tracks

The production of linear melt tracks on solid material provided a means to asses the effect of the electron beam. Melt tracks were created by generating solid 'dummy' components and positioning them an arbitrary height above the base plate in *Magics* software. Support structures were then produced, manually edited and exported as wafer supports. Table 3.3 lists the standard settings for wafer supports. By importing the supports onto the S12 and changing current, speed and *focus offset* values; properties of the beam when melting were mimicked. The *Back and forth* setting was changed to a value of FALSE and the *Repetitions* value changed to 1. This prevented the beam traversing over the defined melt track twice.

Prior to evacuating the chamber, the base plate was levelled, as normal, before placing a substrate sample onto the base plate. The *build table* was then dropped by the thickness of the sample and the rake arm removed to prevent it from moving the sample. Melting was carried out in manual mode. An example of a melt track made directly onto a base plate is given in Figure 3.12; the direction of beam travel was left to right. Measurement of melt track depths and widths were used as a means of validating a numerical model.

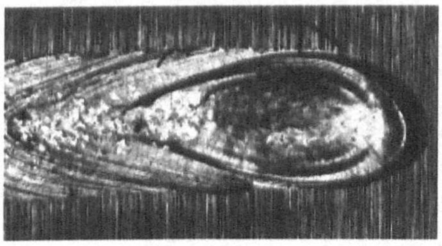

Figure 3.12 : Confocal micrograph of an individual melt track (760 µm wide) on a stainless steel base plate. Direction of beam travel left to right.

Table 3.3 : Standard Arcam wafer support settings.

Melt category	Melt parameter	Value	Units
Wafer	Enable	TRUE	-
	Current	2.2	mA
	Speed	275	mms^{-1}
	Focus offset	8	-
Heating	Enable	TRUE	-
	Max heating time	12	s
	Heating factor	1	-
Repetitions	Minimum distance	0.5	mm
	Back and forth	TRUE	-
	Repetitions	2	-

Figure 3.13 shows an example of the experimental set up used to produce melt tracks on titanium substrate material. The substrate could be left at ambient temperature, or raised to elevated temperature by using the preheating *theme*.

3.2.2. As-built Surface Roughness

A potential Achilles heel of EBM processing (and other ALM methods) is the quality of the as-built surface and the extent of the surface roughness. The roughness is a function of layer thickness, powder size and machine compliance. Qualitative measurements of surface roughness were made using a Taylor-Hobson Talysurf, shown schematically in Figure 3.14. The stylus tip was used to travel across a measurement distance of 8 mm parallel and perpendicular to the *z*-axis of as-built

EBM samples. As the stylus traverses, the surface roughness results in a vertical translation, which is stored as a surface roughness profile.

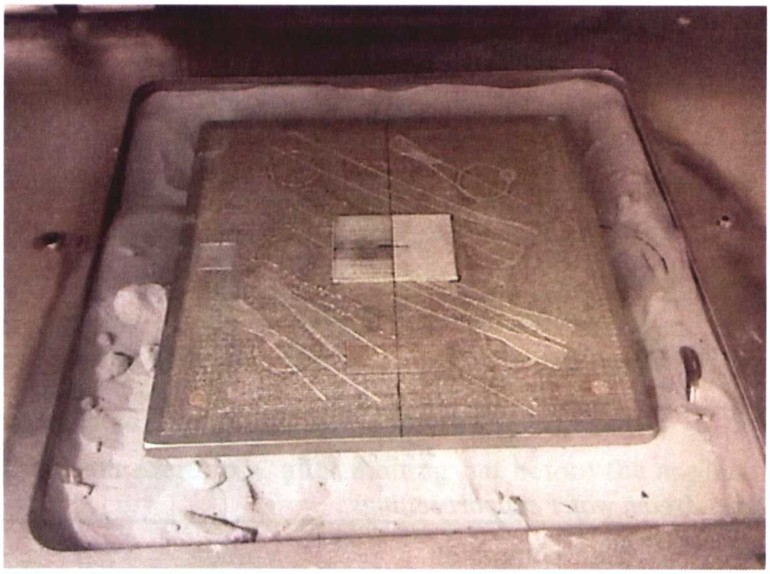

Figure 3.13 : Image of a levelled base plate with two centralised titanium substrate samples, the rake arm has been removed.

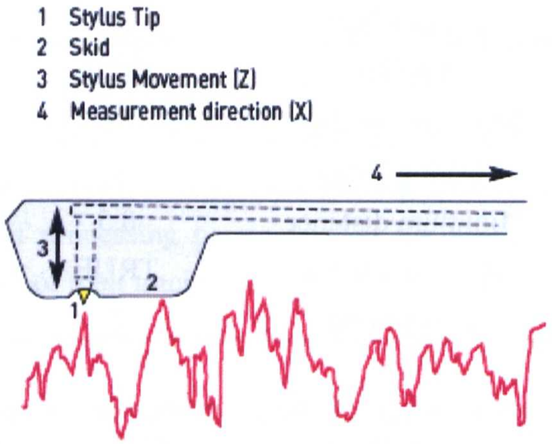

Figure 3.14 : Schematic of surface roughness measurement using a stylus (roughness profile not to scale). Image from www. taylor-hobson.com/pdf/uk/DUO.PDF.

From the surface roughness profiles, the roughness parameter, R_a, was also obtained. R_a is the mean departure of the profile from a mean line [87] and can be calculated as shown in Figure 3.15 and Equation (3.1). A reference sample, with an R_a of 6 μm, was used to check the calibration and function of the Talysurf prior to use.

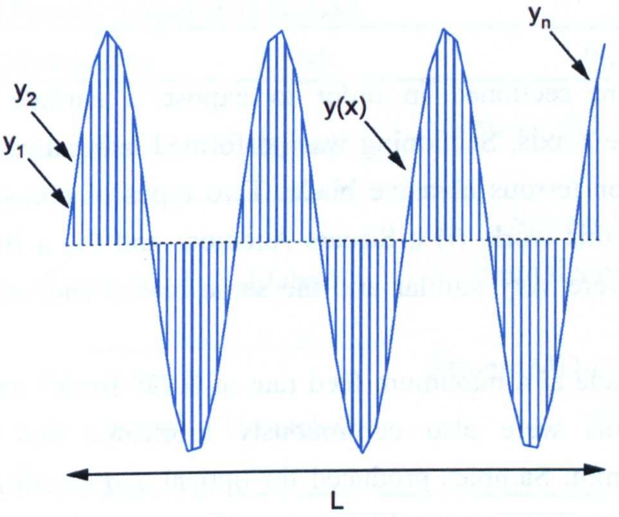

R_a = average deviation of profile y(x) from the mean line = total shaded area / L

$$R_a = \frac{1}{L}\int_0^L \left| \; y(x) \; \right| dx \cong \frac{1}{N}\sum \left| \; y_i \; \right| \tag{3.1}$$

Figure 3.15 : Schematic surface roughness profile and method for calculating R_a, adapted from [88].

3.2.3. Heat Treatment

Heat treatments were performed on samples of dimensions 5 × 5 × 10 mm ($h \times w \times l$), in a tube furnace with flowing argon gas to prevent oxidation. Martensitic microstructures were formed by heating the samples at 1030 °C for 30 minutes before water quenching. Martensitic samples were tempered, tempering of these martensitic microstructures was carried out at 650 °C for times between 60 and 1050 minutes followed by either water quenching or furnace cooling.

3.3. Specimen Preparation

Microscopic techniques have been used to investigate several types of microstructure including: (i) powder microstructures, (ii) as-built microstructures and (iii) post heat treatment microstructures. The microscopy techniques carried out in this study include: light microscopy (LM) and scanning electron microscopy (SEM). Electron back-scattered diffraction (EBSD) has also been performed to characterise both grain structure and orientation. Specimen preparation for all of the microscopic techniques was essentially identical.

3.3.1. Sectioning

EBM samples were sectioned in order to expose a surface either parallel or perpendicular to the z-axis. Sectioning was performed using a rotating abrasive saw equipped with a non-ferrous abrasive blade. Two types of abrasive saw were used over the course of this work, (i) a Struers Accutom and (ii) a Beuhler Isomet 500. Both instruments were very similar and the same blades and cutting practice were employed on each.

All cuts were made at a maximum feed rate of 0.035 mms^{-1} and a blade speed of 1500 rpm. All cuts were also continuously lubricated and were accurate to approximately 0.1 mm. Samples produced for optical and electron microscopy were generally sectioned so that they would fit into a 32 mm sample holder (when mounted in Bakelite). Samples used for EBSD were required to be a specific size depending on the sample holder used.

3.3.2. Grinding and Polishing

Grinding and polishing was carried out on a Struers Abramin automatic grinding/polishing machine. Three steps were performed for sample preparation utilising a Struers MD-Piano diamond abrasive disc to produce a planar surface (~3 minutes grinding), a Struers MD-Largo composite disc for initial polishing (~7 minutes polishing) and a Struers MD-Chem polishing mat for final polishing (~11 minutes polishing). Table 3.4 gives a summary of the preparation methods used for each microscopy technique. A 9µm water-based diamond suspension was applied during the initial polish and a mixture of colloidal silica (silco), hydrogen peroxide (H_2O_2) and water in the ratio 4:1:5 for final polishing. It was found that the addition of hydrogen peroxide was not required if a 1:1 mixture of silco and water was used.

3.3.3. Etching

Optical and SEM samples were etched in Kroll's reagent composed of 2 ml HF, 4 ml HNO_3 and 100 ml H_2O. Samples were submerged in the etchant for 10 seconds before neutralising the sample in a lime solution and washing with water. Samples for EBSD were not etched.

Table 3.4: Summary of sample preparation methods.

Technique	Dimensions	Finish	Process
Optical Microscopy	< 32 mm Ø	Etched	Struers MD-Piano (+ water) ↓ Struers MD-Largo (+ 9 μm diamond suspension) ↓ Struers MD-Chem (+ colloidal silica)
SEM	< 32 mm Ø	Etched	
EBSD	10 × 10 × 6 mm 30 × 10 × 6 mm (l × w × t)	Un-etched	

3.4. Light Microscopy

A Polyvar light microscope equipped with an Axiocam camera was used to take digital micrographs of samples at magnifications ≤ 1000 ×. Quantitative analysis performed using light microscopy included grain size determination, phase characterisation and volume fraction of transformation after heat treatments.

3.4.1. *Grain Size*

Grain size was measured manually using the mean linear intercept method. A line was drawn across a micrograph and its length and the number of intersections with grain boundaries was recorded. The relative standard error (S) can be calculated from the mean linear intercept grain size $(\bar{L})$, the number of grains per unit length $(\bar{N}_L)$ and the number of grains counted, n., as per Equation (3.2).

$$\frac{S(\bar{L})}{\bar{L}} = \frac{S(\bar{N}_L)}{\bar{N}_L} \approx \frac{0.65}{\sqrt{n}} \qquad (3.2)$$

3.4.2. *Volume Fraction Transformed*

Volume fraction of transformed material, resulting from heat treatments, was determined from micrographs by point counting. A grid of appropriate size was drawn onto the micrographs with care being taken to ensure the grid was of sufficient size to prevent counting the same region twice. Points were discriminated in three ways: (i) transformed, (ii) not transformed and (iii) uncertain i.e. lying on the boundary between transformed and non-transformed.

3.4.3. Alpha Colony Size

In general, three microstructural features were measured; these were: (i) prior β grains size, (ii) α lath width and (iii) α colony size. Both (i) and (ii) were measured using the previously described linear intercept method. Although still making use of the linear intercept method, α colony size was measured in a slightly different manner.

Tiley *et al.* [89] describe how the determination of α colony size is difficult without making assumptions regarding colony shape and morphology. The method suggested for colony measurement is to use a random grid, overlaid onto a micrograph, onto which colony intersections are marked. The mean intercept length gives a *colony scale factor* which describes colony size but not shape. An example of the determination of α colony scale factor is shown in Figure 3.16.

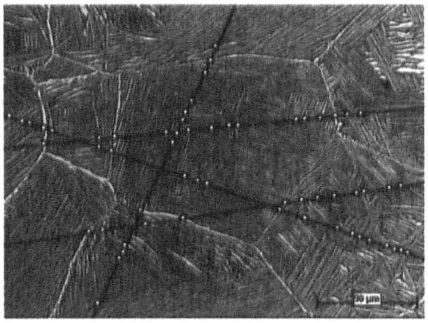

Figure 3.16 : A random grid overlaid onto a colony Ti-6Al-4V microstructure with colony intersections marked for the determination of α colony scale factor [89].

3.4.4. Secondary Dendrite Arm Spacing (SDAS)

The spacing of dendrite arms during the solidification of alloys can be related to the cooling rate via the secondary dendrite arm spacing (SDAS). An increase in cooling rate results in a decrease in dendrite size; this can be described by the following equation:

$$\lambda_2 = \frac{B}{\dot{T}^n} \tag{3.3}$$

where λ_2 is the secondary dendrite arm spacing, B is a constant, $\dot{T}$ is cooling rate and n is a constant [90]. Dendrites were observed on individual melt tracks produced on stainless steel base plates. Measurement of λ_2 and the use of Equation (3.3) allowed cooling rates to be calculated.

3.4.5. Microindentation Hardness Testing

Hardness testing was performed on a variety of samples; preparation of samples for hardness testing was the same as that for light microscopy, including etching. A Mitutoyo HM-101 hardness tester, fitted with a diamond, square-based pyramid, Vickers indenter was used. The load used for the indentations was 100 g applied for a dwell time of 10 seconds. After the indentation was made, the distance between both indentation diagonals was measured, an average taken, and the Vickers hardness (HV) calculated. Vickers hardness is calculated using the following equation:

$$HV = \frac{2000P\sin(\alpha/2)}{d^2} = \frac{1854.4P}{d^2} \qquad (3.4)$$

where d = mean diagonal length in μm, P is the applied load in gf and α is the angle between pyramidal faces (136°). Indents were spaced at distances >2.5d from each other to ensure results were not influenced by the plastic deformation and the associated strain field created by a previous indent.

3.4.6. Image Analysis of Powder

Freeware image analysis software, ImageJ (http://rsbweb.nih.gov/ij/index.html), was used to measure powder size from micrographs of powder particles. A threshold procedure was used to distinguish the powder particles from the background prior to performing the automated measurement; this can be seen in Figure 3.17. In some cases powder particles touched and were not fully separated by the threshold process. In such cases, a layer of pixels between the particles were manually removed so that each powder particle was detected individually. The image scale was entered into the software before the function entitled *Analyze Particles* was used to determine the area of the measured particles. Powder particles intersecting the edge of the micrograph were discounted. Measured powder areas were converted into equivalent diameters by assuming all particles were perfectly circular in section.

Validity of the image analysis method was investigated by comparing manual measurements of powder diameter to equivalent diameters determined via image analysis. Results of this comparison can be seen in Table 3.5, with excellent agreement between the two methods. The more efficient image analysis process was therefore used, with confidence, as a method for the measurement of powder particle size.

Table 3.5 : Comparison between manual measurements and image analysis of virgin powder size.

	Manual measurements	Image analysis
number of measurements, n	228	223
mean, $\bar{x}$	97.14 μm	97.78 μm
standard deviation, σ	32.00 μm	30.01 μm
standard error of mean, $\sigma/\sqrt{n}$	2.11 μm	2.00 μm

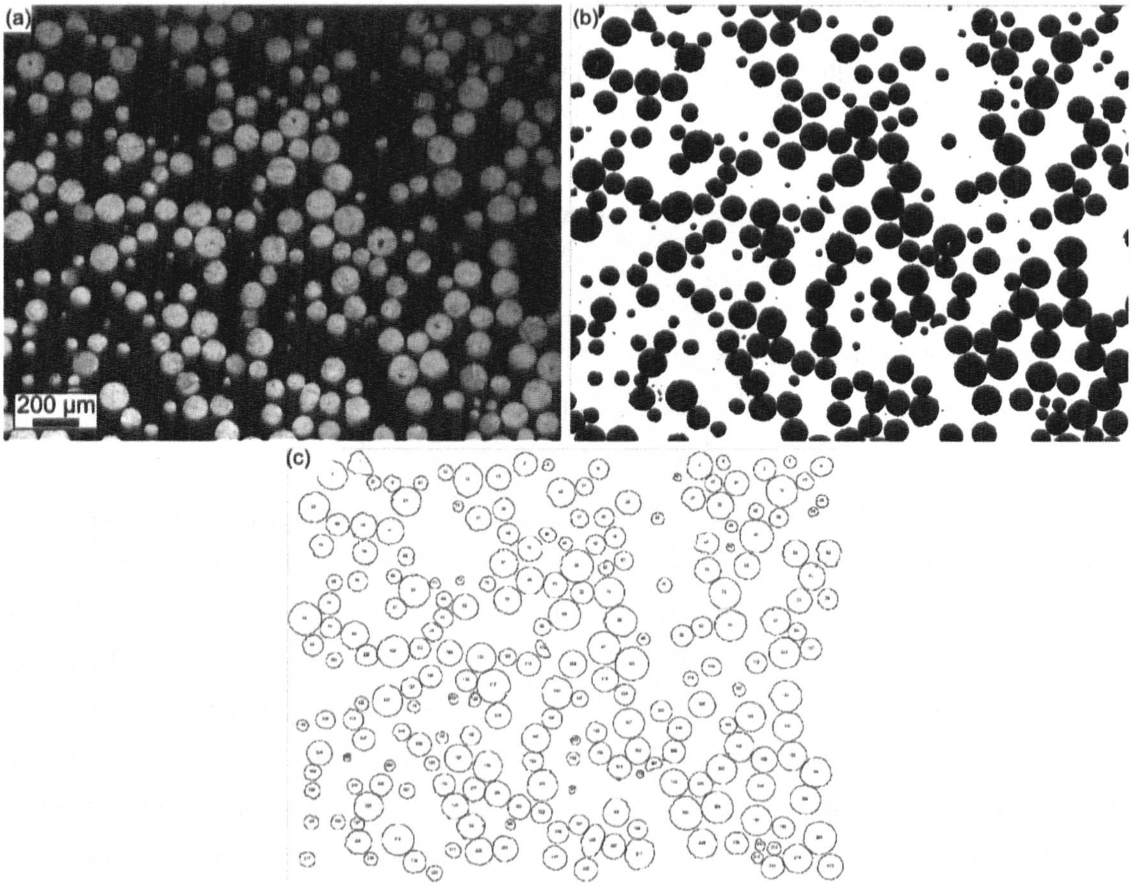

Figure 3.17 : Example of (a) micrograph of virgin powder, (b) threshold image to reveal powder particles and (c) measurement of virgin powder particles using Analyze Particles in ImageJ.

3.4.7. Scheil Analysis

Although true of all metallographic samples, the sectioning of powder samples has a significant influence on quantitative measurements. Optical microscopy and image analysis of spherical powder particles results in the measurement of circle diameters. The circles arise from sectioning of the spheres by the polishing plane. Higginson and Sellars [91] discuss in detail how microstructures may be described numerically and how two-dimensional observations may be related to three-dimensional, volumetric results. When considering sectioned powders, the probability of sectioning a large particle is greater than that of sectioning a small particle. Also, spherical particles may be sectioned at any point. As such, when sectioned, powder particles of diameter D may be observed to have a distribution of diameters from 0 to D.

To correct for sectioning errors when measuring powder samples, Scheil analysis was used. A matrix of coefficients relates the number of circles in size group i that occur from sectioning of spheres in size group j. From the matrix, a set of coefficients $(\alpha(j,i))$ are derived and used to calculate the number of spheres per unit volume in size group j from the number of circles in size group i, where $i = 1$ to k [91]. Equation (3.5) calculates the volume fraction of spheres in size group j ($N_V(j)$) by utilisation of the coefficients, the number per area of circles in each size group (N_A) and the size group interval Δ. The coefficients used to correct the data were taken from the Woodhead method for calculating particle size distribution [91]. Thus, measurements of powder particle size were corrected for sectioning error.

$$N_V(j) = \frac{1}{\Delta}\{\alpha(j,j)N_A(j) + \alpha(j,j+1)N_A(j+1) + \dots \\ + \alpha(j,k)N_A(k)\} \qquad (3.5)$$

3.4.8. Coulter LS130 Particle Size Analyser

As well as powder size measurement from micrographs, powder size analysis was performed using a Coulter LS130 particle size analyser. The equipment is capable of measuring particle sizes between 0.1 μm and 900 μm in diameter. Powder particles are added to a water reservoir before the powder/water mixture is pumped into the main body of the equipment, containing a laser. The powder particles diffract the laser and, based upon the diffraction patterns, the equipment calculates the size of the particles causing the diffraction.

Ti-6Al-4V powder was mixed thoroughly with glycerol. The addition of glycerol helped to prevent the powder floating at the top of the reservoir during the test and also helped to disperse powder particles, in an attempt to reduce agglomeration.

Prior to all measurements, a background reading was taken and automatically subtracted from the results. The glycerol/powder mixture was added to a water reservoir until an obscuration level between 8 and 12 % was achieved. At this point the measurement cycle was started. Measurement took 90 seconds to complete, each sample was measured 3 times and a pause of 30 seconds was left between each cycle. During loading of the sample (into the reservoir), before each run and during the run, the water was ultrasonically agitated in order to further reduce particle agglomeration.

3.5. Electron Microscopy

Scanning electron microscopy was used for more detailed microstructural analysis of EBM specimens. The analysis of crystallographic texture was performed using electron backscatter diffraction (EBSD). Two scanning electron microscopes were used during the course of this work: (i) a FEI Sirion FEGSEM and (ii) a FEI Inspect F FEGSEM. Both microscopes were equipped with a Nordlys EBSD camera and HKL Channel 5 acquisition and manipulation software. SEM images were typically acquired from secondary electrons although some features were identified more readily using backscattered electron imaging. A JEOL 6400 SEM equipped with a calibrated Oxford Instruments energy dispersive x-ray spectrometer and INCA software was also used for quantitative chemical analysis.

3.5.1. Electron Back-Scattered Diffraction (EBSD)

EBSD was a very useful means of investigating EBM microstructures. Orientation mapping using small step sizes (≤ 2 µm) resolved individual α laths; increasing step size produced larger maps that allowed complete prior β grains to be reconstructed and their texture determined; β reconstruction will be discussed in more detail later.

3.5.2. EBSD Principles and Equipment

An illustration of a typical EBSD setup is shown in Figure 3.18 in which a standard SEM arrangement is equipped with a retractable electron detector and video camera. Samples are tilted to 70° before inserting the detector. The detector uses a phosphor screen, caused to fluoresce by impacting electrons diffracted by the sample. A charge coupled device (CCD) video camera is used to view the diffraction patterns.

Electrons from the SEM electron beam are inelastically scattered by the sample; these electrons may be diffracted by atomic planes. Diffraction occurs if the scattered electrons are travelling at the Bragg angle with respect to the atomic planes. The principal of diffraction can be seen in Figure 3.19; Bragg's Law is derived in Equations (3.6) to (3.8).

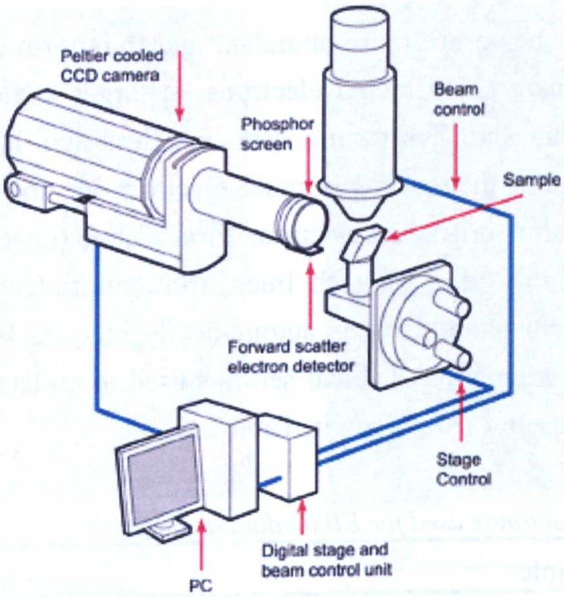

Figure 3.18 : Illustration of the EBSD equipment setup. Image from Oxford Instruments, http://www.ebsd.com/ebsd-explained/basicsofebsd1.htm.

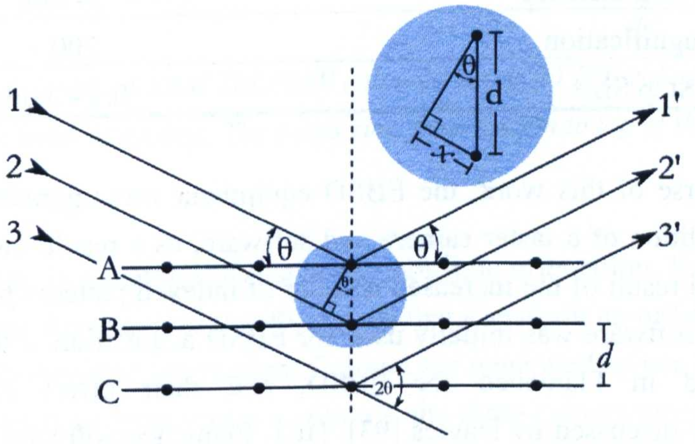

Figure 3.19 : Electron diffraction from lattice planes A, B and C.

$$x = d\sin\theta \qquad (3.6)$$

$$2x = 2d\sin\theta \quad \text{where } n\lambda = 2x \text{ for diffraction} \qquad (3.7)$$

$$n\lambda = 2d\sin\theta \quad n = 1, 2, 3, \ldots\ldots \qquad (3.8)$$

where n is an integer, λ = electron wavelength, d = distance between diffracting atomic planes and θ = angle of incidence.

Electrons travelling at $+\theta°$ and $-\theta°$ are diffracted and result in an intensity change compared to the background intensity. Diffracted electrons travelling at an angle closest to the incident beam are more abundant and thus form a bright line (greater than background intensity). Diffracted electrons, at larger angles from the incident beam, are less abundant and thus form a dark line (less than background intensity). Lines are observed rather than points because electrons are inelastically scattered in three dimensions and thus diffracted electrons form a cone (observed as a line in two dimensions) [92]. A collection of such lines, from multiple diffractions within a crystal, forms a Kikuchi pattern that is automatically indexed by EBSD software to determine the crystal orientation. Typical settings used to collect EBSD data on both EBSD-equipped microscopes are given in Table 3.6.

Table 3.6 : Microscope settings used for EBSD data acquisition.

Variable	Value
Accelerating Voltage	20 kV
Spot Size	3 – 5
Working distance	14 mm
Magnification	200 ×
Step Size	0.4 - 5 μm

Over the course of this work, the EBSD equipment was upgraded. The upgrade involved the addition of a faster camera and software; as a result, larger maps could be produced as a result of the increased number of indexed patterns per second (pps). HKL Flamenco software was initially used for EBSD acquisition, a discussion of the parameters used in Flamenco for EBSD, and their effect on mapping, is comprehensively discussed by Davies [93]. HKL Flamenco software was superseded by HKL Fast Camera Acquisition software, capable of running at higher speeds. The enhanced capability of the upgraded system meant that EBSD data could be acquired at 25 – 50 pps as opposed to 5 – 12 pps with the older apparatus.

3.5.3. Presentation of EBSD Data

Orientation maps obtained from EBSD can be displayed in a variety of ways. All maps were processed and produced in HKL Channel 5 software. Mappings were coloured using either inverse pole figure (IPF) colouring or Euler colouring as appropriate. IPF colouring provides a quick method of viewing crystallographic orientation by indicating the atomic planes parallel to a user defined direction (*x*, *y* or *z*). This can be seen in Figure 3.20 (a); regions coloured red indicate areas where {0001} planes are parallel to the sample surface. IPF colouring does not display absolute texture.

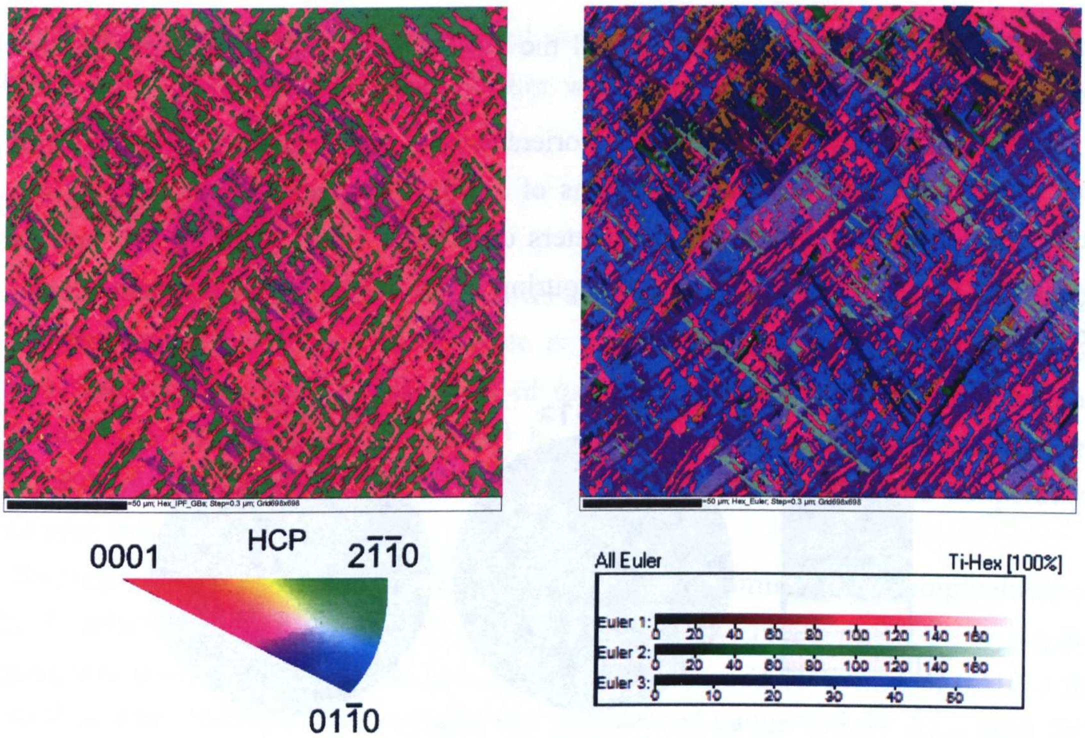

(a) *(b)*

Figure 3.20 : An example of EBM Ti-6Al-4V coloured using (a) IPF colouring and (b) Euler colouring with the associated keys. The z-axis runs from bottom to top of the page. Scale bars = 20 µm.

Euler colouring is a method of displaying absolute orientation. Each orientation is described by three Euler angles (φ_1, Φ and φ_2) that transform an orthogonally oriented unit cell to the determined orientation. Colours are generated as per the key shown in Figure 3.20 (b); each angle provides a colour – the three colours are mixed to give the Euler colouring. As such, orientation is less intuitive in comparison to IPF colouring.

In some cases, noise reduction was performed in order to 'clean' EBSD data. Where necessary, *wild spikes* were removed; wild spikes are individual pixels with orientations significantly different from surrounding pixels. Such an occurrence is indicative of a mis-indexed point. Zero solutions were also extrapolated where it was clear that the likely reason for the zero solution was failure to index a diffraction pattern.

3.5.4. *Texture Representation*

Pole figures (PFs) have been employed to present the texture of room temperature α phase and reconstructed prior β phases. Pole figures have been generated with the *z*-axis of an EBM sample normal to the plane of the page as a convention. The two key crystallographic directions for which the PFs were generated were the <0001> and the

<11-20> directions for the α phase and the <110> and <111> directions for the β phase.

A PF of scattered data indicates the orientation of each pixel whilst a contouring step clusters the data to indicate regions of similar / preferred orientations. Unless otherwise stated, the contouring parameters used were a half width of 10° and data clustering of 5°. The units for contouring were multiples of uniform density, abbreviated as MUD.

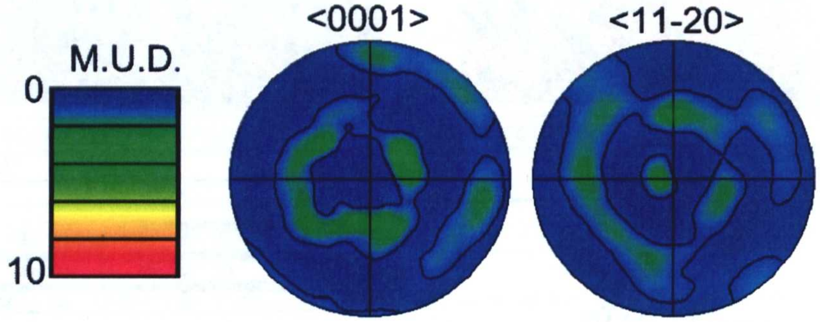

Figure 3.21 : An example of hexagonal pole figures used to display α phase texture.

3.5.5. Prior β Phase Reconstruction from Room Temperature EBSD Data

Post-processing of EBSD data, by utilization of the Burgers relationship, allows the high temperature prior β grain structure to be determined and gives further insight into how the EBM process takes place. One parent β grain gives rise to a possible 12 distinct α orientations, also termed variants. Using software developed by Davies [93], it is possible to automatically reconstruct the parent beta microstructure from the inherited alpha phase microtexture obtained from EBSD analysis. A grain reconstruction procedure is used to determine the extent of each parent beta grain; each grain is reconstructed by examining misorientations between neighboring alpha pixels to establish whether they belong to the same variant, or different variants, inherited from the same parent beta grain.

Pixels from different variants are deemed to be inherited from the same parent grain if both the angle and the axis of the misorientations are close to the 11 specific misorientations that occur between alpha variants inherited from the same parent grain [94]. To determine the prior beta orientations from each alpha variant, all misorientations along the boundary between it and neighboring variants are calculated. Each of these experimental misorientations will be close to 1 of the 11 misorientation types; 8 out of these 11 misorientation types result in the calculation of a single solution for prior β grain orientation [95]. In cases where a single solution cannot be determined, a second reconstruction pass is used to determine the prior β orientation of the non-reconstructed variants, based on the prior β orientations of the reconstructed variants. A more detailed description of the technique is given by Davies [93] whose work draws on earlier work conducted in the field by Gey and Humbert [94, 95].

3.6. Build Temperature Variation

As previously discussed, Figure 3.11 shows the temperature profile of a 10 mm *build.* The temperature at which a steady state is maintained can be varied by changing *theme* settings. In doing so, the effect of *build temperature* on microstructure and mechanical properties was investigated by changing the preheating *mean current* parameter in the preheat *theme*. Increasing *mean current* increased bed temperature (and vice versa).

Four separate but identical *builds* were carried out at nominal *build* temperatures of 625 °C, 650 °C, 675 °C and 700 °C. These temperatures were achieved by varying the *mean current* between 12 and 20 mA. Each build contained 10 cylinders (Ø10 × 80 mm) that were machined into tensile test samples of gauge Ø5.64 $\pm^{0}_{0.02}$ mm and gauge length of 32 ± 0.2 mm. Half of the samples from each build were tested in the *as-built* condition whilst the remaining samples were hot isostatically pressed (HIP) by Bodycote H. I. P. Ltd, Chesterfield, UK, for 2 hours at 920 °C and under a pressure of 100 MPa. Samples were cooled to room temperature at a rate of 6 ± 2 °Cmin^{-1}. Room temperature tensile testing was performed at a UKAS accredited test laboratory at a strain rate of 0.05 mm/min, until 0.2% proof stress was achieved; at this point strain rate was increased to 3.50 mm/min until failure.

3.7. Jominy End Quench

The Jominy end quench test is a method by which, typically, the hardenability of ferrous alloys can be investigated. The test has been utilised by Ahmed and Rack [20] on wrought Ti-6Al-4V in order to associate microstructure with cooling rate. The experiment used a modified Jominy specimen, instrumented with thermocouples, and insulated to encourage axial rather than lateral heat flow during quenching. Using this work as an inspiration Davies [93] investigated the effects of cooling rate on the microstructure of titanium alloy Timetal 834. In this investigation, a Jominy end quench has been performed on Ti-6Al-4V produced via EBM to gain a better understanding of the material hardenability. The as-built and machined sample geometries are shown in Figure 3.22. During machining, four 1.1 mm diameter holes of 11 mm in depth were drilled at distances of 3 mm, 15 mm, 35 mm and 65 mm from the quenched end. These holes were to allow four n-type thermocouples (accurate to ± 1 °C) to be inserted and record sample temperature. Thermocouples were attached to a PicoTech TC-08 data logger with a logging frequency set to 1Hz.

After inserting and securing the thermocouples, Kaowool was used as insulation and held in place with nichrome wire. In an attempt to ensure that the sample remained above the beta transus during transfer from furnace to quench stand, the temperature across the sample was held at 1030 °C. The sample was held at temperature for 30 minutes before transferring to the stand and quenching. A modified quench stand plate was used to hold the Jominy specimen. Usually a plate with a circular hole is used; in this case a slotted plate was used because of the presence of the thermocouples. Figure 3.23 shows a schematic of the experimental setup for the quench test.

The internal diameter of the water supply pipe was 13 mm and the height of the water jet, without the test piece in position, was set to 65 mm; quenching was stopped when all thermocouple readings were below 25 °C. The temperature of the water used for quenching was measured as 10 °C ± 1 °C.

3.8. Boron Additions to Ti-6Al-4V

Boron was added to Ti-6Al-4V to produce Ti-6Al-4V-*x*B alloys with boron concentrations over the nominal range of 0 to 1.05 wt% B. Direct addition of elemental boron to powdered Ti-6Al-4V was tried as was the production of substrate material by arc melting. The experimental methods used and the reasoning are fully discussed in Chapter 6.

3.9. Summary

This chapter has presented the experimental techniques used to produce and characterise electron beam melted Ti-6Al-4V samples. The following chapters discuss the results obtained from the use of these techniques and their implications, beginning with characterisation of the electron beam and numerical modelling.

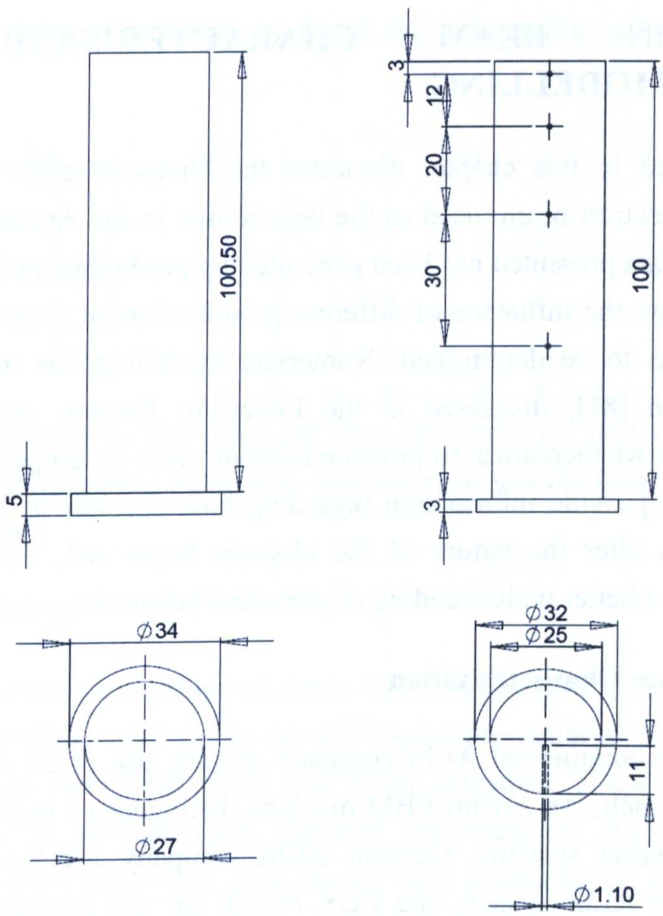

Figure 3.22 : As-built (left) and machined (right) dimensions for Jominy end quench specimen

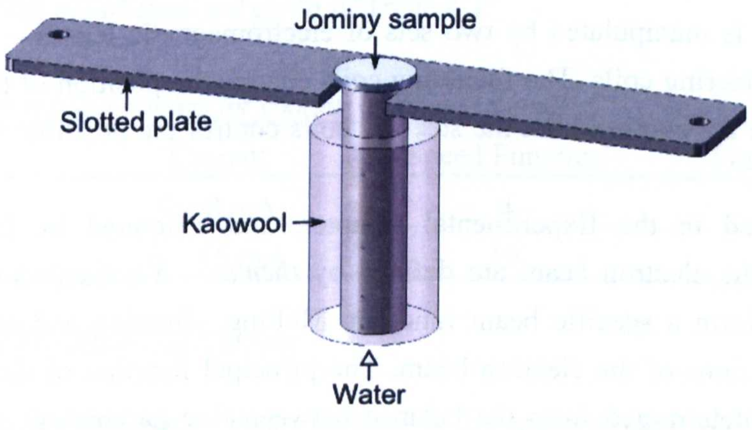

Figure 3.23 : Experimental set up of instrumented Jominy end quench.

4. ELECTRON BEAM CHARACTERISATION AND NUMERICAL MODELLING

The work presented in this chapter discusses the characterisation and numerical modelling of the electron beam, used as the heat source in the Arcam EBM process. The experimental data presented has been generated by producing melt tracks on solid substrates and allows the influence of different groups of input parameters, on beam form and character, to be determined. Numerical modelling has made use of the Rosenthal Equation [81], discussed in the Literature Review, and mathematical modelling software, Mathematica, to produce contour maps of temperature isotherms. The intention is to provide information regarding how changes in individual, user-defined parameters alter the nature of the electron beam and, through numerical modelling, to yield a better understanding of prevalent behaviour

4.1. Electron Beam Characterisation

Currently, the only commercial ALM company making use of an electron beam is Arcam AB and as such, the Arcam EBM machine distinguishes itself from the more widespread laser-based systems. German ALM company Electro Optic Systems (EOS), produce an ALM system, the EOS M270, for the production of metallic components that uses a 200 W Yb-fibre laser [96]. In comparison to such a laser, the Arcam electron beam is more powerful, with a maximum power of 3500 W, and therefore more versatile in terms of melting capacity. During EBM processing, the electron beam is manipulated by two sets of electromagnetic lenses – the focussing coils and the steering coils. The focussing coils change the position of the focal point of the beam in the z-axis whilst the steering coils control the position of the beam in the xy plane.

As discussed in the Experimental Chapter, and reiterated in Table 4.1, the properties of the electron beam are defined by *themes* – a collection of parameters needed to perform a specific beam function. Melting, sintering and heating are the three key functions of the electron beam. The principal function of the beam at any given time is determined from the balance between five parameters, namely, *beam current*, *beam speed*, *beam focus offset*, *line offset* and *line order*.

The meaning of the two parameters *line offset* and *line order* are illustrated in Figure 4.1. *Line offset* determines the distance between beam scan lines during the bulk melting (*hatching*) process. *Line order* defines the order in which the beam travels along scan lines; Figure 4.1 (b) and (c). Heat input may be increased by decreasing the *line offset*; a decrease in heat input can be achieved by increasing the *line order*. The default *line order* is 1 and the default *line offset* is 0.24 mm for *hatching*.

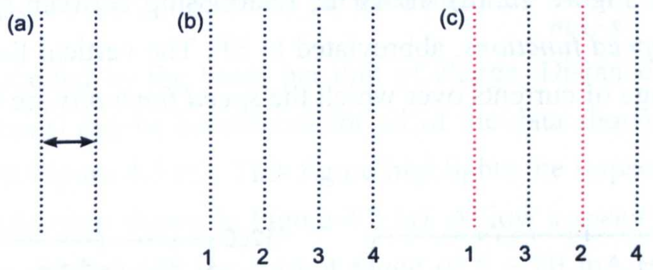

Figure 4.1 : Schematic of (a) line offset and (b) a line order of 1 and (c) a line order of 2. Dotted lines represent electron beam path, numbers represent the order in which the beam travels along the path.

4.1.1. *Methodology*

The effects of changes to *beam speed, focus offset* and *current* have been investigated by producing individual melt tracks on solid substrate material. Substrate materials used were stainless steel base plates and EBM deposited Ti-6Al-4V. Experiments were carried out at ambient and elevated temperatures. As described in the Experimental Chapter, individual melt tracks were produced by generating dummy support structures (one per melt track) and assigning each with a *wafer support theme*. The *wafer support theme* was modified to mimic the specific *theme* under investigation. The standard settings for component outlines (*contours*) and bulk melting (*hatching*) parameters are given in Table 4.1.

Table 4.1 : Electron beam settings for contour and hatch themes.

Theme	Current	Speed Function	Focus Offset
Contour	5 – 8 mA	4	22 mA
Hatch	6 – 15 mA	19	17 mA

4.1.2. *Speed Function and Current*

A critical parameter in electron beam melting is the speed of the beam traverse (v). Users cannot make changes to beam speed directly; instead, a change in *beam current*, or a parameter called *speed function*, brings about a change in v. The *speed function* is a relationship between *beam speed* and *current* that is built into the EBM control software. The aim of the *speed function* is to ensure that a constant melt depth is maintained regardless of the *current* used i.e. an increase in *current* is accompanied by an increase in *speed* to negate the effect of the increased beam power. As shown in Table 4.1, the *contour* and *hatch* themes are defined by a current range rather than a specific value; the actual value used is determined by the *Auto Power Calc* (see Section 3.1.9). The *beam speed* therefore varies within the stated range, according to the *speed function*. Figure 4.2 (a) shows the relationship between *speed* and *current* for five different *speed functions*, abbreviated to SF. The vertical lines from SF4 and SF19 mark the range of currents over which the *speed functions* are typically used, as per Table 4.1.

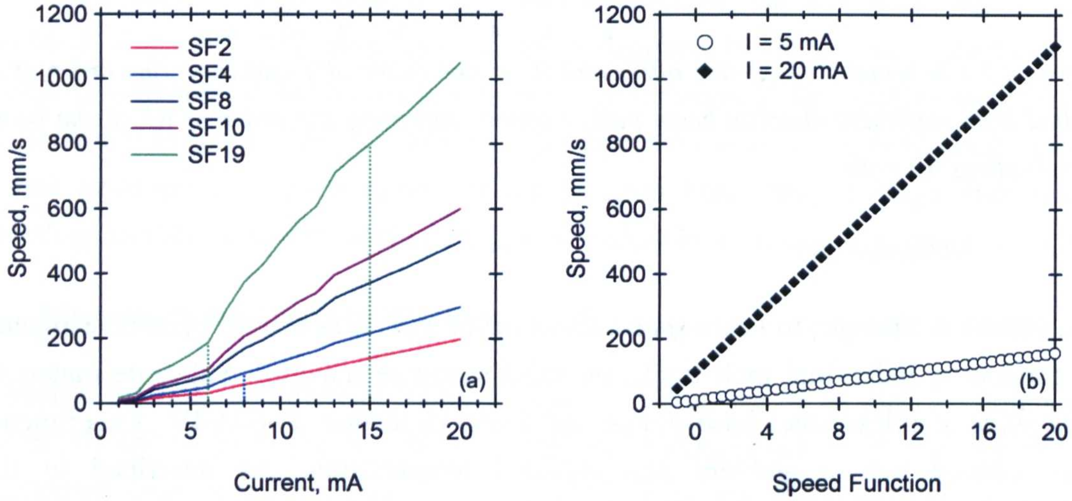

Figure 4.2 : (a) Relationship between speed and current for five different speed functions. Vertical lines indicate the typical range of currents used at speed functions of 4 and 19. (b) Beam speed versus speed function for beam currents of 5 mA and 20 mA. Data supplied courtesy of Arcam AB, Sweden.

The speed functions presented in Figure 4.2 (a) are non-linear and the non-linearity becomes more pronounced as *speed function* increases. The deviations from linearity are somewhat unexpected as one would anticipate that each increment in current would result in a standard increment in speed – it is not known how the equipment manufacturers have generated the *speed function*. A linear relationship does exist between *speed function* and speed for a given *beam current* (Figure 4.2 (b)). In short, *beam speed* increases linearly with *speed function* but non-linearly with *current*. However, over a specific current range it is possible to approximate *speed functions* using a linear fit. In Figure 4.3 (a), current versus speed for *contour* (SF = 4) and *hatch* (SF = 19) *speed functions* are presented over the current range 5 – 20 mA. The approximate linear relationship between current (I) and speed (v) are given in Equations (4.1) and (4.2), both of which have correlation coefficients of 0.99.

$$v = 60.5\,I - 124.3 \quad (\mathrm{SF} = 19) \qquad (4.1)$$

$$v = 17.5\,I - 47.9 \quad (\text{SF} = 4) \qquad (4.2)$$

The gradient of the lines in Figure 4.3 (a) have the units $\frac{mm}{mA \cdot s}$, equivalent to $\frac{mm}{mC}$ i.e. a distance travelled by the beam per unit of charge. Distance travelled per unit charge (speed/current) can be considered for all of the data shown in Figure 4.3 (a) and is presented in Figure 4.3 (b). This figure highlights the impact of the non-linear speed-current relationship shown in Figure 4.2 (a). At low a *speed function* (SF4) the variation in speed/current over the current range of 5 – 20 mA is 6.8 mm.mC^{-1}; at SF19 this increases to 22.7 mm.mC^{-1}.

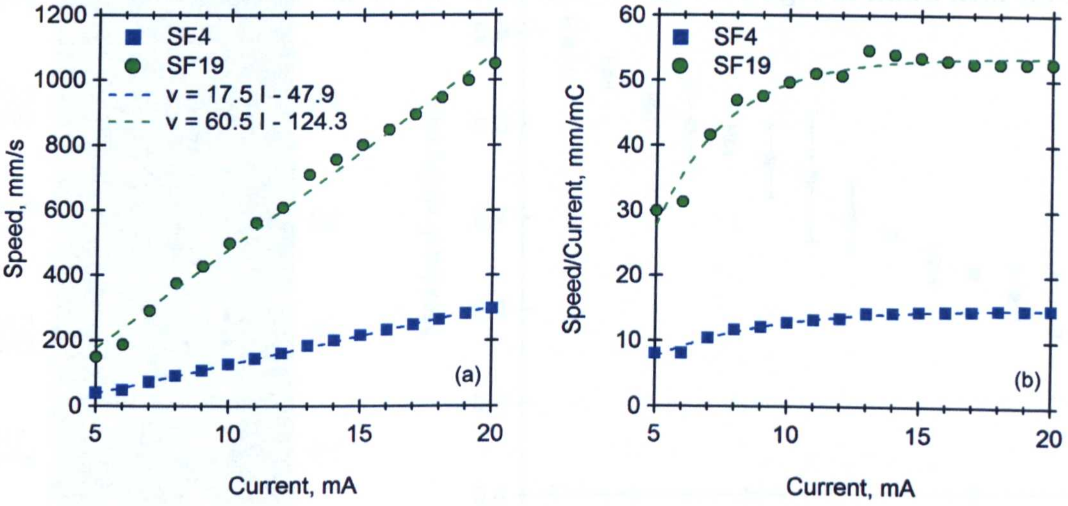

Figure 4.3 : (a) Relationship between speed and current for speed functions 4 and 19 and linear best fit lines. (b) Speed/current against current for SF4 and SF19.

Figure 4.3 (b) highlights that, for a given *speed function*, the manner in which speed compensates for a change in current is questionable, especially at currents < 8 mA. Based on Figure 4.2 and Figure 4.3, it is unlikely that the intended outcome of using *speed functions* (a constant melt depth) will be achieved and this will be discussed further in the following sections. Because of the ambiguity of the *speed function* term henceforth any mention of *speed function* will be accompanied either by the true beam speed or the value of speed/current, for clarity.

Optical micrographs of melt tracks produced on a stainless steel base plate, with a constant *beam current* (7 mA) and *speed function* ranging from 5 to 11 (88.0 – 175.0 mms^{-1}), are shown in Figure 4.4. The corresponding measurements of melt track width are shown below the micrographs. As one would expect, increasing the beam speed results in a decrease in the width of the melt track produced. Figure 4.4 indicates that the melt track width decreases linearly with speed function. This is unsurprising given the plot of *speed function* against *beam speed*, in Figure 4.2 (b).

A commonly used term in ALM and welding is the energy input per unit length, calculated by the power of the heat source divided by the speed, giving a result with units of Joules per unit length. In the case of the EBM system, beam power is calculated form the equation:

$$P = I \times V \qquad (4.3)$$

in which P is beam power in watts, I is beam current and V is beam accelerating voltage. The accelerating voltage during EBM is constant at 60 kV and thus power is increased only by an increase in *beam current*. The range of energies per unit length for the melt tracks in Figure 4.4 are thus between 4.77 $\mathrm{Jmm^{-1}}$ and 2.40 $\mathrm{Jmm^{-1}}$.

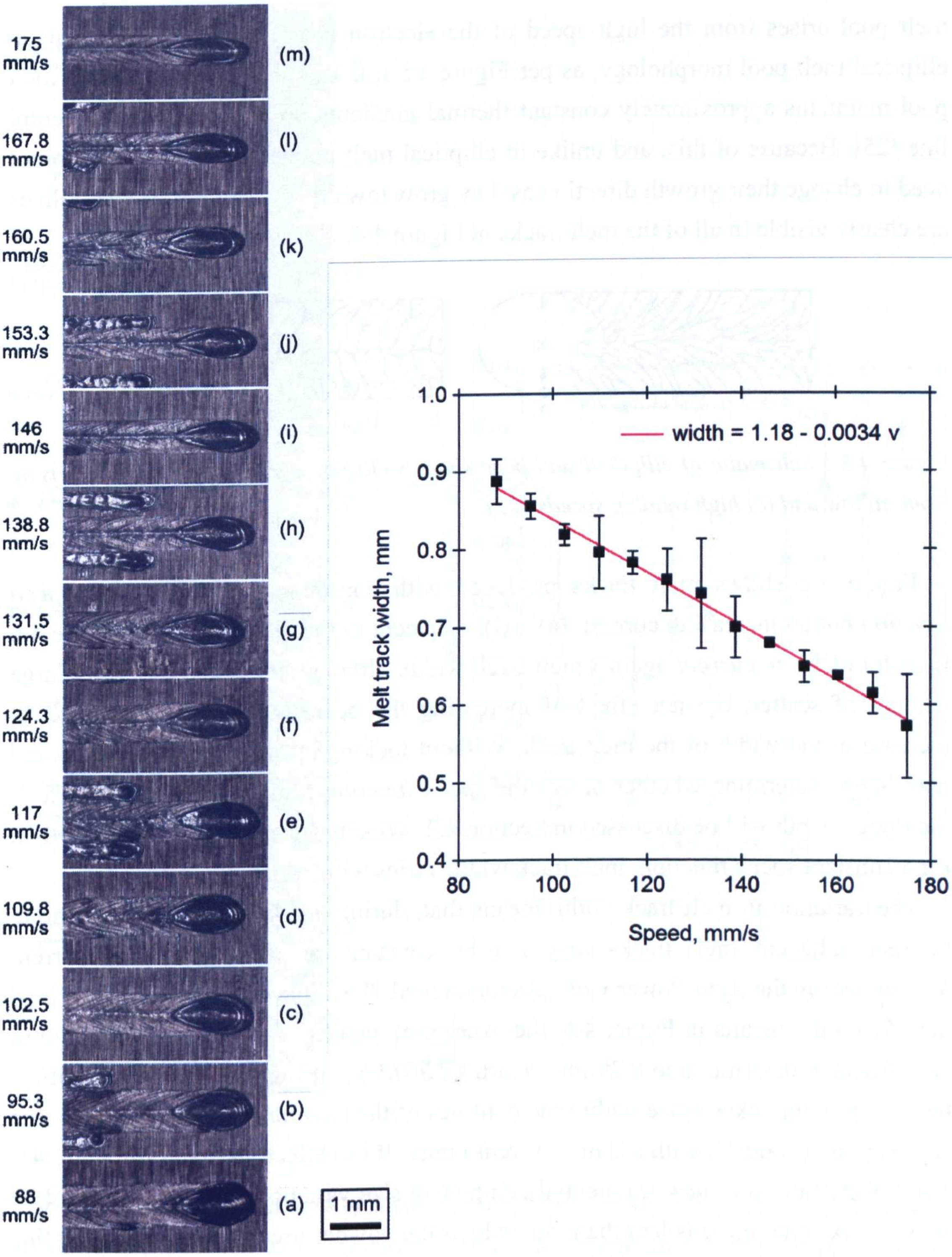

Figure 4.4 : Optical micrographs of melt tracks on stainless steel with increasing speed function (a) to (m). The adjacent chart plots melt track width versus beam speed, error bars represent 95% confidence limits. In all cases focus offset = 22 mA and beam current = 7 mA. Speed function ranges from (a) 5 to (m) 11 in steps of 0.5.

The morphology of the melt pools, in all cases, takes the form of the '*pear shape*' as described by Porter and Easterling [25] and shown in Figure 4.5 (b). This shape of melt pool arises from the high speed of the electron beam; lower speeds result in elliptical melt pool morphology, as per Figure 4.5 (a). The angular, pear-shaped melt pool maintains approximately constant thermal gradients up to the melt track centre line [25]. Because of this, and unlike in elliptical melt pools, growing crystal do not need to change their growth direction as they grow towards the centreline. Centrelines are clearly visible in all of the melt tracks in Figure 4.4.

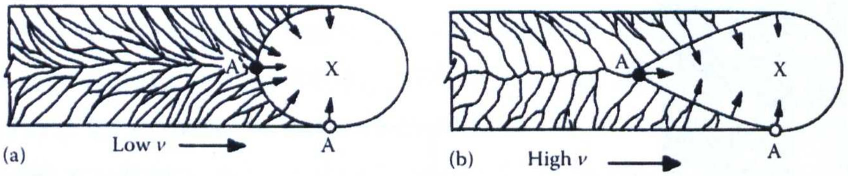

Figure 4.5 : Schematic of elliptical and pear shape weld pools and crystal growth arising from (a) low and (b) high welding speeds [25].

Figure 4.6 shows melt tracks produced with constant *focus offset* and *speed function* but an increasing current, (a) – (j). Adjacent to the micrographs in Figure 4.6 is a plot of *beam current* against melt track width; although there is a relatively large amount of scatter, the net effect of increasing the beam current is to produce an increase in the width of the melt track. Without looking at melt pool depth, it is not possible to determine whether or not the *speed function* achieves the desired effect; melt track depth will be discussed in Section 4.2. What is clear from Figure 4.6 is that, for a constant *speed function*, melt track width varies with current.

The variation in melt track width means that, during *hatching*, the size of overlap between adjacent melt tracks may not be constant; as a result of the current determined by the *Auto Power Calc*. As mentioned, the value of the *line offset* is 0.24 mm. From the results in Figure 4.6, the overlap of adjacent melt tracks can therefore vary between 0.38 mm and 0.29 mm. During *hatching*, such a variation is not critical because melting takes place within the confines of the *contours*. Table 4.1 shows that *contours* are produced with a 3 mA current range; if the effect observed in Figure 4.6 also affected the *contours*; a potential component size variation of ± 13 μm would be possible. As this figure is less than the scale of the powder used, it is unlikely that this variation in melt track width would be detrimental to component accuracy.

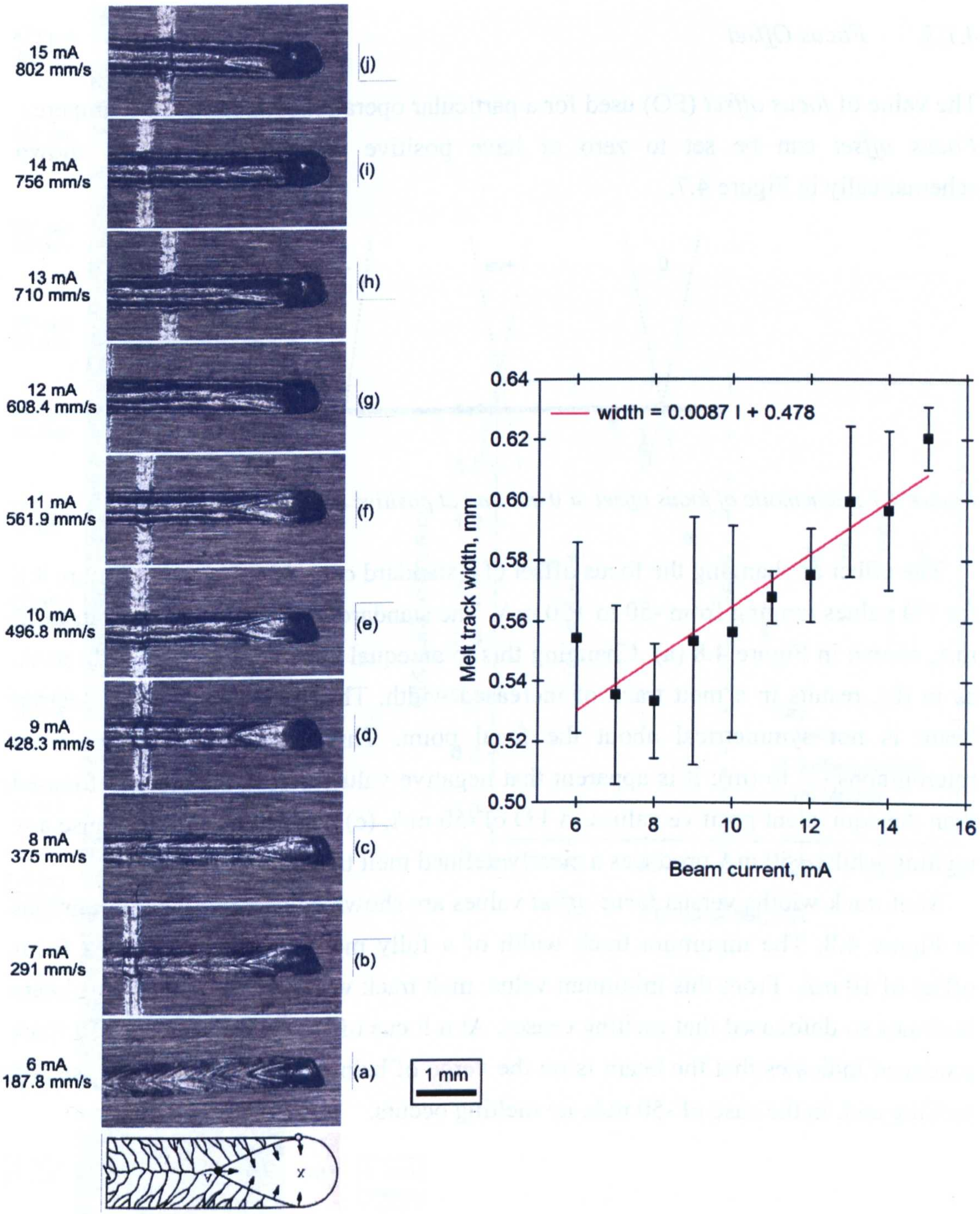

Figure 4.6 : Optical micrographs of hatch melt tracks on stainless steel with increasing beam current (a) to (j); in all cases focus offset = 22 mA and speed function = 19. Beam currents range from 6 – 15 mA. The adjacent chart plots melt track width versus beam current; error bars represent 95% confidence limits.

4.1.3. Focus Offset

The value of *focus offset* (FO) used for a particular operation is given in milliamperes. *Focus offset* can be set to zero or have positive and negative values shown schematically in Figure 4.7.

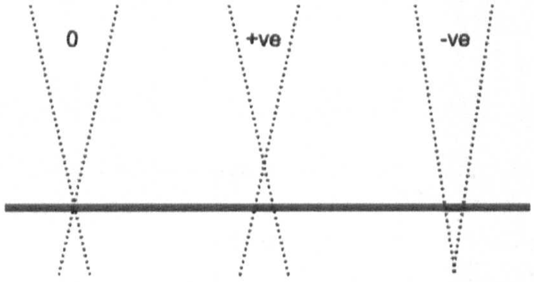

Figure 4.7 : Schematic of focus offset at 0 mA and at positive and negative values.

The effect of changing the focus offset of a standard *contour* is shown in Figure 4.8 for FO values ranging from -50 to +50 mA. The standard FO value for a contour is 22 mA, shown in Figure 4.8 (a). Changing this to an equal but opposite value (-22 mA), as in (b), results in a melt track of increased width. This indicates that the electron beam is not symmetrical about the focal point. This asymmetry is clear from micrographs (c) to (m); it is apparent that negative values of FO are more defocused than the equivalent positive values. A FO of -50 mA, (c), is not sufficient to cause any melting whilst +50 mA produces a clearly defined melt track, (m).

Melt track widths versus *focus offset* values are shown adjacent to the micrographs in Figure 4.8. The minimum track width of a fully melted track occurs at a focus offset of 10 mA. From this minimum value, melt track width increases until the beam becomes so defocused that melting ceases. At a focus offset of -40 mA the melt track produced indicates that the beam is on the verge of being too defocused to cause any melting and, in the case of -50 mA, no melting occurs.

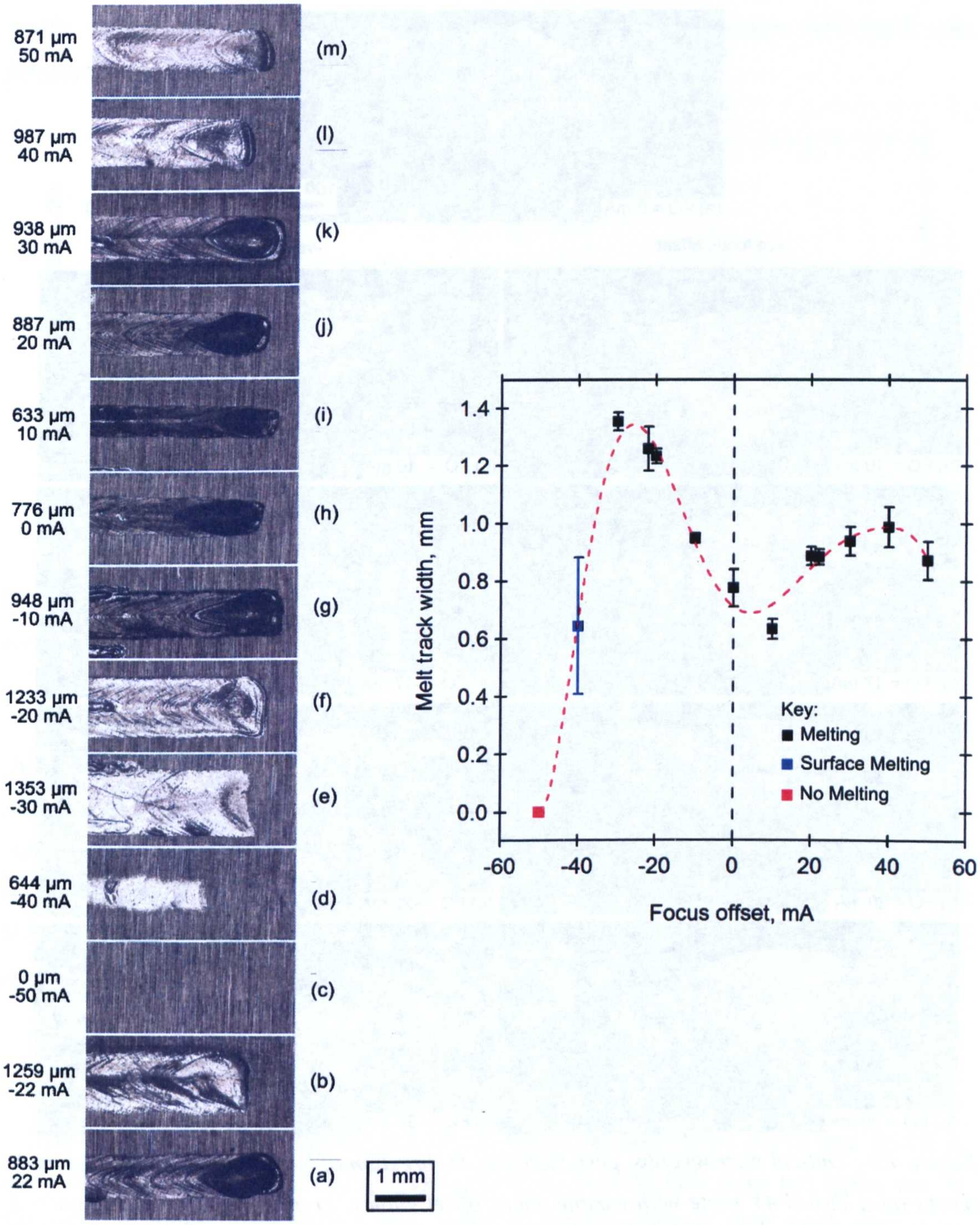

Figure 4.8 : Optical micrographs of contour melt tracks on stainless steel with various focus offset values; in all cases speed function = 4 (73.5 mms^{-1}) and beam current = 7 mA. Focus offset values and melt track widths are given next to the micrographs. The adjacent chart plots melt track width versus focus offset; error bars represent 95% confidence limits. The red dashed line is a guide for the eye only.

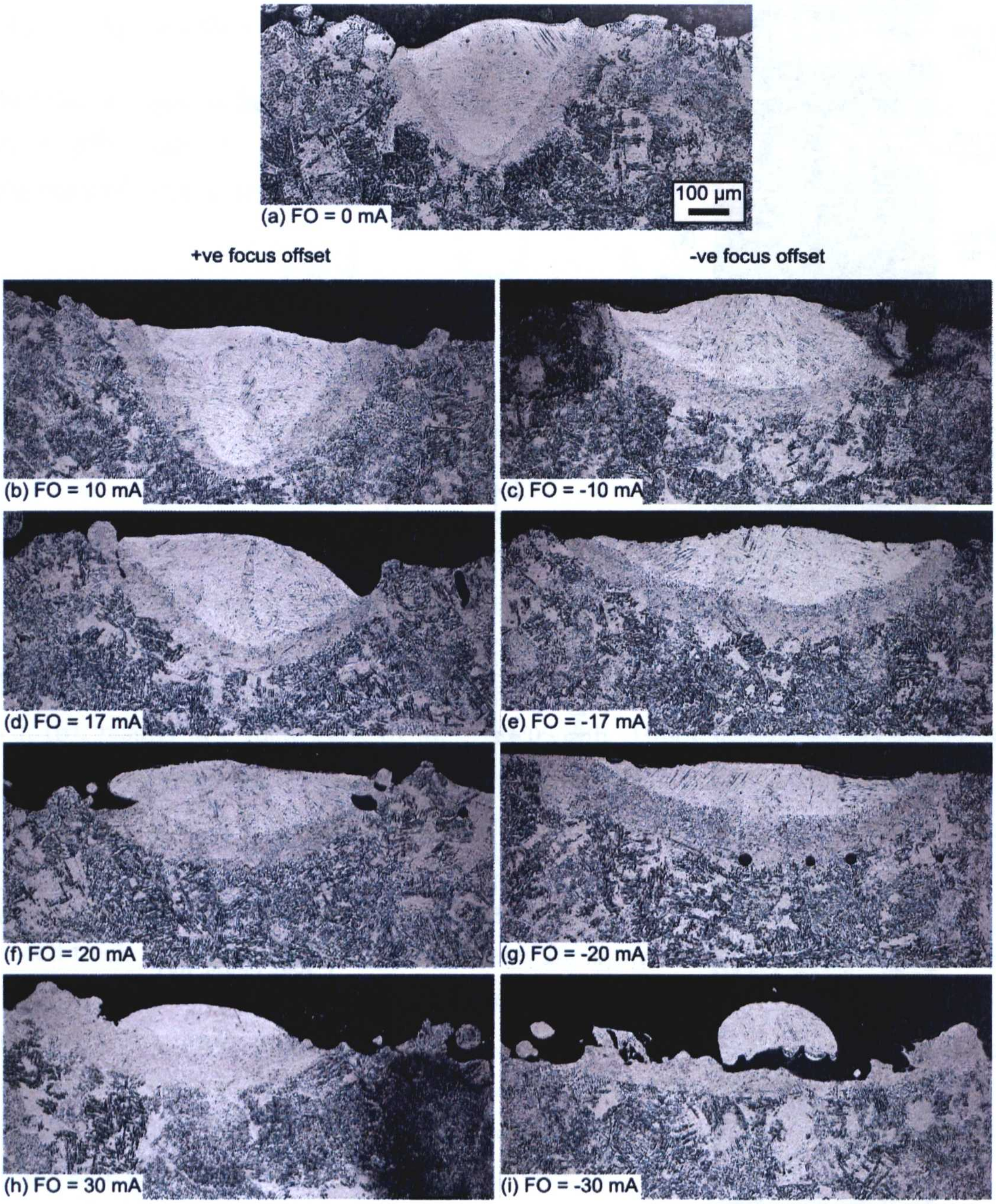

Figure 4.9 : Optical micrographs, perpendicular to direction of beam motion, of contour melt tracks on a Ti-6Al-4V plate with various focus offset values; in all cases speed function = 4 (49 mms^{-1}) and beam current = 6 mA.

Focus offset controls melt volume – a more defocused beam (wider track) produces a shallower melt pool. Melt pool depth is critical during EBM to ensure proper consolidation between layers. If the *focus offset* is too large, it is possible to melt a powder layer without also melting the underlying material. Micrographs of melt track width and depth (perpendicular to beam motion) are shown in Figure 4.9 produced at ambient temperature on a Ti-6Al-4V EBM plate. Changes in both width and depth have been measured and are presented in Figure 4.10. In this case, the minimum track width was found at a focus offset of 0 mA although the deepest melt track was produced at a focus offset of 10 mA.

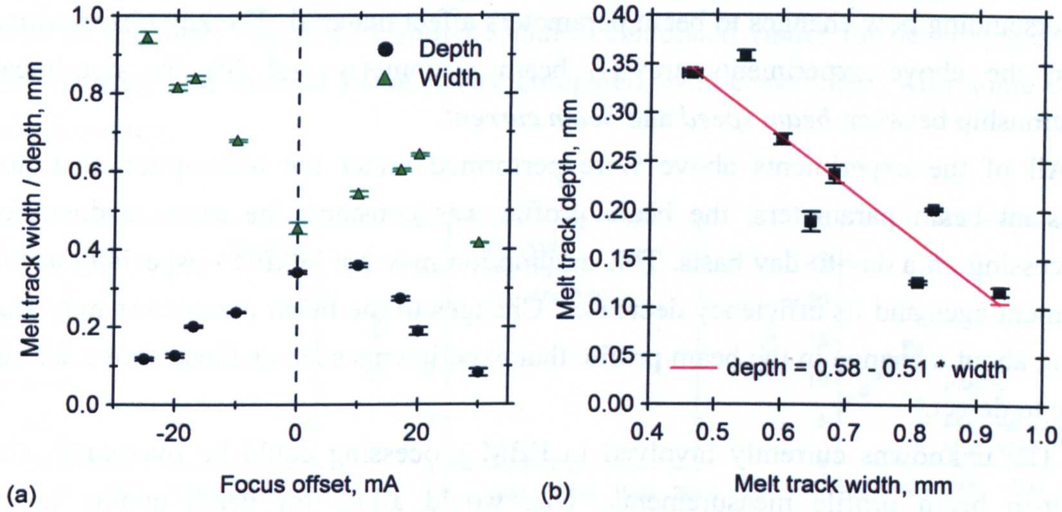

Figure 4.10 : (a) Melt track widths and depths versus focus offset and (b) melt track width versus depth (excluding ±30 mA focus offsets) for melt tracks in Figure 4.9.

Generally, melt track width and depth are inversely proportional to each other, as shown in Figure 4.10 (b). This proportionality breaks down at large positive and negative values of focus offset where melting, if any, is shallow because of the low power density. In Figure 4.10 (b) focus offsets of ± 30 mA have been excluded because of this. For focus offsets between + 20 mA and -25 mA, a *beam current* of 6 mA and *speed function* of 4 (49 mms^{-1}), melt track width and depth (in millimetres) are related in the following way:

$$depth = 0.58 - 0.51 \times width \qquad (4.4)$$

The asymmetry about the focal point in terms of both track depth and width is again obvious in Figure 4.10 (a). Although the current system does not make use of the negative *focus offset* values, the ability to melt a shallow melt track may have useful future applications such as 'healing' of defects. If a live defect detection system was in place, and a defect was identified within a layer, the 'healing' process could make use of a negative *focus offset* beam. The advantage would be that only the defect containing layer could be re-melted (avoiding the introduction of deeper defects during the repair process) and, due to the width of the beam, a large *line offset* could be used, minimising the time taken to perform repairs.

4.1.4. *Summary*

Characterisation of the electron beam on solid substrates is a relatively quick means of understanding how changes to beam parameters affect material. The key observations from the above experiments are: (i) beam asymmetry and (ii) the non-linear relationship between *beam speed* and *beam current*.

All of the experiments above were performed under the assumption that, for constant beam parameters, the beam profile was constant; the same is done for processing on a day-to-day basis. This assumption may not be true - especially as the filament ages and its efficiency decreases. Changes to the beam parameters may also bring about a change in the beam profile that experiments such as those above are not able to detect.

The unknowns currently involved in EBM processing could be overcome with built-in beam profile measurements. This would allow for beam quality to be measured as a function of filament age and, if necessary, processing parameters could be changed to compensate for an ageing filament.

Control of the electron beam is fundamental to the EBM process and the results of the experiments presented and discussed above demonstrate the influence of three parameters: *focus offset*, *beam speed* and *beam current*. In the following section, the influence of standard beam settings (as per Table 4.1) on the solidification conditions of Ti-6Al-4V are presented and discussed.

4.2. Numerical Modelling of Solidification Conditions

4.2.1. *Material Properties*

Rosenthal's solution for heat flow in the quasi-stationary state [81] is based upon three assumptions:

(i) The physical properties of the material are constant and do not vary as a function of temperature.
(ii) Speed and rate of heat input are constant.
(iii) Convection and radiation are absent.

Clearly, the simplifying assumptions made above are a source of error. The four material properties required to solve the Rosenthal equation are the density, ρ, thermal conductivity, k, specific heat capacity, C_p, and thermal diffusivity, α, where $\alpha = k / C_p$. Like all material properties, and unlike the assumption made in (i) above, there is a significant variation in these properties with temperature. Although it is only possible to use one value for each of the four thermal properties in solving the Rosenthal equation, greater accuracy is achieved if the values used are at elevated temperature.

Use of thermodynamic software JMatPro 4.0 (developed by Sente Software, UK) allows the determination of key physical properties as a function of temperature. The determination of these properties requires the input of the material chemistry into the JMatPro software. Figure 4.11 shows JMatPro calculated values for density, specific heat capacity and thermal conductivity compared, where available, with some data from literature.

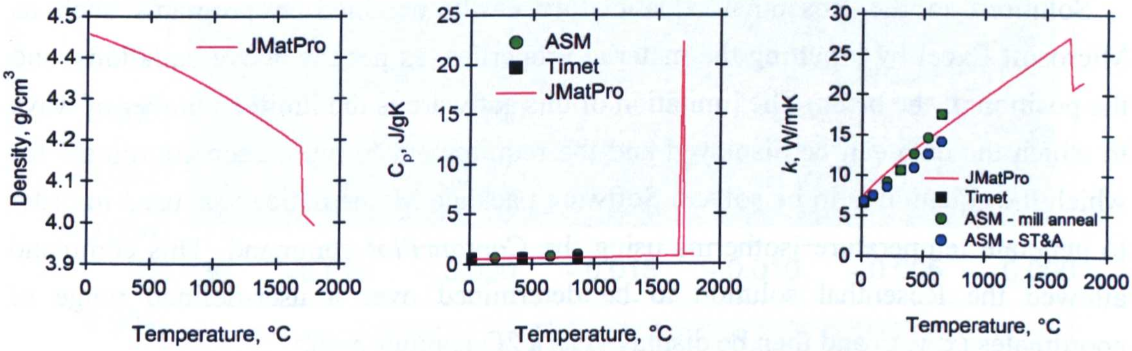

(a) *(b)* *(c)*

Figure 4.11 : Ti-6Al-4V properties as a function of temperature: (a) density, (b) specific heat capacity and (c) thermal conductivity from JMatPro, Timet [97] and ASM [98] data.

By excluding data above the solidus temperature (1938 K), the data for all three properties can be fitted with a polynomial function. This was done simply by using the *Add Trendline* option in Microsoft Excel and choosing a second order polynomial fit. In all three cases the R^2 value was > 0.999; the polynomial fits match the predicted data very closely.

Equations (4.5) to (4.7) give the temperature dependence of the properties given in Figure 4.11 in which T_0 is temperature in Kelvin. Using these equations, the thermal properties of Ti-6Al-4V can be determined at the temperature of interest e.g. the *build temperature,* which is typically between 923 and 973K (650 – 700 °C).

$$k = 4.053 + 0.0136T - 9.84 \times 10^{-7}T_0^2 \ (\mathrm{Wm^{-1}K^{-1}}) \qquad (4.5)$$

$$\rho = 4.485 - 8.027 \times 10^{-5}T - 3.80 \times 10^{-8}T_0^2 \ (\mathrm{gcm^{-3}}) \qquad (4.6)$$

$$C_\rho = 0.564 + 7.25 \times 10^{-6}T - 5.844 \times 10^{-8}T_0^2 \ (\mathrm{Jg^{-1}K^{-1}}) \qquad (4.7)$$

4.2.2. *Temperature Isotherms*

As well as the assumptions described above, a further limitation of the Rosenthal solution occurs at the origin of the heat source; $x, y, z = (0, 0, 0)$, where an infinite temperature is predicted. In this work, the temperature isotherms of interest are the solidus, liquidus and the beta transus isotherms. These isotherms are not in the vicinity of the heat source thus the infinite temperature prediction is not an issue.

Solutions to the Rosenthal equation are easily obtained in programs such as Microsoft Excel by inputting the material properties, as per the above equations, and the position of the beam. The limitation of this software is the limited number of ways in which the data can be displayed and the requirement to input each coordinate for which the equation is to be solved. Software package Mathematica was used in order to generate temperature isotherms using the *ContourPlot* command. This command allowed the Rosenthal solution to be determined over a user-defined range of coordinates (x, y, z) and then be displayed as a 2D contour map.

The temperature isotherms generated in Mathematica, for electron beam processing, are shown in Figure 4.12. The contour maps correspond to three z-positions in a Ti-6Al-4V substrate: 0, 400 and 800 μm below the surface. The physical properties of the material were calculated from Equations (4.5) to (4.7) using a T_0 value of 923 K (650 °C); beam properties used were a current of 6 mA and a velocity of 0.188 ms^{-1}, corresponding to a *speed function* of 19, i.e. standard *hatch* settings. The solidus isotherm (1938 K) and beta transus isotherm (1273 K) are labelled in the figure.

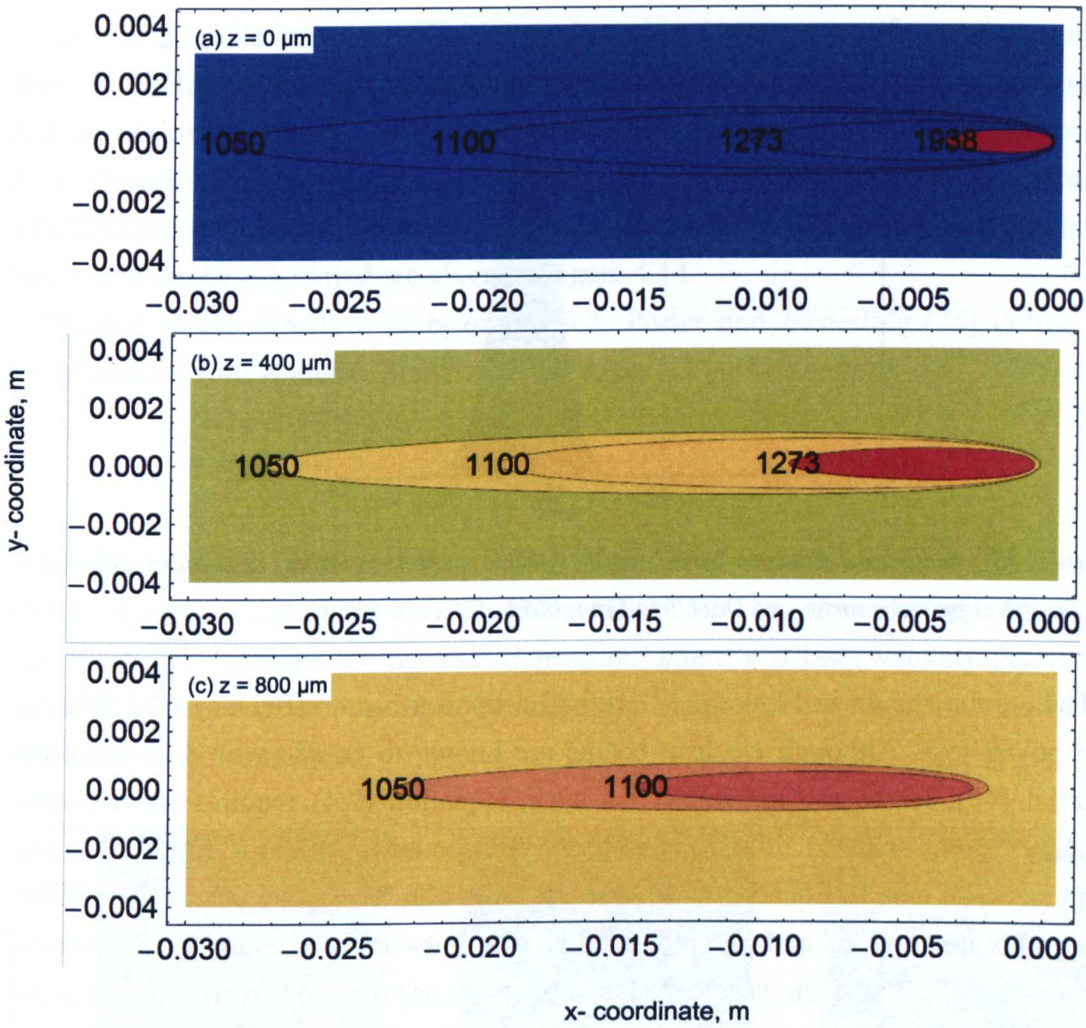

Figure 4.12 : Contour plots of predicted temperature isotherms (in K) looking down on a melt track, electron beam moving from left to right. Beam current = 6 mA, v = 0.188 ms^{-1}. (a) at the surface, (b) 400 μm below the surface and (c) 800 μm below the surface. Contour labels are in Kelvin, η = 1.

The Rosenthal solution is based upon a moving point heat source whereas the real electron beam: (i) has a Gaussian profile (see Figure 4.13) and (ii) can change size as a result of the *focus offset* settings. The appearance of the electron beam was discussed with Arcam AB [99] to try and establish the true energy distribution. Measurement of the beam profile, made by Arcam and given in Figure 4.13, shows the Gaussian distribution of energy. Unfortunately, the measurements of energy were relative (*y*-axis of the figure), leaving the actual energy distribution unknown. Thus the measurement made by Arcam only reveals the Gaussian shape of the beam and not its true energy distribution.

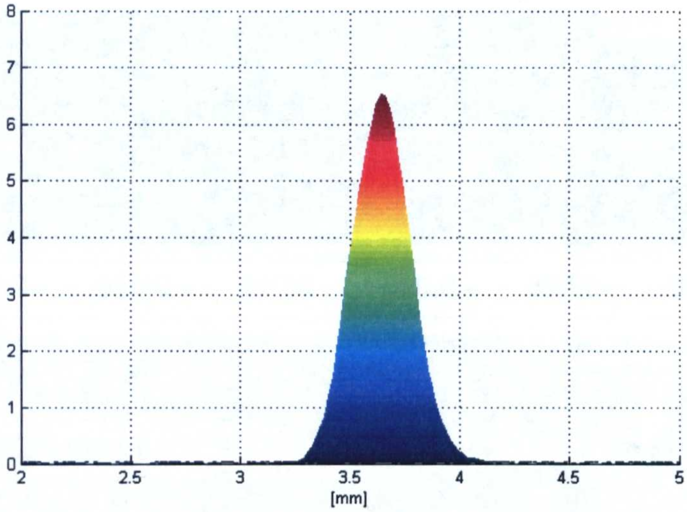

Figure 4.13 : Measured electron beam profile (y-axis scale is relative) at a focus offset of 0 mA. Graph supplied courtesy of Dr. Ulric Ljungblad of Arcam AB.

The results shown in Figure 4.12 are based upon a beam efficiency of 100% i.e. zero power loss. Although electron beams are known to couple well with substrate material [40], losses are inevitable. As such, Equation (2.4) requires modification through the addition of a fitting parameter, η, to account for both the energy loss and beam size, as given in Equation (4.8). Essentially, η can be used as a fitting parameter to corroborate experimental and modelled results and will be specific for a set value of *focus offset*. This is the case because, whilst the beam is approximated to a point source, in reality *focus offset* changes the energy input per unit area. As the beam becomes more defocused (less melting) the value of η must therefore decrease to accommodate for the spread of power.

$$\mathrm{T} - \mathrm{T}_0 = \frac{\eta \mathrm{q}}{2\pi \mathrm{kR}} \exp\left(\frac{-\mathrm{v}(\mathrm{x}+\mathrm{R})}{2\alpha} \right) \tag{4.8}$$

The contour plots shown in Figure 4.12 are viewed in the *xy* plane and provide information on melt pool width (*y*) and length (*x*) at a fixed depth (*z*). Conversely, melt track width (*y*) and depth (*z*) can be determined by viewing the results in the *yz* plane, at a fixed position of *x*. By stepping through a series of *x* positions, the shape of the melt pool can be determined as a function of *x* but also as a function of time because:

$$t = \frac{x}{v} \tag{4.9}$$

This is possible because solutions to Equation (4.8) are in the quasi-stationary state. Rosenthal comments that in this state '*an observer stationed at the point source fails to notice any change in the temperature around him as the source moves on*' [81]. Determining melt pool shape as a function of time allows one to calculate solidification parameters. Temperature isotherms in the *yz* plane and a schematic of how time may be calculated are given in Figure 4.14.

Parallel to the direction of beam motion, Porter and Easterling [25] define the solidification front velocity, *R*, during welding as:

$$R = v \cos \theta \tag{4.10}$$

in which θ = the angle between the direction of beam motion and the direction of crystal growth. Gäumann *et al.* [77] utilise the above equation to predict solidification conditions during laser deposition where *v* is laser velocity parallel to the direction of beam motion. Here, solidification parallel to the *z*-axis, on a stationary *yz* plane, will be considered.

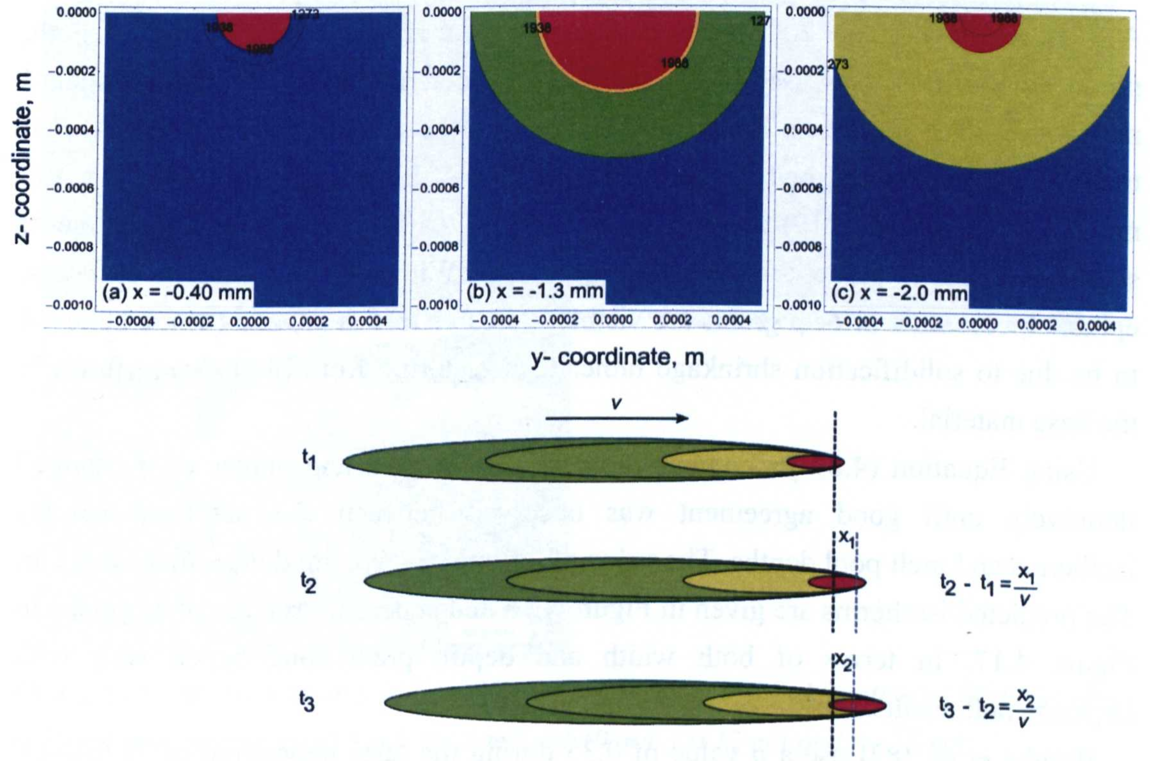

Figure 4.14 : Contour plots in the yz plane at (a) 0.40 mm, (b) 1.3 and (c) 2.0 mm behind the heat source for beam properties I = 6 mA, v = 0.188 ms^{-1} and η = 1. Below, a schematic of isotherms moving through a stationary yz plane (black dashed line) and calculation of time. Grey dashed line represents previous position of isotherms.

When considering a *yz* plane, solidification velocity can be calculated by determining the distance travelled in the z-direction by the solidus isotherm over a time increment such that:

$$R = \frac{dz}{dt} \tag{4.11}$$

Thermal gradient for solidification, *G*, can be calculated from the distance between the solidus and liquids isotherms:

$$G = \frac{dT}{dz} \tag{4.12}$$

Calculation of *R* and *G* allows EBM solidification conditions to be plotted onto the calibrated solidification map for Ti-6Al-4V (see Figure 2.23).

4.2.3. Determination of the Fitting Parameter, η

A solid Ti-6Al-4V plate 2.5 mm in thickness, 25 mm in width and 35 mm in length, produced by EBM, was used as the substrate for determination of η for a standard melt *theme*. The plate was heated to 923 K using the electron beam before 4 melt tracks were produced at beam currents of 6 – 15 mA, beam velocities 0.188 – 0.802 ms^{-1} (*speed function* = 19) and a *focus offset* of 17 mA. The resulting melt tracks, sectioned in the *yz* plane, are given in Figure 4.15. Within the individual melt pools, epitaxial, columnar prior β grains are visible. Pores visible in (b) and (d) are believed to be due to solidification shrinkage rather than resulting from pre-existing flaws in the base material.

Using Equation (4.8), *yz* contour plots were generated and values of η changed iteratively until good agreement was observed between the predicted solidus isotherms and melt pool depths. The value of η found to give good agreement was 0.6. The predicted isotherms are given in Figure 4.16 and superimposed on micrographs in Figure 4.17. In terms of both width and depth, predictions match well with experimental results.

Bontha *et al.* [82] use a η value of 0.35 during the laser deposition of Ti-6Al-4V however; electron beam processing is known to be more efficient than laser processing because of the reduced impact of reflectivity that more severely affects lasers. White and Bakish [57] report an efficiency value of 0.55 during the electron beam welding of Ti-6Al-4V and as such the value of 0.6 determined here, although incorporating both efficiency and *focus offset* effects, seems reasonable.

Predictions and experimental results in Figure 4.17 indicate that the melt pool generated by a 6 mA beam is larger than those produced at 8 – 15 mA beam currents. The 8 – 15 mA melt pools are similar in size and are good examples of the effective implementation of the *speed function*. The larger melt pool produced by a 6 mA beam should not be surprising given the results of Figure 4.3 (b) indeed; at 6 mA the value of speed/current is 31.3 mm.mC^{-1} whilst from 8 – 15 mA it ranges between the much similar values of 47 – 53 mm.mC^{-1}. Figure 4.18 shows a linear relationship between the value of speed/current and the predicted depth of the melt pool and demonstrates the effect of the speed/current relationship.

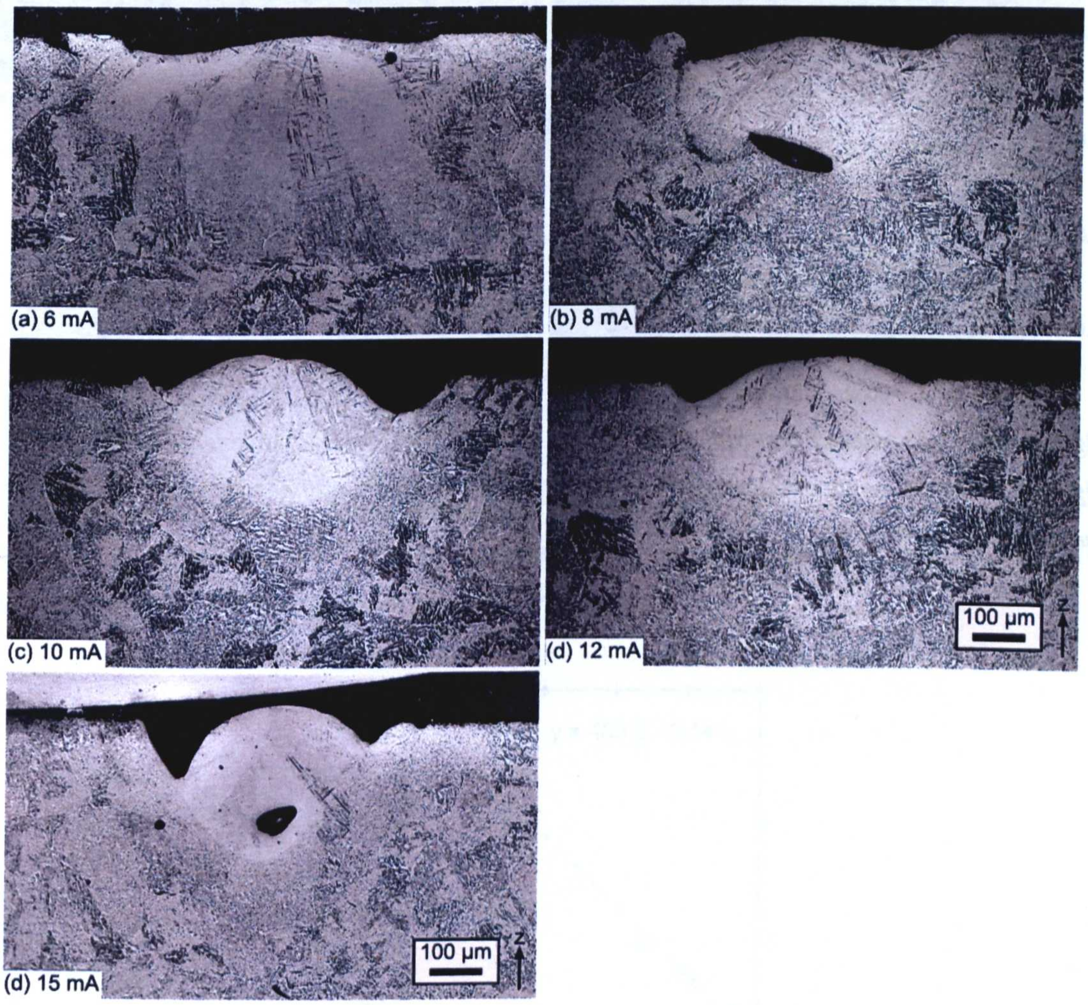

Figure 4.15 : Melt tracks on a Ti-6Al-4V plate produced at a speed function of 19, focus offset of 17 mA and current of (a) 6 mA, (b) 8 mA, (c) 10 mA, (d) 12 mA and (e) 15 mA.

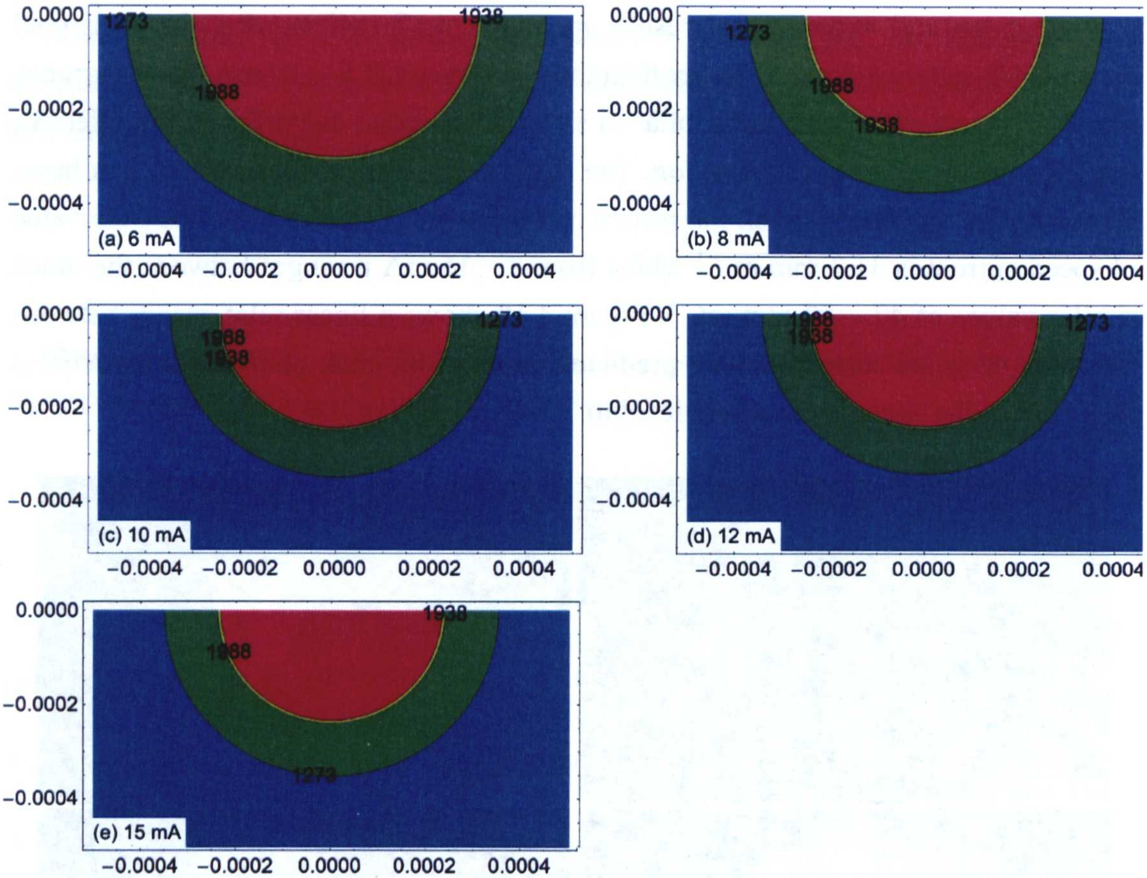

Figure 4.16 : Predicted contour plots in the yz plane using the parameters described in Figure 4.15 and a beam efficiency of $\eta = 0.6$*. Solidus, liquidus and beta transus isotherms are shown.*

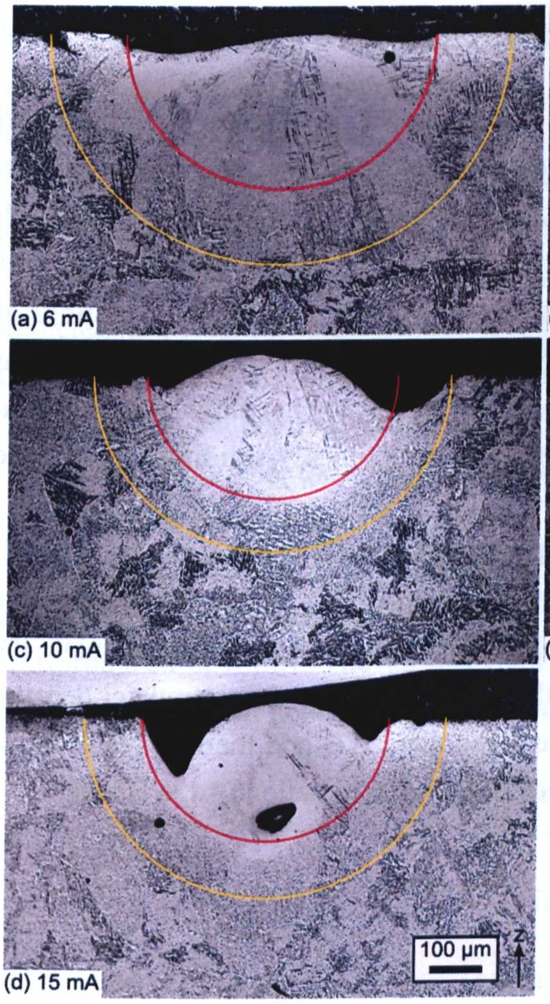

Figure 4.17 : Predicted solidus (red) and beta transus (orange) isotherms from Figure 4.16 superimposed onto the micrographs shown in Figure 4.15.

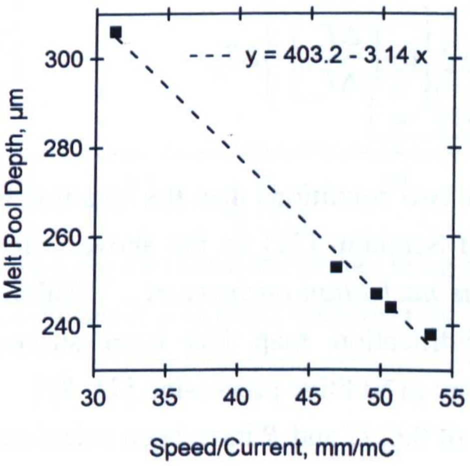

Figure 4.18 : Speed/current versus predicted melt pool depth for melt pools in Figure 4.17.

4.2.4. Columnar to Equiaxed Transition and Solidification Conditions

The successful prediction of melt pool size, shown in Figure 4.17, allowed solidification parameters, G and R, to be calculated. As mentioned previously, Kobryn and Semiatin [71] produced a solidification map for Ti-6Al-4V from which microstructural morphology can be determined, based on the values of G and R, as per Figure 4.19. In their work, Kobryn and Semiatin [71] produced cylindrical castings of different sizes resulting in different solidification conditions and therefore different microstructures. Modelling of the solidification of these castings allowed G and R to be determined; G and R were also measured from directionally solidified, float zone material.

Kobryn and Semiatin's solidification map was generated by plotting G vs. R for all of their experimental conditions before making use of the Hunt-criterion for the columnar to equiaxed transition [100]. Hunt [100] developed a model to calculate the columnar to equiaxed transition (CET) in the steady state based upon nuclei density, N_0; nucleation undercooling, ΔT_n; solutal undercooling, ΔT_c and thermal gradient, G. Fully equiaxed growth is predicted when the condition in Equation (4.13) is met:

$$G < 0.617 N_0^{\frac{1}{3}} \left\{ 1 - \left(\frac{\Delta T_n}{\Delta T_c} \right)^3 \right\} \Delta T_c \tag{4.13}$$

Fully columnar growth is predicted when the condition in Equation (4.14) is achieved:

$$G > 2.864 N_0^{\frac{1}{3}} \left\{ 1 - \left(\frac{\Delta T_n}{\Delta T_c} \right)^3 \right\} \Delta T_c \tag{4.14}$$

If G lies between these two conditions then the resulting microstructure is referred to as mixed. Kobryn and Semiatin [71] fit the above criteria to their experimental results by '*...adjusting the nucleation parameters...*'. Although derived from casting microstructures, the solidification map has been successfully used to predict microstructural morphology in additive processing [71, 82].

Based on a value of η of 0.6, G and R have been calculated here for beam currents of 6 mA ($v = 0.188$ ms^{-1}) and 12 mA ($v = 0.608$ ms^{-1}) and are given in Figure 4.19. G and R values are not displayed for the other beam currents in Figure 4.17 because of their similarity with the 12 mA beam. At both beam currents, solidification begins in the fully columnar region, largely as a consequence of the high thermal gradient. The slight difference between the two currents is a result of the larger melt pool formed by the 6 mA beam. The increased melt pool size acts to decrease thermal gradient, *G* (and as such *R* also decreases) – the net effect is a shift downward and to the left compared to the 12 mA beam.

In both cases, as solidification progresses and melt pool size diminishes, the thermal gradient decreases whilst solidification velocity increases (see Figure 4.20). A transition from fully columnar to a mixed (columnar and equiaxed) regime is predicted as a result. Experimentally (Figure 4.17), this transition is not observed and it is believed that, as solidification time is so brief, once columnar grain growth is established, it occurs preferentially over the nucleation of new equiaxed grains. Experiments show that the conditions favour growth dominated solidification kinetics over those where nucleation is dominant.

As well as showing the progression of *G* and *R* with time, Figure 4.20 also highlights the difference in predicted solidification time as a result of the larger melt pool produced at 6 mA. The 12 mA melt pool is predicted to take 4 ms to solidify whilst the 6 mA melt pool is predicted to take almost twice as long at 7.4 ms.

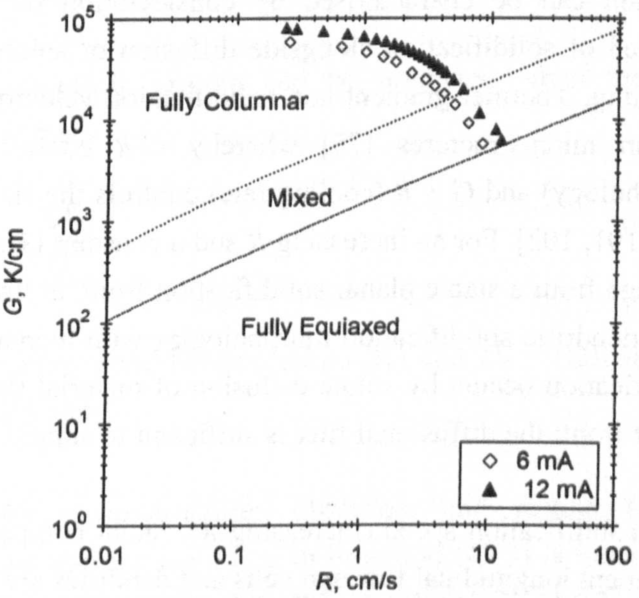

Figure 4.19 : Solidification map for EBM material melted using 6 and 12 mA beam currents showing the evolution of solidification conditions. Microstructural regions taken from [71]. $T_0 = 923K$, $\eta = 0.6$.

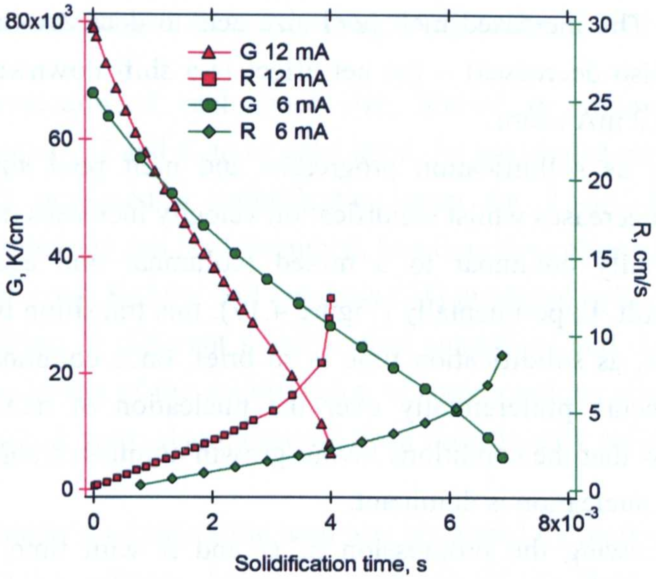

Figure 4.20 : Change in predicted values of G and R during solidification as a function of time for 6 mA and 12 mA melt pools.

Alloy solidification can be characterised by consideration of the temperature distribution and speed of solidification alongside diffusion of solute, alloy freezing range and undercooling. Thermal gradient and solidification velocity can be used to predict solidification microstructures [75] whereby G/R controls the mode of solidification (morphology) and $G \times R$ (cooling rate) controls the size and spacing of dendrites and cells [101, 102]. For an increasing R and a constant G, solidification can be observed to change from a stable planar solidification front, at low values of R, to cellular and finally dendritic solidification morphologies with increasing values of R [103]. Planar solidification occurs by solute diffusion of material through the liquid, normal to the planar front; the diffusional flux is sufficient to supply the latent heat of fusion.

With increasing solidification speed (increasing R), radial components of flux are necessary to supplement longitudinal flux and cells and dendrites are formed [103]. At the highest values of R, a planar front is again stable [102]. A summary of the morphologies produced, based on the relative values of G and R is given in Figure 4.21.

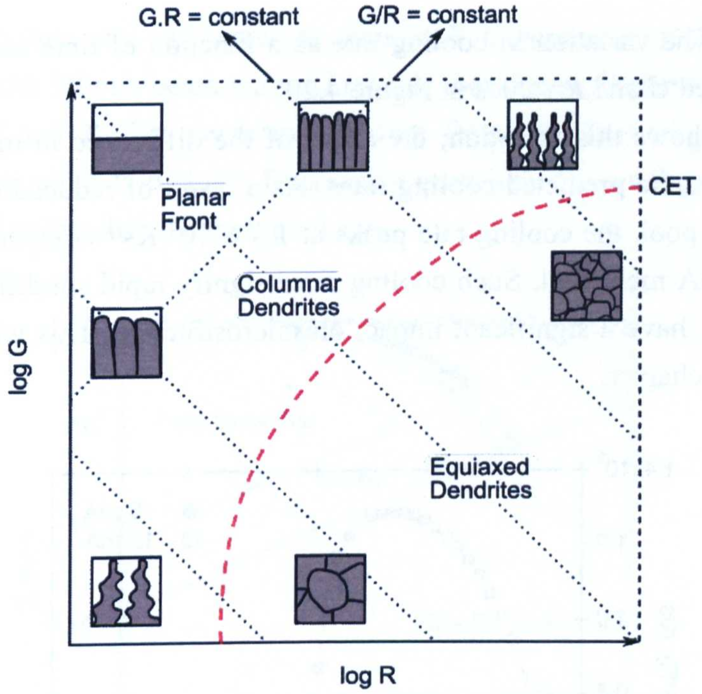

Figure 4.21 : Schematic summary of microstructural morphology depending on G and R, adapted from [102]. Red dashed line represents the columnar to equiaxed transition.

Cellular and dendritic growth can be predicted when the criterion given in Equation (4.15) is met:

$$\frac{G}{R} < \frac{\Delta T_E}{D_L} \qquad (4.15)$$

where ΔT_E = alloy solidification range (K) and D_L = diffusivity of solute in the liquid metal (m^2s^{-1}) [75].

The Ti-6Al-4V microstructures observed, and results from the numerical modelling, indicate that the condition in Equation (4.15) is indeed met in the case of electron beam processing under standard conditions. In Ti-6Al-4V ΔT_E = 50 K and, for most liquid alloys, the diffusion coefficient is approximately $10^{-8} - 10^{-9}$ m^2s^{-1} [75]. The criterion for cellular and dendritic growth for Ti-6Al-4V can thus be approximated as $G/R < \sim 5 \times 10^9$ Ksm^{-2}. From Figure 4.19, maximum G/R values of 3.2×10^9 Ksm^{-2} for a 12 mA beam and 2.2×10^9 Ksm^{-2} for a 6 mA beam are predicted – the criterion for plane front instability is thus fulfilled. The same result was observed by Rai *et al.* [75] during keyhole mode laser welding of Ti-6Al-4V. When heat flow is unidirectional the product $G \times R$ is equivalent to cooling rate [102]. Assuming heat flow occurs only along the *z*-axis during EBM, cooling rates at the beginning of solidification can be approximated as $\sim 10^4$ Ks^{-1} for both 6 and 12 mA beam currents. The variation in cooling rate as a function of time can be calculated from the predicted *G* and *R* values in Figure 4.20.

Figure 4.22 shows this variation; the effect of the difference in melt pool size is again reflected in the predicted cooling rates. As a result of reduced melt volume in the 12 mA melt pool, the cooling rate peaks at 1.3×10^5 Ks^{-1} compared to 7.6×10^4 Ks^{-1} for the 6 mA melt pool. Such cooling rates signify rapid solidification and will thus, potentially, have a significant impact on microstructure. This will be discussed in the following chapter.

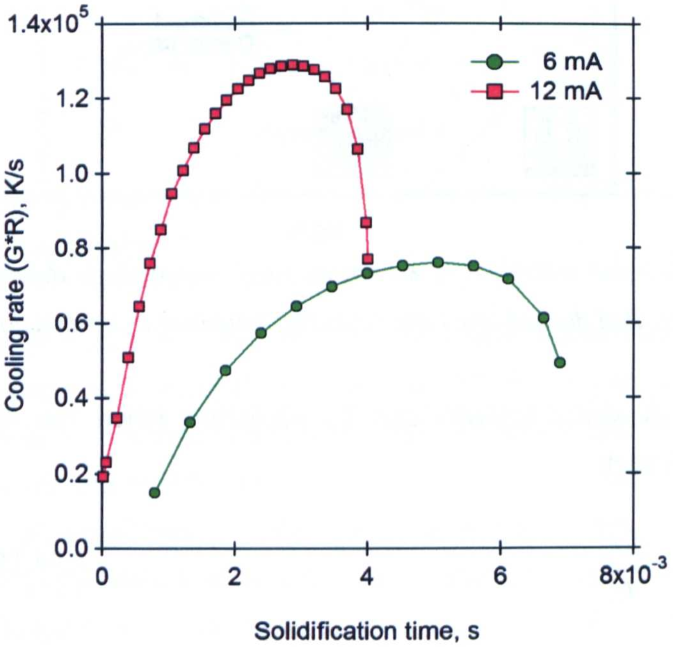

Figure 4.22 : Calculated cooling rate (G × R) versus solidification time for 6 mA and 12 mA melt pools.

Using Equation (4.8) and the solidification map in Figure 4.19, electron beam speed and current can be decoupled (by ignoring the *speed function*) to perform some theoretical calculations. This allows exploration of current-speed combinations not permissible during standard processing. Two such current-speed combinations are shown in Figure 4.23 in which solidification conditions of beams with a current of 30 mA and speeds of 0.188 and 0.004 ms^{-1} are shown. Two points can be determined from Figure 4.23: (i) the effect of changing beam current whilst maintaining a constant speed and (ii) the effect of changing beam speed whilst maintaining a constant current.

Comparison of the solidification conditions of the 6 mA beam with that of the 30 mA beam (green squares), both moving at 0.188 ms^{-1}, indicates that at constant speed, an increase in current decreases *G*. As mentioned above, a decrease in *G* also decreases the cooling rate and therefore reduces *R*. Comparison of the solidification conditions for both 30 mA beam currents reveals that decreasing beam velocity again reduces both *G* and *R*. The same trends were found by Bontha [104] for blown powder, laser deposited Ti-6Al-4V. Decreasing beam speed is analogous to increasing current; both act to increase the melt pool size.

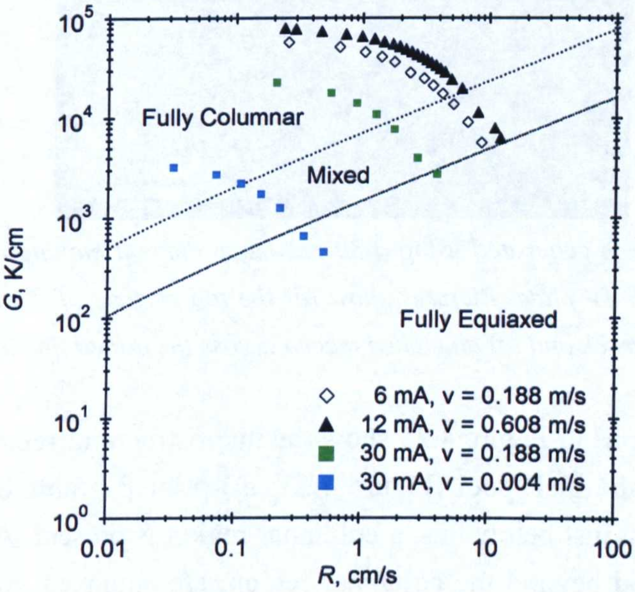

Figure 4.23 : Solidification map for EBM material under standard conditions (6 mA and 12 mA) and predicted morphology for material melted with a 30 mA beam at two different velocities. $T_0 = 923K$, $\eta = 0.6$.

To verify (i) the prediction of an equiaxed morphology and (ii) the suitability or otherwise of using a non-standard current-speed combination, a single melt track was produced on an EBM deposited, 10 mm thick plate. The plate was heated to 923 K before producing a single melt track with a beam current of 30 mA and a beam speed of 0.004 ms^{-1}. The result of this experiment is shown in Figure 4.24.

The most striking result found by using a 30 mA beam current is the size of the melt track produced. This width varies between 9 mm at the start of the melt track and 7 mm at the end (right hand side). The depth of the melt track was sufficient to cause through-thickness melting of the 10 mm thick substrate material, as shown in Figure 4.24 (b) and (c). Either side of the white dashed lines in Figure 4.24 (c) a typical, as-deposited EBM microstructure can be seen, within the bounds of the white dashed line are two regions, a region of equiaxed grains bounded by the white and green dashed lines and a region of mixed morphology, bounded by the green dashed lines.

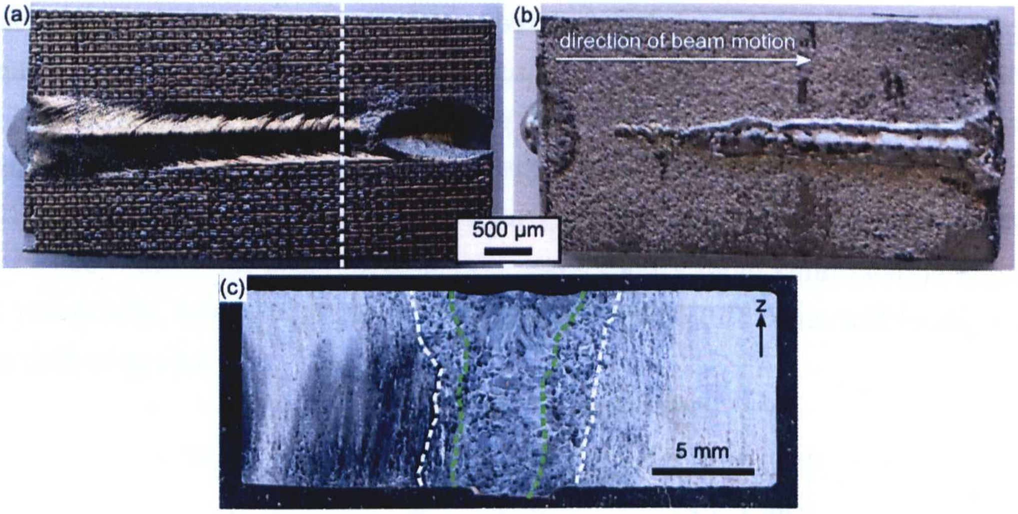

Figure 4.24 : Melt track generated using a 30 mA beam current moving at $0.004 ms^{-1}$ *on an EBM deposited Ti-6Al-4V plate. Pictures show (a) the top surface of the melt track, (b) the underside of the melt track and (c) an etched macro across the dotted line in (a)*

Optical micrographs in Figure 4.25 show the microstructural regions more clearly. At the very top of the melt pool (Figure 4.25 (a)) prior β grains have an equiaxed microstructure whilst just below this, a columnar region is present. At the very centre of the melt pool, and beyond the columnar region, are equiaxed grains as in Figure 4.25 (c). As predicted, the parameter set used here results in a mixed prior β morphology. However, comparison between the predicted solidus isotherm and the green dashed line in Figure 4.25 indicates that the 30 mA beam appears to have generated a keyhole; this would explain the depth of the weld. Taniguchi [56] states that the shape of a melt pool resulting from direct heat conduction should be approximately hemispherical (as observed in Figure 4.17), unlike Figure 4.25.

Effectively, running at the speed-current combination of 0.004 ms^{-1} – 30 mA produces a macro-scale electron beam weld of ~10 mm in depth; processing under standard conditions produce micro-scale welds. Although morphology has been correctly predicted using the solidification map, this is likely to be coincidental; the predicted extent of the melt pool does not match the observed results because of the apparent keyhole effect.

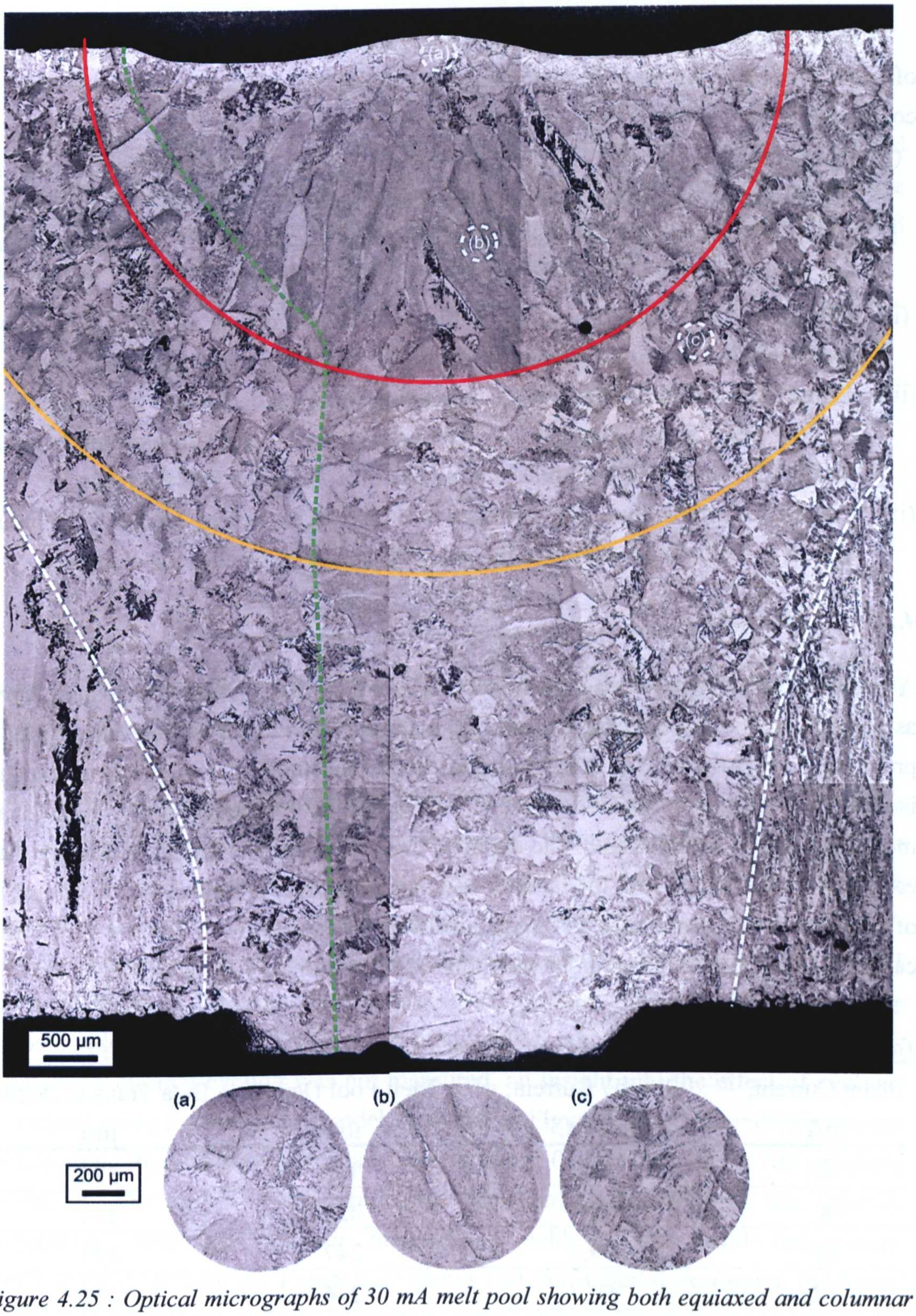

Figure 4.25 : Optical micrographs of 30 mA melt pool showing both equiaxed and columnar prior β grain morphologies. Outside of the white dashed line is the unaffected substrate material. The green dashed line highlights one half of a 'shadow' potentially created by the beam forming a keyhole. Solid lines show predicted solidus (red) and beta transus (orange) isotherms.

It is clear that ALM processing using these conditions is not a possibility because of melt pool size. As well as melt pool size, full-scale operation under the above conditions is not viable; there are several reasons for this including:

(i) Filament life – typical filament life is ~ 60 hours under standard operating conditions. By significantly increasing filament current, filament life will reduce adding expense to the process and limiting the dimensions of components that can be produced.

(ii) Deposition rate – decreasing the beam speed by two orders of magnitude drops the deposition rate to unacceptable levels increasing both lead time and expense.

(iii) Temperature control – even if the deposition rate was deemed to be acceptable, the low beam speed, coupled with the large current, results in extreme heating locally, the large melt pool makes it impossible to produce fine features.

(iv) Chemical composition – this is linked to temperature control; such a large input of heat is likely to contribute to the volatilisation of some alloying elements.

4.2.5. Thermal Cycling

A feature of all ALM processes is the unique thermal history of each deposited layer as a result of the incremental addition of material. Two key features during EBM processing of Ti-6Al-4V are the melt pool depth and the depth of the beta transus isotherm. Whilst melt pool depth can be determined experimentally, numerical modelling allows calculation of the depth of the beta transus isotherm. Knowing that each EBM layer is 100 µm, the number of times each layer is molten and the number of times each layer is cycled through transus can be determined. Table 4.2 lists the calculated melt pool and beta transus depths for the melt pools in Figure 4.17.

Table 4.2 : Melt pool and beta transus isotherm depths for melt pools in Figure 4.17.

Beam Current, mA	Speed / Current, mm.mC^{-1}	Melt Pool Depth, µm	Beta Transus Depth, µm
6	31.3	306	528
8	46.9	253	434
10	49.7	247	423
12	50.7	244	418
15	53.5	238	407

As with the melt pool depth (Figure 4.18), the depth of the predicted beta transus isotherm also shows a linear relationship with the value of speed/current:

$$\beta \text{ transus depth} = 700.9 - 5.6 \times \left(\frac{v}{I}\right) \qquad (4.16)$$

Table 4.2 indicates that each deposited layer is melted 2 – 3 times and cycled above the β transus a further 2 times. After a total of 4 – 5 excursions above a significant transformation temperature, further thermal cycling occurs within the α + β phase field. This thermal cycling is shown schematically in Figure 4.26.

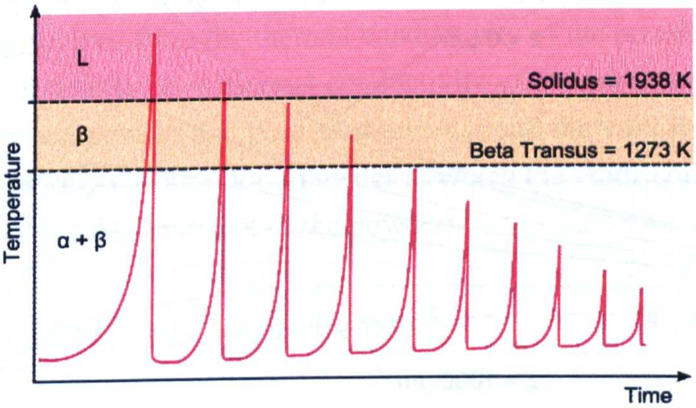

Figure 4.26 : Schematic representation of thermal cycling based upon solidus and beta transus isotherms given in Table 4.2.

Owing to the current EBM hardware making use of only one thermocouple (which must be used to monitor the *build temperature*, T_0), the measurement of temperatures other than T_0 was not possible over the course of this project. However, it is the intention of the research group to upgrade the system and install a vacuum feed-through. This would allow the use of extra thermocouples and recording of thermal history at multiple locations. Such data would provide important information for thermal models and give an important insight into the process conditions.

Although thermal cycling was not measured, an insight into the effect of cycling, determined using the numerical model, is shown in Figure 4.27. Predicted temperature profiles along the *x*-axis at depths (*z* values) between 0 and 1000 μm, in 100 μm steps are shown. The *y*-axis of the graph has been limited to 1988 K, the liquidus temperature. Although globally material is held at the build temperature (approximately isothermal), Figure 4.27 shows that, for material exposed to the beam, temperature conditions are non-isothermal. Based on the numerical model, each 100 μm layer is cycled above the T_0 temperature approximately 80 times before being completely beyond the influence of the beam. Thus deposited material only experiences approximately isothermal conditions once it is ~ 8 mm below the deposition surface. Prior to this, the thermal cycling may provide sufficient energy to promote microstructural change. Further work is required to determine the effect, if any, of this thermal cycling on microstructure.

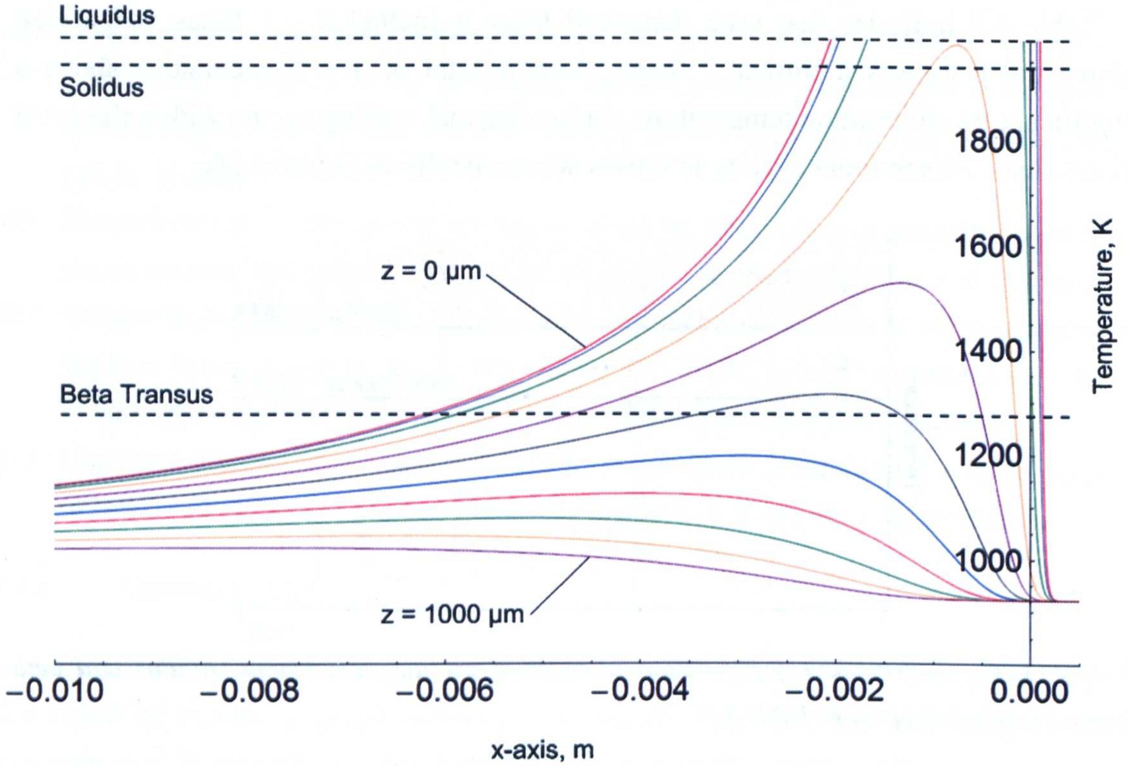

Figure 4.27 : Predicted temperature profiles along the x-axis (at $y = 0$) at different depths ranging from $z = 0$ μm to 1000 μm in 100 μm steps. Dashed lines mark the liquidus, solidus and β transus temperatures. $\eta = 0.6$, $T_0 = 923$ K.

4.3. Powder System Considerations

The numerical modelling performed in this chapter, and experimental validation, has been predicated upon the use of a solid substrate. Solid substrates clearly reveal the extent of influence of the electron beam from which relatively quick beam characterisation measurements can be made. Experiments such as those shown in Figure 4.4 to Figure 4.10 provide the EBM user with a firm understanding of how varying user-defined parameters will affect processing.

However, in all cases above, the effect of powder has not been considered. Powder adds another dimension of complexity to modelling of the EBM process; powder size distribution, and the degree to which the beam sinters powder prior to melting both influence the final density of the pre-melt powder layer. This final density then determines thermal properties of the powder layer. During melting, the electron beam melts the 100 μm layer of powder plus some of the underlying substrate material and as such thermal properties change at the powder/substrate boundary.

Thermal conductivity of powders has been investigated by Hadley [105] and Bala *et al.* [106,107]. The authors compare experimental results with derived models for powdered materials surrounded by a pore-medium of liquid or gas. Heat transfer in a powdered material arises from (i) conduction between contacting particles, (ii) gas conduction in the pores and (iii) particle to gas conduction and vice versa. The importance of each factor depends upon powder size, gas pressure, powder material and temperature [107].

The thermal conductivity equations [105, 106, 107] provide an effective thermal conductivity, k_{eff}; derived from the thermal conductivity of the powdered material as a solid at theoretical density, k_{TD}; thermal conductivity of the pore medium, k_g; thermal conductivity between powder and pore medium, k_{pg}; and the void fraction, φ. Bala *et al.* derive the following equation for a powder in which the voids contain a gas of low thermal conductivity relative to that of the powder:

$$k_{eff} = k_{TD}(1-\varphi)^{4/3} + k_g\left[1-(1-\varphi)^{2/3}\right]^2 \tag{4.17}$$

If it is assumed that a perfect vacuum exists in the pores between powder particles in the EBM process; k_g equals zero and the second term on the right-hand side of the above equation can be ignored, giving:

$$k_{eff} = k_{TD}(1-\varphi)^{4/3} \tag{4.18}$$

Figure 4.28 shows the application of Equation (4.18) at different temperatures, ranging from room temperature to the solidus temperature, as a function of void fraction. Utilisation of this data is not possible in the Rosenthal solution due to (i) the use of constant thermal properties and (ii) the use of only one value of thermal conductivity. Effective use of the data presented in Figure 4.28 could be achieved via the development of a finite element (FE) model for which a powder layer could be modelled on top of a solid Ti-6Al-4V layer. Both powder thermal conductivity and changes in conductivity with temperature could be incorporated into such a FE model.

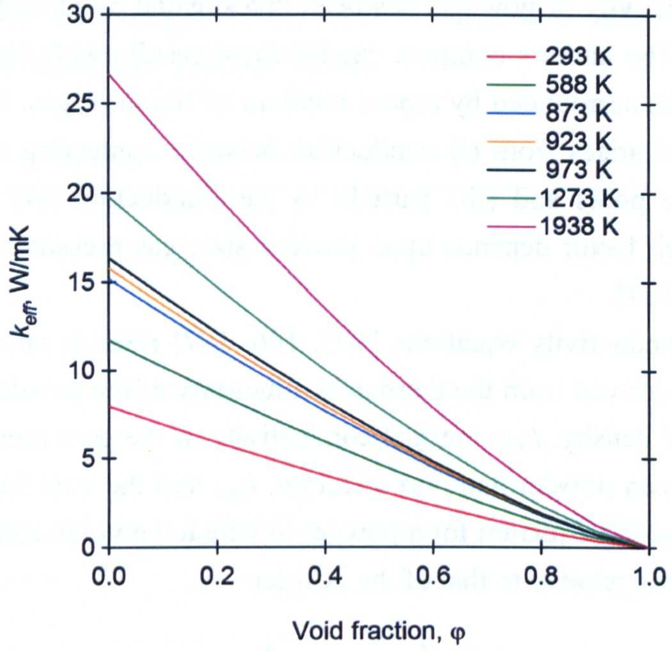

Figure 4.28 : Change of effective thermal conductivity, k_{eff}, of Ti-6Al-4V with temperature and void fraction, φ.

Consideration of Equation (4.8) and Figure 4.28 indicate that, with increasing void fraction, the depth over which the electron beam has an influence would decrease i.e. melt penetration would decrease. The value of η is also likely to decrease as a result of coupling between the electron beam and powder being less efficient than that between the electron beam and solid material. Therefore, any model developed to represent the true conditions within the EBM system would require the behaviour of sintered Ti-6Al-4V powder to be determined.

4.4. Summary and Conclusions

- Solid substrate material has been used to investigate the effect of changing electron beam parameters at ambient and elevated temperatures.
- By using a stainless steel base plate, at ambient temperatures, observation of melt tracks indicate that:
  - At a constant beam current, *speed function* and melt track width have a linear relationship.
  - For a constant *speed function*, melt track width increases with increasing beam current.
  - The electron beam is asymmetrical about the focal point; positive values of *focus offset* are less defocused than equivalent negative values.

- The Rosenthal solution has been used to predict melt pool size on a Ti-6Al-4V substrate at elevated temperature (923 K). Predictions match experimental results well when a fitting parameter, η, of 0.6 is used. The fitting parameter incorporates the effects of beam efficiency and focus offset under standard hatch conditions (6 – 15 mA, *focus offset* = 17 mA, *speed function* = 19).
- Under these standard conditions it is apparent that a beam current of 6 mA produces a larger melt pool in comparison to beam current of 8 – 15 mA. The speed applied by the *speed function* at 6 mA is believed to be too slow.
- Using the numerical model, thermal gradient and solidification velocity have been determined and plotted onto a solidification map. Under standard processing conditions, solidification is predicted to be fully columnar – this is observed experimentally.
- The solidification map indicates the potential to produce an equiaxed grain morphology using non-standard processing conditions. However, the predictive capacity of the numerical model breaks down under the beam conditions used and the correctly predicted morphology is perhaps coincidental. Although the type of microstructure produced under these conditions is desirable, the beam properties required to bring about the equiaxed morphology are not viable for production purposes.
- The numerical model has been used to predict the number of times material is thermally cycled. Predictions indicate that material is cycled above the β transus temperature 4 – 5 times before being cycled to temperatures above the T_0 temperature ~ 80 times. The effect of thermal cycling on microstructure would be an interesting area for further investigations.
- Further investigations would also need to be carried out to modify the numerical model or produce a FE model that incorporates the properties of Ti-6Al-4V powder. To do so effectively, powder properties as a function of temperature and packing density would need to be determined.

With the electron beam characterised, the following chapter discusses the microstructures found in EBM processed Ti-6Al-4V.

5. MICROSTRUCTURAL CHARACTERISATION

Within this chapter, the microstructures and textures produced as a result of EBM processing Ti-6Al-4V will be discussed. Early literature on the EBM process (see Table 2.10) tends to focus primarily on the process and advantages associated with the design aspects of ALM. Work describing microstructures developed by EBM is relatively scarce and, of the available literature, processing conditions tend to be omitted. To date, there has also been no discussion of the texture of EBM Ti-6Al-4V in the as-deposited state. Owing to the lack of literature available for powder bed EBM, the papers listed in Table 2.10 will be heavily referenced in this chapter.

A brief characterisation will be made of the Ti-6Al-4V powder, used as feedstock for the EBM process, before the EBM microstructures are themselves discussed.

5.1. Powder Size Analysis

Pre-alloyed Ti-6Al-4V PREP powder, supplied by Arcam AB, was the feedstock material used to produce all samples in this study. The powder conformed to the chemical requirements of specification ASTM B348, grade 5 and had a quoted size range of 45 – 100 μm. As mentioned in the Experimental Chapter, two methods were adopted for the measurement of powder size distribution; automated powder size analysis by laser diffraction and image analysis.

5.1.1. Results and Discussion

Powder morphology is shown in optical micrographs in Figure 5.1 and SEM micrographs in Figure 5.2. The vast majority of powder particles were found to have a spherical morphology. In the as-received condition, the powder microstructure is fully martensitic (Figure 5.1 (b)) as could be expected from rapid solidification of the metal droplets during powder production.

Powder size distribution, determined by the use of a Coulter LS130 particle size analyser, yielded the results shown in Figure 5.3 for virgin Ti-6Al-4V powder. The average powder diameter was found to be 115.74 ± 10.0 μm at the 95% confidence limit (henceforth 95% CL). Image analysis of optical micrographs, performed using ImageJ software (http://rsbweb.nih.gov/ij/index.html), yielded an uncorrected average powder diameter of 81.39 ± 1.52 μm (95% CL). As discussed in Section 3.4.7, a Scheil-type analysis must be performed on the data to correct for the affect of sectioning. The Woodhead analysis, described by Higginson and Sellars [91], was used in this case. As a result of this correction, an average powder diameter of 58.91 ± 4.00 μm (95% CL) was determined. Image analysis of SEM micrographs (non-sectioned powder) was also performed using ImageJ software, giving an average powder diameter of 63.06 µm ± 1.20 µm (95% CL); concurrent with the corrected optical micrograph analysis.

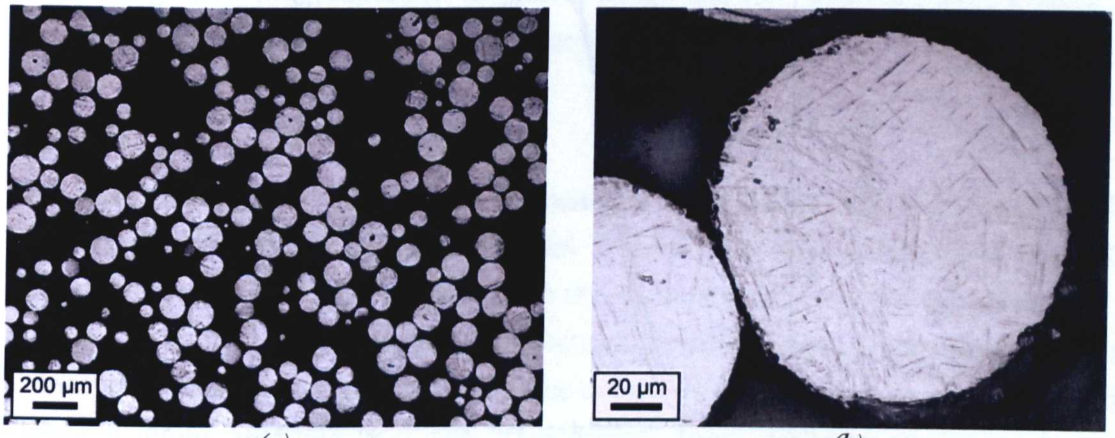

(a) (b)

Figure 5.1 : Optical micrographs of virgin Ti-6Al-4V powder (batch P337) at (a) low and (b) high magnification. Martensitic laths as a result of fast solidification and cooling rates are observed in (b).

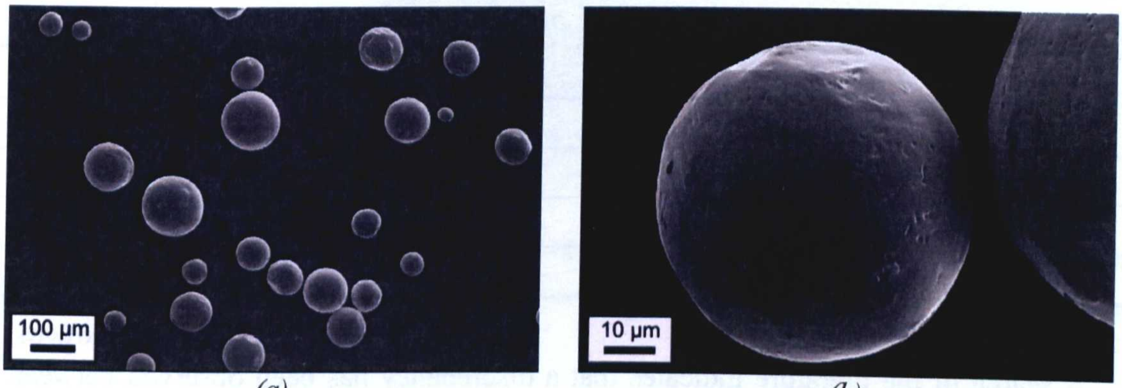

(a) (b)

Figure 5.2 : SEM micrographs of virgin Ti-6Al-4V powder (batch P337) at (a) low and (b) high magnification.

A summary of the average powder diameters determined from the various methods is given in Table 5.1. Clearly there is a discrepancy between automated particle size analysis and image analysis. The results of the automated particle size analysis are also at odds with the supplier-quoted size range. The reason for such a discrepancy is believed to be a result of particle agglomeration during the automated measurement process.

Of the three methods used to determine powder size, all are prone to error introduced from biased sampling and measurement of a non-representative sample. In this work, a bulk sample was taken from thoroughly mixed powder. The bulk sample was well mixed prior to taking any smaller samples for analysis.

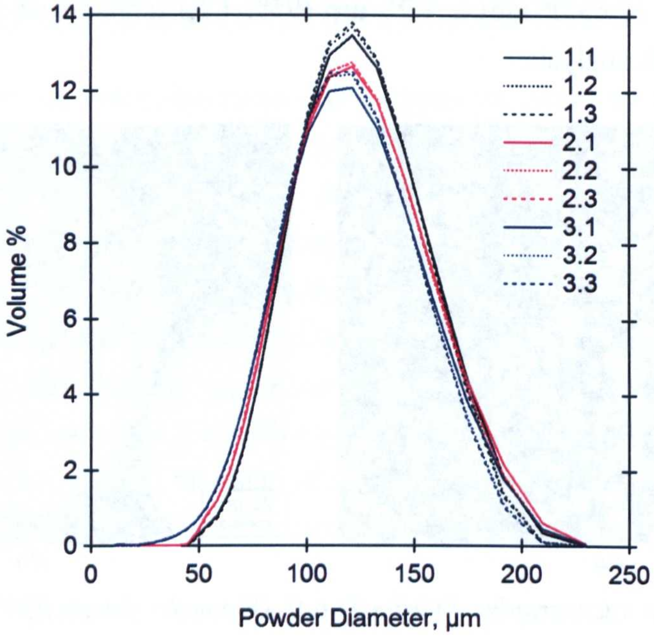

Figure 5.3 : Coulter LS130 particle size analysis for powder batch P337 (virgin powder).

Table 5.1 : Summary of virgin powder size results.

Method	Average Powder Particle Diameter
As-received	45 – 100 µm (supplier quoted range)
Coulter LS130	115.74 ± 10.0 µm (95% CL)
Optical image analysis (corrected)	58.91 ± 4.00 µm (95% CL)
SEM image analysis	63.06 µm ± 1.20 µm (95% CL)

A search of the literature indicates that a discrepancy has been observed between Coulter LS130 measurements and results from sieving [108] and between Coulter LS130 measurements and image analysis [109]. In both cases, a reason for this discrepancy is not given. When considering the methods used in this work, SEM image analysis is only subject to sampling error because, in the SEM micrographs themselves, the full extent of each powder particle is visible.

Although care was taken to minimise the amount of agglomeration during automated particle size analysis, results indicate that agglomeration did occur. During measurement, rather than pass by the detector, some powder was observed to float on top of the input reservoir and form small clumps. It is possible that this agglomeration also occurred during the measurement process, falsely increasing the measured powder size. It also seems highly unlikely that powder supplied in the 45 – 100 µm size range would have an average diameter of 115.74 µm.

Although more laborious, it is suggested that optical or SEM image analyses are the best means of determining powder size in this instance. SEM image analysis is both quicker in terms of sample preparation time and the lack of correction required compared to the sectioned optical powder samples. SEM analysis is also free from sectioning errors in comparison to optical image analysis, although more images are required because of the higher SEM magnification.

5.2. Microstructure

Samples produced for microstructural analysis were made using the standard EBM *themes* documented in the Experimental Chapter. To fully characterise the EBM microstructure, samples were taken from the *xy* plane and one of the equivalent *xz* / *yz* planes as shown in Figure 5.4. By sectioning in this way, microstructures were observed parallel and perpendicular to the *z*-axis. Microstructures of interest were the prior β grain structure and the transformed, room temperature microstructure. Microstructures were investigated at three key positions, namely (i) at the interface with the base plate, (ii) in the bulk of a sample and (iii) at the top of a sample.

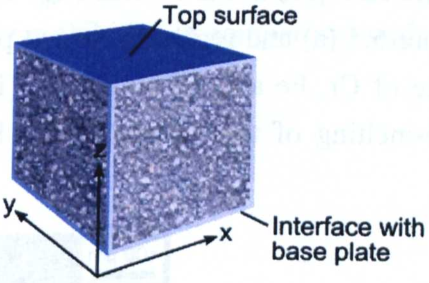

Figure 5.4 : Schematic of coordinate system and interface regions. Side regions are in contact with powder, the bottom interface contacts a base plate and the top is open to the vacuum environment.

5.2.1. Base Plate Interface Microstructure

As previously described in the Experimental Chapter, standard EBM practice is to melt onto a 10 mm thick stainless steel base plate. The base plate fulfils two roles; the first is to provide a solid platform onto which powder layers may be applied and the second is to provide heat at the start of a build. Initial heating of the base plate to 760 °C provides heat to the first layers; this aids powder sintering prior to melting. Base plates are square and come in three sizes, 150 mm, 180 mm and 210 mm, all of which are 10 mm thick. They are made from a proprietary grade of stainless steel manufactured by Outokumpu Ltd. and designated 253 MA^{TM}. The MA designation stands for micro-alloying and the steel is described by the manufacturers as '*...a nitrogen alloyed heat resistant Cr-Ni austenitic stainless steel...*' [110] having good creep resistance at high temperature. Table 5.2 gives the chemical composition of the base plate alloy.

Table 5.2 : Chemical composition of 253 MA base plate material.

	C	Cr	Ni	Si	N	Ce
min.	0.05	20.0	10.0	1.4	0.14	0.03
max.	0.10	22.0	12.0	2.0	0.20	0.08

An advantage of using stainless steel is that the Ti-6Al-4V components weld to it at high temperatures. At low temperatures the interface cracks and parts can be manually removed from the base plate without the need for cutting. Whilst the lack of cutting is advantageous in terms of time and cost, there is a negative effect on the material. Figure 5.5 shows two back-scattered electron images taken at the bottom of a sample that contacts the base plate during the build. Atomic number (Z) contrast highlights a layer of approximately 500 μm in Figure 5.5 (a) corresponding to a contaminated region. Several cracks are also visible within this region as a result of its brittle nature. Z-contrast in Figure 5.5 (b) shows Ti-6Al-4V powder particles that have been entrapped by contaminated liquid at the bottom edge of a sample. EDX analysis of the bright region in Figure 5.5 (a) and regions between powder particles in Figure 5.5 (b) reveals the presence of Cr, Fe and Ni alongside Ti, Al and V. Clearly, this region results from the co-melting of the surface of the base plate and the initial powder layers.

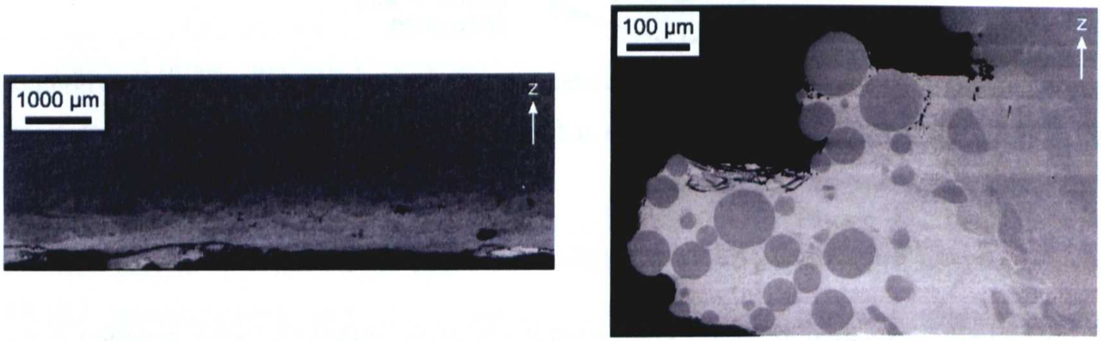

(a) *(b)*

Figure 5.5 : Back scattered electron imaging of the bottom interface with the base plate; (a) a ~ 500 μm contaminated region and (b) Ti-6Al-4V powder particles entrapped in solidified intermetallic.

Cr, Fe and Ni all stabilise the β phase in titanium and as such, influence microstructure at the bottom of EBM components. Figure 5.6 (a) is a SEM micrograph of the bottom of an EBM component in which two regions can be identified. The bottom of the micrograph shows α laths surrounded by a large volume of β phase. Above the dashed line, a more typical α + β microstructure is present in which α laths are delineated by β phase, much finer than that observed below the dashed line. Figure 5.6 (b) shows the result of quantitative EDX performed at the bottom of an EBM sample and reveals the extent of the migration of base plate material into a component.

At a *z*-height of 580 μm, Fe content is 1.14 wt%; all deposited material up to and including this height is out of specification – to be classified as grade 5 material, the Fe content of Ti-6Al-4V must be <0.25 wt%. At a *z*-height of 800 μm, no Fe was detected. Therefore, between 580 and 800 μm lies a position where the material becomes acceptable in terms of chemical composition. The effect of this co-melted region can further be seen in Figure 5.6 (c) which shows the micro-hardness of a 2 mm tall sample as a function of height. Hardness is approximately 10% higher at the bottom of the sample in comparison with the average hardness for all other positions.

Whilst the choice of base plate material may be considered trivial, its effect on chemistry should not be overlooked. The use of the standard stainless steel plate requires a sacrificial region (solid or support structures) to raise the component ~ 800 μm above the base plate to ensure that a fully Ti-6Al-4V component is produced. The use of a Ti-6Al-4V base plate may also be an option although, initial cost and cutting may prove to be financially prohibitive in comparison with a sacrificial region.

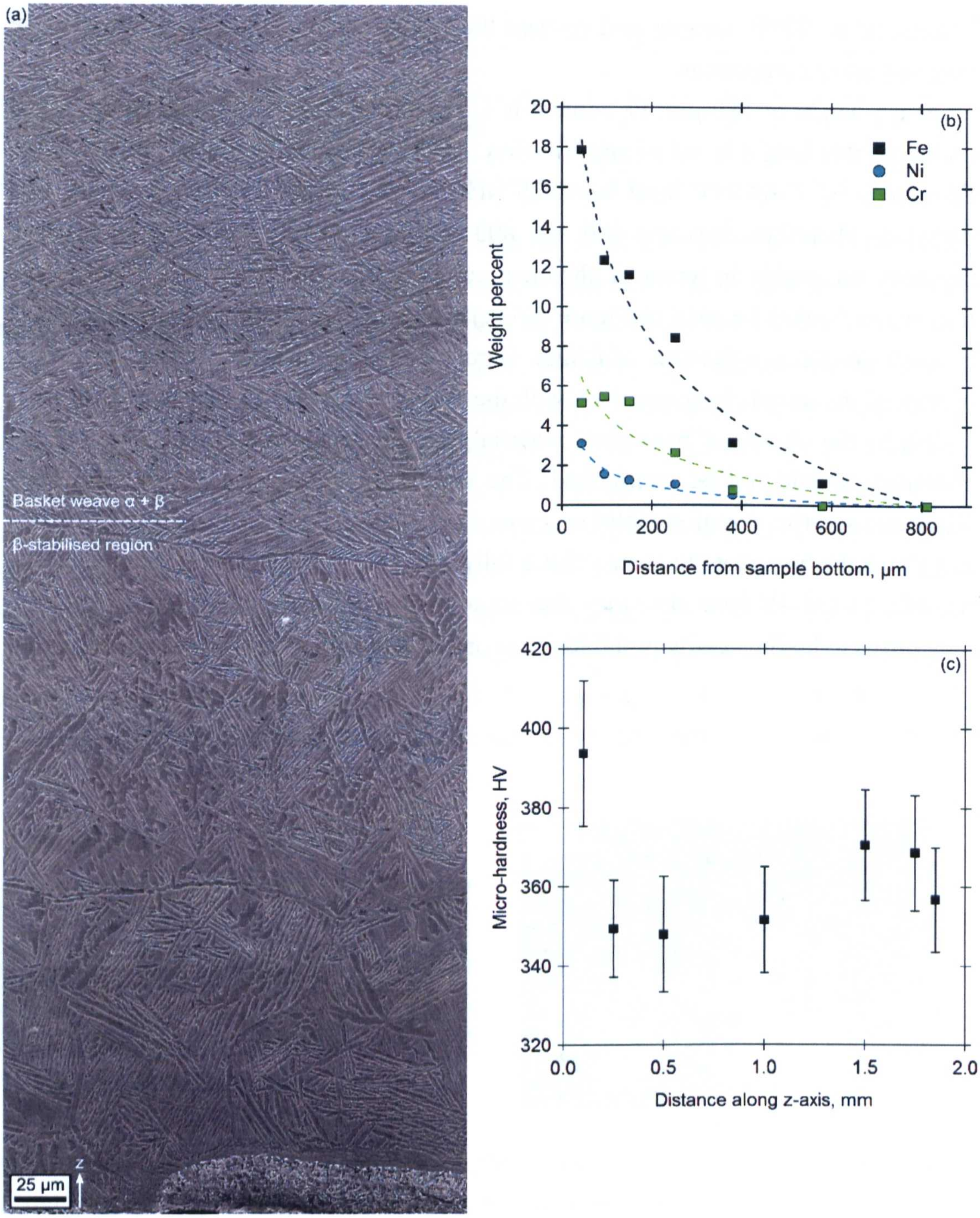

Figure 5.6 : (a) SEM micrograph at the bottom of an EBM build showing the β stabilised region as a result of co-melting of Ti-6Al-4V powder and the stainless steel base plate, (b) quantitative EDX results showing Fe, Ni and Cr concentrations as a function of distance from the base plate and (c) micro-hardness profile along a 2 mm tall sample; an increased hardness 0.1 mm from the sample bottom results from the β stabilised region. Error bars represent 95% CL.

5.2.2. *Bulk Microstructure*

Away from the base plate region, EBM Ti-6Al-4V possess a transformed $\alpha + \beta$ microstructure with laths of α delineated by fine β phase; see above the dashed line in Figure 5.6. Prior β grain structure is similar to that reported by authors depositing Ti-6Al-4V by laser ALM methods [70, 71, 72]. The long axis of the columnar prior β grains lie nominally parallel to the *z*-axis and extend through many layers as a result of epitaxial growth. Micrographs at low magnification are shown in Figure 5.7 both perpendicular and parallel to the *z*-axis.

Parallel to the *z*-axis, Figure 5.7 (a), the columnar nature of prior β grains is a direct consequence of the thermal gradient that exists in the *z*-direction. The base plate and deposited material act as a heat sink during deposition whilst the electron beam provides the source of heat from above. Components produced via EBM are surrounded by loose/lightly sintered titanium powder that acts as insulation; as such, heat losses are dominated in one dimension, along the *z*-axis. Perpendicular to the *z*-axis, prior β grains appear equiaxed, as in Figure 5.7 (b).

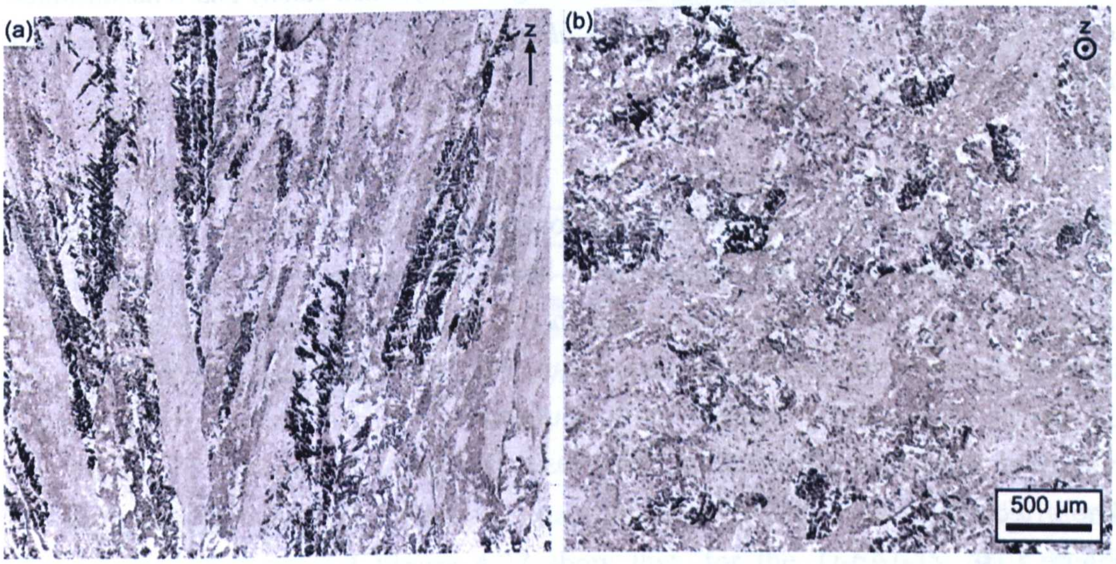

Figure 5.7 : Low magnification optical micrographs of (a) EBM Ti-6Al-4V parallel to the z-axis and (b) EBM Ti-6Al-4V perpendicular to the z-axis.

At low magnification, prior β morphology is discernable; however, accurate determination of the location of prior β grain boundaries can be difficult. At higher magnifications, prior β grains are more easily identified when continuous grain boundary α (α_{GB}) is present along prior β grain boundaries; the presence of α_{GB} is shown in Figure 5.8. Grain boundary alpha is generally considered to be a deleterious microstructural feature in titanium, its presence reduces ductility and the resistance to fatigue crack initiation; this is because cracks tend to propagate in or near interfaces such as those formed by α_{GB} [7]. As well as the formation of α_{GB}, transformation of prior β grains results in a fully lamellar microstructure in which α laths have both colony and Widmanstätten morphologies, as shown in Figure 5.8.

Figure 5.8 : Typical bulk microstructure exhibiting a transformed colony and Widmanstätten $\alpha + \beta$ *microstructure with continuous* α_{GB} *along prior* β *grain boundaries. Arrowheads indicate some examples of* α_{GB}.

Thermo-mechanical processing (TMP) of Ti-6Al-4V allows the production of equiaxed, bimodal and fully lamellar microstructures. Fully lamellar microstructures in TMP are generated by a homogenisation and aging treatment, shown schematically in Figure 5.9 (a). The critical parameter in this production route is the cooling rate from the homogenisation step; this cooling rate defines α lath size, α colony size and the extent of α_{GB} along prior β grain boundaries [17]. As a comparison, thermal history of Ti-6Al-4V deposited by direct laser fabrication is shown in Figure 5.9 (b). The effect of α colony size (slip length) on properties is shown schematically in Figure 5.10.

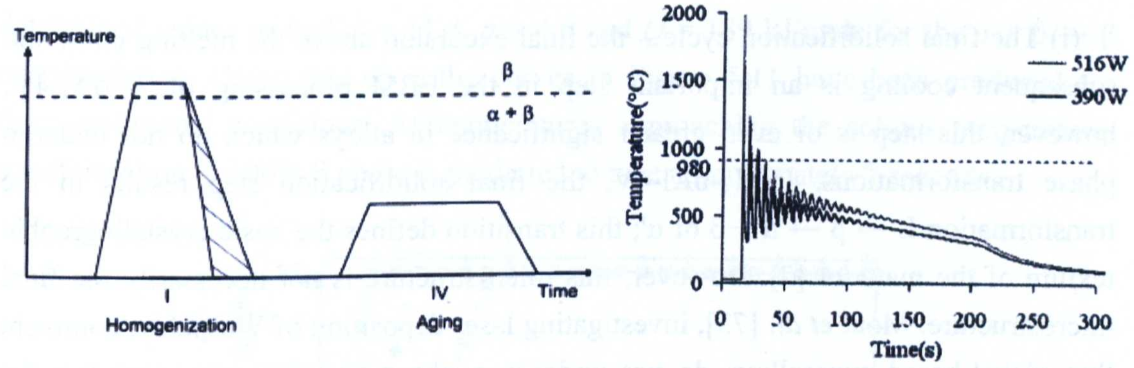

(a) (b)

Figure 5.9 : (a) Schematic processing route for the production of fully lamellar structures by conventional TMP [17] and (b) temperature-time plot during the deposition of Ti-6Al-4V by the direct laser fabrication process [69].

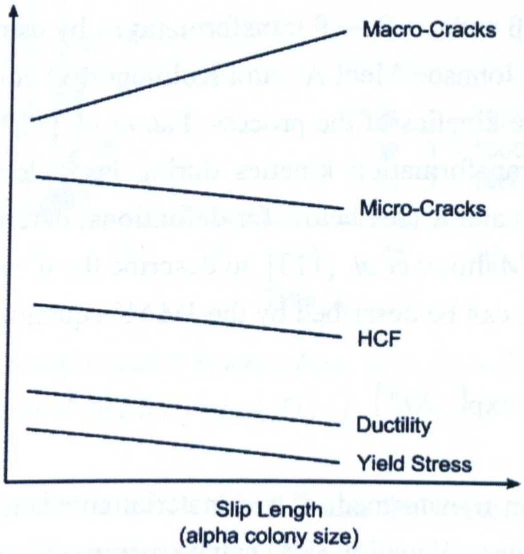

Figure 5.10 : Schematic effect of slip length on properties of titanium alloys, adapted from [17].

As discussed in Section 4.2.5, thermal cycling results in a layer-specific thermal history. Figure 4.26 and Figure 4.27 show that, for the Ti-6Al-4V alloy system, thermal cycling may result in three outcomes. These outcomes are: (i) melting/re-melting, (ii) heating to above a phase transition or (iii) heating (with no phase transition). Unlike the relatively simple thermal history needed to generate fully lamellar TMP microstructures, similar EBM microstructures arise from a combination of these three thermal cycling outcomes. A further factor, unique to the hot EBM system, is the *build temperature*.

The development of the room temperature microstructure is therefore dependant on: (i) the final solidification cycle, (ii) excursions above the β transus, (iii) thermal energy supplied without causing a phase transformation and (iv) the *build temperature*. These points will now be discussed further.

(i) The final solidification cycle – the final excursion above the melting point and subsequent cooling is an important step in the EBM processing of Ti-6Al-4V, however, this step is of even greater significance in alloys which do not undergo phase transformations. In Ti-6Al-4V, the final solidification step results in the transformation L → β → α + β or α'; this transition defines the basic crystallographic texture of the material [7]. However, this microstructure is not necessarily the final microstructure. Moat *et al.* [73], investigating laser deposition of Waspaloy, comment that nickel-based superalloys do not undergo a phase transformation that has the potential to refine the grain structure.

(ii) Excursions above the β transus – although, in terms of temperature, thermal cycling results in material transitioning above the β transus, the kinetics of the transformation will determine the microstructure. Elmer *et al.* [111] investigated the kinetics of the β → α + β and α + β → β transformations, by using time-resolved XRD (TRXRD). The JMAK (Johnson Mehl Avrami Kolmogorov) equation, Equation (5.1), was used to describe the kinetics of the process. Fan *et al.* [112] also used the JMAK equation to describe transformation kinetics during laser deposition, however, the authors used values of *n* and *K* (see below for definitions) determined for the β → α + β transformation, after Malinov *et al.* [113], to describe the α + β → β transformation. Transformation kinetics can be described by the JMAK equation in which:

$$X(t) = 1 - \exp\left(-Kt^n\right) \qquad (5.1)$$

where $X(t)$ = fraction transformed, K = a material constant, t = time and n = the JMAK or Avrami exponent. Equation (5.1) can be rearranged to give Equation (5.2).

$$\ln\left[\ln\left(\frac{1}{1-X(t)}\right)\right] = n\ln t + \ln K \qquad (5.2)$$

A plot of $\ln\left[\ln\left(\frac{1}{1-X(t)}\right)\right]$ versus $\ln t$ therefore yields a straight line with n as the gradient and K as the y-intercept. The value of K is temperature dependant following the relationship:

$$K = K_0 \exp\left(-\frac{Q}{RT}\right) \qquad (5.3)$$

where K_0 is a pre-exponential factor, Q is the activation energy for transformation, R is the universal gas constant and T is the absolute temperature. Elmer *et al.* [111]

determined values of $\ln(K_0) = 11.4$, $n = 4.0$ and $Q = 189$ kJ/mole for the $\alpha + \beta \rightarrow \beta$ transformation. Using this data, the curves in Figure 5.11 have been produced for three isothermal conditions. At temperatures approaching the solidus temperature, transformation to 100% β phase is predicted to take approximately 2 seconds.

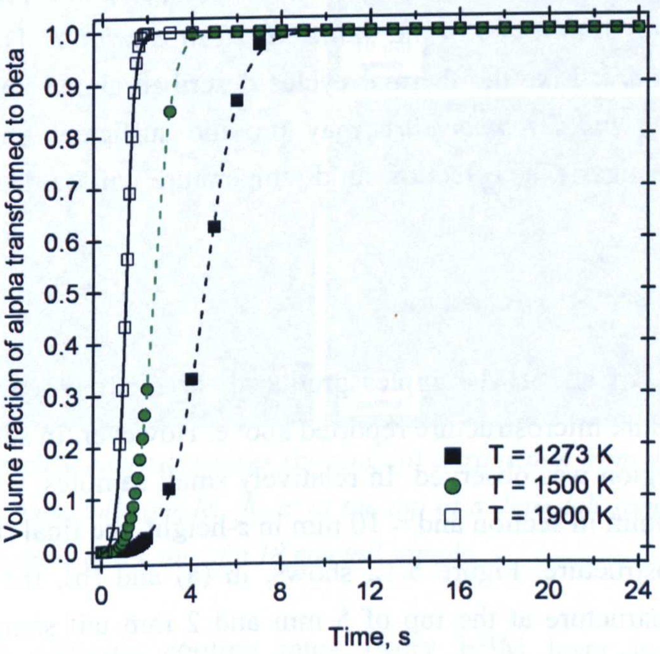

Figure 5.11 : Isothermal transformation kinetics from $\alpha + \beta \rightarrow \beta$ *in Ti-6Al-4V based on the JMAK values determined by Elmer et al. [111].*

Using Equation (4.8), the data in Table 4.2 and the value of η determined in the previous chapter, the maximum time spent above the β transus without melting, can be calculated. For a 6 mA beam moving at 0.188 ms^{-1} (*speed function* = 19) this time is calculated to be 28 ms; for a 12 mA beam moving at 0.608 mms^{-1} (*speed function* = 19) this time is calculated to be 17 ms. In comparison to the time required for transformation, both of these times are small and as such it appears unlikely that any significant transformation to β phase will occur upon cycling. The implication of this is that, during EBM processing, fully β microstructures only form during solidification ($L \rightarrow \beta \rightarrow \alpha + \beta$ or α'). After solidification, further excursions above the β transus result in a momentarily superheated $\alpha + \beta$ or α' microstructure. It can be concluded that the final solidification cycle is thus responsible for the type of transformed microstructure (diffusional or martensitic), the initial α colony size and the extent of α_{GB}.

(iii) Thermal energy supplied without causing a phase transformation – based on the previous calculations, all thermal cycles that do not cause melting, do not cause a phase transformation to β. Cycling therefore provides additional energy, on top of that from the *build temperature*, to the material and may thus promote microstructural change.

(iv) *Build temperature* – having a typical value of 650 °C, this temperature influences cooling rates from the liquid phase and from above the β transus. This temperature can be thought of as analogous to the aging step in Figure 5.9 (a); Arcam describe EBM Ti-6Al-4V to be in the '*naturally aged condition*' [114] as a result of the *build temperature*. Like the thermal cycles described above, the thermal energy resulting from the *build temperature* may provide sufficient energy to promote microstructural changes. The effect of build temperature will be discussed in Section 5.2.7.

5.2.3. Top Surface Microstructures

The vast majority of all EBM samples produced for microstructural analysis were composed of the bulk microstructure reported above. However, in some cases, another microstructural region was observed. In relatively small samples, with dimensions of up to 20 mm × 20mm in section and < 10 mm in *z*-height, the final (top) layers have a martensitic microstructure. Figure 5.12 shows, in (a) and (b), the presence of this martensitic microstructure at the top of 5 mm and 2 mm tall samples. A transition from an $\alpha + \beta$ to a α' microstructure is marked by the dotted line in Figure 5.12 (a). A fine, diffusional $\alpha + \beta$ microstructure is shown in the micrograph in Figure 5.12 (c) taken at the top of an 18 mm tall sample, the scale of the α laths suggests that cooling rates in this region are high. The presence of a martensitic microstructure raises the question: do the final EBM layers cool at a different rate to that of the underlying bulk material?

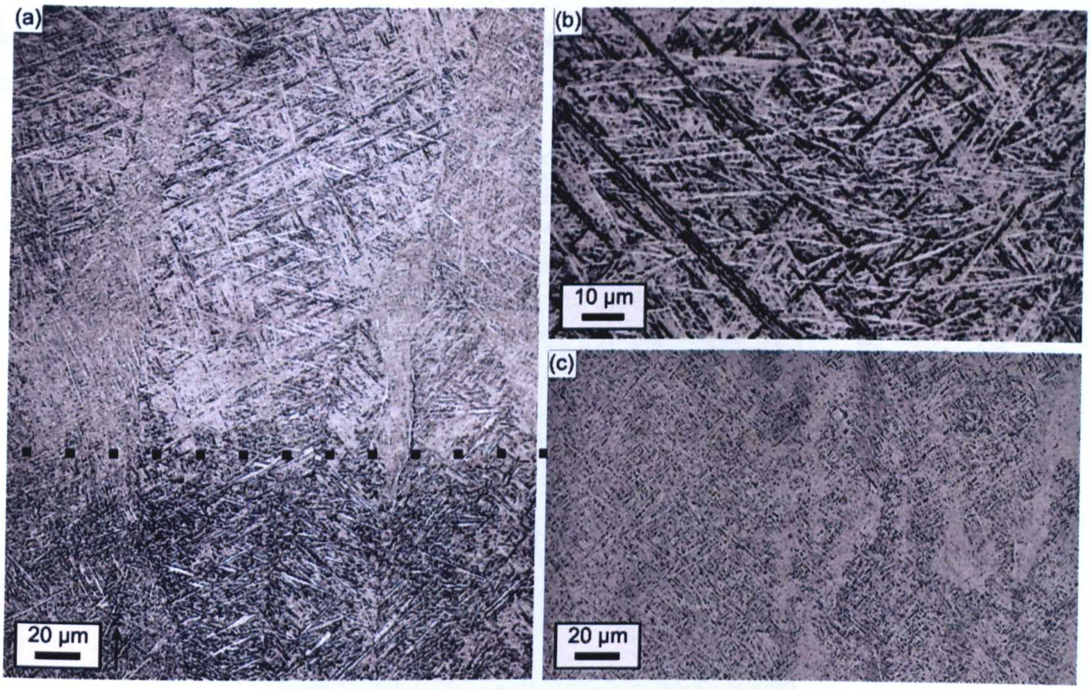

Figure 5.12 : Top surface microstructures showing (a) a transition from diffusional $\alpha + \beta$ to diffusionless α' in a 5mm tall sample, (b) α' at the top of a 2mm tall sample and (c) a fine, diffusional $\alpha + \beta$ structure at the top of a 18 mm tall sample.

With regard to differing cooling rates, every EBM layer is exposed to the controlled vacuum environment during solidification; it seems unlikely that the top layers of a component should cool at a quicker rate than that of the underlying material. Based on this assumption, it seems that, in the case of samples shown in Figure 5.12 (a) and (b), initial solidification forms a martensitic structure before this structure is thermally decomposed to $\alpha + \beta$. Facchini *et al.* [115] state that the martensitic microstructure formed during EBM is transformed to $\alpha + \beta$ by soaking at the *build temperature*. The thermal decomposition of a martensitic EBM microstructure will be investigated further in section 5.2.5.

Figure 5.12 also indicates that (i) in spite of processing at ~ 650 °C, a martensitic microstructure is formed and (ii) EBM microstructure can have a geometric dependency. As discussed in the Literature Review, and summarised in Table 2.6, there is some confusion in the literature regarding the M_s temperature, the cooling rate required to form martensite and whether or not there is a significant temperature range between the M_s and M_f temperatures. The presence of α' in the EBM process provides evidence that the M_s and M_f temperatures are in excess of 650 °C. The presence of α' in EBM material is further supported by the lack of a β peak in the XRD trace (Figure 5.13) of a 1mm tall sample. In bulk material, from a much larger sample, a β peak is present as would be expected from the transformed microstructure.

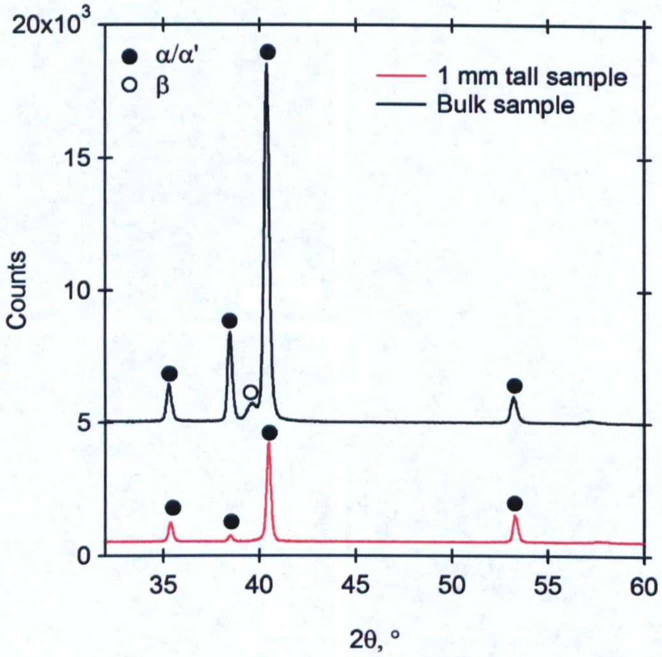

Figure 5.13 : XRD trace of bulk material from a 25 mm tall sample and from the top of a 1 mm tall sample. No β peak is detected for the 1 mm tall sample. Traces are shifted in the y-axis for clarity.

The lack of α' in Figure 5.12 (c) indicates a mechanistic change in transformation product from the prior β phase. This change must occur as a result of the difference in cooling rates and/or local temperature experienced by solidifying layers in small and large samples. The size of a component in the *z*-direction (*z*-height), for samples with the same cross sectional area, is indicative of the thermal mass of the sample. When samples are small (small *z*-height), cooling rate is high and the martensitic structure may form. With increasing thermal mass (increasing *z*-height), cooling rate decreases and a diffusional transformation product results. A schematic of the type of transformation occurring (diffusional or diffusionless) is given in Figure 5.14 where thermal mass affects both local temperature and cooling rate.

The characterisation of EBM Ti-6Al-4V microstructures in literature is scarce; the current most published authors on the subject (Murr *et al.* [64, 66]) also report that microstructure has a geometric dependence. Solid, monolithic microstructures were found to have a Widmanstätten α phase structure whilst cellular foam structures, as shown in Figure 5.15, are reported to be predominantly martensitic due to rapid solidification of cell ligaments [66]. Murr *et al.* [66] also report a mixed α + β + α' microstructure. Baufeld *et al.* [116] report the presence of both martensitic and Widmanstätten microstructures in adjacent prior β grains as a result of an alternative ALM process, shaped metal deposition (SMD), of Ti-6Al-4V. From the observations made in this work (Figure 5.12) and the literature available, it is apparent that ALM deposition of Ti-6Al-4V is, at times, on the cusp of the boundary between diffusional and diffusionless transformations.

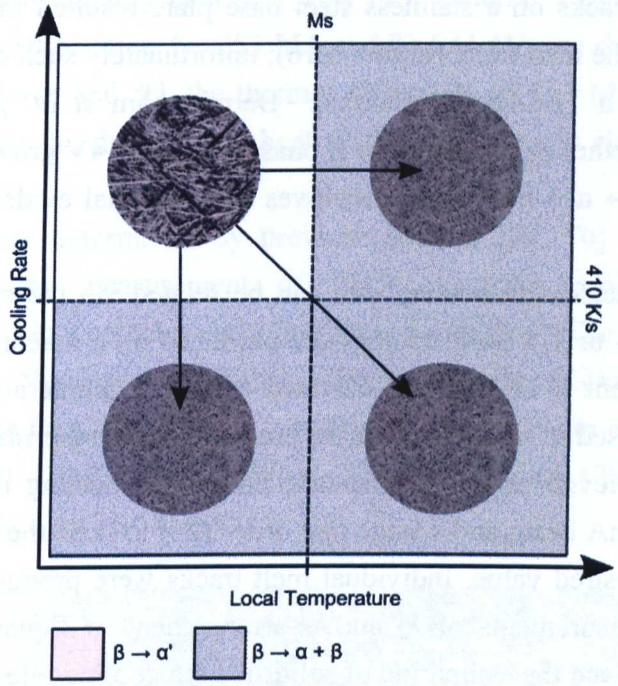

Figure 5.14 : Schematic of how changes in local temperature and cooling rate, due to thermal mass, results in diffusional or diffusionless transformation products. The critical cooling rate of 410 K/s is taken from the work by Ahmed and Rack [20].

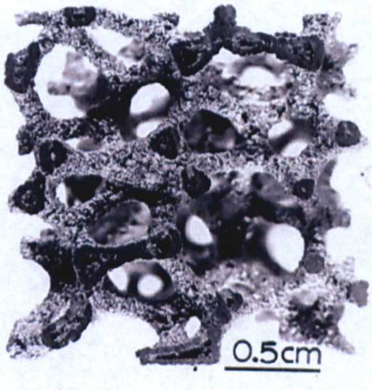

Figure 5.15 : Ti-6Al-4V EBM cellular foam structure with hollow cell ligaments resulting in rapid solidification and a martensitic microstructure [66].

5.2.4. EBM Cooling Rate

As mentioned in Section 2.7.11, earlier studies into the laser deposition of H13 tool steel and Ti-6Al-4V have determined cooling rates to be of the order of ~10^5 Ks^{-1} [69, 70]. Numerical calculations in this work, based on thermal gradient and solidification front velocity, have determined cooling rates under standard conditions to be between 7.6×10^4 and 1.3×10^5 Ks^{-1} for 6 mA and 12 mA beam currents, respectively. Direct measurement of cooling rate during EBM is difficult given the dynamic nature of the process and the powder bed environment. However, it was found that the production of individual melt tracks on a stainless steel base plate resulted in visible dendrites along the length of the melt track (Figure 5.16); unfortunately such dendrites were not visible when using a Ti-6Al-4V substrate. Bermingham *et al.* [117] state that it remains unclear whether or not the prior β phase in Ti-6Al-4V grows dendritically or forms cells; the β → α + β transition removes any potential evidence of a dendritic microstructure.

Microstructural scale and cooling rate can be related via the secondary dendrite arm spacing (SDAS or λ_2). Melt tracks were produced on a machined stainless steel base plate at ambient (~32 °C) and elevated (650 °C) temperatures; the elevated temperature being used to simulate standard process *build temperature*. Heating of the base plate was achieved using the standard base plate heating *theme*. This *theme* makes use of a 30 mA beam and a large *line order* (20) to raise the temperature of the base plate to the desired value. Individual melt tracks were produced using standard *hatch* settings. Measurements of λ_2 and re-arrangement of Equation (3.3), to give Equation (5.4), allowed the estimation of solidification cooling rate.

$$\dot{T} = \left(\frac{B}{\lambda_2} \right)^{\frac{1}{n}} \qquad (5.4)$$

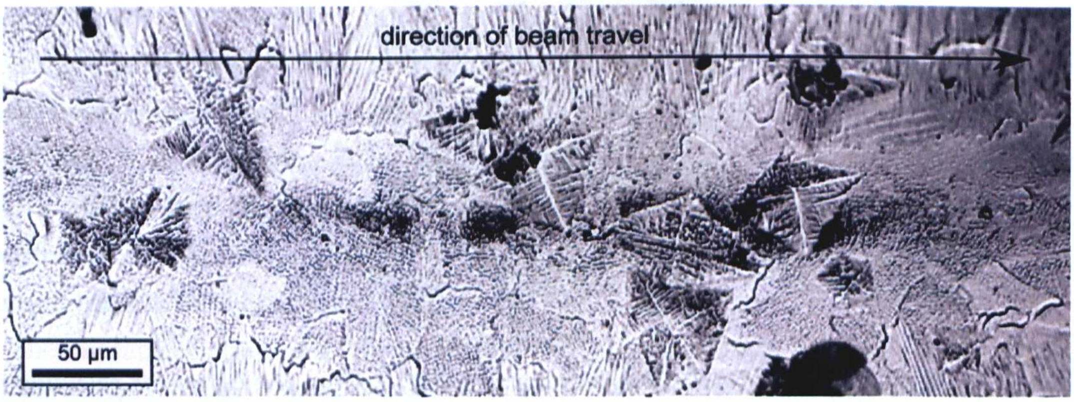

Figure 5.16 : Dendrites within a melt track on a SS base plate, at ambient temperature. Direction of beam motion is from left to right.

For a 440 stainless steel, values for material constants *B* and *n* are 60 and 0.41 respectively [90]; these values of *B* and *n* were used in this work. Measurement of λ_2, from dendrites such as those shown in Figure 5.17, result in a mean value of 1.62 ± 0.18 μm (95% CL) and a calculated cooling rate of ~10^3 Ks^{-1} at a temperature of 650 °C. This cooling rate is two orders of magnitude slower than those calculated from predicted solidification conditions. A contributing factor to this may arise because of the use of the stainless steel base plate rather than Ti-6Al-4V. Although Ti-6Al-4V is well known for having a relatively poor thermal conductivity, it is thermal diffusivity, α, which defines how rapidly heat will flow in a material. Comparison of JMatPro predicted thermal diffusivities, for 253 MA and Ti-6Al-4V, are shown in Figure 5.18. At temperatures above 380 °C, the thermal diffusivity of 253 MA is lower than Ti-6Al-4V and as such the diffusion of heat in the base plate is slower, resulting in a slower cooling rate.

The cooling rates determined by previous authors [69, 70] were performed at ambient temperature; measurement of EBM dendrites produced at ambient temperature resulted in a calculated cooling rate of ~10^4 Ks^{-1}. The measurement of λ_2, calculations in the Numerical Modelling Chapter and the microstructures given in Figure 5.12 indicate that, during EBM, cooling rates are well in excess of the highly referenced figure of 410 Ks^{-1}, suggested by Ahmed and Rack [20] to be the cooling rate required to form α' in Ti-6Al-4V.

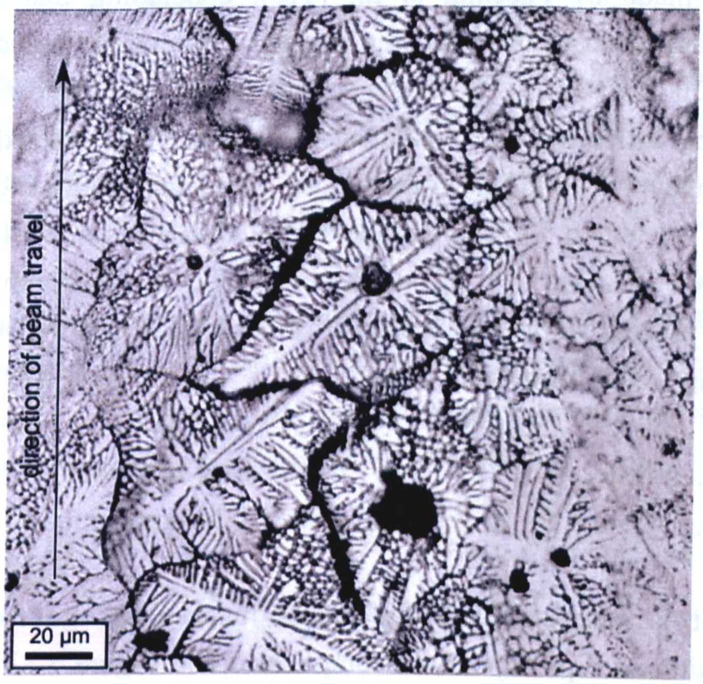

Figure 5.17 : Dendrites within a melt track on a stainless steel base plate, at 650 °C. Direction of beam motion is from bottom to top. Current = 6 mA, focus offset = 17 mA, speed = 0.188 ms-1 (speed function = 19).

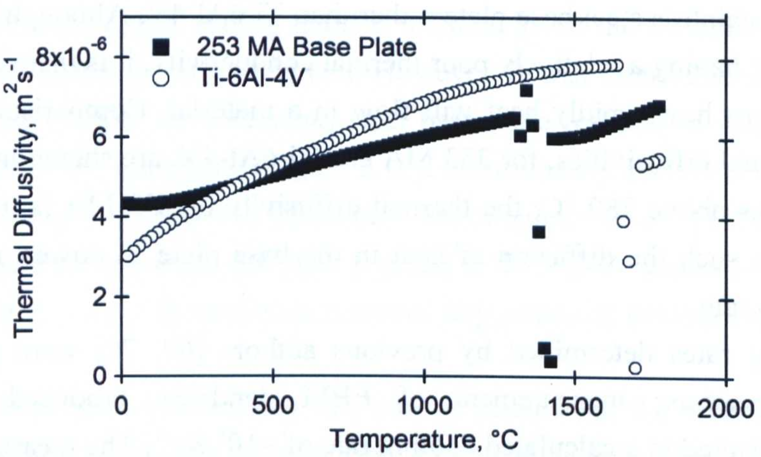

Figure 5.18 : Comparison between predicted thermal diffusivity of 253 MA base plate material with Ti-6Al-4V.

5.2.5. Decomposition of α'

The statement made by Facchini *et al.* [115], concluding that the EBM build temperature is sufficient to fully decompose any α' formed, is based upon the work carried out by Gil Mur *et al.* [118]. These authors investigated the decomposition of α' → α + β during tempering heat treatments, followed by a water quench, over the temperature range 400 – 800 °C. In their study, the degree of transformation from α' to α + β was related to Vickers hardness; full decomposition of martensite was reported to have occurred when hardness reached a maximum value. Such a decomposition process would mean that the solidification and transformation during EBM processing would follow the route:

1. powder → L → β → α' (melting, solidification and transformation)
2. α' → α + β (thermal decomposition)

However, it is suggested that the actual mechanisms governing the overall structural transition are perhaps more complicated and Figure 5.12 (a) demonstrates how it is possible to have martensitic microstructures, which remain in the final component when thermal mass is low. However, when α' is present, it has been observed at the top of a sample with an underlying α + β microstructure. This underlying microstructure is thought to arise from thermal decomposition by the combined effects of the *build temperature* and thermal cycling, rather than the *build temperature* alone. When thermal mass is high, solidification and transformation are thought to follow the route:

3. powder → L → β → α + β (melting, solidification and transformation)

The effect of elevated temperature on martensite is therefore of interest because of the range of microstructures presented in Figure 5.12 and because of its role in determining the overall mechanism of microstructural formation. The key question therefore is whether or not the *build temperature* is capable of decomposing a metastable, fully martensitic microstructure to form one which is at equilibrium.

In order to determine the effect of isothermal exposure on martensitic structures, several heat treatments were carried out. As mentioned, the investigation carried out by Gil Mur *et al.* [118] related the degree of martensitic decomposition to Vickers hardness; the authors reported that full decomposition (maximum hardness) could be achieved by a heat treatment at 700 °C. Their results have been reproduced in Figure 5.19. Based on these findings, it may be concluded that any martensite formed during EBM may be thermally decomposed to form an α + β microstructure at temperatures ≥ 700 °C.

The typical *build temperature* during EBM is 650 °C; this temperature was not investigated by Gil Mur *et al.* [118] and so it was decided to determine whether or not full decomposition was possible at this temperature and how long was required for the α' → α + β transformation to plateau, as per Figure 5.19. Fully martensitic microstructures (generated by holding EBM material at 1030 °C for 30 minutes followed by a water quench) were tempered at 650 °C for times between 60 and 1050 minutes in an argon atmosphere, followed by a water quench to arrest transformation. Optical micrographs of the martensitic and tempered microstructures can be seen in Figure 5.20; arrowheads indicate regions of transformed α.

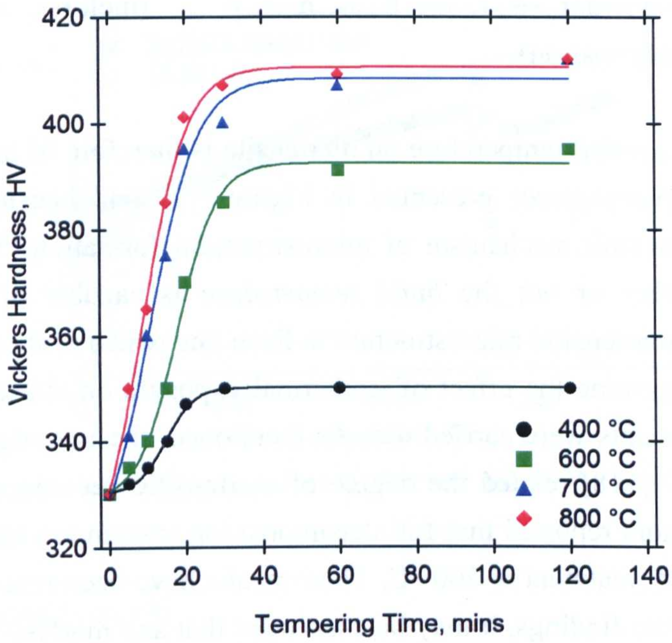

Figure 5.19 : Vickers hardness versus tempering time at four tempering temperatures, adapted from [118].

Figure 5.20 (b) – (e) show the volume fraction (V_f) of transformed α increasing with longer tempering times, as expected. However, even after prolonged heat treatment (1050 minutes), a fully transformed microstructure was not observed. With some exceptions, the figures indicate that the α laths formed appear to lie along previous martensitic lath boundaries. A grid, overlaid onto micrographs in the different conditions of heat treatment, was used to determine $V_f\,\alpha$. Volume fraction of transformed α is plotted in Figure 5.21 (a), along with a curve derived from JMAK analysis.

As previously mentioned, by plotting $\ln\left[\ln\left(\frac{1}{1-X(t)}\right)\right]$ versus $\ln t$ (Figure 5.21 (b)) values of n (the JMAK exponent) and K (a material constant) can be determined and were found to be $K = 0.021$ and $n = 0.32$. The volume fraction of α phase, as a result of tempering Ti-6Al-4V martensite at 650 °C, can thus be described by Equation (5.5).

$$V_f(\alpha) = 1 - \exp\left(-0.021t^{0.32}\right) \qquad (5.5)$$

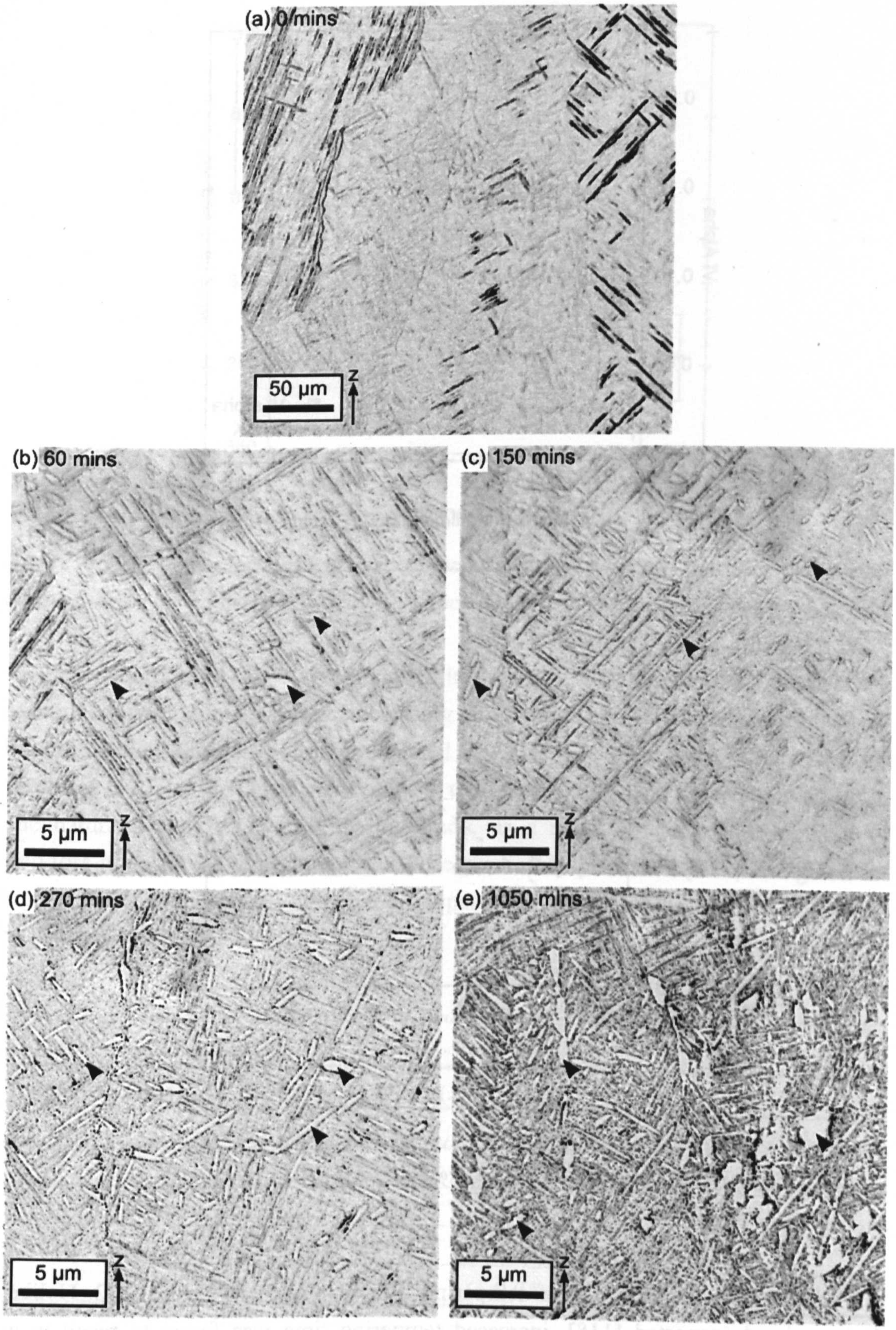

Figure 5.20 : Optical micrographs of fully α' microstructures, as in (a), tempered at 650 °C for (b) 60 minutes, (c) 150 minutes, (d) 270 minutes and (e) 1050 minutes, followed by a water quench. Arrowheads identify regions of transformed α.

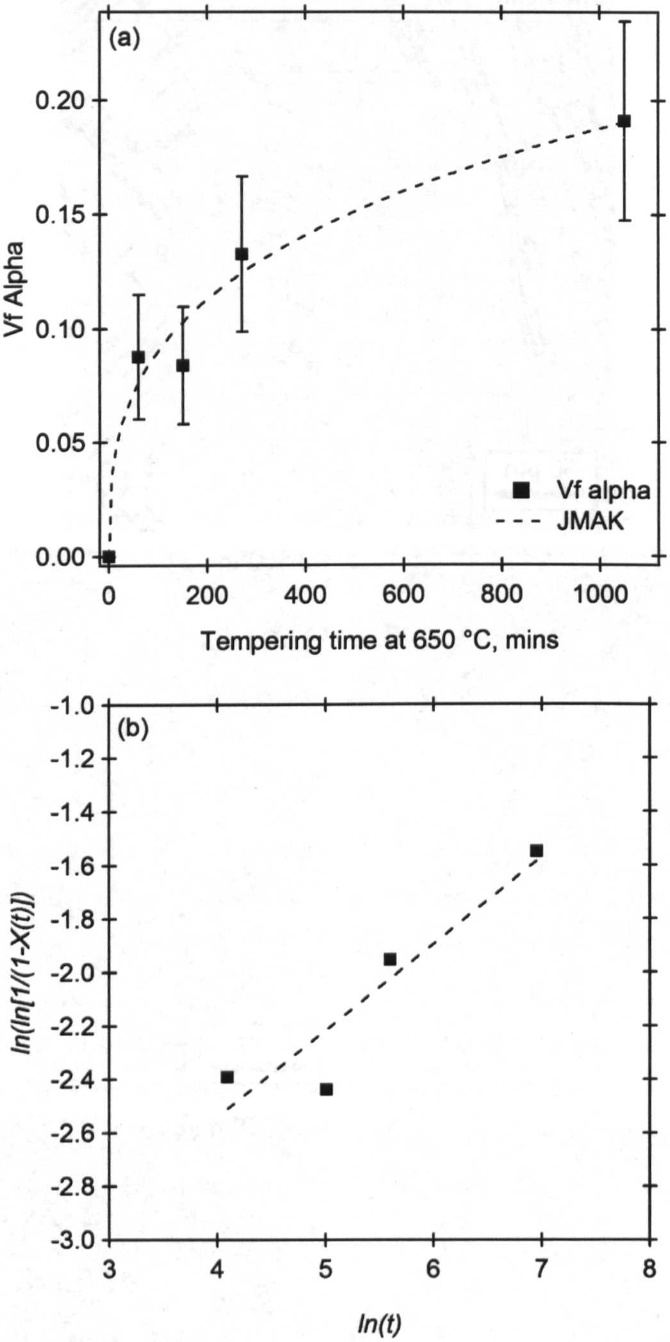

Figure 5.21 : (a) Tempering time at 650 °C versus volume fraction of alpha for tempered martensitic samples. Error bars represent ± 95% CL. (b) A plot of ln[ln(1/1-X(t))] versus ln(t) to determine n and K. .

Vickers micro-hardness versus tempering time is plotted in Figure 5.22. Unlike that previously reported [118], increased tempering time was found to result in a modest decrease in hardness. Whilst Gil Mur *et al.* [118] reported a 60 HV increase after tempering α' at 600 °C for 120 minutes, in this work a drop of 24 HV was observed after 1050 minutes at 650 °C.

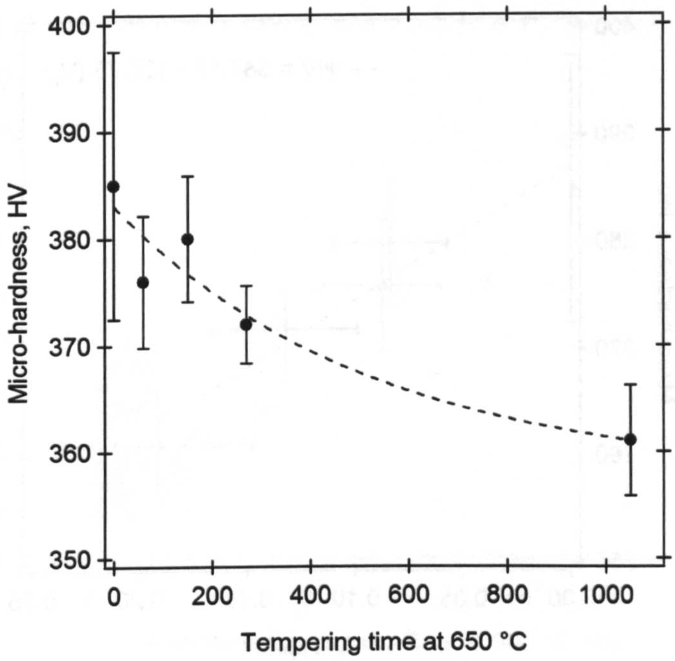

Figure 5.22 : Vickers micro-hardness versus tempering time for tempered martensitic samples. Error bars represent ± 95% CL. Dashed line is used only as a guide for the eye.

Vickers hardness against $V_f\,\alpha$ is plotted in Figure 5.23 and highlights the reduction in hardness with increasing $V_f\,\alpha$ (increasing tempering time). The results presented in Figure 5.21 - Figure 5.23 are summarised in Table 5.3; even after prolonged heat treatment (17.5 hours) decomposition of α' to α is only 19 ± 4 % complete at 650 °C. The hardness results obtained in this study, as a result of martensite tempering, therefore are a direct contradiction to those previously published [118] and given in Figure 5.19. To understand why this discrepancy exists, the decomposition of α' will be discussed in further detail.

Table 5.3 : Summary of volume fraction and hardness results for tempered martensite samples.

Tempering Time (650 °C), mins	$V_f\,\alpha$ (± 95% CL)	HV (± 95% CL)
0	0	385 (± 12.5)
60	0.088 (± 0.03)	376 (± 6.18)
150	0.084 (± 0.03)	380 (± 5.88)
270	0.13 (± 0.03)	372 (± 3.63)
1050	0.19 (± 0.04)	361 (± 5.22)

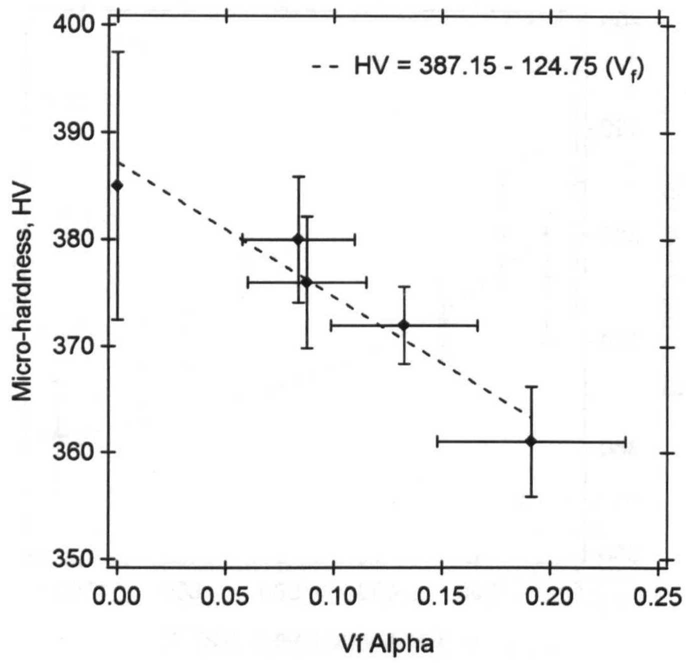

Figure 5.23 : Vickers hardness versus volume fraction alpha for tempered martensitic samples. Error bars represent ± 95% CL.

Welsch *et al.* [10] discuss the microstructure of fusion zones in welding processes with high cooling rates, including electron beam welding. Martensite formed in the fusion zone is said to have high strength and hardness as a result of its fine acicular morphology [7, 10]. This supports the results of the previous two figures in which martensite exhibits a high hardness.

Further investigation into the hardness of a martensitic microstructure, relative to that of a transformed microstructure, has been determined by performing a modified Jominy end quench. In this experiment, an instrumented Jominy sample was water quenched from 1030 °C, as described in the Experimental Section. The micro-hardness results as a function of instantaneous cooling rate at 900 °C are presented in Figure 5.24. The data shows a relatively large amount of scatter, such scatter has also been reported by Davies [93] for the same experiment performed on near-α alloy Timetal® 834. However, the results indicate that there is a general decrease in hardness with decreasing cooling rate; the highest hardness values occur when a martensitic structure is present.

Welsch *et al.* [10] describe two types of heat treatments applied to fusion welds with a martensitic microstructure, both of which are performed to stress relieve the fusion zone and surrounding material. The two treatments are described as:

(i) Relatively low temperature heat treatments at 450 – 600 °C.

(ii) Higher temperature heat treatments > 600 °C.

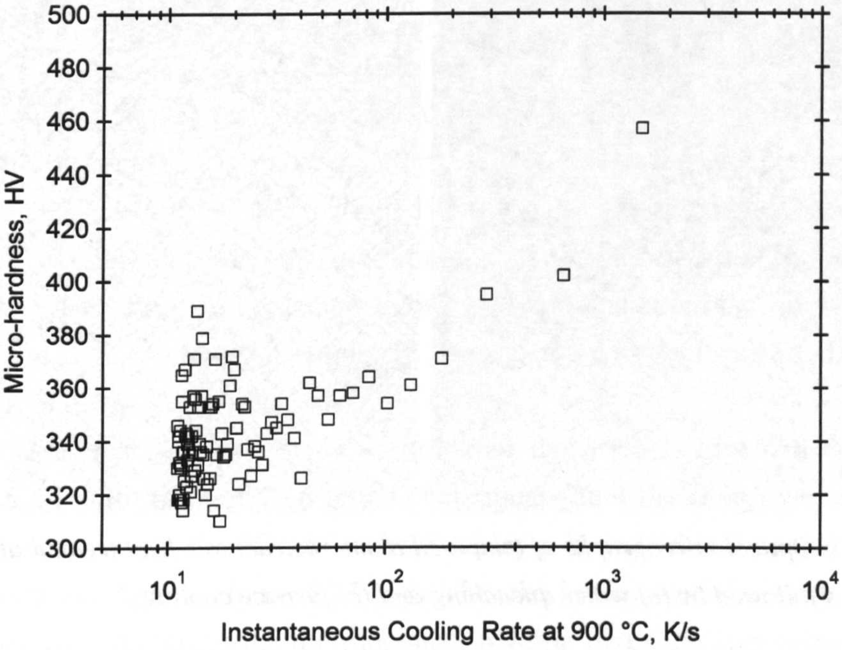

Figure 5.24 : Micro-hardness results as a function of instantaneous cooling rates at 900 °C for a Ti-6Al-4V Jominy end quench sample.

The purpose of both types of post-weld treatment is stress relief; however, microstructural changes also result. Low temperature heat treatments, as in (i), age the martensitic microstructure and can increase strength, whilst decreasing ductility and toughness. Higher temperature heat treatments, as in (ii), results in the formation and coarsening of α; this causes softening and an increase in ductility and toughness. The trends observed in Figure 5.21 - Figure 5.23 are therefore believed to be analogous to the softening process resulting from higher temperature heat treatment of martensitic structures. Lutjering and Williams [6] also comment that the transformation of martensitic microstructures to fine, lamellar α + β results from annealing in the 700 – 850 °C temperature range.

It has been demonstrated that prolonged heat treatment at 650 °C, followed by a water quench, does not fully decompose a martensitic microstructure. However, components produced by EBM are cooled slowly to room temperature with cooling rates more akin to a furnace cool. As such, continued transformation during cooling may occur; Figure 5.25 shows the result of tempering a fully martensitic microstructure at 650 °C for 1050 minutes followed by (a) a water quench and (b) a furnace cool.

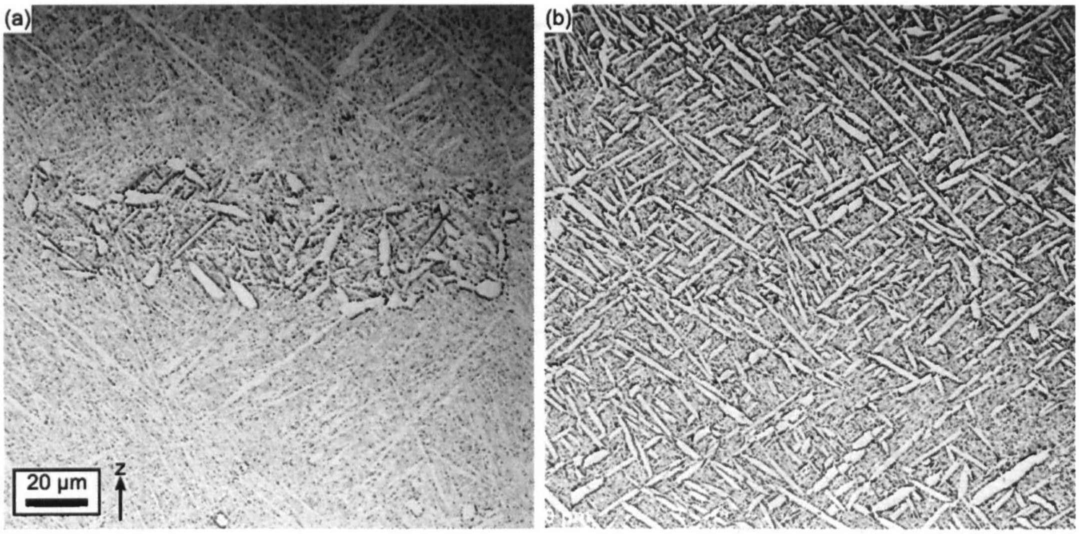

Figure 5.25 : Optical micrographs of tempered α' microstructures heat treated at 650 °C for 1050 minutes followed by (a) water quenching and (b) furnace cooling.

It is clear from these micrographs that furnace cooling from 650 °C has a notable effect on the volume fraction of transformed α present in the structure; the water quenched sample contains a V_f of 19 ± 4 % α whilst this value increases to 41 ± 5 % α after furnace cooling.

The preceding discussion therefore establishes that isothermal tempering of fully martensitic Ti-6Al-4V, at 650 °C for times ≤ 17.5 hours, has been found to result in incomplete decomposition of α' → α + β. In samples where martensite has been observed in the uppermost layer, the underlying bulk α + β microstructure cannot be attributed solely to the *build temperature*; another source of thermal energy is therefore required for full decomposition to occur. It is proposed that a combination of the *build temperature* and the superimposed thermal cycling, as discussed in the previous chapter, result in the full decomposition of α'.

5.2.6. The Effect of Z-Position on Microstructure

In all layer-based manufacturing methods, two types of thermal history can be described. The first is the thermal history of the component as a whole; in EBM this can be thought of as the *build temperature*. The second thermal history is that of an individual layer; in a component made from 100 layers there are 100 unique thermal histories. EBM is currently considered to be one of the few ALM processes capable of economically producing bulk components and this is largely a result of the relatively high deposition rates achieved by this method (up to 60 cm^3/hour) against competing laser systems (~11 cm^3/hour [119]). Even so, for components that have a large *z*-dimension, approaching the full height (350 mm) of the build chamber, the difference in time at temperature between the first and last layer may be measured in tens of hours.

To investigate the potential microstructural effect of very different thermal histories within a single component, a 330 mm tall sample was produced and is shown in Figure 5.26. The sample was supplied courtesy of Dr Michael Blackmore who produced the geometry and measured the distance between the flat surfaces to determine whether or not component accuracy is maintained over the full height of the build chamber. Once this was completed, the sample was sectioned to perform the microstructural analysis reported here.

The thermocouple reading for the duration of the *build* is given in Figure 5.27, showing a total build time of 76.6 hours. This means that the first layer spends 76.6 hours at temperatures ≥ 275 °C whilst the final layer is melted and cooled directly to room temperature. Again, Figure 5.27 highlights the issue associated with using only one thermocouple. Although the thermocouple reading gives the approximate thermal history of the first layers of deposited material, the size of the sample means that the temperature of the powder bed during deposition of layers far from the thermocouple is unknown.

The lack of a temperature recording system at the surface of the powder bed represents a significant weakness in the EBM process, especially as the thermocouple reading is, for small samples, used by the operator to control *build temperature* by changing *theme* parameters when necessary. Figure 3.11 in the Experimental Chapter shows the thermal history of a 10 mm tall sample in which a constant temperature of ~ 675 °C was maintained. As sample size increases, maintaining a constant thermocouple reading physically means increasing the temperature at the deposition surface. For tall samples, the thermocouple reading gives no information to the operator regarding the temperature at the deposition surface and the *build* cannot be controlled on this basis. The user has no option but to let the machine run – from a process control perspective the author believes that this ambiguity is an area that requires improvement. A significant enhancement to the current system would be the ability to record temperature at or near to the powder bed surface by making use of more thermocouples and/or a thermal imaging/pyrometer system.

Although to the user of the EBM system, the temperature at the top surface is unknown, the EBM software attempts to maintain a constant deposition temperature by making use of the *Auto Power Calc* function, described previously. Based on this calculation, a beam current required to maintain a constant surface temperature is calculated. However, the effectiveness of the *Auto Power Calc* is yet to be determined.

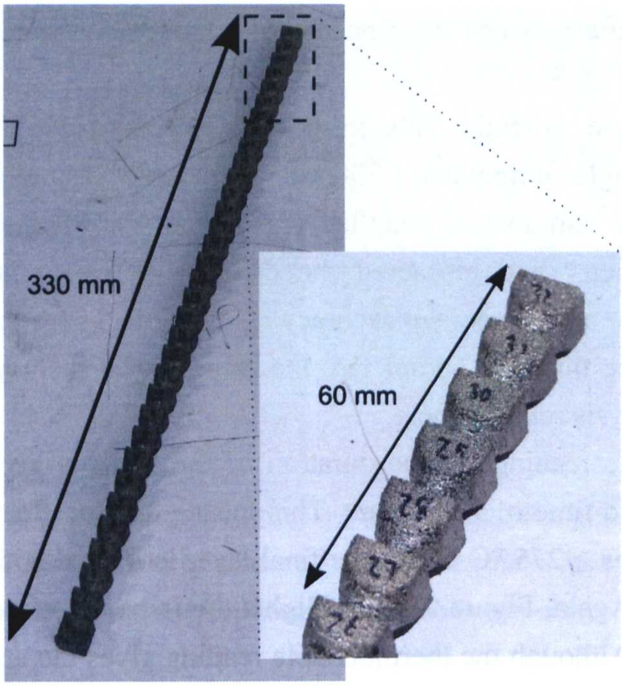

Figure 5.26 : 330 mm tall sample used to determine microstructure as a function of height.

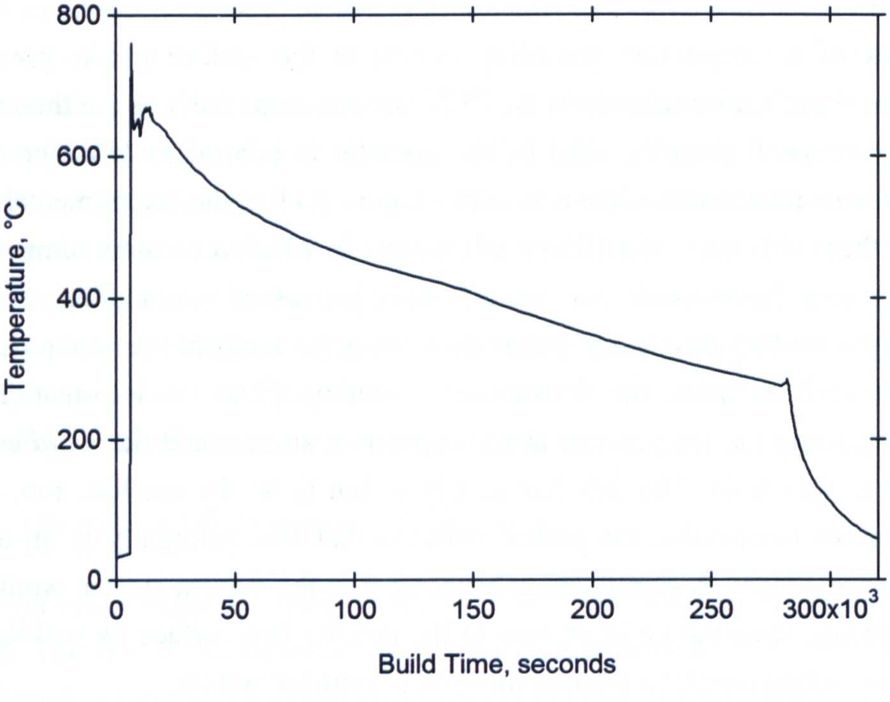

Figure 5.27 : Thermocouple reading for the 330 mm tall sample shown in Figure 5.26 with build time given in thousands of seconds.

Hence, the experimental results discussed shortly will provide an insight into the effectiveness of the *Auto Power Calc* and the effect, if any, of the vastly different thermal histories. The component shown in Figure 5.26 is made up of connected 10 mm tall blocks; these blocks were labelled 0 to 32 with increasing *z*-height. Samples were taken at 70 mm intervals and prepared for metallographic analysis. In typical quantitative metallography, grain size analysis is performed using the line intercept method in which the numbers of grain boundaries, crossing a line of known length, are counted. However, in the lamellar microstructures observed in EBM material, the linear intercept method is influenced by the orientation of the α laths relative to the traverse line.

Searles *et al.* [120] developed an automated method to determine α lath width by rotating a line grid over a threshold image. The α laths in the threshold image were subtracted from the line grid to leave segmented lines. A new grid was then rotated and the process repeated until the grid had been rotated by 360°; average thickness was calculated from all of the segmented line grids. Brooks *et al.* [121] Also used image manipulation to threshold micrographs, followed by software measurements, to determine α phase spherodisation in Ti-6Al-4V.

In this work, the linear intercept method was used, as well as direct measurements of α lath width. Traverse lines on micrographs were drawn perpendicular to the *z*-axis for the linear intercept method. Direct measurement of α lath width involved measuring the distance perpendicular to the long axis of the laths. When the microstructure consisted of α colonies, many α lath widths could be measured simultaneously. This direct measurement method has been used previously by Chen *et al.* [122].

Optical micrographs of the microstructures taken at 70 mm intervals are shown in Figure 5.28. At all locations, the microstructure consists of the typical bulk Widmanstätten/colony α + β and α_{GB} structure. Results of Vickers hardness and α lath width measurement, versus location, are given in Figure 5.29 (a) and (b) respectively.

The variation in hardness along the sample is relatively small with an average hardness range of 14.9 HV. Alpha lath widths, determined by direct measurement, vary between 1.73 μm and 3.04 μm. The linear intercept method was found to overestimate the lath width by an average of 31 % because of the influence of lath orientation relative to the traverse lines.

Although microstructural scale is a known indicator of cooling rate [17], the α lath widths shown in Figure 5.29 (b) are a combination of cooling rate at the time of deposition and any microstructural coarsening occurring as a result of holding at the *build temperature*. As such the α lath width cannot be used to interpret cooling rates at the different locations. What is clear from Figure 5.29 is that there is some microstructural variability along the length of the sample.

Using the approximate relationship between Vickers hardness and yield strength, given in Equation (5.6); Murr *et al.* [79] have determined the yield strength of EBM Ti-6Al-4V based on hardness results. In doing so here, it is predicted that, within the

330 mm tall sample there is a potential yield strength variation of approximately 50 MPa. This value represents a 4.2 % decrease in strength when compared to the strongest (hardest) region.

$$YS \approx HV \times \left(\frac{10}{3}\right) \tag{5.6}$$

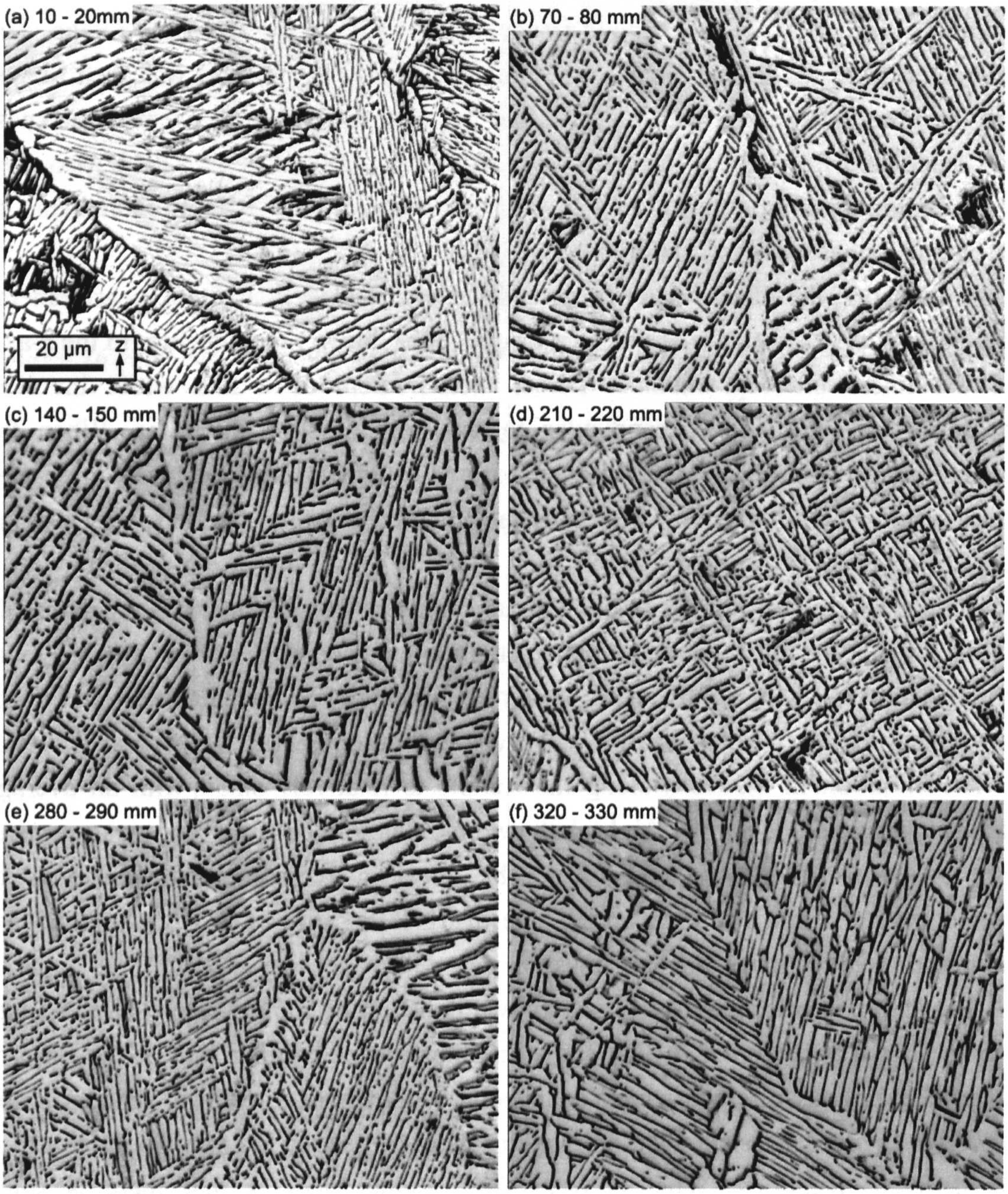

Figure 5.28 : Optical micrographs taken at intervals along a 330 mm tall sample.

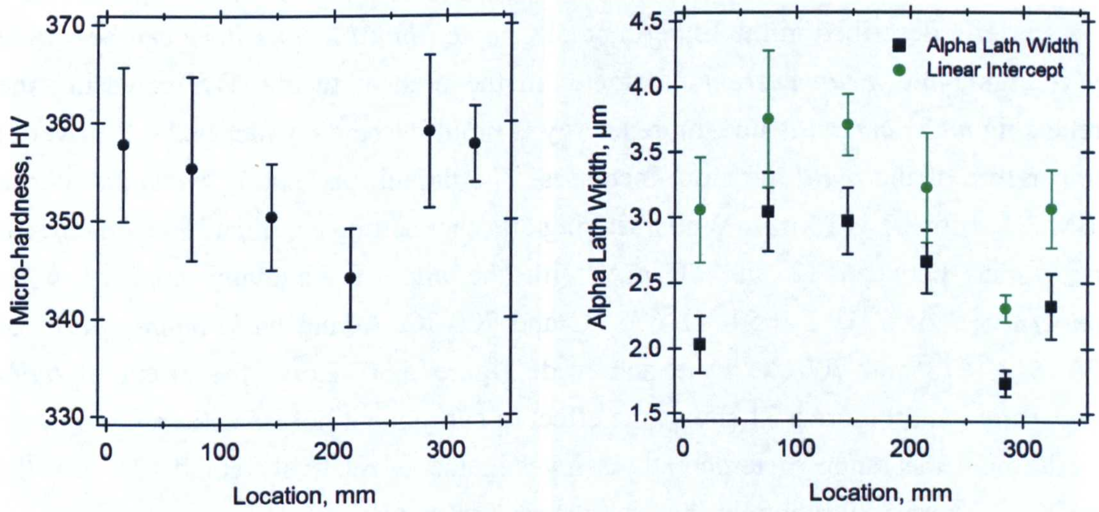

(a) *(b)*

Figure 5.29 : (a) Sample location versus Vickers hardness and (b) sample location versus alpha lath width for the 330 mm tall sample. Error bars represent ± 95% CL.

The results in Figure 5.29 indicate that:

- Microstructural scale may show a modest variation along the *z*-dimension of a component. In this case, the cross sectional area of the sample was relatively constant. However, some geometries may have large changes in cross sectional area, in such circumstances microstructural heterogeneity may be more pronounced from a combination of different solidification cooling rates and layer-based thermal histories.
- The same comment applies to mechanical properties, governed by the microstructural scale. This raises and interesting point regarding the characterisation of EBM mechanical properties. Generally, samples made directly on the base plate are tested. A study of the variation in mechanical properties as a function of *z*-position would be an interesting area of further work.

5.2.7. The Effect of Build Temperature on Microstructure

The previous section has demonstrated that, for tall samples, physical control of *build temperature* is all but impossible using the current EBM system. However, for small samples, it is possible to maintain a constant thermocouple reading for the entire build. This section will discuss the effect of changing this *build temperature* on microstructure and mechanical properties. The effect of a hot isostatic pressing treatment on the samples produced at the different build temperatures will also be investigated.

As briefly described in the Experimental Chapter, *build temperature* can be varied by changing the *mean current* parameter in the preheat theme. By increasing the preheating *mean current* value, more energy is input into the powder bed – the overall temperature of the *build* therefore increases. The default preheating *mean current* in EBM 3.1 software is 15 mA. Whilst leaving all other settings at default, *mean current* was varied between 12 and 20 mA with the aim of achieving nominal *build temperatures* of 625 °C, 650 °C, 675 °C and 700 °C. Actual *build temperatures* of 626, 644, 678 and 700 °C were achieved. Figure 5.30 shows the effect of *build temperature* and Figure 5.31 shows the effect of subsequent hot isostatic pressing.

Although the range of temperatures investigated is relatively small (74 °C), the results in Figure 5.30 highlight that there is microstructural sensitivity over this range. At build temperatures ≤ 678 °C, microstructures are similar. However, at a *build temperature* of 700 °C, a significantly coarser microstructure is observed as per Figure 5.30 (d).

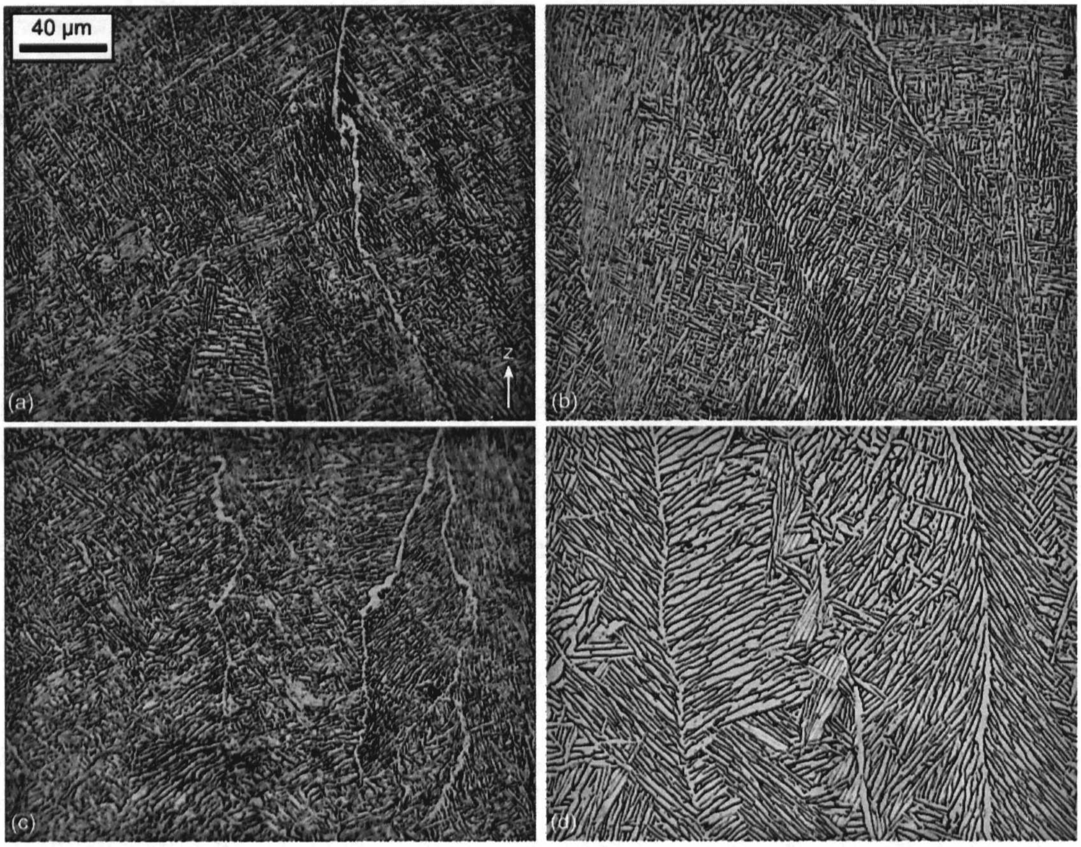

Figure 5.30 : The influence of build temperature on microstructure. Build temperatures of (a) 626 °C, (b) 644 °C, (c) 678 °C and (d) 700 °C.

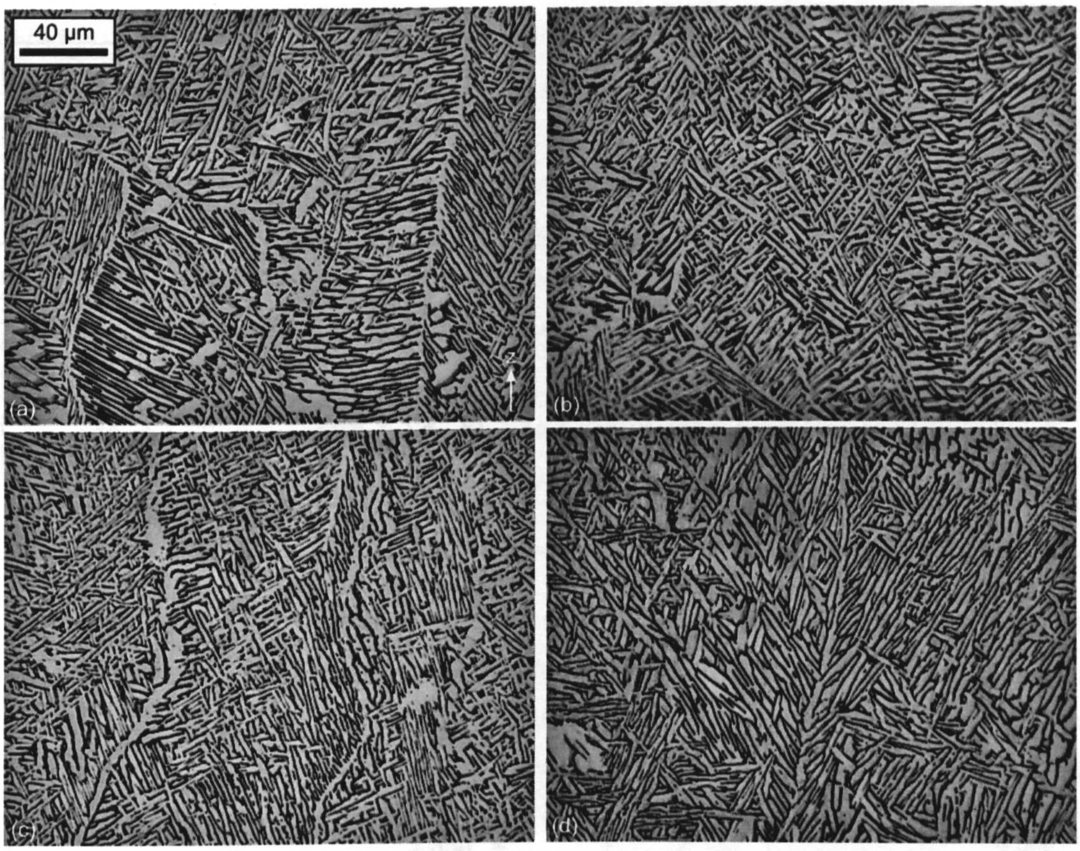

Figure 5.31 : The influence of a HIP cycle on samples produced at bed temperatures of (a) 626 °C, (b) 644 °C, (c) 678 °C and (d) 700 °C. HIP performed at Bodycote, Chesterfield, UK.

Components made by casting and powder metallurgy are often subjected to a HIP treatment in order to eliminate porosity that is deleterious to mechanical performance. The effect of a 2 hour HIP treatment at a temperature of 920 °C, pressure of 100 MPa and cooled at 6 ± 2 Kmin^{-1} is shown in Figure 5.31. Regardless of *build temperature*, the post-HIP microstructures are similar. The HIP process is observed to homogenise the microstructure whereby all samples, regardless of starting microstructure, coarsen to approximately the same level.

Quantitative analyses of the microstructures in Figure 5.30 and Figure 5.31 are presented in Figure 5.32. Alpha lath width and α_{GB} thickness are plotted against *build temperature* in Figure 5.32 (a) and (b). In the as-built condition, both α lath width and α_{GB} thickness are almost constant between 626 °C and 678 °C. At a *build temperature* of 700 °C an increase in both of these features occurs; as-built α lath width is approximately 1 µm coarser and α_{GB} thickness is approximately 2 µm coarser than the lower *build temperature* samples.

As expected, and confirmed in Figure 5.32 (c), the increased microstructural scale results in a reduction in mechanical properties. A 5% reduction in yield strength is observed as a result of higher temperature processing, there are also reductions in UTS and elongation which are documented in Table 5.4.

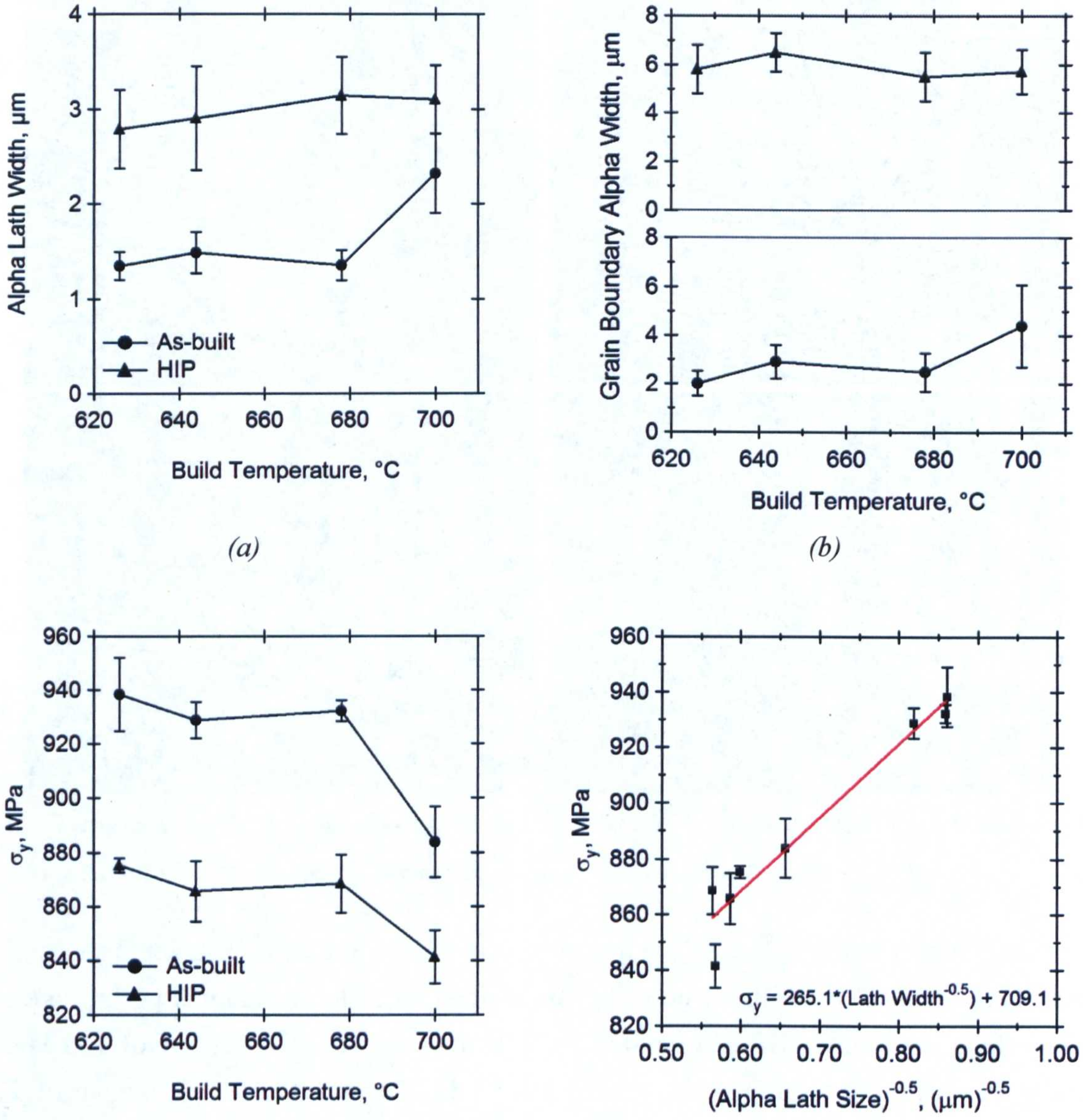

(a) *(b)*

(c) *(d)*

Figure 5.32 : The effect of build temperature on (a) α lath width, (b) α_{GB} width, (c) yield strength and (d) variation of yield strength with inverse square root of α lath size. Error bars represent 95%CL.

Table 5.4 : Tensile strength and elongation of as-built and heat treated samples.

Build Temperature, °C	Condition	Tensile Strength (± 95%CL), MPa	Elongation (± 95%CL), %
700	As-built	993.9 (± 5.6)	13.6 (± 0.9)
678	As-built	1031.9 (± 2.6)	11.6 (± 1.5)
644	As-built	1028.9 (± 4.3)	13.0 (± 0.7)
626	As-built	1029.1 (± 14.9)	13.2 (± 0.4)
700	HIP	938.8 (± 7.1)	13.6 (± 1.3)
678	HIP	974.2 (± 10.8)	13.4 (± 1.7)
644	HIP	969.2 (± 8.0)	14.0 (± 1.6)
626	HIP	977.6 (± 3.0)	13.6 (± 0.5)

Figure 5.32 (a) and (b) also confirm, quantitatively, what is evident from the micrographs in Figure 5.31. Post-HIP, the scale of the microstructure is almost identical, regardless of the initial starting microstructure. This microstructural coarsening results in a reduction in both yield and tensile strength but causes a slight increase in elongation. The same trend has been reported by Facchini *et al.* [115] who also observe an increase in fatigue performance as a result of a HIP treatment.

Although microstructures of the HIP samples are very similar, the trend in mechanical properties observed in the as-built samples remains. Samples built at 700 °C and then HIPed have the lowest yield strength. However, the average difference between the yield strength of the 700 °C sample and the other build temperatures drops from 5 % to 3 % in the HIP condition.

Yield strength is plotted against the inverse square root of α lath size in Figure 5.32 (d). The data tends to fit well with the linear trend line, having a correlation coefficient of 0.97. Sen *et al.* [29] performed the same analysis when investigating the effect of the addition of boron, used to refine microstructure, in Ti-6Al-4V. As reported here, the authors found a good correlation between yield strength and the inverse square root of α lath size. The correlation was attributed to microstructural refinement (decreasing α lath width) causing a reduction in the effective slip length.

Although α lath width shows a good correlation with yield strength, Lütjering [17] comments that the most important microstructural parameter influencing mechanical properties of fully lamellar microstructures is the α colony size. Colony scale factor measurements were made (using the method described in Section 3.4.3) on the material shown in Figure 5.30 and Figure 5.31. The results of these measurements are presented in Figure 5.33 for which the correlation coefficient of the best-fit line is 0.90. Although lath width is a good indicator of slip length, the true slip length is governed by colony size. The plot of colony scale factor is thus a better way of presenting the mechanical property data.

The trends in yield strength observed in Figure 5.32 are also generally applicable to the colony scale factor, namely:

- In the as-built condition, α colony scale factor is significantly larger at a *build temperature* of 700 °C.
- The HIP treatment homogenises the α colony scale factor to the same level regardless of the starting structure.
- Yield strength is inversely proportional to the α colony scale factor (increasing slip length, see Figure 5.10).

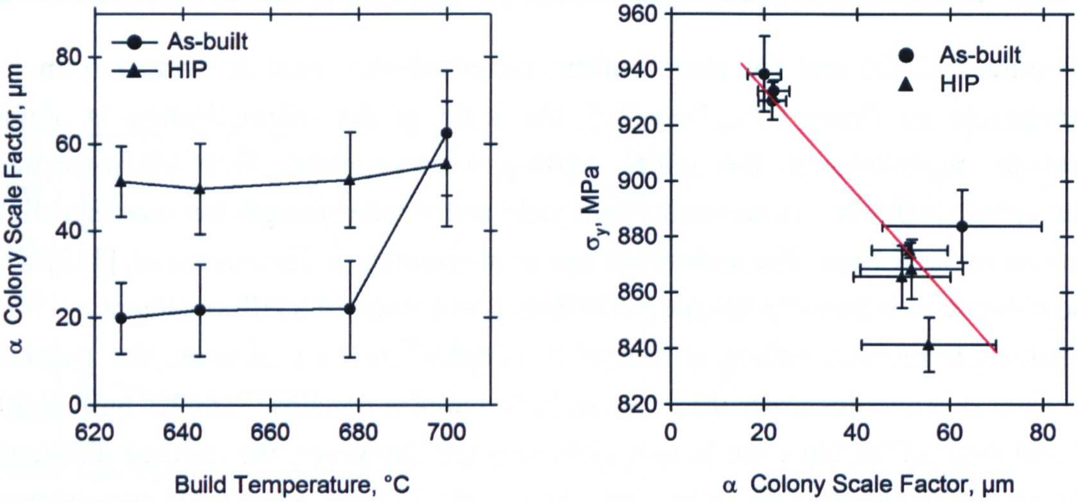

(a) *(b)*

Figure 5.33 : Alpha colony scale factor plotted against (a) build temperature and (b) yield strength, for material shown in Figure 5.30 and Figure 5.31.Error bars represent 95% CL.

Up to this point, discussions of mechanical strength have been based solely upon microstructural observations. A further variable that has been investigated is chemical composition, owing to the observations of Cormier *et al.* [59] in which some elemental vaporisation occurred in the high temperature vacuum process. As *build temperature* increases, the likelihood of the temperature rise (caused by the electron beam during melting) volatilising some of the alloying may lead to changes in chemistry and hence properties. To investigate whether this was so, bulk chemical analysis was performed on the entire group of samples.

Chemical analysis was performed at London Scandinavian Metallurgical Co. Ltd, Fullerton Road, Rotherham, UK. Samples were tested to determine oxygen (by Leco analysis), aluminium and vanadium contents (by x-ray fluorescence). The results are presented in Table 5.5.

Table 5.5 : Aluminium, vanadium and oxygen content of samples tested in the as-built and HIP conditions.

Build Temperature, °C	Condition	Al, wt%	V, wt%	O, wt%
700	As-built	5.74	4.20	0.228
678	As-built	5.86	4.19	0.233
644	As-built	5.73	4.11	0.246
626	As-built	5.89	4.20	0.243
700	HIP	5.82	4.25	0.222
678	HIP	5.72	4.31	0.218
644	HIP	5.61	4.13	0.239
626	HIP	5.64	4.13	0.237

In Figure 5.34, plots of the results from the above table, against yield strength, are given; no clear correlation between Al, V or O content and yield strength are apparent over the tested range. Bulk chemical differences between samples can therefore be dismissed as a having an effect on yield strength in this case.

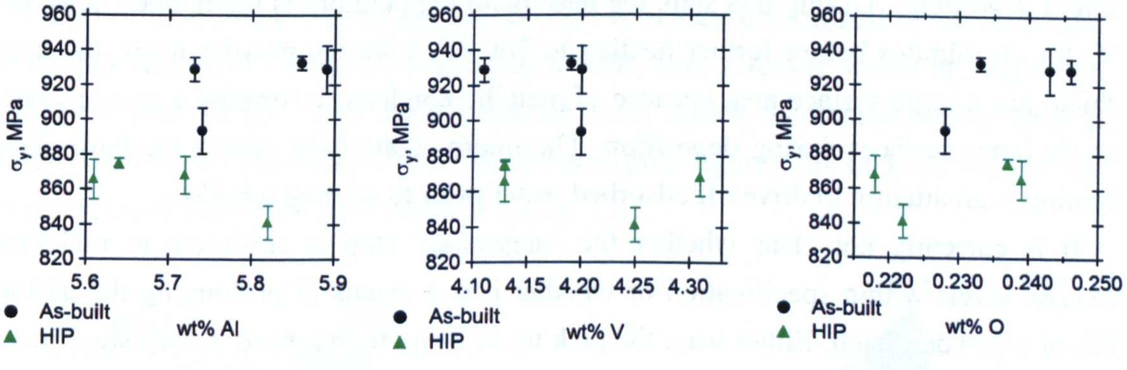

(a) *(b)* *(c)*

Figure 5.34 : Yield strength versus (a) wt% Al, (b) wt% V and (c) wt% O for as-built and HIP samples.

However, a significant problem encountered by additive manufacturing, especially when using titanium alloys, is evident in Table 5.5 and Figure 5.34 (c). Over time, there is potential for the feedstock powder to change chemistry, specifically oxygen content. Whilst virgin powder meets the specification of Ti-6Al-4V Grade 5 material, with an oxygen content of < 0.20 wt%, the oxygen content of the material analysed in Figure 5.34 is above this limit. Standard EBM practice is to use recycled powder; the exact number of times the powder used to make the tensile specimens here was not documented but, it was well in excess of twenty times.

It is clear from Table 5.5 that during a usage cycle (as described in Section 3.1.4), powder picks up oxygen. Titanium's affinity for oxygen is well known and during arc melting described later in this work (Chapter 6), titanium was used as an oxygen getter for this very reason. The reaction between oxygen and titanium is increasingly rapid with increasing temperature. Donachie [7] states that at temperatures above 427 °C, atmospheric protection must be provided to avoid the pick up of oxygen and nitrogen.

During the whole EBM process cycle, including recycling, powder only reaches high temperature (>> 427 °C) whilst inside the evacuated vacuum chamber. Potential sources for the pick up of oxygen are therefore: (i) air leaks or (ii) moisture within the chamber. The pressure within the vacuum chamber is maintained at controlled vacuum of 2×10^{-3} mbar (5×10^{-6} mbar vacuum + high purity He) and thus the pickup of oxygen from the vacuum environment seems unlikely.

The most likely source of oxygen during the EBM process is therefore from the adsorption of water onto internal surfaces of the vacuum chamber and the powder itself. Whilst no experiments have been carried out, discussions with Arcam and a recent software update points towards this conclusion. EBM control software version 3.2.27 now incorporates a step, during the heating of the base plate, designated '*heat shield degassing*'. During this step, the base plate temperature is maintained at ~ 400 °C for 20 minutes before further heating to 760 °C. Like the powder itself, the heat shield has a large surface area because of metallic condensate forming a porous layer on its inner surfaces during deposition. The intermediate hold during the base plate heating is an attempt to drive off adsorbed water prior to starting a build.

It is currently not clear whether the '*degassing*' step is sufficient to maintain oxygen levels within specification or whether it is a means of prolonging the usable life of a powder batch. Either way, the pick up of oxygen represents a very significant processing consideration; powder chemistry needs to be frequently monitored to ensure it is within specification. Scheduled monitoring and limited powder life adds cost to the process. This cost is further increased if it is not acceptable to mix powder batches in order to dilute the oxygen concentration.

5.2.8. Summary

Prior to considering the texture of EBM material, a brief summary will be made of the microstructural characteristics discussed so far:

- Generally two, but sometimes three microstructural regions may be observed in a Ti-6Al-4V EBM sample. These are (i) a beta stabilised, stainless steel contaminated layer of the order of 800 μm thick, (ii) a bulk transformed

Widmanstätten/colony α + β microstructure and (iii) a martensitic region at the top of small EBM samples < 10 mm in height.

- Microstructural scale (α lath width) shows a modest variation in samples that span the full height of the build chamber. This highlights the potential for mechanical property variation with *z*-position.
- Components produced at *build temperatures* between 626 °C and 678 °C can be considered almost identical from a microstructural and mechanical property perspective. However, a *build temperature* of 700 °C results in a significant increase in microstructural scale in terms of both α lath width and α colony scale factor. As a result, mechanical properties decrease significantly.

5.3. Texture

Texture of thermo-mechanically processed metals and alloys has been widely investigated and is known to have a significant impact on mechanical response [123]. However, texture investigations of ALM products are very limited. This section seeks to provide initial studies of textures formed during EBM of Ti-6Al-4V and give further insight into how the process influences material on a micro, meso and macro structural scale.

EBSD of EBM material was performed on two scales, determined by the step size. At smaller step sizes (≤ 3 μm), individual α laths were resolved whilst at larger step sizes (> 3 μm), larger maps were collected from which whole/near-whole prior β grains could be reconstructed. The IPF (inverse pole figure) colour keys used in the presentation of EBSD data are given in Figure 5.35.

(a) (b)

Figure 5.35 : EBSD colour code keys for (a) IPF colouring of HCP α phase, (b) IPF colouring of BCC β phase.

At the time of writing this thesis, no published work regarding the texture of EBM Ti-6Al-4V was found. The presence of texture in deposited materials in general, has been studied by Wu *et al.* [124] and Moat *et al.* [73] for powder bed systems. Wu *et al.* [124] report that during the direct laser deposition of a burn resistant Ti alloy onto Ti-6Al-4V '*no particular texture*' was found. The chemistry of burn resistant titanium is very different to that of Ti-6Al-4V; TiC precipitates are present (that pin prior β grain boundaries) and there is a difference in solidification behaviour [125], compared to Ti-6Al-4V. As a result, textural evolution is likely to differ. Moat *et al.* [73] reported '*reasonably high levels of preferred orientation*' during laser deposition of Waspaloy which was found to exhibit preferred orientation with a microtexture controlled by the melt pool angle.

Whilst neither pieces of literature are directly comparable with this work, two interesting points arise: (i) for some alloy systems, texture may be varied by changes to the ALM heat source and (ii) given the correct alloy system it is possible, by ALM, to produce a randomly textured deposit.

5.3.1. Prior β Phase Reconstruction

Room temperature, EBSD analysis allows for texture determination of the transformed, fully lamellar EBM microstructure. It is possible to use light microscopy, with some uncertainty, to determine the position of prior β grain boundaries owing to the presence of α_{GB}. However, EBSD data, combined with the application of the Burgers relationship, provides a means of calculating both prior β grain position and orientation.

Prior β phase reconstruction was performed using software developed at the University of Sheffield by Davies [93]. EBSD data imported into the software is reconstructed based on misorientations between neighbouring pixels and variants. An exhaustive description of software development and capabilities can be found in the thesis written by P. Davies [93]. Here, a brief description of the program and underlying theory are given.

EBSD data, collected in HKL Channel 5 software as a *.cpr file, is exported to a *.ctf text file and imported into the *Beta Reconstruction* program. Davies [93] based the reconstruction methodology on that described by Humbert *et al.* [95]. When the coordinate system of a crystal is determined (in this case by EBSD), the orientation is defined as "*the position of the crystal coordinate system with respect to the specimen coordinate system*" [34]. The crystal coordinate system, C_C, sample coordinate system, C_S, and orientation, g, are related as per Equation (5.7). The orientation g can be expressed as a rotation or orientation matrix.

$$C_C = g \cdot C_S \qquad (5.7)$$

For the cubic β phase in titanium, g^{β} can be expressed as a set of 24 rotations given in Equation (5.8) in which $S_1^{\beta}...S_i^{\beta}...S_{24}^{\beta}$ are the 24 rotations of symmetry in the cubic crystal group [126].

$$S_1^{\beta} g^{\beta},\ldots S_i^{\beta} g^{\beta},\ldots S_{24}^{\beta} g^{\beta} \quad (5.8)$$

The Burgers relationship describes the relation between the BCC β crystal structure and the HCP α crystal structure. This relationship may also be described by a rotation, D. The orientations of the transformed α variants, g^{α}, are thus given by:

$$DS_1^{\beta} g^{\beta},\ldots DS_i^{\beta} g^{\beta},\ldots DS_{24}^{\beta} g^{\beta} \quad (5.9)$$

The symmetry of the hexagonal crystal allows the α variants to be described by 12 rotations, denoted S_j^{α}. It is therefore possible to describe the possible α orientations by:

$$S_j^{\alpha} DS_1^{\beta} g^{\beta},\ldots S_j^{\alpha} DS_i^{\beta} g^{\beta},\ldots S_j^{\alpha} DS_{24}^{\beta} g^{\beta} \quad (5.10)$$

Although it is seems from Equation (5.10) that there are 24 hexagonal variants arising from one parent β orientation Humbert *et al.* [95] showed there are only 12 distinct α variants characterised by 12 rotations.

When considering a single, inherited α variant Humbert *et al.* [95] also showed that there are six potential parent cubic orientations from which the α variant may have transformed. However, the six potential solutions may be reduced to four or fewer (and in many cases a single solution) when the misorientation between two α variants from the same β parent is determined. The software developed by Davies [93] compiles the misorientation between indexed points (within the same and adjacent variants); the parent β orientation is given by the most frequent solution. In cases where a single solution cannot be determined, a second reconstruction pass is used to determine the parent orientation of the non-reconstructed variants based on the orientations determined for the reconstructed variants. A schematic representation of the determination of a parent β phase orientation from three inherited α variants is shown in Figure 5.36.

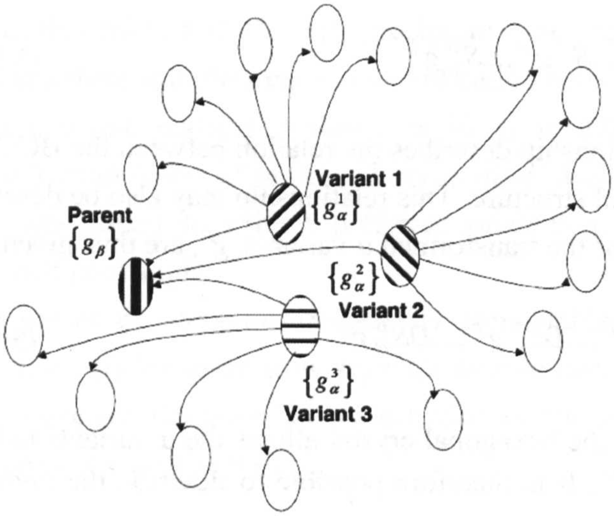

Figure 5.36 : Schematic representation of how the orientation of a parent, cubic β grain {g $_\beta$} is derived from three α variants with orientations {g $_\alpha^{1, 2, 3}$}, [126].

5.3.2. Deposited EBM Texture Parallel to the Z-Axis

Figure 5.37 shows IPF colouring, with respect to the *z*-axis, of (a) transformed α, (b) stabilised β, (c) reconstructed prior β grains and in (d) a misorientation plot of high angle (> 15°) and low angle (> 5°) grain boundaries; henceforth these shall be denoted HAGBs and LAGBs respectively. The EBSD data was collected a small distance from the base plate interface region of a bulk sample. The effect of the chemical interaction zone, as mentioned in Section 5.2.1, is clearly visible in (a) and (b) of the figure. The bottom 350 μm of the sample is indexed as fine grained, equiaxed β phase. This confirms that the concentration of β stabilising elements from the base plate is potent enough to maintain β at room temperature – above this region, α phase is dominant.

The equiaxed nature of this region is thought to be analogous to the chill zone in castings whereby nucleation preferentially initiates on the outer most surfaces of the metal, in contact with a mould wall as well as on inoculants such as oxide films [127]. Stabilized β grains initially nucleate with random orientation at the SS base plate due to rapid heat loss through conduction into the plate. Heat loss via radiation also occurs from the top of the melt pool; for several layers the width of the melt pool is greater than the thickness of the deposited material and as such heat loss via radiation is significant.

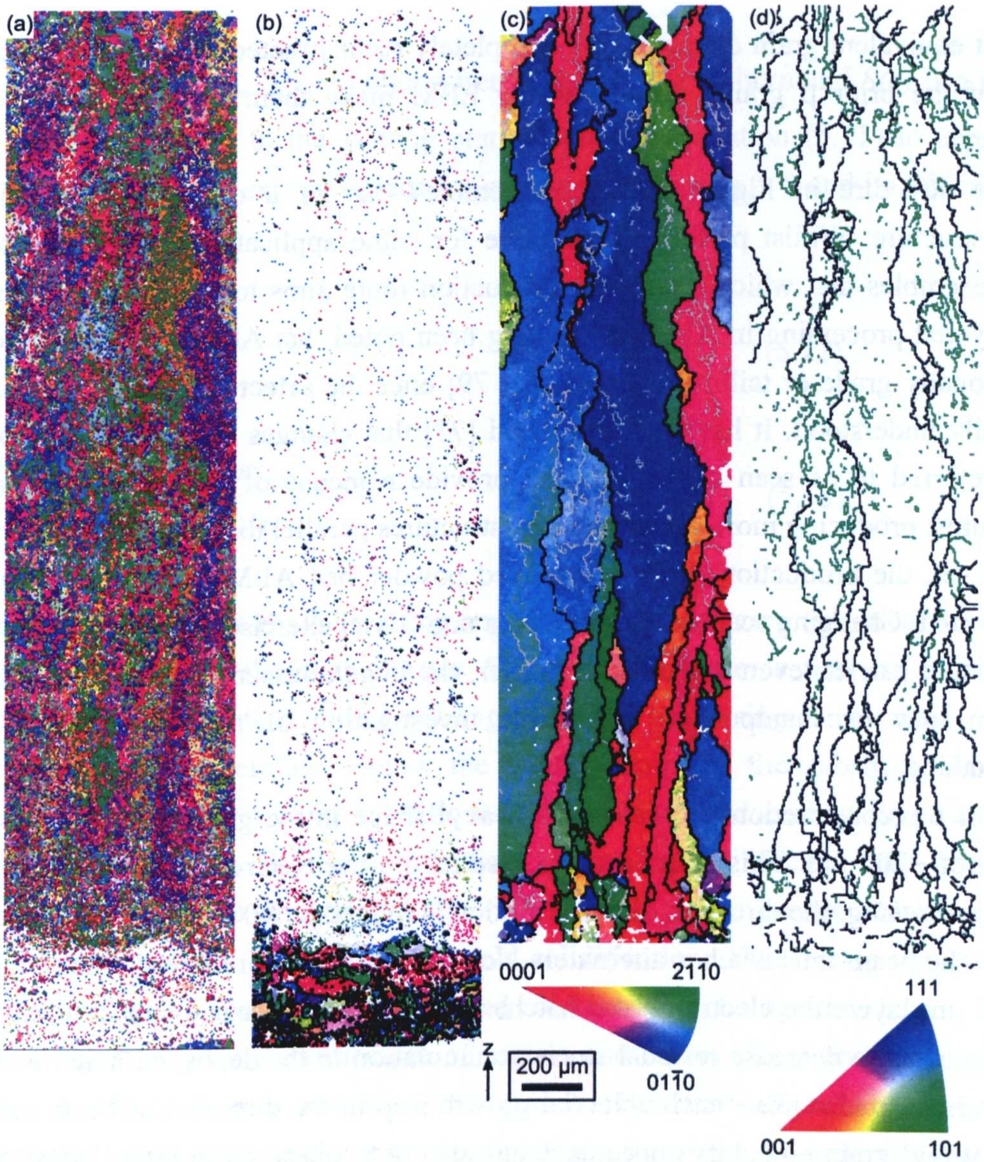

Figure 5.37 : IPF colouring of EBSD data parallel to the z-axis showing (a) the indexed α phase, (b) the indexed β phase, (c) a prior β grain reconstruction and (d) a misorientation plot. In (a) – (c) black lines represent HAGBs > 15° misorientation and grey lines represent LAGBs > 5° and ≤ 15° misorientation. In (d) LAGBs are represented in green for clarity. Step size = 5 µm.

In Figure 5.37 (c), prior β grain reconstruction reveals the high temperature microstructure. An equiaxed to columnar transition can be seen directly above the β stabilized region; this results from powder grains initially forming individual prior β grains, before epitaxial growth ensues. The columnar prior β grains extend through tens of layers and as such, their full extent is not easily measured. Although it appears to extend further than shown in the EBSD map, the blue prior β grain in the middle of the map has an equivalent grain diameter of 758 µm and an aspect ratio of 8.1. The largest aspect ratio of a completely reconstructed prior β grain is 11.8 whilst the largest equivalent grain diameter of a completely reconstructed grain is 424 μm. The size of the prior β grains formed during EBM make them visible, by eye, after etching.

The structure in Figure 5.37 (c) resembles that of a directionally solidified microstructure. Whilst perfectly acceptable for some applications, this morphology also resembles that which a wrought production route aims to break up. Because of the layered processing in ALM, it has long been noted that ALM may be utilized to functionally grade or tailor properties [61, 79] once the effect of process parameters are fully understood. It has been suggested [73] that changes to beam motion paths, also referred to as scan strategies, may provide a means of interrupting columnar structures; producing more equiaxed microstructures parallel to the build direction.

As yet, the production of fully equiaxed powder bed ALM components remains unreported. Changing scan strategy can be a non-trivial exercise with control software a potential barrier; even without this barrier, the huge number of ways energy beam motion may be manipulated makes the investigation of scan strategies a vast undertaking.

Prior β reconstruction also reveals a 'wavy' shape in the grain boundaries with a period of ~200 μm. This is believed to result from the electron beam scan strategy. During *hatching*, the direction of beam motion is rotated by 90° about the z-axis every layer. The beam thus hatches alternately along the x- and y-directions; when building in 100 μm layers the electron beam hatches along the same axis every 200 μm. This strategy aims to decrease residual stress accumulation in the deposited material but is shown here to also skew each epitaxial growth step in the direction of beam motion. This 'wavy' grain boundary appearance has also been observed in laser deposited Ti-6Al-4V [71, 125].

5.3.3. *Epitaxial Solidification*

As evident from Figure 5.37 (c), solidification of the high temperature β phase takes place epitaxially. Fukai and Ando [128] suggest that epitaxial solidification results when nucleation is more sluggish than epitaxial growth. However, both David *et al.* [129] and Easterling [130] state that, during weld solidification, there is no barrier to nucleation. The EBM process is analogous to autogenous welding in which solidification occurs spontaneously (and epitaxially) on partially melted grains, with no significant liquid undercooling required [129]. The free energy of heterogeneous solidification, ΔG, is given by Equation (5.11):

$$\Delta G = \left\{ -\frac{4}{3}\pi r^3 \Delta G_v + 4\pi r^2 \gamma_{SL} \right\} S(\theta) \qquad (5.11)$$

where r = cap radius, ΔG_v = volume free energy of the embryo and $S(\theta)$ is a shape factor that depends on θ, the wetting angle. Equating Equation (5.11) to zero and differentiating gives an expression for the critical embryo size (r^*) and its critical free energy (ΔG^*):

$$r^* = \frac{2\gamma_{SL}}{\Delta G_v} \tag{5.12}$$

$$\Delta G^* = \frac{16\pi\gamma_{SL}^{\ 3}}{3\Delta G_v^{\ 2}} \times S(\theta) \tag{5.13}$$

During epitaxial growth, the wetting angle (θ) is equal to zero (identical substrate and deposit material), the shape factor $S(\theta) \approx 0$ and there is thus no barrier to solidification. Solidification during welding and EBM processing can therefore occur spontaneously at temperatures below the melting point of the substrate material. [130]. The free energy during solidification of welding and casting processes are shown in Figure 5.38. Whilst a reduction in free energy occurs only after the formation of an embryo of a critical size (r^*) in casting, free energy decreases with increasing r, regardless of size, during weld solidification. This is also the case for ALM processing and as a result the observed columnar morphology develops.

When discussing the solidification of metals and alloys, Kurz and Fisher [102] consider constrained and unconstrained growth. Constrained (columnar) growth occurs when heat flow is opposite to the direction of growth. As such, dendrites are constrained to grow at a velocity dictated by the isotherm velocity [102]. In unconstrained growth, dendrites may grow freely and radially at a velocity governed by the liquid undercooling. Although a small volume of liquid is present during EBM solidification the imposed solidification conditions are such that constrained growth of the prior β phase occurs.

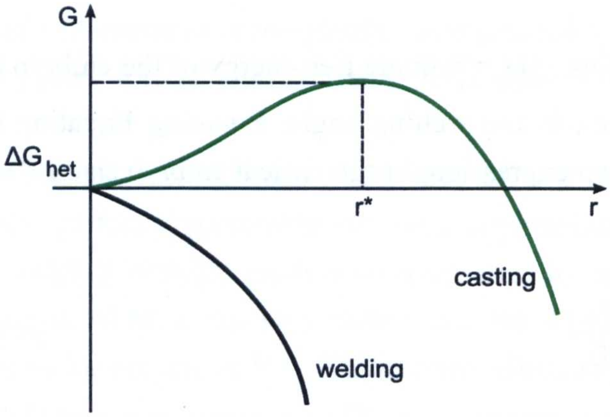

Figure 5.38 : Change of free energy, G, with embryo radius, r, for welding and casting. Adapted from [130].

5.3.4. Substructure Parallel to the Z-Axis

As well as the formation of columnar prior β grains, EBSD and β reconstruction reveals LAGBs throughout the map. LAGBs are visible in Figure 5.37 (c), and are more apparent in (d), indicating the presence of substructure within the deposited material. High resolution EBSD data of bulk material (0.4 μm step size), parallel to the z-axis, is shown in Figure 5.39. IPF colouring of the α phase in (a) reveals the Widmanstätten α laths and continuous α_{GB}. Prior β phase reconstruction is displayed in both IPF colouring (b) and Euler colouring (c). As expected, the HAGBs of prior β grains are nominally parallel to the z-axis; however, this is also the case for LAGBs present within the microstructure.

The right hand side of Figure 5.39 shows the BCC crystal orientation for the traverse line at regions A – M. Cubes labelled H – M correspond to the orientations within the dominant prior β grain (the red grain on the right hand side of Figure 5.39 (a)). Figure 5.40 (a) gives the misorientation profile across the dotted line in Figure 5.39 (c), across the whole map (A – M) and dominant prior β grain (H – M). A maximum misorientation of 17.4° is present across the dominant prior β grain (relative to position H) and, as evident from the BCC crystal orientations, this misorientation is a result of rotation about a common <001> axis.

The misorientation distribution of LAGBs (in the range 4 – 7°) for the entire map is shown in Figure 5.40 (b) and indicates that LAGBs arise from a rotation about the [001] pole. Pole figures for the orientation of the dominant β grain and transformed α within this grain are given in Figure 5.40 (c). The comparison of <0001> and <110> pole figures indicate that transformation of the dominant prior β grain does not result in any variant selection of the α phase.

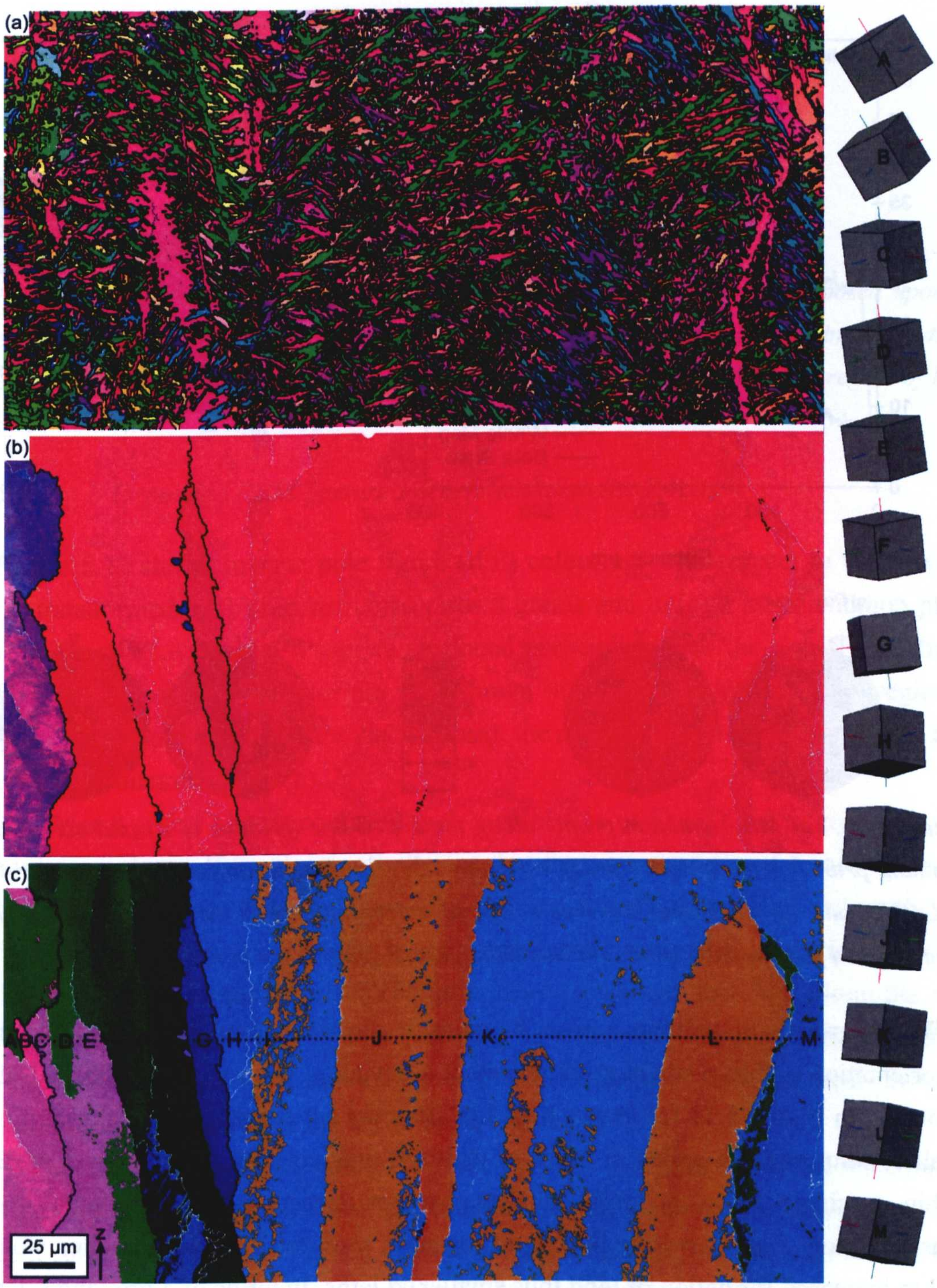

Figure 5.39 : IPF colouring of EBSD data parallel to the z-axis showing (a) the indexed α phase, (b) a prior β grain reconstruction and (c) Euler colouring of the β grain reconstruction. Black lines represent HAGBs > 15° and grey lines represent LAGBs > 5°. The letters along the dotted line in (c) correspond to the crystal orientations shown on the right hand side of the figure. Step size = 0.4 µm.

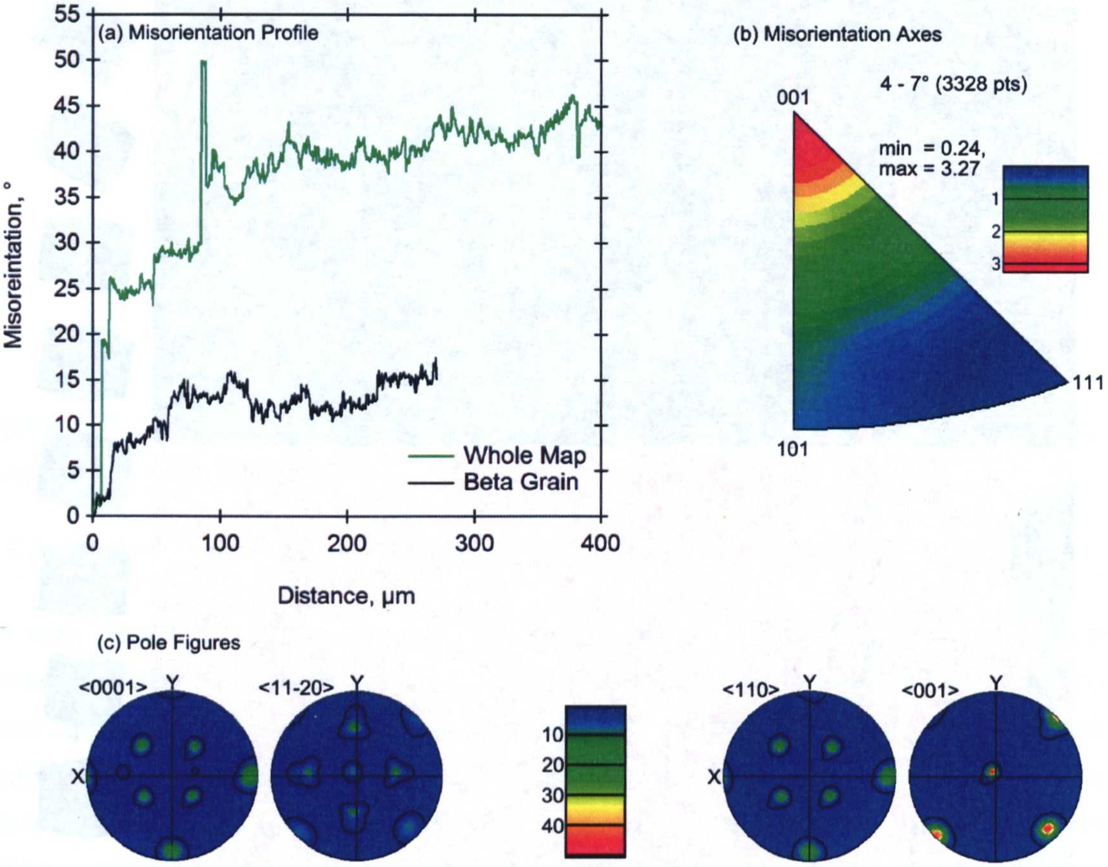

Figure 5.40 : (a) Misorientation profile along the dotted line (relative to A) and across the dominant prior β grain (relative to H) in Figure 5.39, (b) misorientation distribution for 4 – 7° LAGBs and (c) HCP and BCC pole figures corresponding to the transformed α and reconstructed β orientation within the dominant prior β grain in the previous figure.

Whilst growth of columnar prior β grains is clearly epitaxial, the LAGBs and misorientation within a single grain represent a deviation from perfect epitaxy. Euler colouring in Figure 5.39 (c) shows how LAGBs may act to split a prior β grain into smaller, columnar sub-grains in terms of width. It may also be possible that LAGBs, within a single prior β grain, nucleate and/or arrest growing α laths upon transformation. Both cases are beneficial for grain size; more nucleation sites would lead to increased formation of (and thus smaller) α laths. In terms of a growing α lath, the presence of a LAGB may limit its length to within the boundaries of the columnar sub-grain rather than the full columnar grain width. Potential evidence for this is presented in Figure 5.41 (a) and (b) in which LAGBs (shown in red) in the prior β phase are superimposed upon the α phase. Without further work it is not possible to say with any certainty whether this is in fact the case, however, LAGBs are potentially an important feature influencing microstructural scale.

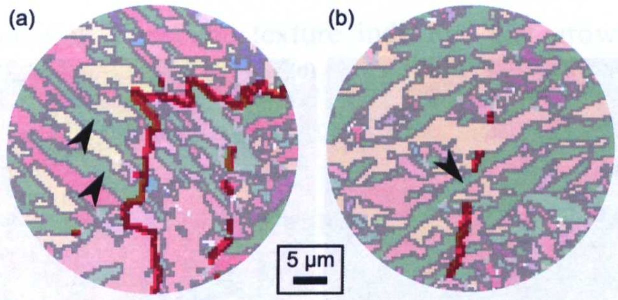

Figure 5.41 : LAGBs (in red) in the prior β phase in Figure 5.39 superimposed upon IPF colouring of the α lath grain structure. In (a) arrowheads indicate α laths beginning/ending at a LAGB whilst in (b) the arrowhead highlights an α lath extending through a region of LAGB discontinuity. 5° < LAGB < 15°.

5.3.5. Deposited EBM Texture Perpendicular to the Z-Axis

Figure 5.42 shows inverse pole figure (IPF) colouring, with respect to the *z*-axis, of (a) transformed α, (b) reconstructed prior β grains and in (c) a misorientation plot of HAGBs and LAGBs for a sample sectioned perpendicular to the *z*-axis. Pole figures for the α phase and β phase are also shown in the figure. Whilst large regions of similarly oriented α grains are visible in (a), the most striking result can be seen in the prior β reconstruction in (b).

Prior β grains appear equiaxed with a grain size of 114.73 ± 0.54 μm at the 95% confidence limit. IPF colouring indicates that the vast majority of prior β grains are oriented with their <001> poles parallel to the *z*-axis. During solidification, the most favourable orientation for growth is always the preferred dendrite direction, the <001> direction in cubic metals [127]. The near one-dimensional heat flow along the *z*-axis thus promotes the growth of this preferred direction; an additional factor favouring selection of this grain orientation may be that such grains provide the most favourable path for heat flow through the liquid-solid region [127].

The preferential transformation of some variants over others, variant selection, has been observed in titanium alloys hot rolled above the β transus and also where heavy cold rolling has been performed prior to β annealing [131]. It has been shown in the previous section that, within a single prior β grain, all 12 α variants were formed. The hexagonal <0001> pole figure in Figure 5.42 shows that all 12 α variants are present within the transformed microstructure. Here, comparison of the prior β <110> pole figure with the transformed α <0001> pole figure, for a large number of grains, indicates that variant selection does not occur during transformation. This is apparent due to the almost identical intensity distributions. Although substructure has been identified in the deposited EBM material, the amount of strain present is not comparable to that found in heavily mechanically processed titanium. The lack of variant selection is therefore unsurprising.

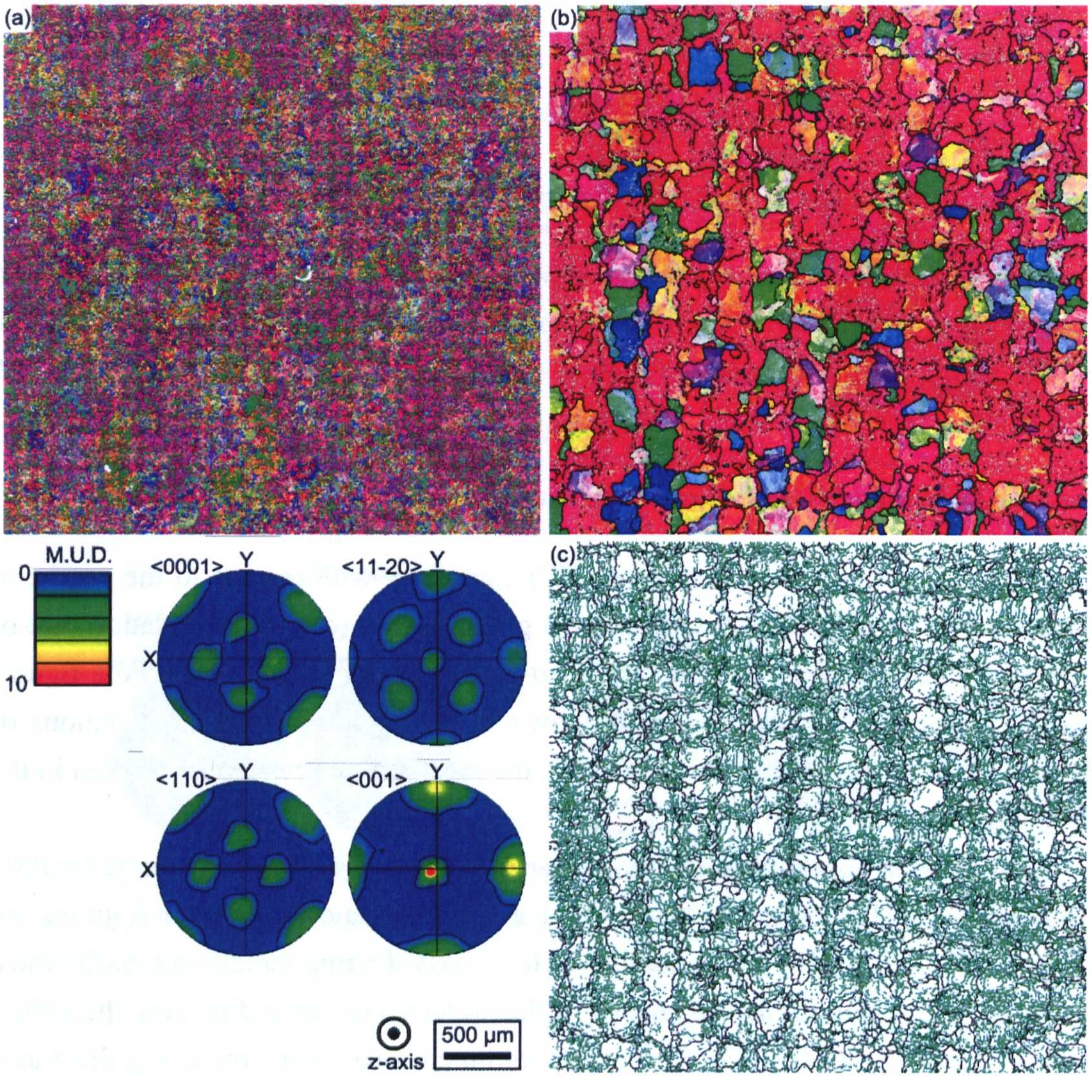

Figure 5.42 : IPF colouring of EBSD data perpendicular to the z-axis showing (a) the indexed α phase, (b) a prior β grain reconstruction and (c) a misorientation plot and associated pole figures. In (a) and (b) black lines represent high angle grain boundaries > 15° and grey lines represent low angle grain boundaries > 5°. In (c) low angle grain boundaries are represented in green for clarity. Step size = 5 µm.

The prior β <001> pole figure in Figure 5.42 shows not only the strong, 10 times random preference for the [001] pole to align itself with the z-axis; but also the alignment of all of the <001> poles with the orthogonal axes, giving rise to a cube texture. This texture is much like that observed in rolled sheet metals [132]. Glavicic *et al.* [133] discuss the texture in the columnar region of cast Ti-6Al-4V ingots. Due to the preferred <001> growth direction in cubic metals, the authors state that an ingot would be expected to have a <001> fibre texture with boundaries between adjacent columnar grains being tilt in nature and having primarily random misorientations. Although not observed in Figure 5.42, it was expected that a fibre texture would also be found in EBM material. The cube texture indicates that growth in *x*, *y* and *z* directions is constrained resulting in the <001> poles lying parallel to the orthogonal axes. A rotation of ± 16.5° about the [001] pole is the only deviation away from the perfect cube texture.

The preference of the <001> poles in the BCC unit cell to align themselves with the orthogonal axes is unexpected. However, Figure 5.43 indicates another preferred orientation. Regions within the map have been highlighted (A – F) and the pole figures for each region are given below the map. <001> pole figures show that the cube orientation prefers to be aligned with or at ~45° to the *x*- and *y*-axes. The pole figure of the entire map indicates the development of a <001> fibre-like texture parallel to the *z*-axis and results from deviations from the nominally 0° and 45° rotations about the *z*-axis.

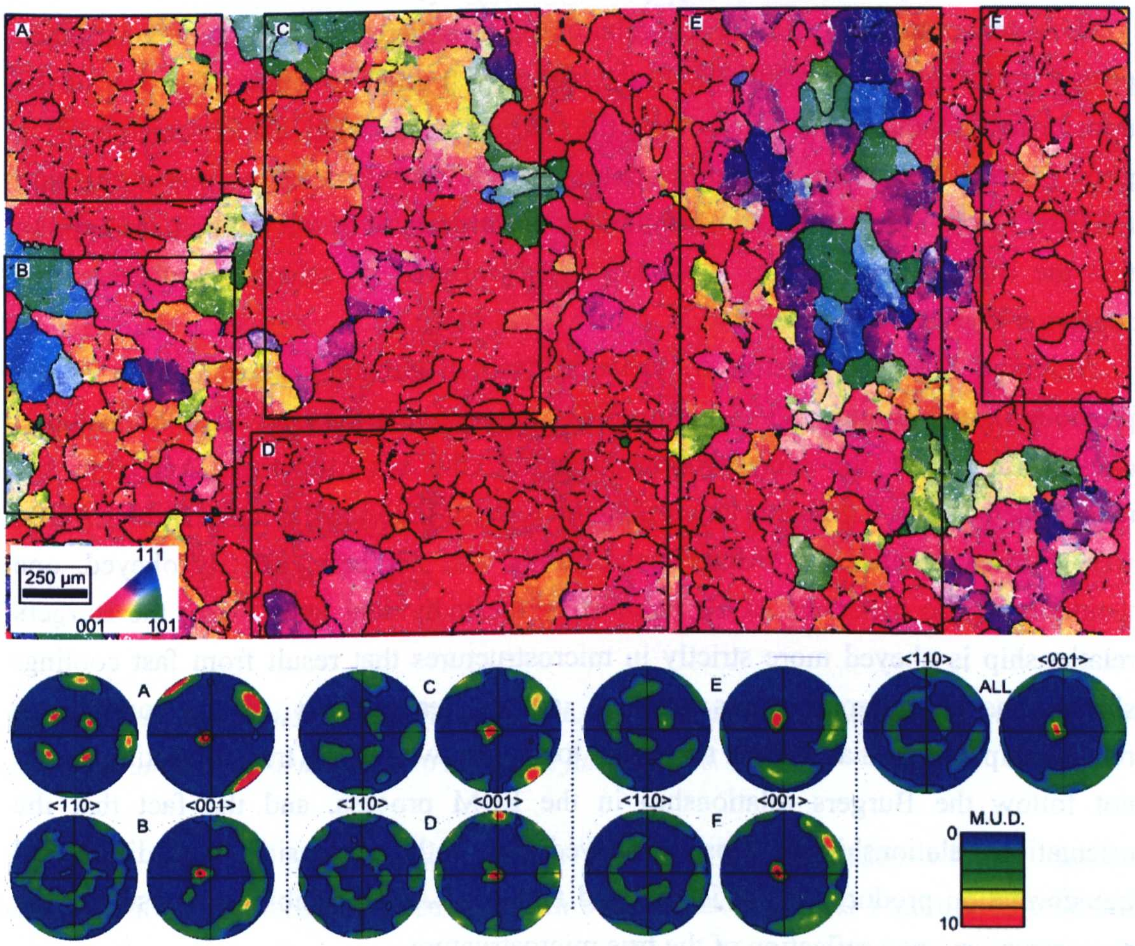

Figure 5.43 : IPF colouring of a prior β grain reconstruction from EBSD data, perpendicular to the z-axis; black lines represent high angle grain boundaries > 15° and grey lines represent low angle grain boundaries > 5°.

5.3.6. *Substructure and Localisation*

As well as material texture, the previous two figures show a significant amount of substructure present within the prior β microstructure. These microstructural features are only made visible as a result of the reconstruction process; this, therefore, poses an important question: is the substructure real or an artefact of the reconstruction process?

The output of the reconstruction software is a collection of BCC orientations, calculated from application of the Burgers relationship. Upon transformation from β → α, there are two possible outcomes:

(i) β → α, strictly following the Burgers relationship
(ii) β → α, deviating from the Burgers relationship.

If, as per scenario (i), the Burgers relationship is adhered to, then the reconstructed prior β grains would correctly reflect the real prior β grain structure. However, if the transformed α laths do not strictly obey the Burgers relationship, as per scenario (ii), a prior β grain free from any substructure may be reconstructed as one containing LAGBs. Errors in reconstruction would thus occur because of the implicit assumption that the Burgers relationship is always strictly obeyed. A schematic of these two scenarios is given in Figure 5.44.

Although it is not possible to view the prior β structure, consideration of the previous figures (Figure 5.39 - Figure 5.43) suggests that the Burgers relationship is obeyed. In all of the aforementioned figures, the scale of the LAGBs in the reconstructed prior β grains is larger than the scale of individual α laths. If the LAGBs were formed because the Burgers relationship was not being strictly obeyed, one would expect to observe LAGBs delineating the individual laths. Also, the Burgers relationship is obeyed more strictly in microstructures that result from fast cooling; slower cooled microstructures tend to adhere less strictly to the orientation relationship. Given that there is no reason to suggest why phase transformation would not follow the Burgers relationship in the EBM process, and the fact that the orientation relationship is closely obeyed for both martensitic and diffusional transformation products [6], it is believed that the LAGBs visible as a result of the reconstruction are a reflection of the true microstructure.

Because of the complex thermal history experienced by EBM components; the origin of the substructure is not entirely obvious. It is possible that the substructure exists as a result of:

- Contraction during solidification. This could be as a result of either pure solidification contraction or the combined effect of this coupled with stresses generated during rapid solidification.

- The β → α phase transformation. Greenwood and Johnson [134] describe the effect of materials undergoing a phase transformation whilst under the application of a small stress. They found that during transformation, irreversible plastic deformation is accommodated in the weaker phase (β phase in Ti-6Al-4V) with a permanent shape change. The thermal gradient along the *z*-axis may provide a thermal stress that causes some plastic deformation in the β phase.

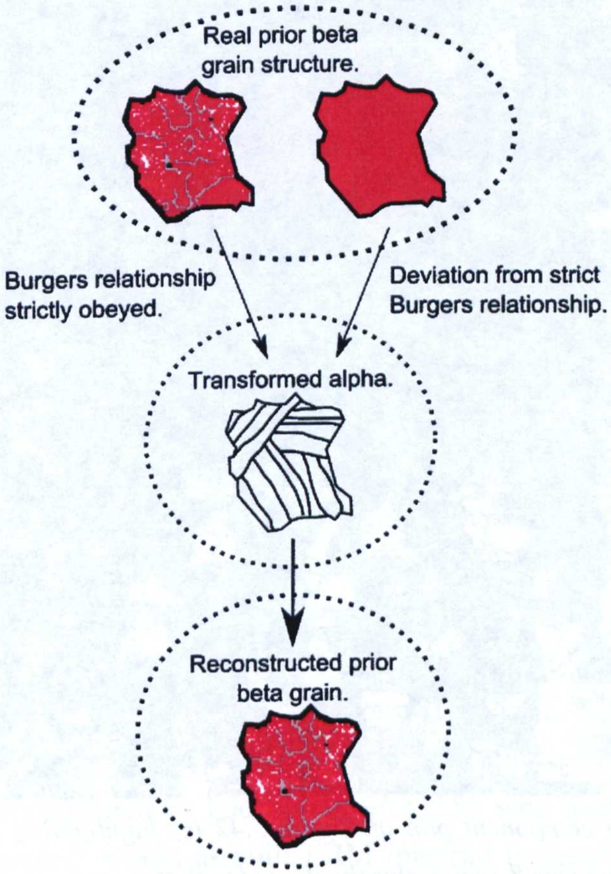

Figure 5.44 : Schematic of the production of LAGBs during reconstruction to give either the correct prior β grain structure or to introduce false LAGBs.

Whilst the two previous suggestions may not be dismissed without further investigation, an interesting observation in both Figure 5.42 and Figure 5.43 tends to suggest that substructure is not homogeneous. The LAGBs within the microstructure tend to be most dense within grains of a certain orientation; specifically in grains coloured red (<001> poles parallel to the *z*-axis). Grains of other orientations contain much fewer low angle grain boundaries.

This phenomenon is more clearly visible in the texture component plots shown in Figure 5.45 and Figure 5.46. Grains are coloured according to the deviation of their

[001] pole from alignment with the *z*-axis. Small angular deviations result in darker colourings whilst larger angular deviations result in light grey/white colouring. LAGBs are more concentrated in grains with their [001] pole closely aligned with the *z*-axis. This provides further evidence against the substructure being an artefact; if this was the case it would be expected that LAGBs would be evenly distributed rather than present in grains of a specific orientation.

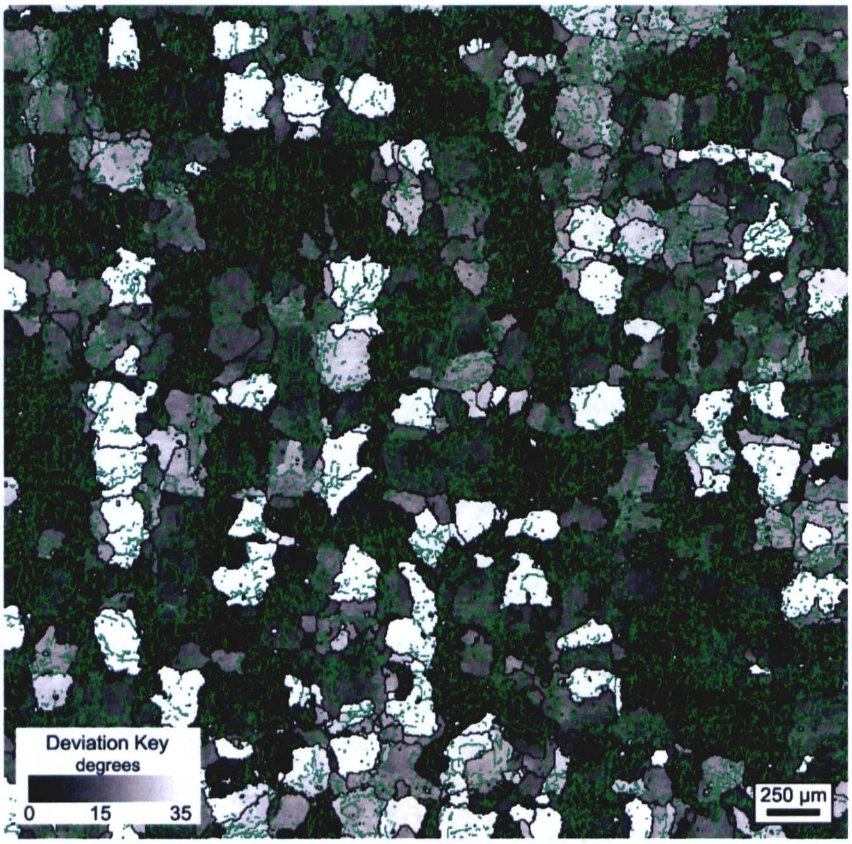

Figure 5.45 : Texture component plot of Figure 5.42 (c) highlighting the concentration of LAGBs (light green) in prior β grains closely aligned with the z-axis.

In considering the orientation of LAGBs in Figure 5.39, their presence may be, in small part, a result of constrained growth. Kurz and Fisher [102] describe constrained growth in which high angle grain boundaries lie parallel to the primary dendrite axes and are continuous along the length of the solid. Within this structure it is stated that "*Each dendrite forms low-angle grain boundaries with its neighbours and many trunks, formed by repeated branching, together make up one grain*" [102]. The LAGBs parallel to the *z*-axis in Figure 5.39 thus potentially delineate interdendritic regions of primary dendrites.

From a localisation perspective, LAGBs between dendrites would be sectioned most frequently in grains most closely aligned with the *z*-axis. However, whilst this explanation goes some way to explaining how/why localisation occurs, it does not account for the large difference in LAGB density observed. LAGB density in grains of different orientations is much greater than this explanation alone can account for. Determining how and why LAGBs form during EBM deposition would be an interesting area of further work.

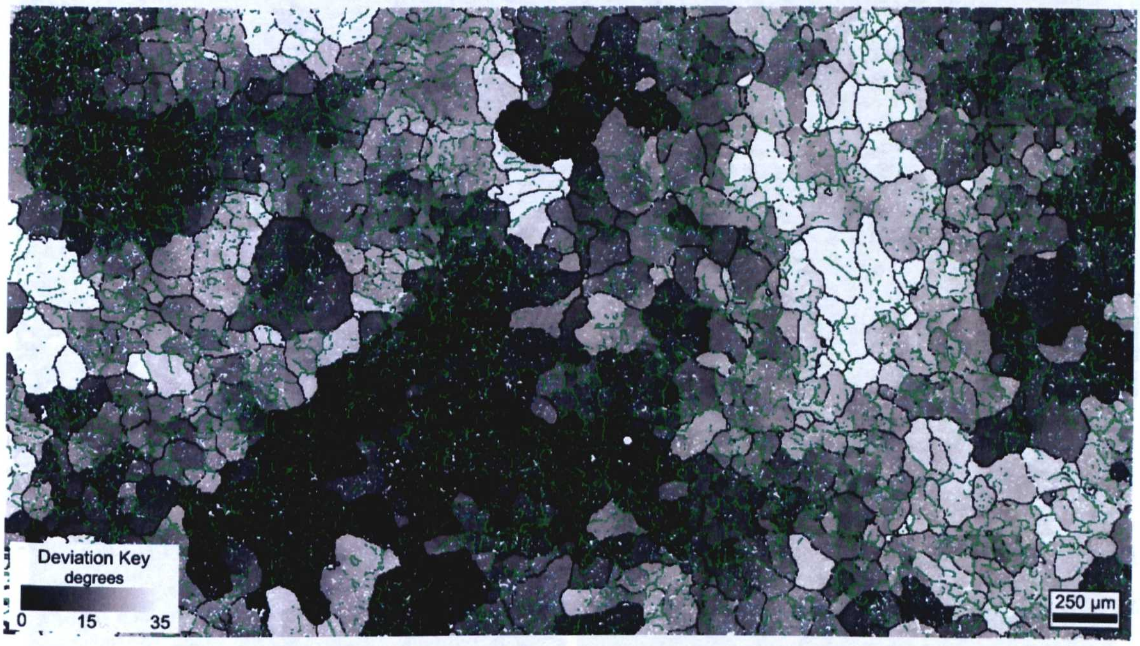

Figure 5.46 : Texture component plot of Figure 5.43 highlighting the concentration of LAGBs (light green) in prior β grains closely aligned with the z-axis.

Regardless of the mechanism of formation, the presence of substructure within EBM Ti-6Al-4V is a potential indicator of a strained material. Stored energy may be available to promote microstructural change upon exposure to elevated temperatures. This avenue has been explored by Facchini *et al.* [115], who have demonstrated that the level of strain present within as-built EBM material is insufficient to produce a change in the α phase morphology. In their work, a comparison was made between as-built and '*pre-strained*' EBM Ti-6Al-4V. Pre-strained material was taken from the necked regions of broken tensile samples.

A comparison of the two material conditions, treated for 1 hour at three temperatures and furnace cooled, is shown in Figure 5.47. The results show that, in the as-built condition, the heat treatments act to coarsen the microstructure. However, for the pre-strained material, a combination of temperature and strain results in globularisation of the α phase.

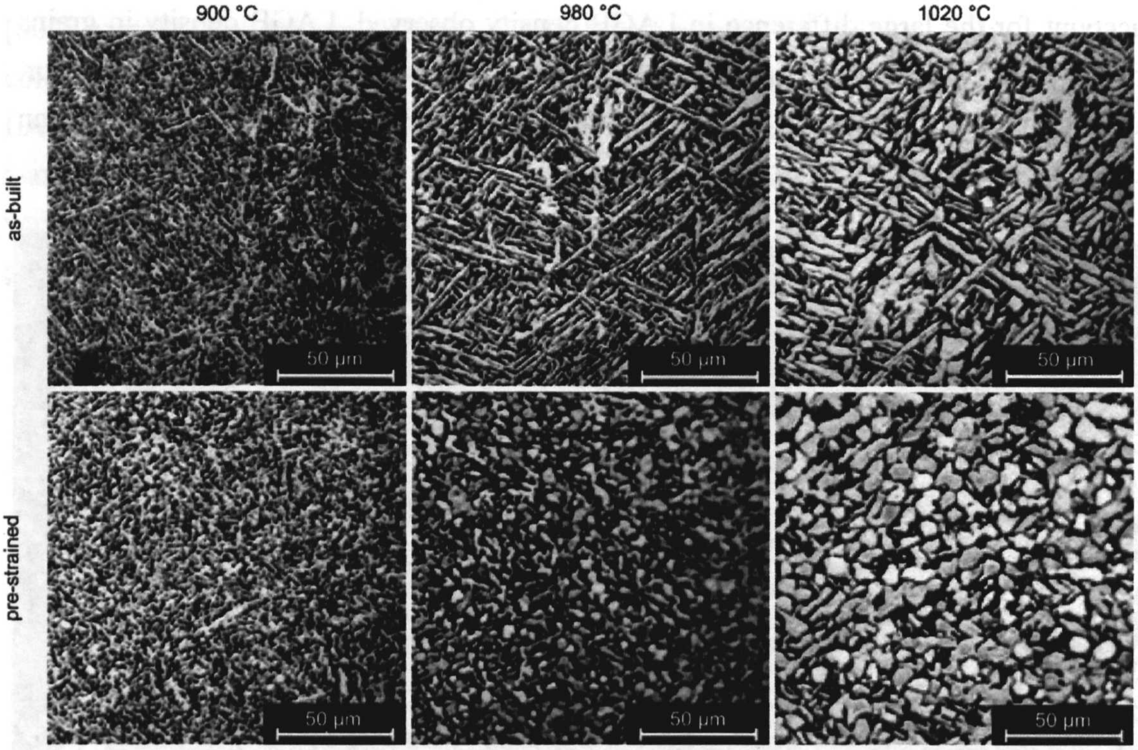

Figure 5.47 : Optical micrographs of heat treated EBM samples in the as-built and pre-strained conditions, taken from [115].

5.4. Defects

Although not a key area of investigation in this study, it is necessary to acknowledge the presence of defects within material processed by EBM; a brief discussion of internal and external defects will be made. Defects, whether internal or external, are not widely reported in ALM literature although their presence is acknowledged in terms of component density being less than 100% [115]. Mechanical properties of EBM materials tend to be quoted in the machined condition. Whilst this gives important information regarding the material properties, potential use of ALM is to produce novel structures where it may not be possible to access all surfaces for machining. In these applications, the as-deposited surface becomes critical.

5.4.1. Internal Defects

Defects in ALM are, in general, a result of incomplete melting of powder; some examples of defects found during microstructural investigations are shown in Figure 5.48. Micrographs (a) – (e) are taken with the z-axis parallel to the long axis of the page, in (f) the *z*-axis is perpendicular to the plane of the page. Defects tend to be layer-based and lie perpendicular to the *z*-axis; in most cases powder particles that have not been melted, or are partially melted, are present. Although further investigation would be required to categorise and determine the origin of such defects, there are several potential causes.

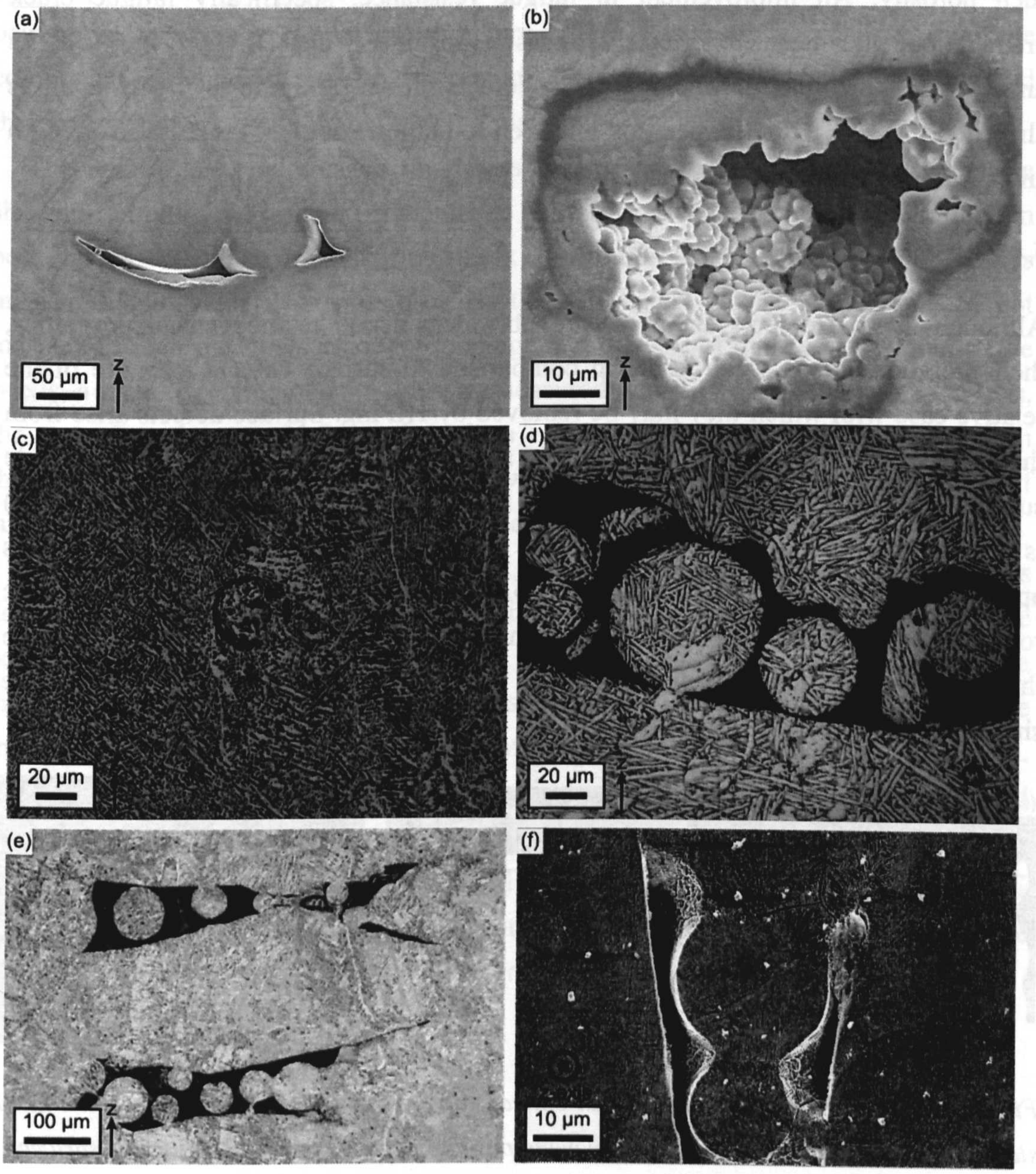

Figure 5.48 : Optical and SEM micrographs showing examples of defects observed in EBM Ti-6Al-4V.

A fluctuation of power in the electron beam or an abnormally thick region of powder, could both result in only partially melted regions. The defects in Figure 5.48 (e), situated directly above each other, suggest that their presence is unlikely to be random as one would expect from a power fluctuation. Repeat defects are likely to be caused by a hardware/setup issue. For example, damaged rake blades could result in repeated, local regions of thick powder that is too thick to be fully melted.

Regardless of the origin of internal defects, it is likely that wide-scale adoption of EBM components will require them to be hot isostatically pressed in order to close such porosity. An improvement in fatigue resistance, specifically fatigue crack propagation, has been reported [115] as a result of the HIP process; this is unsurprising given the morphology of the defects shown in Figure 5.48. However, as already discussed, the HIP operation has been found to result in a decrease in strength and a minimal improvement in elongation.

5.4.2. External Surface Defects

Although internal defects are unquestionably detrimental to mechanical properties, their presence is less of an issue, in comparison to surface defects, because of the relative ease with which they may be removed by HIPing. Surface defects arise from the as-deposited surface finish. Figure 5.49 shows in (a) a threshold image of the side surface of a typical sample, with the *z*-axis running from right to left. Figure 5.49 (b) is a micrograph of a tilted SEM sample showing the as-deposited surface. It is apparent from (a) and by handling a Ti-6Al-4V EBM sample, that a macroscopic roughness exists on the surface. This roughness is a combination of powder stuck to the surface of the material, as shown in (b), superimposed upon an undulating surface shown in (a).

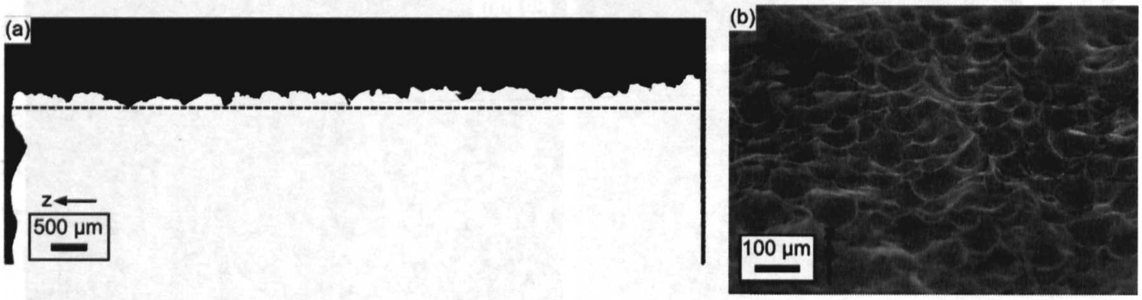

Figure 5.49 : (a) Threshold image of an optical micrograph showing an as-deposited EBM side surface and (b) SEM micrograph showing powder particles on the as-deposited surface.

The surface shown in (a) has several regions that are ideal sites for crack initiation. As well as being detrimental to static mechanical properties, such a surface can be severely detrimental to fatigue life. Under low-cycle fatigue (LCF) conditions, the fatigue life is dominated by resistance to crack propagation. By decreasing the stress/strain amplitudes, the portion of the material life attributable to crack initiation increases – high cycle fatigue (HCF) strength is therefore considered to be a good measure of the resistance to crack initiation in titanium alloys [8]. Given the surface shown in Figure 5.49 (a), it is likely that resistance to fatigue crack initiation is poor.

As well as being a detriment to properties, the current as-built surface reduces the near net shape capabilities of the process. If a machined plane face was required on the sample shown in Figure 5.49 (a), approximately 0.5 mm of material would need to be removed. Given that the surface in Figure 5.49 (a) corresponds to the surface of the component CAD model, the accurate reproduction of surfaces (post machining) would therefore require at least 0.5 mm of extra material on each surface of the CAD model.

The results of some surface roughness measurements, on as-built samples, are shown in Figure 5.50 (a) and (b) alongside that of a reference sample (R_a = 6 μm). In both travel directions, a maximum peak to trough distance of ~ 200 μm was measured. However, it is possible that the full extent of the crevices were not measured because of the surface morphology and the size of the stylus. Parallel to the *z*-axis, a mean R_a value of 28.1 μm was measured whilst perpendicular to the *z*-axis, the mean R_a value was 31.2 μm. R_a values > 25 μm are similar to those expected on the surface of poor sand castings and sawn material [135]. Clearly this quality of surface finish is unacceptable for an engineering component.

Whilst it has been assumed that the presence of external surface defects is detrimental to mechanical properties, it is the size of the reduction that determines the potential, or lack of, to use components in the as-deposited condition. The data presented in Figure 5.51 has been kindly supplied by Dr Michael Blackmore of the Innovative Materials Processing Centre (IMPC), based at the University of Sheffield. The results in the figure show static mechanical properties in both the machined and as-deposited conditions. In the machined condition, tests were performed on samples with the tensile axes parallel to the *x*, *y*, and *z* axes. In the as-deposited condition, tests were performed on samples oriented with the tensile axis parallel to the *z*-axis. The results given in each orientation are the average of five tests.

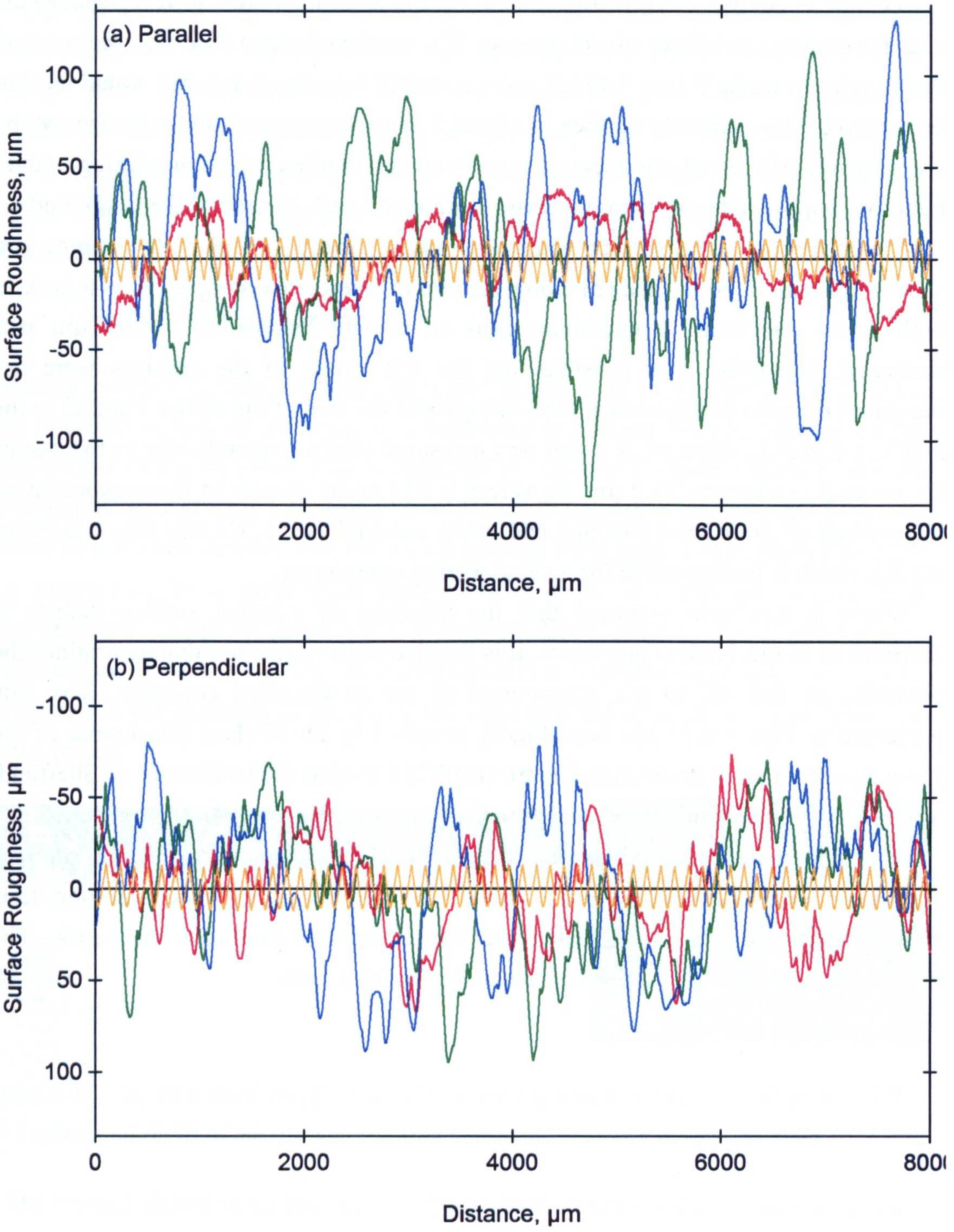

Figure 5.50 : Surface roughness profiles (a) parallel to and (b) perpendicular to the z-axis. Also included in orange is a reference sample with a R_a of 6 µm.

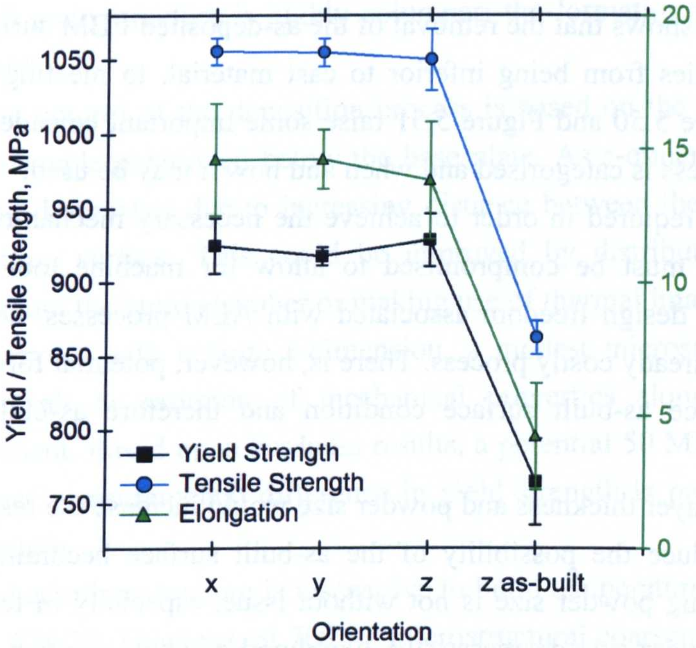

Figure 5.51 : Mechanical properties of EBM material deposited in the machined (x, y and z) and as-built (z) conditions. Data supplied courtesy of Dr Michael Blackmore of the IMPC.

The results above highlight the severe detrimental effect that the as-deposited surface has on mechanical properties. An average drop of 17%, 18% and 70% are found for the yield strength, tensile strength and elongation respectively. It is expected that fatigue properties would behave in the same way. The figure also indicates the consistency in properties of the machined samples in which orientation does not appear to significantly influence properties – an encouraging result. A comparison of as-built and machined samples, in the *z*-orientation, with a wrought and cast ASTM specification are given in Table 5.6.

Table 5.6 : Comparison of machined and as-built samples, tested in the z-orientation, to wrought and cast ASTM requirements.

Condition	Yield Strength, MPa	Tensile Strength, MPa	Elongation, %
Machined, *z*	928	1050	13.8
As-built, *z*	765	863	4.2
ASTM F1108 minimum (cast)	758	860	8
ASTM F1472 minimum (wrought)	860	930	10

The comparison shows that the removal of the as-deposited EBM surface increases mechanical properties from being inferior to cast material, to meeting the wrought specification. Figure 5.50 and Figure 5.51 raise some important considerations about how the EBM process is categorised and when and how it may be used.

If machining is required in order to achieve the necessary mechanical properties, component design must be compromised to allow for machine tool access. This severely limits the design freedom associated with ALM processes, not to mention adding cost to an already costly process. There is, however, potential for improvement which may enhance as-built surface condition and therefore as-built mechanical properties.

A reduction in layer thickness and powder size would increase the resolution of the process and introduce the possibility of the as-built surface becoming acceptable. However, decreasing powder size is not without issue, especially in terms of health and safety. As powder size decreases, the likelihood of explosion/fire increases and greater considerations for powder handling are required.

5.5. Chapter Summary

ALM processing, as a concept, is a simple process by which it is possible to produce geometrically complex, metallic components. However, the EBM process introduces complexity in the form of elevated temperature, with the Ti-6Al-4V alloy system introducing further complexity due to multiple phase transformations. The poorly instrumented EBM hardware makes interpretation and understanding of the process somewhat challenging.

In spite of this, several key points can be drawn from the work in this chapter:

- Bulk, EBM Ti-6Al-4V samples, produced using standard *themes*, consist of a bulk colony/Widmanstätten α + β microstructure. Typically, α_{GB} lies along prior β grain boundaries. In all cases, melting onto a stainless steel base plate results in a ~ 800 μm contaminated, β stabilised bottom layer.
- At the top of small samples, (< 20 mm × 20 mm × 10 mm; x, y, z) a martensitic microstructure has been observed that results from rapid cooling rates ($\sim 10^3$ Ks^{-1}). Cooling rate has been determined from secondary dendrite arm spacing measurements made on stainless steel base plates.
- Full thermal decomposition of a martensitic microstructure is not possible at an isothermal temperature of 650 °C and times ≤ 17.5 hrs. Thus, for structures containing α + β and α', it is proposed that α + β forms from a combination of thermal cycling and the *build temperature* rather than purely from holding at the *build temperature*.

- Prior β grain structure is highly columnar; the formation of prior β grains is epitaxial.
- Current control of the deposition process is based on the reading of a single thermocouple positioned below the base plate. As *z*-dimension increases this reading diminishes due to increasing distance between the thermocouple and deposition surface. This could be improved by distributing thermocouples throughout the build chamber or making use of thermal imaging systems.
- For samples with a large *z*-dimension, a modest microstructural variability may result in variation of mechanical properties along the height of a component. Based upon hardness results, a potential 50 MPa (calculated from hardness measurements) difference in yield strength is present in a 330 mm tall sample.
- Deposited microstructure is insensitive to build temperatures over the range of 625 – 678 °C. However, at 700 °C microstructural coarsening and a reduction in static mechanical properties is observed.
- Powder chemistry does not remain constant with time, specifically, oxygen content has been observed to increase to a level at which it does not meet the specification for grade 5 Ti-6Al-4V. This has been attributed to the adsorption of water onto powder and the vacuum chamber walls.
- Hot isostatic pressing has been found to coarsen as-built microstructures to the same scale, regardless of starting microstructure (for build temperatures 625 – 700 °C). The microstructural coarsening also brings about a reduction in static mechanical properties.
- Prior β reconstruction of EBSD data reveals a strong ~ 10 × random preference of the <001> pole to align itself with the *z*-axis. A cube texture and a 45° rotated cube texture have been found to be the preferred orientations of the prior β grains. Within prior β grains, a large amount of substructure, present as LAGBs, has been observed.
- LAGBs are more prevalent in prior β grains in which the [001] pole is most closely aligned with the *z*-axis. The origin of the LAGBs and the reason for their localisation is unknown and would be an interesting area of further work.
- Variant selection of α orientations has not been observed after transformation of the prior β phase.
- Internal and external defects have been identified as potential regions for crack initiation. In particular, the as-built samples ($R_a > 25$ μm) fail to meet wrought the requirements of ASTM F1108 (cast material) without the removal of ~ 500 μm of material from each component surface.

5.5.1. *Issues with Discussing Phase Transformations in Ti-6Al-4V*

Although it has been acknowledged by authors familiar with the field of ALM, that the nature of the process makes microstructural transformations and their interpretation difficult [73, 136], this difficulty is exacerbated by variety in the available literature. In the 1990 paper by Flower on titanium alloys [9], it is explicitly stated that '*contrary to . . . a widely reproduced schematic . . . the martensitic start and finish temperatures are very close to one another*'. However, in a book published in 1994 which is also widely referenced [10], a figure (reproduced in Figure 2.4 (b)) shows the M_s and M_f temperatures separated by an appreciable distance. This, coupled with the differences in reported M_s temperature and required cooling rate, and the relatively small amount of information available regarding transformation kinetics, results in a rather grey area.

Work published by Crespo and Vilar [136] discusses phase transformations in laser powder deposition (LPD). In their work, as in this, the authors made reference to several earlier studies for information regarding phase transformation. As an example of this, Crespo and Vilar used the work of Malinov *et al.* [113] for JMAK constants for the $\alpha \rightarrow \beta$ transition; the work of Ahmed and Rack [20] for the cooling rate required to form α'; M_s and M_f temperatures from Elmer *et al.* [111] and JMAK constants for martensitic decomposition from Gil Mur *et al.* [118]. Many of these works have also been referenced in this work. However, in the work of Crespo and Vilar [136]: (i) the M_s temperature from the work by Elmer *et al.* (650 °C) is used rather than the figure given by Ahmed and Rack (575 °C); (ii) an M_f temperature is used (400 °C) in contradiction with Flower [9] and (iii) although the kinetics of martensitic decomposition have been taken from the work of Gil Mur *et al.* [118], the authors later state that the hardness of the α, β and α' phases are 320, 140 and 350 HV respectively. These hardness results are more akin to those reported in Figure 5.22 of this work and in disagreement with that given by Gil Mur *et al.* [118] from which kinetic properties were taken.

The previous paragraph is in no way intended to be derogatory towards the work of Crespo and Vilar, rather it is intended to illustrate how discussion of phase transformations in titanium are complicated by the diversity present in literature that has been quoted many times. In writing this work, interpretive difficulties were also encountered due to this diversity. This highlights an avenue for further work from which a better, and hopefully unified, understanding of the phase transformations (especially the martensitic transformations) in titanium may be understood.

6. GRAIN REFINEMENT VIA BORON ADDITIONS TO Ti-6Al-4V

The previous two chapters have demonstrated that EBM processing, under standard operating conditions, results in a columnar, textured prior β microstructure. Whilst it has been shown in the Numerical Modelling Chapter that the production of equiaxed prior β grains is possible; the conditions used to achieve such a microstructure are effectively those required to produce an electron beam weld and are thus inappropriate for ALM.

A review of the literature reveals the potential to refine Ti-6Al-4V microstructures through the addition of relatively small amounts of boron (≤ 1 wt%). As well as refining the scale of Ti-6Al-4V microstructures, boron additions have also been reported to weaken the texture of a solidified ingot [137]. This chapter will discuss the addition of boron to Ti-6Al-4V, and the effect of EBM processing, in an attempt to interrupt the constrained growth of prior β grains and produce a less textured, more equiaxed prior β microstructure.

6.1. Introduction

After the formation of columnar prior β grains during EBM, transformation on cooling generally results in continuous layers of α_{GB} along prior β grain boundaries. In some cases, single/large α colonies may form within a prior β grain, resulting in macro-scale structural units that are detrimental to mechanical properties. For many applications, this standard EBM microstructure would not be considered ideal.

The control of microstructure is highly sought after in ALM processing and a process in which morphology could be controlled would undoubtedly attract much interest. The first step towards controlling microstructure is the production of equiaxed or even 'less columnar' prior β grains. To date, refinement of the prior β grain structure in EBM is unreported. Microstructural refinement may be possible by two methodologies; (i) changing beam scan strategies in order to interrupt solidification conditions [73] and/or (ii) refinement of grain structure by the addition of a grain refiner. Whilst scan strategies may eventually result in the formation of equiaxed grains, changes to the beam path during EBM would require access to the underlying beam control software.

A relatively recent development, and a potential avenue for future research, is the use of the *multi-beam* capability introduced into the Arcam system. *Multi-beam* technology has been used in electron beam welding and involves rapid deflection of the electron beam. Rapid deflection allows the beam to be 'split' into many beams; in reality, the beam moves extremely quickly between positions. Arcam have implemented *multi-beam* to melt the *contours* of components with the ability to maintain up to 50 melt pools simultaneously. Zhao *et al.* [138] discuss the use of a *multi-beam* electron beam welding system to reduce residual stresses in the weld in which the electron beam is 'split' into three beams with different properties. The three beams correspond to (i) a defocused preheating beam ahead of the weld, (ii) a focussed melting beam producing the weld and (iii) a defocused melting beam behind the weld for smoothing. Although the three beams are used in order to reduce stress, from an EBM perspective, 'split' beams travelling behind the main beam could be used to decrease the cooling rate and thermal gradient during solidification. In theory, the potential exists to modify the solidification conditions and promote equiaxed solidification by making use of *multi-beam*.

Control of solidification conditions is perhaps the best way of controlling microstructure. The reason for this is that the morphology could be varied spatially within a component and thus default (columnar) or modified (equiaxed) microstructures could be produced as and where necessary. However, such process control is likely to be a long term goal.

Boron additions to cast titanium alloys have already been identified as a relatively simple means of producing bulk grain refinement. The grain refinement arises because of enhanced nucleation via constitutional supercooling. In this work it was hoped that the enhanced nucleation would help to refine the prior β grain structure. Experiments have been carried out on Ti-6Al-4V powder with the addition of elemental boron and on solid Ti-6Al-4V-*x*B substrate materials – the reasons for this will be discussed in the following sections.

Figure 6.1 shows schematically the current solidification of a melt pool during EBM ((a), (b) and (c)) and the result hoped for by making additions of boron to promote nucleation ((a), (d) and (e)). Effectively, it was hoped that the addition of boron would result in a region of equiaxed grains thus promoting a columnar to equiaxed transition.

6.2. Direct Melting of Ti-6Al-4V-*x*B

Mixing of 1 μm ⌀ elemental boron powder with 45 – 100 μm ⌀ Ti-6Al-4V powder was carried out to produce a powder mixture containing 0.02 wt% B. The binary Ti-B phase diagram indicates that the solid solubility of B in Ti is <0.02 wt% and Tamirisakandala *et al.* [27] identified a TiB volume fraction of 0.1% after the addition of 0.02 wt% boron to Ti-6Al-4V. The intention of the direct melting experiments was to produce samples at a specific boron concentration, before adding more boron to the powder mixture, to produce a set of EBM samples with increasing boron concentrations. Using standard Ti-6Al-4V melt *themes*, the 0.02 wt% B powder mixture was melted in the Arcam EBM system.

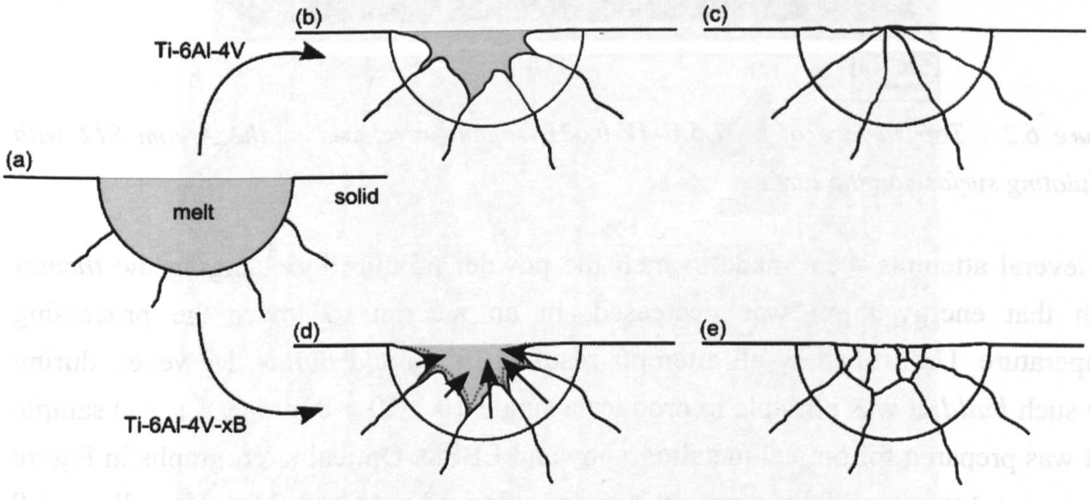

Figure 6.1 : Schematic diagram showing prior β grains during melt pool solidification. Route (a) → (b) → (c) represents the current result of solidification in EBM Ti-6Al-4V. Route (a) → (d) → (e) represents the hypothesised effect of boron additions. In (d), boron partitioning ahead of the solidification front produces a boron-rich boundary layer and promotes nucleation of further grains, disrupting the typical columnar prior β microstructure.

Although a relatively small amount of boron was added to the Ti-6Al-4V powder, this was found to have a significant effect on the melting characteristics. A result of EBM processing of the 0.02 wt% B powder mixture is shown in Figure 6.2; the figure shows the top surface of a 2 mm tall sample. The sample was intended to be 10 mm in height, from which a tensile sample would have been produced. However, the top surface of the sample consists of 'bubbles' which protruded above the surface of the powder bed. During processing, the protrusions caused damage to the *rake* blades. A combination of the undulating surface and the damaged *rake* meant that further powder layers could not be applied and deposition was stopped prematurely. The 'bubbles' were one of two issues encountered during melting; the second issue, and the likely cause of the 'bubbles', was an abrupt increase in temperature during melting. During standard processing, excessive *build* temperatures (> 700 °C) have been observed to result in a poor top surface that is not flat.

In this case, the temperature increase resulted from the exothermic reaction between Ti and B. This reaction has been used for making thermite mixtures in which the reaction is self-propagating owing to the significantly exothermic effect [139]. Clearly, the use of standard Ti-6Al-4V *themes* is not appropriate for melting such a powder mixture.

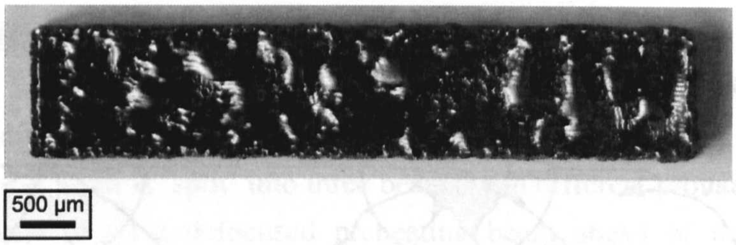

Figure 6.2 : Top surface of a Ti-6Al-4V-0.02B sample produced in the Arcam S12 with undulating surface on the surface.

Several attempts were made to melt the powder mixture by changing the *themes* such that energy input was decreased, in an attempt to lower the processing temperature. Unfortunately all attempts resulted in aborted *builds*. However, during one such *build*, it was possible to produce a single 10 × 10 × 8 mm ($x \times y \times z$) sample that was prepared for optical metallography and EBSD. Optical micrographs in Figure 6.3 show (a) the prior β grain structure under polarised light and (b) the lamellar α + β grain structure within prior β grains.

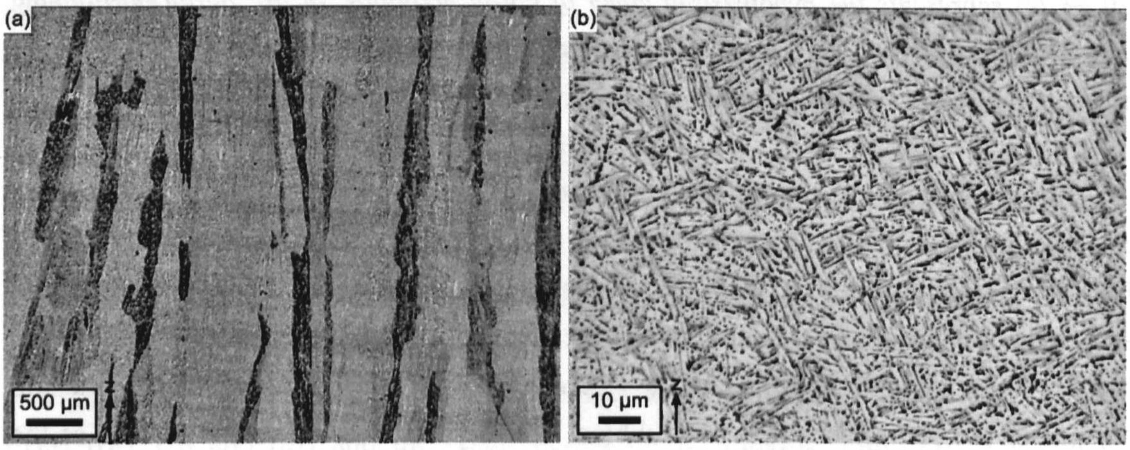

Figure 6.3 : Optical micrographs of Ti-6Al-4V-0.02B showing (a) columnar prior β grain structure under polarised light and (b) the transformed lamellar microstructure.

Figure 6.3 (a), and prior β grain reconstruction of EBSD data in Figure 6.4, both reveal a columnar prior β grain structure. Microstructural refinement of the prior β grain structure was therefore not achieved. Previous work suggests that at boron concentrations below a critical value, approximately 0.06 wt%, any boron rejected into the liquid can be readily dispersed and so grain refinement is small [27]. In order to form a boron-rich boundary layer during solidification, investigations of material with increased boron contents was required. However, the difficulties encountered using the Ti-6Al-4V and elemental boron powder mixture were expected to escalate with increasing amounts of boron; thus an alternative method was employed.

The alternative method was advantageous for two reasons, (i) the material used was pre-alloyed with boron (mitigating the exothermic reaction) and (ii) several boron concentrations were investigated simultaneously.

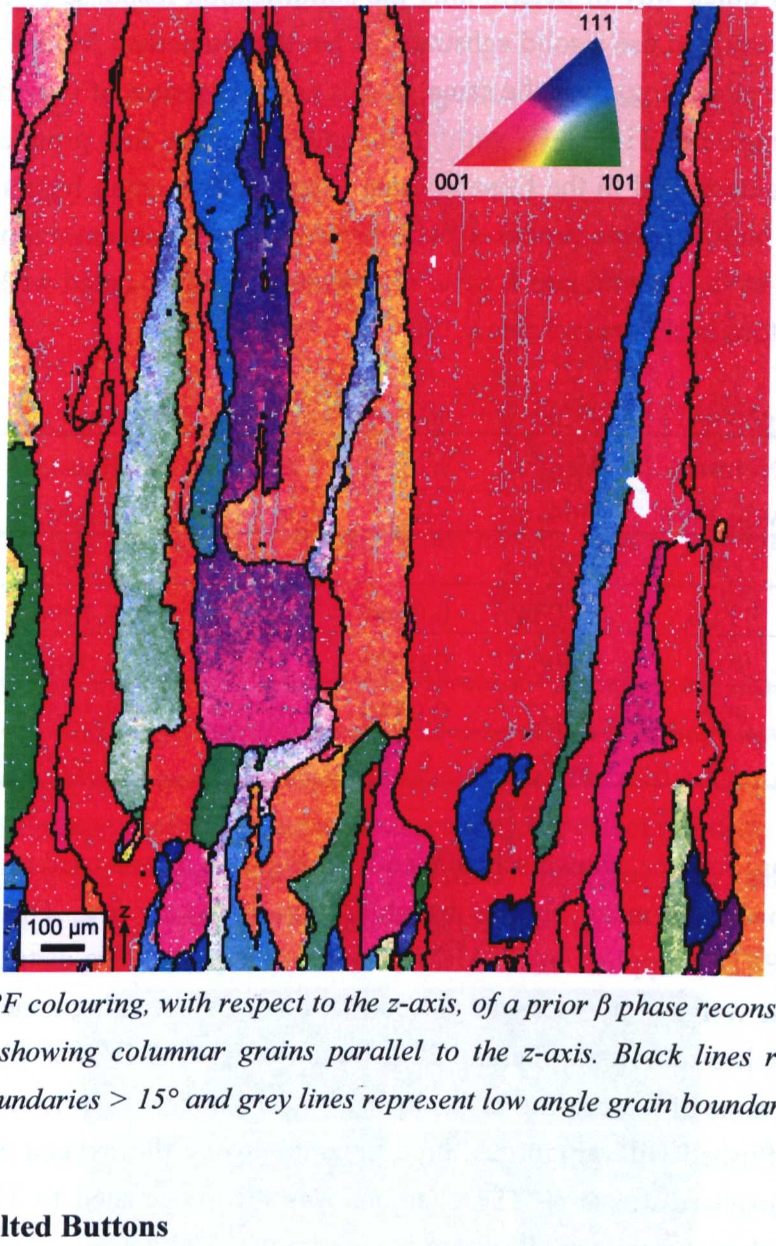

Figure 6.4 : IPF colouring, with respect to the z-axis, of a prior β phase reconstruction of Ti-6Al-4V-0.02B showing columnar grains parallel to the z-axis. Black lines represent high angle grain boundaries > 15° and grey lines represent low angle grain boundaries > 5°. Step size = 5 µm.

6.3. Arc Melted Buttons

The investigation of 'new' materials in the EBM process is challenging for two reasons. Firstly, due to the ease at which powders can become contaminated or accidentally mixed, cleanliness and labelling are of utmost importance. Thus the use of powders with different chemical compositions requires the EBM machine, all auxiliary equipment and all tools to be thoroughly cleaned. The second difficulty arises due to the size of the *build chamber*; even if very small samples are required, each 100 µm layer of powder must cover the area of the powder bed (220 mm × 220 mm). Practically, this means that an experimental batch of powder will weigh approximately 20 kg. The production of bespoke powders is expensive and, when considering multiple chemistries, a 20 kg powder batch would be required for each composition.

A relatively quick way of determining the solidification response of a material to the electron beam is to use a solid substrate, as per the Numerical Modelling Chapter. Although the methodology was the same, in this case substrates of varying chemistry were used. Samples of Ti-6Al-4V with boron additions were first produced by argon arc melting, as described in the Experimental Chapter. Five small ingots (henceforth referred to as buttons) were produced with nominal boron concentrations of 0 wt%, 0.05 wt%, 0.1 wt%, 0.4 wt% and 1 wt%. The nominal and calculated wt % B for each of the five buttons is shown in Table 6.1.

Table 6.1 : Weights of Ti-6Al-4V powder and boron used to make buttons.

Nominal wt% B	Nominal wt% Ti64	Weight Ti64, g	Weight B, g	Calculated wt% B	Button Weight, g	Weight Change, g
0	100	8.5951	0	0	8.5951	0
0.05	99.95	8.7034	0.0060	0.069	8.7096	+0.0002
0.1	99.9	8.0060	0.0080	0.100	8.0144	+0.0004
0.4	99.6	8.522	0.0340	0.399	8.5567	+0.0007
1	99	9.573	0.10	1.045	9.6603	-0.0127

An argon arc furnace, shown schematically in Figure 6.5, was used initially to melt Ti-6Al-4V powder to make buttons weighing approximately 9 g. The powder was produced by PREP, supplied by STARMET and had a quoted size distribution of 125 – 250 μm. The weighed powder was placed into one of the melting zones on a water-cooled copper hearth. An arc melted, 20 g button of Ti-6Al-4V was placed into the other melting zone of the hearth. After closing, the chamber was evacuated to a rough vacuum and flushed with argon gas three times to ensure the oxygen content of the chamber atmosphere was low. The chamber was then evacuated to 10^{-3} Pa before backfilling with high purity argon gas to a pressure of ~ 30 kPa.

Prior to melting the Ti-6Al-4V powder, the 20 g Ti-6Al-4V button was melted and acted as an oxygen getter, removing further oxygen from the chamber atmosphere. The Ti-6Al-4V powder was then melted to form a button weighing approximately 9 g; this was allowed to cool to room temperature under argon. The cooled button was then weighed in a weigh boat and an appropriate amount of solid, elemental boron added to achieve the desired composition. The contents of the weigh boat were then melted as described above to produce a Ti-6Al-4V-xB button. However, the boron containing buttons were turned over and melted four times to promote homogeneity via convection in the liquid material.

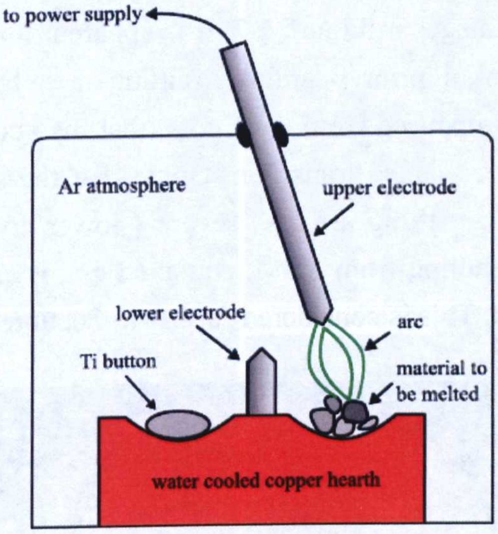

Figure 6.5 : Schematic diagram of the argon arc furnace used to produce Ti-6Al-4V-xB buttons [140].

Images of the arc melted buttons are given in Figure 6.6 with a noticeable difference in the shrinkage cavity formed. The size of the shrinkage cavity decreases with increasing boron content and, at a boron concentration of 0.4 wt% and above, no discernable shrinkage cavity is present. In describing the effect of boron content in Ti-B alloys, Whang [141] notes that lattice parameter increases with increasing boron content as a result of boron occupying interstitial positions.

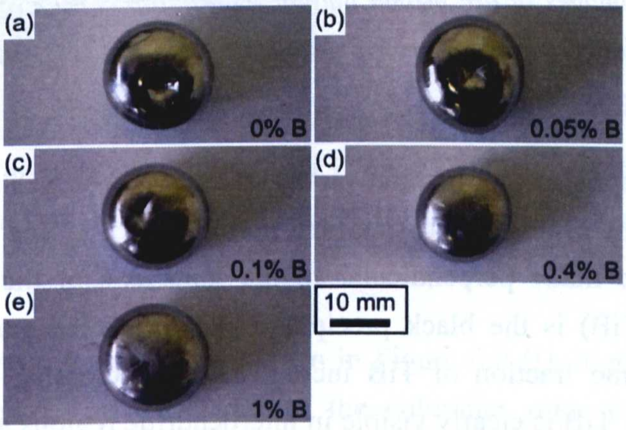

Figure 6.6 : Images of arc melted buttons and target nominal boron concentrations.

Figure 6.7 shows macro-images of the prepared metallographic samples for the 0 and 1.05 wt% B samples. It is clear from the figure that the addition of boron refines the prior β grain size. Whilst in both samples the prior β morphology is columnar, the number of columnar grains is increased in the 1.05 wt% boron sample. In considering the way in which the buttons solidify, grains will nucleate first at the interface between the liquid metal sample and the copper hearth – the position of this interface is at the bottom of the images in Figure 6.7. It is apparent that the presence of boron increases the nucleation of prior β grains resulting in a finer columnar structure. However, it can also be deduced from the figure, that the addition of boron does not result in a columnar to equiaxed transition. Given that the solidification conditions resulting from argon-arc melting are less severe (slower cooling rates and thermal gradients) than those resulting from EBM, equiaxed grains are also unlikely to form during the EBM process. This is considered further in Section 6.3.2.

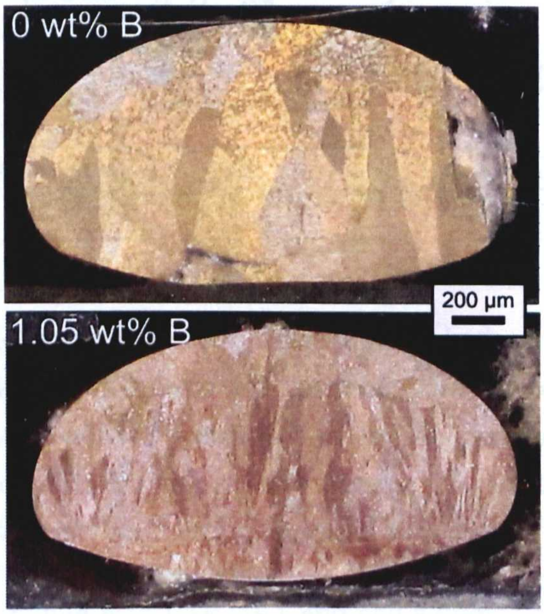

Figure 6.7 : Macro images of arc melted buttons with boron concentrations of 0 wt% and 1.05 wt%. At 0 wt% large, columnar prior β grains are visible. At 1.05 wt% refinement in the prior β grain structure is clear.

Optical micrographs of the material produced can be seen in Figure 6.8 (a) – (e) alongside a graph of prior β grain size measurements in (f). The prior β grain size measurements were made perpendicular to the long axis of the columnar grains. Titanium boride (TiB) is the black precipitate phase in micrographs (b) – (e). As expected, the volume fraction of TiB increases with increasing boron content. In Figure 6.8 (b) – (e), TiB is clearly visible in interdendritic regions as a result of boron rejection into the liquid during solidification. Optical micrographs at higher magnifications are presented in Figure 6.9 and, at boron contents ≥ 0.1 wt%; the interdendritic TiB particles make the dendritic microstructure structure easily identifiable. At the highest concentration of boron, 1.05 wt%, the dendrites become less apparent and larger laths of TiB are present.

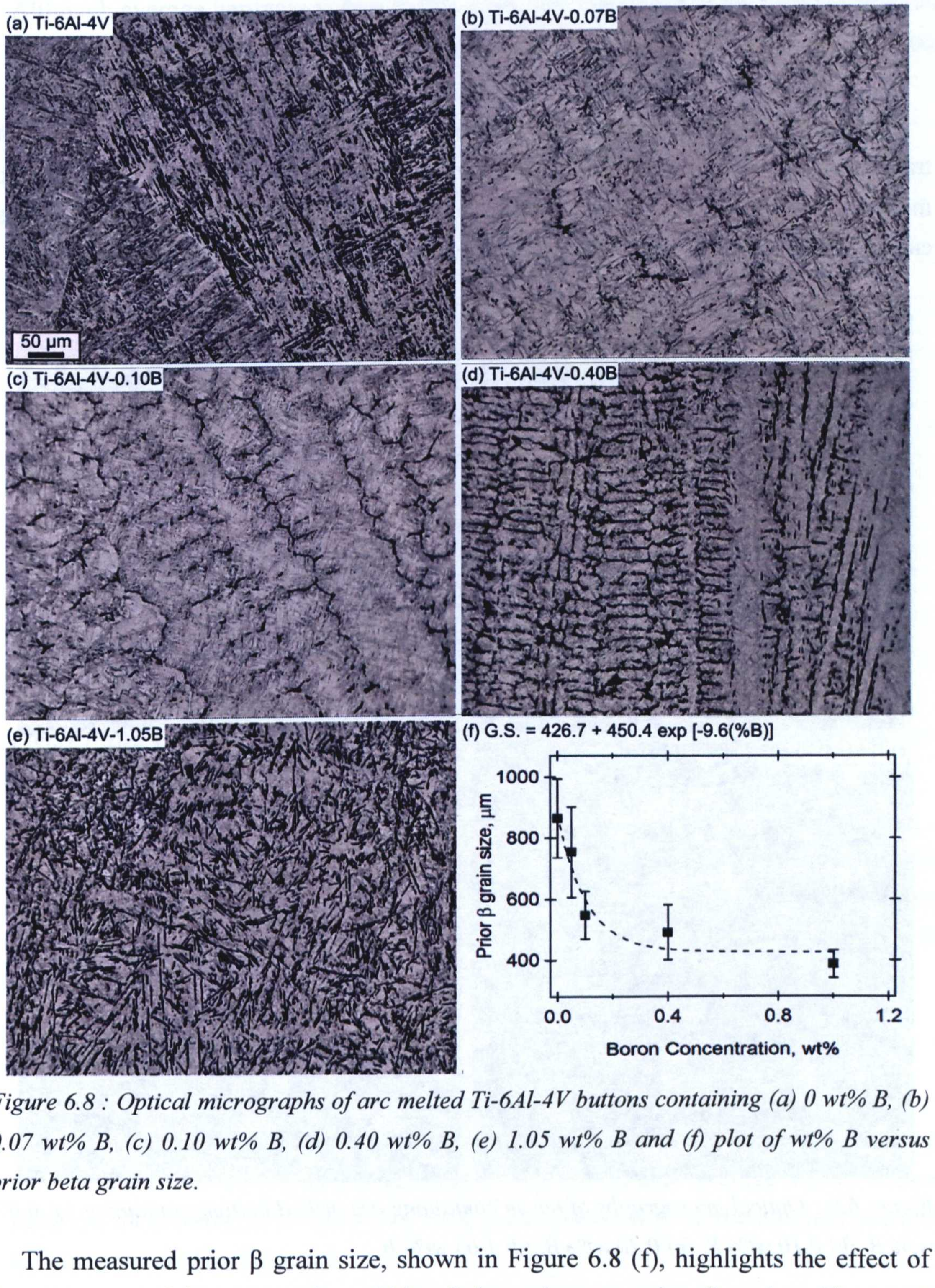

Figure 6.8 : Optical micrographs of arc melted Ti-6Al-4V buttons containing (a) 0 wt% B, (b) 0.07 wt% B, (c) 0.10 wt% B, (d) 0.40 wt% B, (e) 1.05 wt% B and (f) plot of wt% B versus prior beta grain size.

The measured prior β grain size, shown in Figure 6.8 (f), highlights the effect of the presence of boron on the width of the columnar prior β grains. The most significant drop in prior β grain size occurs at boron concentrations of ≤ 0.1 wt%. Although increasing boron concentration produces further refinement, the reduction in grain size is less pronounced. This reduction in refinement at > 0.1 wt% B has also been reported in other work [27]. From Figure 6.8 (f), the relationship between boron concentration and prior β grain size (d_β) has been determined to be:

$$d_\beta = 426.7 + 450.4 \times \exp[-9.6(\text{wt\% B})] \qquad (6.1)$$

Although applicable here, the relationship given in Equation (6.1) is not transferable. It is only applicable to the production of ~10 g buttons by argon arc melting. In other methods of production, e.g. ingot casting, solidification conditions can be significantly different and will influence microstructural scale accordingly.

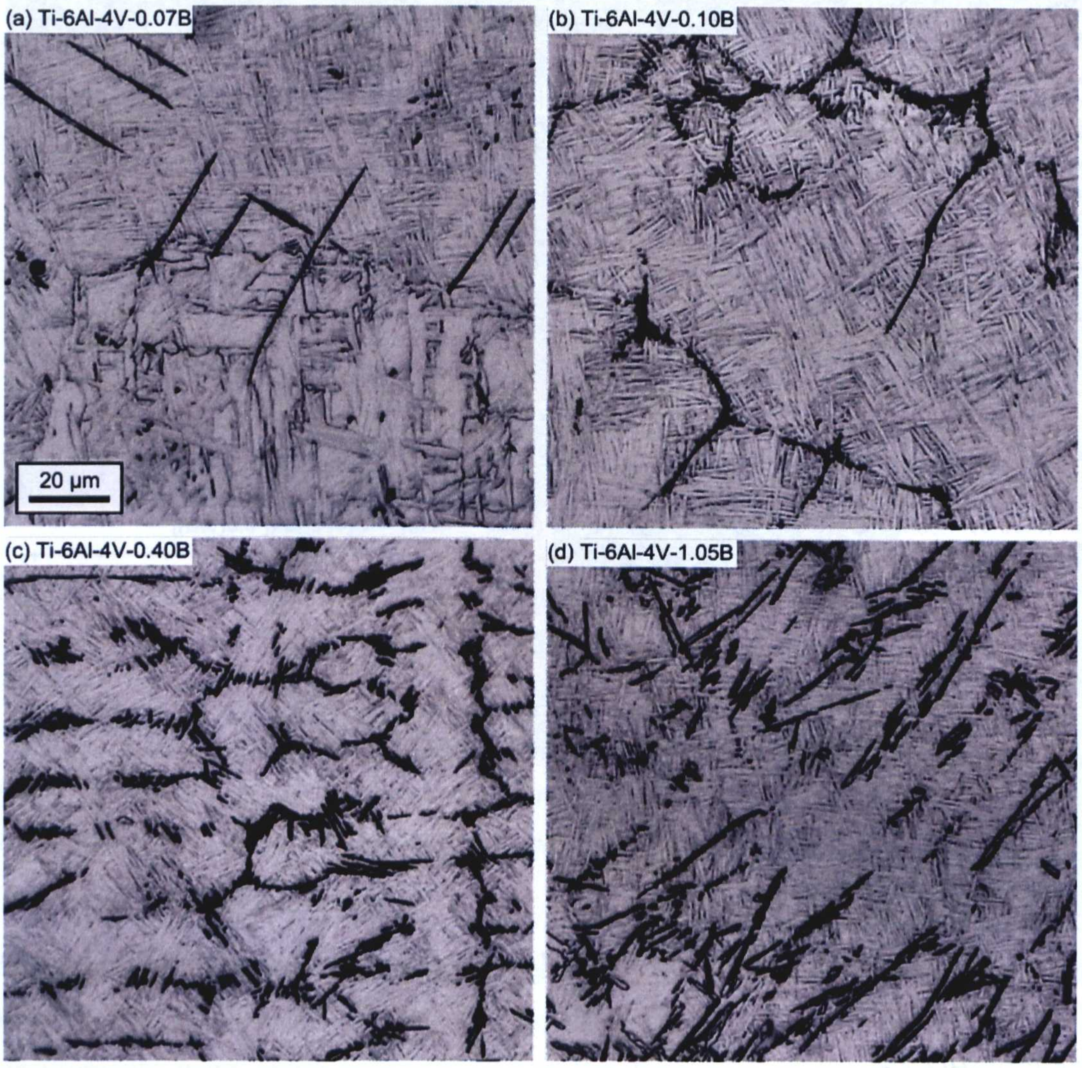

Figure 6.9 : Optical micrographs of boron containing arc melted buttons containing (a) 0.07 wt% B, (b) 0.10 wt% B, (c) 0.40 wt% B, (d) 1.05 wt% B.

The limited amount of material produced by arc melting meant that it was not possible to determine its strength via tensile testing. The effect of boron additions on the mechanical properties of Ti-6Al-4V has been investigated by Sen *et al.* [29]; these results are presented in Figure 2.11 of the Literature Review. Values of Vickers hardness determined in this study and by Sen *et al.* [29] are compared in Figure 6.10.

Although average hardness values in this work are lower than those found in previous work [29], there is a large amount of scatter in the data from the previous work and the results from this study fall within the range of scatter.

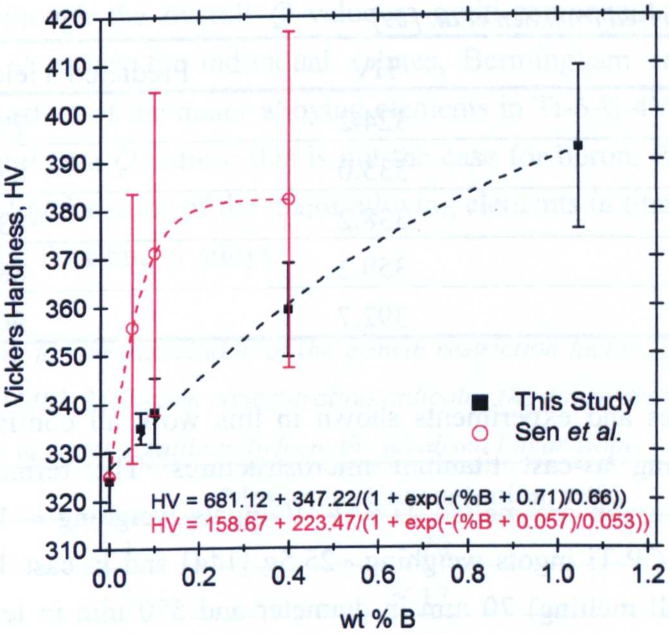

Figure 6.10 : Vickers hardness versus boron content of the arc melted buttons from this study and cast Ti-6Al-4V from [29]. Error bars for data in this study represent 95%CL.

The empirical relationship between Vickers hardness and yield strength (Equation (6.2)) has been used in Chapter 5. The work carried out by Sen *et al.* [29] measures both Vickers hardness and yield strength; using these results and assuming the empirical relationship relating hardness and strength is of the form:

$$\sigma_y = k \times HV \qquad (6.2)$$

where k is the proportionality constant; k can be calculated and covers the range 2.39 – 2.57 with an average value of 2.46. Based on this average value, Vickers hardness measurements in this study have been converted to predicted yield strengths and are presented in Table 6.2.

The increase in hardness (and thus yield strength) with boron concentration is attributable to (i) increasing strength due to the observed microstructural refinement and the reduction in slip length [29] and/or (ii) the load carrying capacity of TiB [142]. At lower levels of boron (≤ 0.4 wt%) strengthening due to the Hall-Petch effect is thought to dominate [29] whilst at increased concentrations of boron (1.6 wt%) the dominant mechanism is reported to be that of load carrying [143]. The effectiveness of TiB particles also depends on their size, morphology and orientation [142].

Table 6.2 : Predicted yield strength of boron containing alloys based on a proportionality constant of 2.46, derived from Sen et al. [29].

wt% B	HV	Predicted Yield Strength, MPa
0	324.2	798.3
0.07	335.0	825.0
0.100	338.2	832.8
0.399	359.2	884.5
1.045	392.7	967.0

Previous studies and experiments shown in this work all confirm that boron is capable of refining as-cast titanium microstructures. The refinement has been observed here in argon arc melted Ti-6Al-4V ingots weighing < 10g, and in both argon arc melted CP-Ti ingots weighing ~25.5g [144] and in cast Ti-6Al-4V ingots (by induction skull melting) 70 mm in diameter and 500 mm in length [27]. It has been discussed briefly in Section 2.4.2 that the mechanism thought to cause microstructural refinement is the rejection of boron into the liquid phase resulting in constitutional supercooling. The presence of TiB in interdendritic regions, as per Figure 6.9, supports this mechanism. As previously mentioned, the relative contribution of a solute to constitutional supercooling can be predicted by use of the growth restriction factor Q; this is discussed further in the following section.

6.3.1. Growth Restriction

Grain refinement, and the degree to which it occurs, is a balance between latent heat production and heat extraction [145]. Under normal circumstances, grain refinement is inefficient because of the latent heat released by the first nuclei to form. Such nucleation events limit the amount of undercooling achievable in the melt [145, 146]. Partitioning rate of the solute at the solid-liquid interface, and its diffusion in the melt, limits the rate of latent heat production.

In idealised binary systems (in which the solidus and liquidus are linear), the diffusion limited growth rate of a sphere, proposed by Maxwell and Hellawell [146], at a given melt undercooling and sphere radius, is inversely proportional to the thermodynamic quantity Q (the growth restriction factor), given in Equation (6.3). This is also true for dendritic growth [147].

$$Q = m_l C_o(k-1) \qquad (6.3)$$

where m_l = the slope of the liquidus, C_o = the solute content, and k = the partition coefficient.

The contribution of a solute to the rate of development of a constitutionally supercooled zone is thus described by Q; the larger the value of Q, the more effective the solute [28]. Although the overall Q value in multi-component systems is the summation of the Q values for individual solutes, Bermingham *et al.* [148,149] determined that the effect of the major alloying elements in Ti-6Al-4V (Al, V, Sn, Zr and Mo) have insignificant Q values; this is not the case for boron. Parameters used for the calculation of Q for some of the major alloying elements in titanium alloys are given in Table 6.3 for Ti-X binary alloys.

Table 6.3 : Parameters for the calculation of the growth restriction factor, Q, in Ti-X binary alloys, adapted from [148]. Maximum concentration indicates the concentration above which the real liquidus slope deviates significantly from the idealised linear slope.

Element	m_l	k	Maximum Concentration, wt%	$m_l(k-1)$
Al	-1.7	$\rightarrow 1$	≤ 20	$\rightarrow 0$
V	-2	$\rightarrow 1$	≤ 12	$\rightarrow 0$
Sn	-1.8	$\rightarrow 1$	≤ 35	$\rightarrow 0$
Zr	-2.3	$\rightarrow 1$	≤ 55	$\rightarrow 0$
Mo	6.5	2	≤ 30	6.5
B	-65	$\rightarrow 0$	≤ 2	65

Using the values of m_l and k from Table 6.3, the variation in prior β grain size and Q have been plotted for the boron containing buttons; these are shown in Figure 6.11 (a). As reported elsewhere [27], good correlation between Q and prior β grain size is indicative of the effect of boron on growth restriction. Comparison between data from this study and that of previous authors, in which boron additions were made to Ti-6Al-4V, are given in Figure 6.11 (b). Although the general effect of boron is comparable, i.e. decreasing prior β grain size and a decrease in effectiveness with boron concentrations > 0.1 wt%, the size of the refinement of prior β grain structure is quite different. In this study, the addition of 0.40 wt% boron reduces prior β grain size by a factor of 1.8. In the work used for comparison and at the same boron concentration, prior β grain size is reduced by a factor of 16.

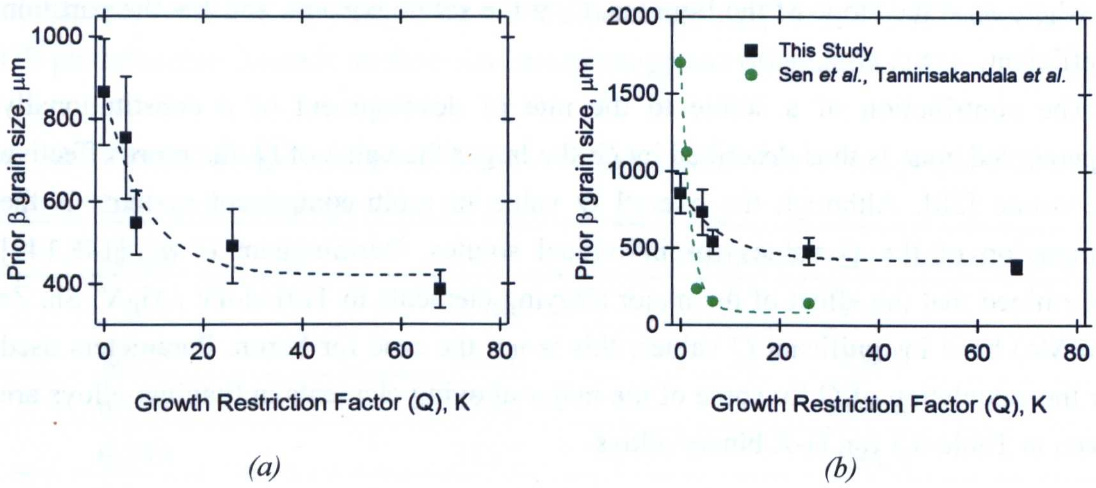

(a) *(b)*

Figure 6.11 : (a) Prior β grain size versus growth restriction factor (Q) for the arc melted buttons and (b) a comparison between results from this study and from the literature [27, 29].

Work by Easton and StJohn [150] reported that grain size could be related to solute content, in aluminium alloys with TiB_2 and Ti additions, using the relationship:

$$d = \frac{1}{\sqrt[3]{\rho \cdot f}} + \frac{b_1 \Delta T_n}{Q} \tag{6.4}$$

where d = grain size, ρ = volume density of nucleant particles, f = fraction of particles that are activated, b_1 = a constant, Q = growth restriction factor and ΔT_n is the undercooling required to activate nucleation. In later work, the refinement of CP-Ti with silicon [149] and CP-Ti with boron [28] were analysed using Equation (6.5) – a simplification of Equation (6.4).

$$d = a + \frac{b}{Q} \tag{6.5}$$

In the semi-empirical relationship, a and b are constants and plots of d against $1/Q$ yield a straight line in which the gradient corresponds to nucleant potency (owing to the development of a constitutionally supercooled zone) and the intercept is related to the availability of nuclei [149]. The data from this study, and the study used for comparison in Figure 6.11, have been plotted according to Equation (6.5) and are shown in Figure 6.12.

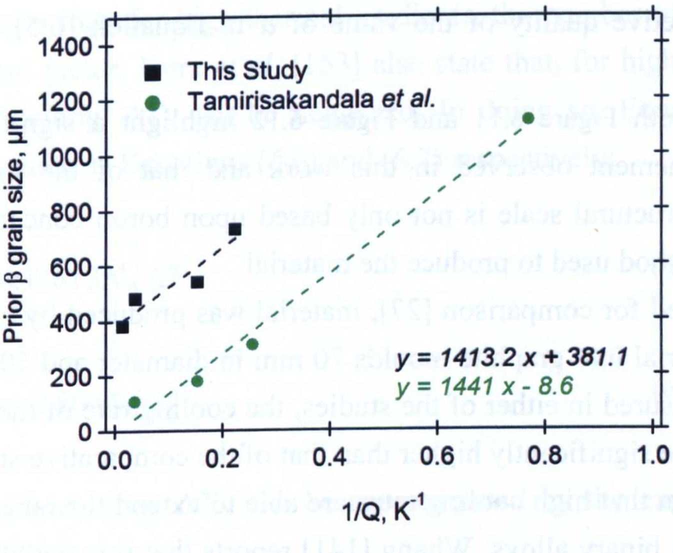

Figure 6.12 : Prior β grain size versus 1/Q for this study and Tamirisakandala et al. [27].

The gradient of both linear best fit lines in Figure 6.12 are similar – 1413 μmK against 1441 μmK. This result is encouraging given that the two separate sets of experiments, using two differing casting techniques, result in a similar value for boron potency (*b* in Equation (6.5)).

When discussing the effect of silicon on grain size in CP-Ti, Bermingham *et al.* [149] compare their data to that of another author using Equation (6.5). The values of *a* are considered to be the minimum grain sizes achievable. However, in this case, the value of *a* in Figure 6.12 for the data shown in green is negative; the reason for this is evident from Figure 6.11 (b). Whilst Equation (6.5) predicts that increasing values *Q* (increasing solute) results in a decreasing value of *d*; this is only valid over a range of boron concentrations due to the decreasing effectiveness of grain refinement above 0.1 wt% B. Physically there is a value of *Q* above which further grain refinement does not occur – this is not taken into consideration in Equation (6.5).

As well as being bounded by a lower grain size limit, values of *Q* in Equation (6.5) should also be bounded by an upper and lower limit when the Ti-B phase diagram is considered. The partitioning effect of boron is only applicable in the hypoeutectic region which lies between boron concentrations of ≥0.02 wt% B and <1.67 wt% B [151]. Thus the range of values over which *1/Q* is physically applicable are 0.009 – 0.77 K^{-1}.

Based on the lower limit of *1/Q* (0.009 K^{-1}), the minimum grain size for the material in this study is predicted to be 394 μm. This limit is not appropriate for work published by the previous authors owing to the apparent saturation reached. Figure 6.11 (b) indicates that the minimum prior β grain size in the previous work is approximately 140 μm. Because of the lack of a means of accounting for a saturation effect, the interpretive quality of the value of a in Equation (6.5), in this case, is questionable.

Nonetheless, both Figure 6.11 and Figure 6.12 highlight a significant difference between the refinement observed in this work and that of the previous authors. However, microstructural scale is not only based upon boron concentration but also the processing method used to produce the material.

In the work used for comparison [27], material was produced by casting induction skull melted material into graphite moulds 70 mm in diameter and 500 mm in length. Although not measured in either of the studies, the cooling rate of the material in this work is likely to be significantly higher than that of the comparative study.

It is well known that high cooling rates are able to extend the range of solute solid solubility. In Ti-B binary alloys, Whang [141] reports that it is possible to extend the solid solubility of B to 2.45 wt% by rapid solidification and suggests that boron atoms become an interstitial solute. Fan *et al.* [152] also reports that melt-spun Ti-6Al-4V-1B fibres contain no TiB precipitates although state '*there was a boron concentrated region between the equiaxed dendrites and columnar grains*'. Whilst it is clear that TiB particles are present in the argon arc melted material it is possible that:

(i) The high cooling rate extended the solid solubility of boron above 0.02 wt% and thus the calculated values of Q are larger than the actual values of Q.

(ii) The short solidification time in argon arc melting limited the number of nuclei that could form in comparison to cast material.

Although smaller than previous work has reported, the addition of boron to Ti-6Al-4V has been observed here to yield a microstructural refinement. Unfortunately this refinement has not been accompanied by a change in morphology. By considering the solidification conditions experienced during EBM, the following section will explore, theoretically, the expected behaviour during EBM of a Ti-6Al-4V-xB alloy.

6.3.2. Columnar to Equiaxed Transition (CET) during EBM

As discussed in Chapter 4, Equations (4.13) and (4.14) describe the solidification conditions necessary to form columnar, mixed and equiaxed grains in Ti-6Al-4V. Figure 6.7 shows the lack of a CET with boron additions to material solidified in the argon arc melter. Given that EBM processing results in faster solidification, the arc melted material indicates that a CET is unlikely to be present in EBM material. Whilst the solidification conditions of the arc melted material are unknown, EBM solidification conditions, calculated in Chapter 4, may be used to predict the response of EBM Ti-6Al-4V-xB.

Hunt [100] states that, for high thermal gradients, the number of nucleation sites, N_0, is an important factor; Kurz *et al.* [153] also state that, for high values of G, the nucleation undercooling, ΔT_n can be neglected. In doing so, Equations (4.13) and (4.14) can be rewritten as Equations (6.6) and (6.7) respectively:

$$G < 0.617 N_0^{\frac{1}{3}} \Delta T_c \tag{6.6}$$

$$G > 2.864 N_0^{\frac{1}{3}} \Delta T_c \tag{6.7}$$

The solutal undercooling, ΔT_c, can be approximated by the expression given in Equation (6.8) [153]:

$$\Delta T_c = \Delta T_0 (a \cdot R)^{\frac{1}{n}} \tag{6.8}$$

where ΔT_0 is the equilibrium solidus-liquidus interval, a and n are material constants and R is the solidification front velocity. Equation (6.8) can thus be substituted into Equations (6.6) and (6.7) giving:

$$G < 0.617 N_0^{\frac{1}{3}} \Delta T_0 (a \cdot R)^{\frac{1}{n}} \tag{6.9}$$

$$G > 2.864 N_0^{\frac{1}{3}} \Delta T_0 (a \cdot R)^{\frac{1}{n}} \tag{6.10}$$

Consideration of the above equations, for constant values of a and n, gives an indication of how boron additions may affect solidification and promote/facilitate a columnar to equiaxed transition. An increase in either N_0 or ΔT_0 will act to increase the threshold values of G, for both the columnar and equiaxed regions, to higher values. Under these circumstances, the columnar region would be contracted whilst the equiaxed region would be expanded.

In order to make use of Equations (6.9) and (6.10), values of N_0, ΔT_0, a and n are required. N_0 has been determined for each of the boron compositions by calculating the number of grains per unit area in the arc melted buttons. Thermodynamic software JMatPro was used to predict the ΔT_0 temperature range for the binary alloys Ti-*x*B and Ti-6Al-4V-*x*B; a ΔT_0 value of 50 K was used for Ti-6Al-4V with no boron additions. The measured values of N_0 and predicted values of ΔT_0 are given in Table 6.4.

Table 6.4 : Measured values of N_0 and JMatPro predicted values of ΔT_0 for boron compositions in this study.

wt% B	N_0, cm^{-3}	ΔT_0, Ti-xB, K	$N_0^{\frac{1}{3}}\Delta T_0$, cm^{-1}K	ΔT_0, Ti-6Al-4V-xB, K
0	354.1	-	354	50
0.07	761.9	119	1087	241
0.1	1001.5	117	1171	254
0.4	1155.4	89	934	320
1.05	1208.3	34	362	340

Interestingly, there is a large discrepancy between the predicted ΔT_0 values for the Ti-xB and Ti-6Al-4V-xB alloy systems. When considering the influence of boron on Ti-6Al-4V, previous authors have consulted the Ti-B binary phase diagram owing to the lack of information regarding the Ti-6Al-4V-xB system. Table 6.5 shows that there is good agreement between JMatPro predictions of ΔT_0 and values taken from the Ti-B phase diagram. However, no information is available to confirm or otherwise the ΔT_0 predictions for the Ti-6Al-4V-xB alloys. Without further work, the use of these values would be somewhat questionable. Based upon previous authors depending on the Ti-B phase diagram, ΔT_0 values for the Ti-B alloy system will be used to calculate the CET in this work.

Table 6.5 : Comparison of JMatPro predicted ΔT_0 values and those taken from a phase diagram of the Ti-B binary system.*

wt% B	ΔT_0 prediction from JMatPro, K	ΔT_0 from phase diagram*, K
0.07	119	122
0.1	117	120
0.4	89	95
1.05	34	44

*see Figure 6.13.

Values of a and n may be calculated, for Ti-6Al-4V, by making use of the solidification map generated by Kobryn and Semiatin [71] and used in Chapter 4. By substituting the determined values of N_0 and ΔT_0 from Table 6.5, and G and R values from the solidification map, Equations (6.9) and (6.10) can be solved to determine a and n. These calculated values of a and n were assumed constant for all of the boron compositions. The calculated values are given in Table 6.7.

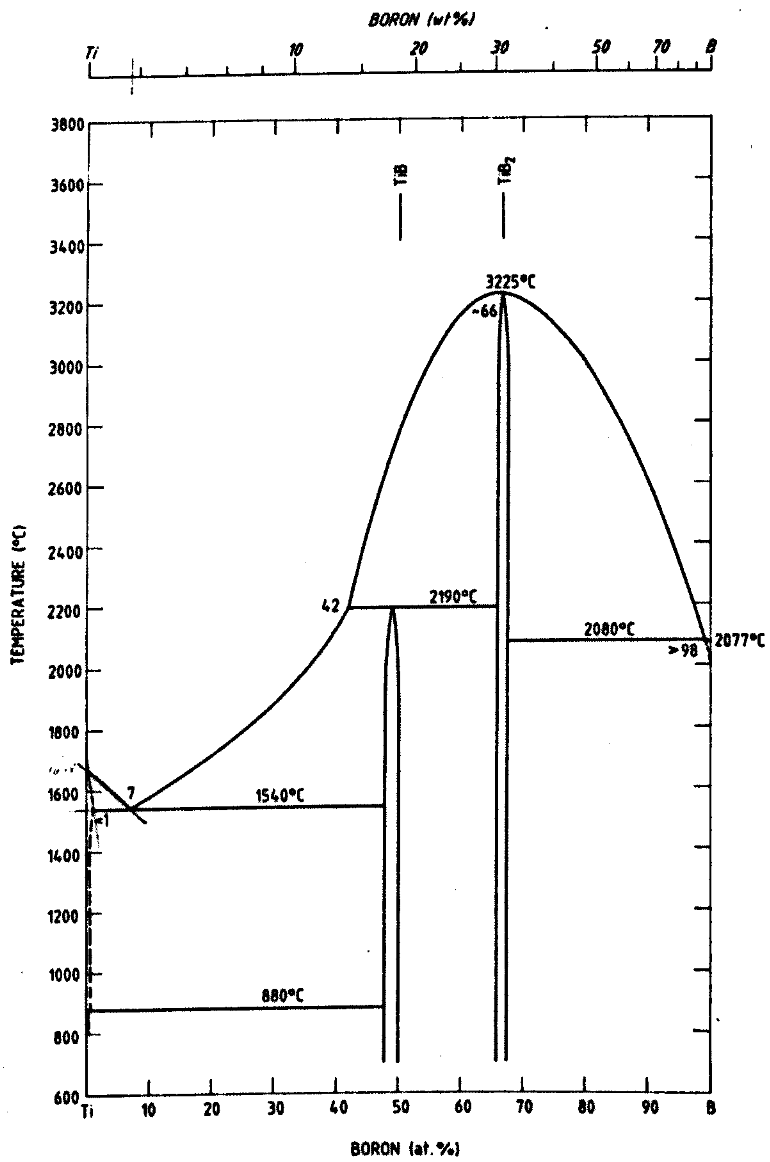

Figure 6.13 : Ti-B binary phase diagram [151].

Table 6.6 : Calculated values of a and n to fit Kobryn and Semiatin's solidification map.

Boundary	*a*	*n*
Equiaxed	38.9	1.92
Columnar	46.3	2.03

It is unsurprising that fitting of the results gives *n* values of ~2; the Kobryn and Semiatin map was based on Hunt's work in which *n* = 2 [153]. The results of the fitting, against values from the solidification map are shown in Figure 6.14. Between solidification velocities of 0.1 and 10 cms^{-1}, there is a good fit between the two sets of results; at higher and lower values of *R*, the fit becomes less accurate. Calculations in Chapter 4 indicate that EBM solidification takes place in the range of 0.1 – 10 cms^{-1};

therefore, the deviations at high and low values of R are not a significant issue in this case.

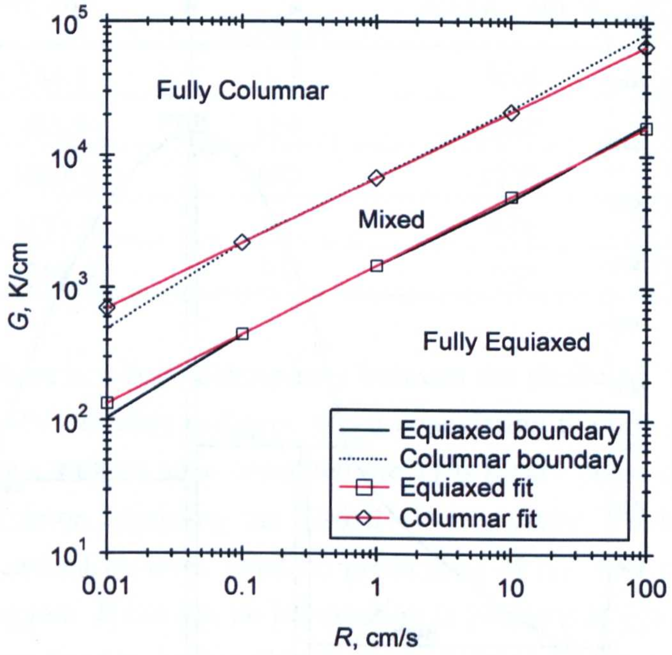

Figure 6.14 : G versus R solidification map from literature [71] fitted with Equations (6.9) and (6.10).

By assuming that the addition of boron does not change the values of a and n, values of ΔT_0 and N_0 from Table 6.4 can be used to calculate the effect of boron additions to the solidification map. The factor influencing the position of the columnar and equiaxed regions is $N_0^{\frac{1}{3}}\Delta T_0$; values for which are given in Table 6.4. It can be seen that for 0 wt% and 1.05 wt% B, this value is very similar and, as a result, the addition of 1.05 wt% B is predicted to have a negligible effect on the position of the columnar and equiaxed regions. However, $N_0^{\frac{1}{3}}\Delta T_0$ values for 0.07 wt%, 0.1 wt% and 0.4 wt% B are significantly larger, the largest change resulting from an addition of 0.1 wt% B. The reason for this effect is that, although increasing boron concentration increases N_0, ΔT_0 decreases. The decrease in ΔT_0 is more significant than the increase in N_0.

Figure 6.15 plots the position of the columnar and equiaxed regions and the calculated shift of these boundaries as a result of the addition of 0.1 wt% B. The addition of this quantity of boron is predicted to make it easier to form grains with a non-columnar morphology, at larger thermal gradients.

Plotted on the graph in Figure 6.16 are the solidification conditions for a 6 mA beam, calculated in Chapter 4. Whilst the addition of 0.1wt% boron is predicted to make the formation of equiaxed grains easier, solidification of EBM material still begins in the columnar region. However, the solidification conditions do span all three (columnar, mixed and equiaxed) morphology types.

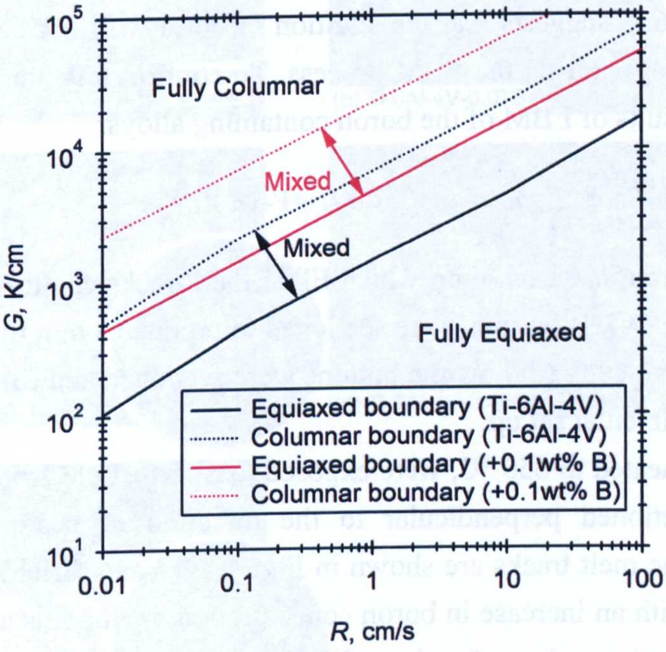

Figure 6.15 : G versus R solidification map from literature [71] and the predicted shift of the morphological boundaries as a result of the addition of 0.1wt% B.

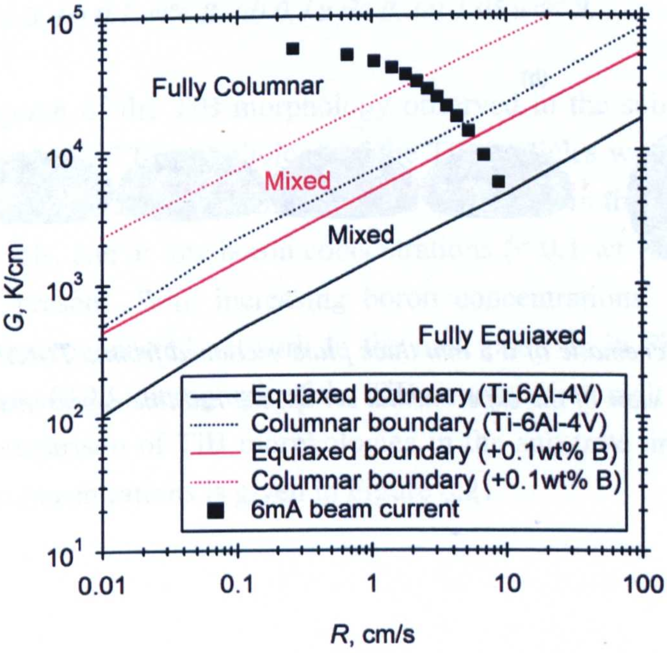

Figure 6.16 : G versus R solidification map from literature [71] and the solidification conditions for a 6 mA EBM beam. .

It has already been observed in Chapter 4 that, when solidification starts in the columnar region, the morphology of the grains produced is columnar. The final solidification conditions do not seem to influence the morphology. This, and the results in Figure 6.7, suggests that the addition of boron will not have any influence on grain morphology during the EBM process. To confirm this, the next section will investigate the results of EBM of the boron containing alloys.

6.3.3. Electron Beam Exposure of Ti-6Al-4V-xB Alloys

To produce substrate material, onto which EBM melt tracks could be produced, each of the five Ti-6Al-4V-*x*B buttons were sectioned to produce 3 mm thick plates. Figure 6.17 shows schematically (a) how the buttons were sectioned and (b) a schematic plan view of the experimental set up.

The samples, heated to 650 °C, were exposed to a 15 mA electron beam melt track before being sectioned perpendicular to the direction of beam motion. Optical micrographs of the melt tracks are shown in Figure 6.18 and differ significantly with boron content. With an increase in boron concentration, melt pools appear darker as a result of the increasing volume fraction of TiB. At 0.40 wt% and 1.05 wt% boron, the top surface of the melt pool has been drawn on to the micrographs for clarity. Without this, distinction between the material and the Bakelite mount is difficult as a result of the high concentration of TiB in the melt pools.

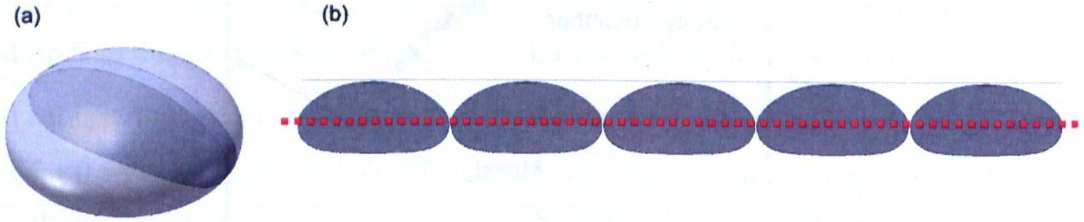

Figure 6.17 : (a) Schematic of a 3 mm thick plate sectioned from a Ti-6Al-4V-xB button and (b) schematic plan view of the experimental set up, the red line represents the electron beam traverse line.

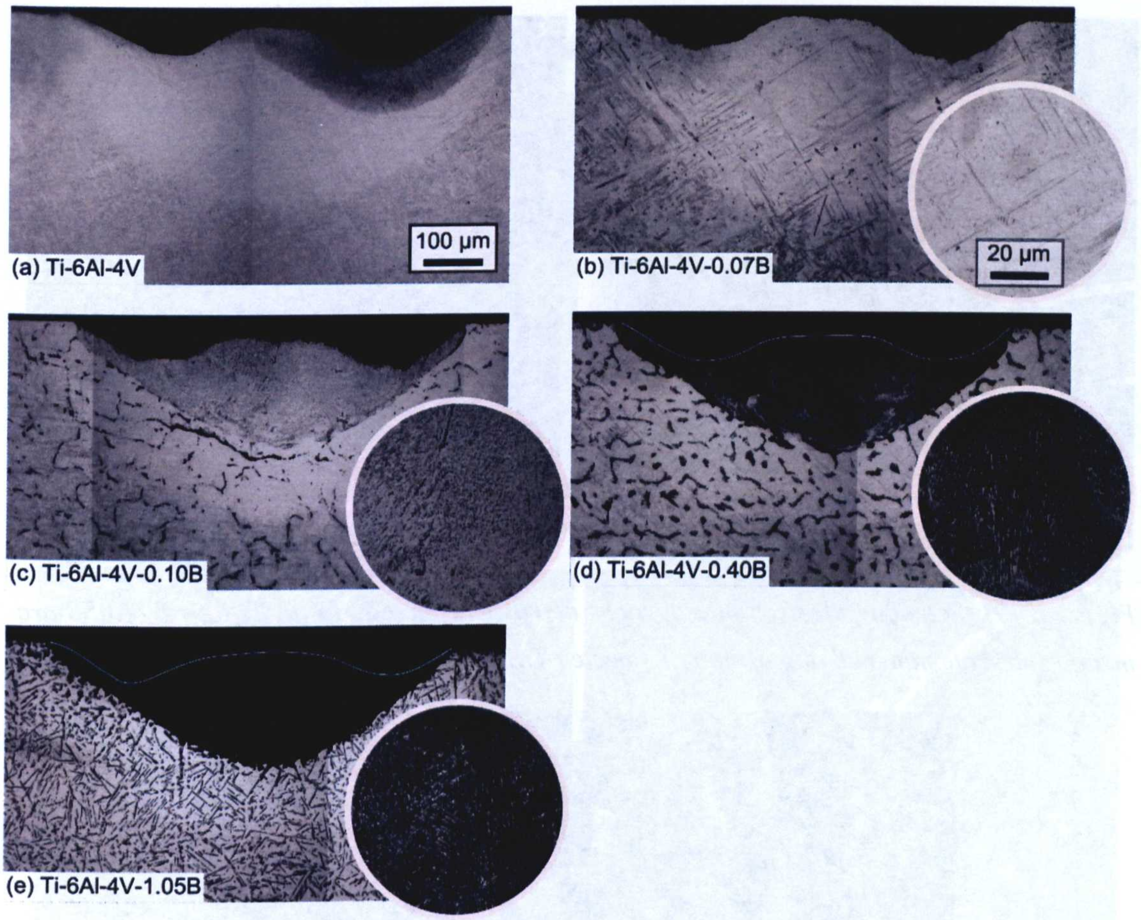

Figure 6.18 : Optical micrographs of melt pools produced on Ti-6Al-4V-xB substrates (a) 0 wt% B, (b) 0.07 wt% B, (c) 0.1 wt% B, (d) 0.4 wt% B, (e) 1.05 wt% B.

A SEM micrograph of the TiB morphology observed in the substrate material is shown in Figure 6.19 (a). The morphology of the TiB particles within the EBM melt tracks (Figure 6.19 (b)) is distinctly different from that found in the substrate material. Within the melt pools, and at low boron concentrations (< 0.1 wt %), fine, individual TiB particles are present. With increasing boron concentrations, TiB forms what appears to be an interconnected network in the melt pool, as in Figure 6.19 (b). A higher magnification SEM micrograph of the TiB structure in a melt pool is shown in Figure 6.20. A comparison of TiB morphologies in the substrate and melt pools for three of the boron concentrations is given in Figure 6.21.

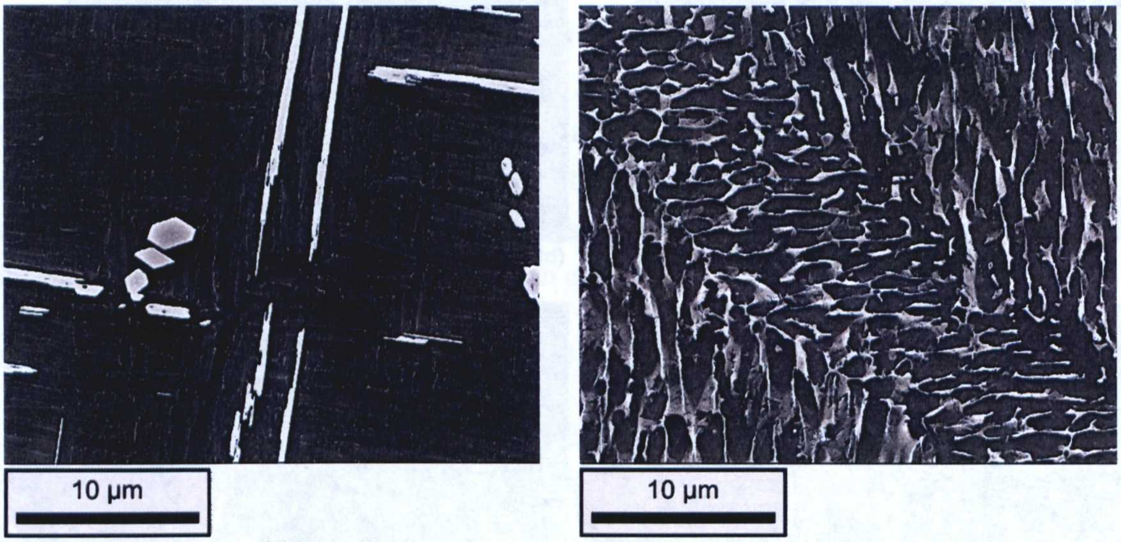

(a) *(b)*

Figure 6.19 : Scanning electron micrographs of TiB morphology in (a) Ti-6Al-4V-1.05B arc melted substrate material and (b) interconnected TiB network Ti-6Al-4V-0.4B melt pool.

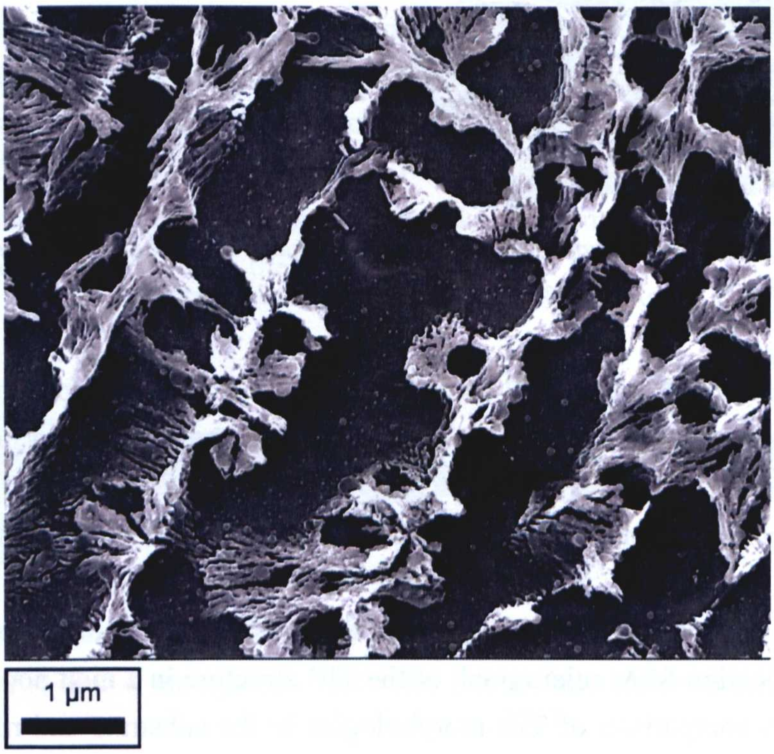

Figure 6.20 : TiB structure within an EBM melt pool for Ti-6Al-4V-1.05B material.

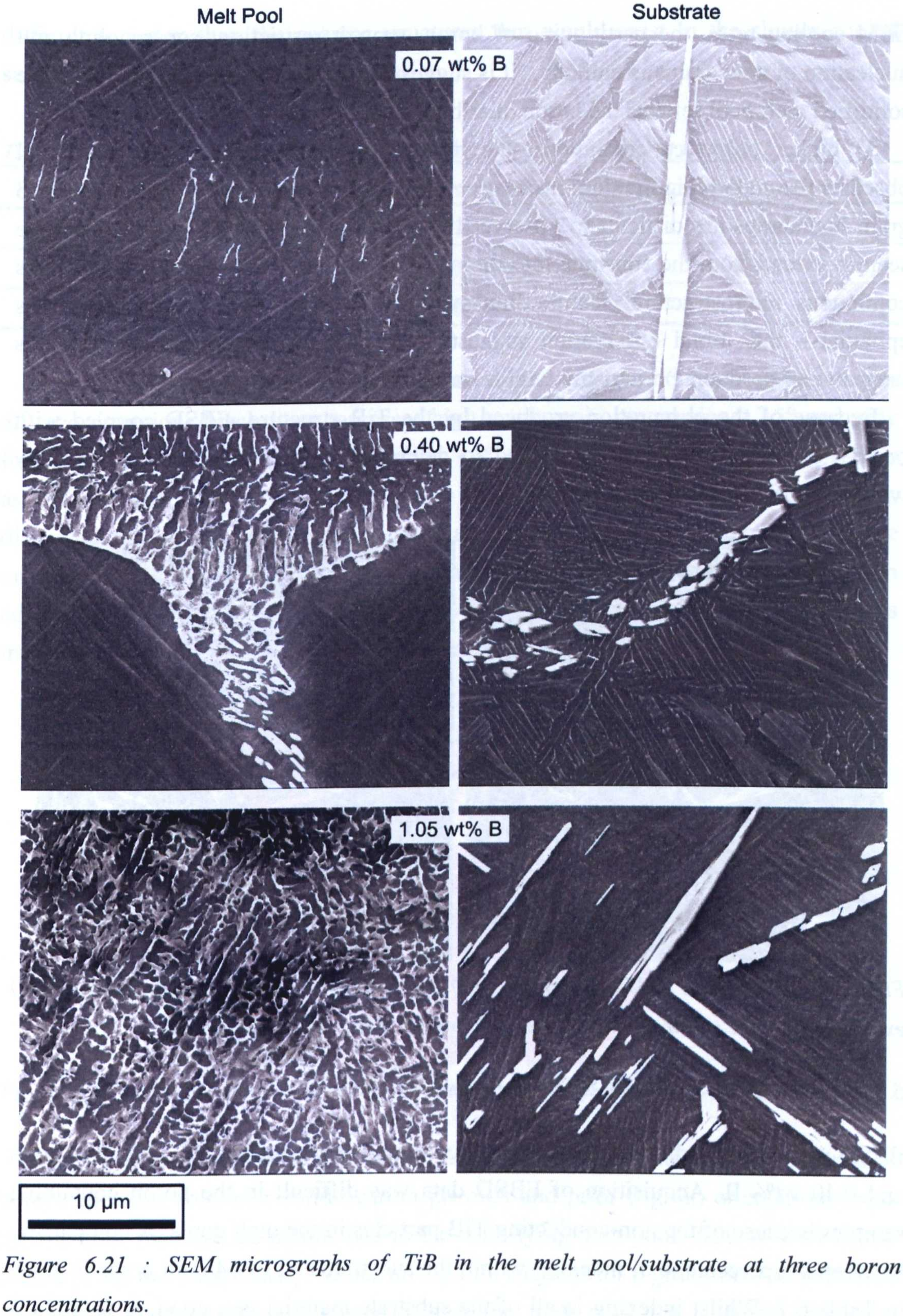

Figure 6.21 : SEM micrographs of TiB in the melt pool/substrate at three boron concentrations.

Although the microstructure of the substrate is clearly a result of boron partitioning (Figure 6.8), the TiB structure within the melt pools appears to have formed in a different manner; this result is unsurprising given the EBM cooling rates. At typical

EBM cooling rates, the partitioning of boron, growth restriction, supercooling and nucleation of new grains is unlikely. It is suggested that the distribution of TiB in the solidified melt pool reflects the boron distribution in the molten melt pool.

At higher boron concentrations, the dense TiB distribution in the melt pool obscures the underlying titanium microstructure, features such as α/α' laths and prior β grain boundaries are difficult to observe. However, in Figure 6.22, a α' lath can be seen to extend from the substrate into the melt pool of the 0.40 wt% B sample. This continuous microstructural feature indicates that growth upon solidification was epitaxial – this initial observation suggests that, under EBM conditions, boron is incapable of producing microstructural refinement, as previously speculated.

Because of the obscuration produced by the TiB structure, EBSD coupled with prior β grain reconstruction was used to determine the solidification morphology within the EBM melt pools.

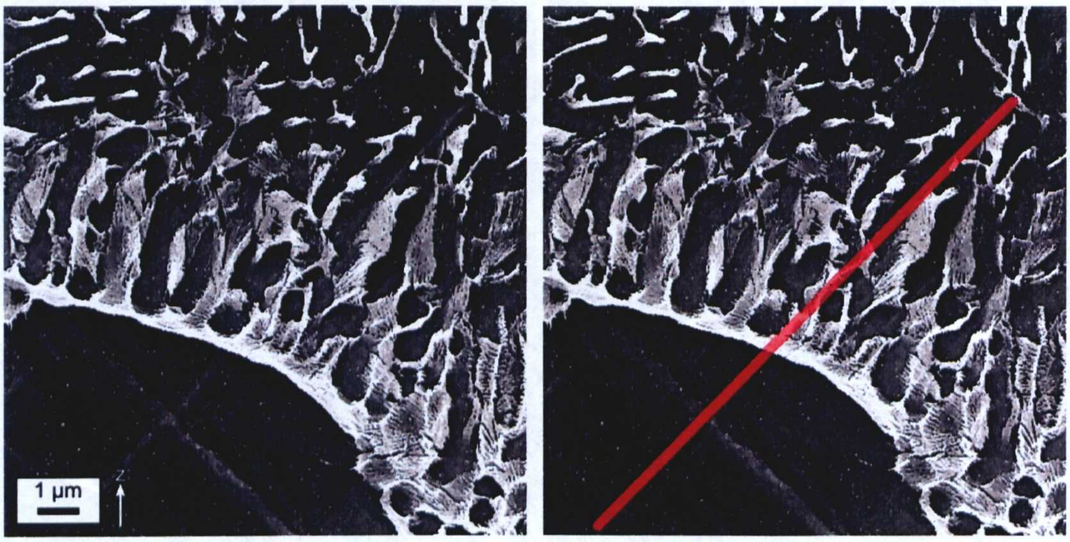

Figure 6.22 : Original SEM micrograph (left) and a highlighted, individual α' lath (right) extending from the substrate into the melt pool of the Ti-6Al-4V-0.40B sample.

6.3.4. EBSD of Ti-6Al-4V-xB Melt Pools

EBSD was performed on samples with three boron concentrations: 0 wt%, 0.10 wt% and 0.40 wt% B. Acquisition of EBSD data was difficult in the boron containing samples because of the non-conducting TiB particles in the melt pools. A comparison between the percentage of indexing within the substrate and EBM melt pools is given in Table 6.7. Whilst indexing in all of the substrate material was good, at 0.4wt% B the percentage of indexed points in the melt pool dropped to 10%. In all three of the samples tested, including the 0wt% B sample, indexing dropped in the melt pool region. Fine microstructures resulting from the fast-cooling melt pools are more difficult to index than the coarser structures that would exist in the slower cooled substrate.

Table 6.7 : Comparison of EBSD pattern indexing in boron containing samples.

Sample	Indexing (substrate)	Indexing (melt pool)
0 wt% B	95%	76%
0.10 wt% B	99%	85%
0.40 wt% B	80%	10%

Prior β reconstructions of the samples are shown in Figure 6.23 – Figure 6.25; in all reconstructions black lines represent high angle grain boundaries > 15° and grey lines represent low angle grain boundaries > 5°. Although indexing dropped to as low as 10% in the 0.40 wt% B melt pool, Davies' [93] β reconstruction program, discussed previously, uses a variant-based approach to β reconstruction. In short, the orientation of a parent β grain is determined from the misorientations between adjacent α pixels and variants. Thus, prior β reconstructions of poorly indexed regions may be carried out as long as there are several, adjacent, indexed pixels.

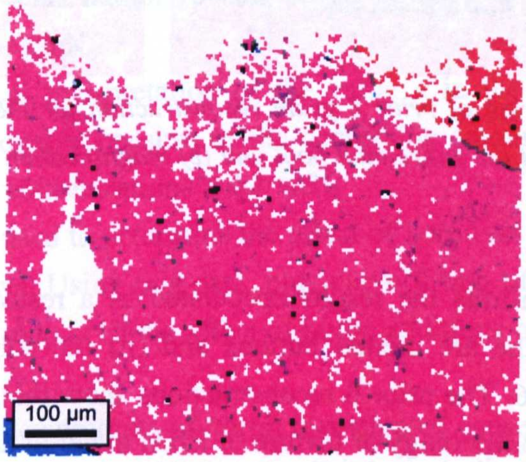

Figure 6.23 : IPF colouring of prior β grain reconstruction for the Ti-6Al-4V-0B melt pool.

The EBSD maps in Figure 6.24 and Figure 6.25 show that, despite the presence of boron, epitaxial columnar solidification prevails and prior β grain orientations from the substrate material are maintained in the solidifying melt pool. At 0.40 wt% B, the region of the melt track analysed lies on top of a single prior β grain; the reconstructed orientation of the material indexed within the melt pool has a single, identical orientation to that of the substrate.

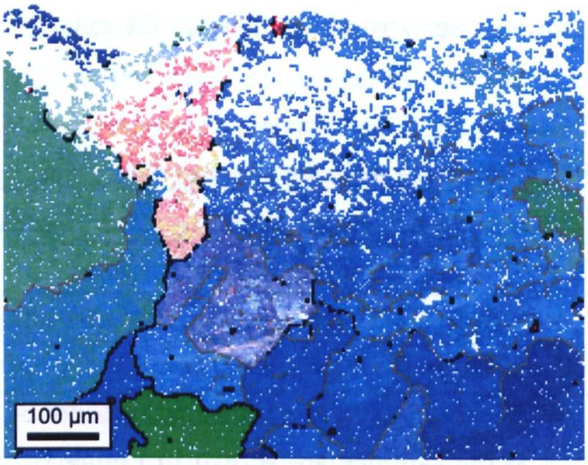

Figure 6.24 : IPF colouring of prior β grain reconstruction for the Ti-6Al-4V-0.10B melt pool.

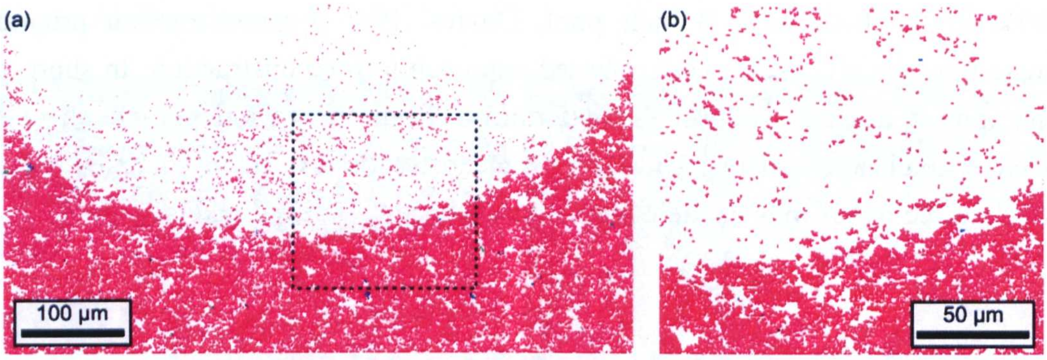

Figure 6.25 : IPF colouring of prior β grain reconstruction for the Ti-6Al-4V-0.40B melt pool. (a) IPF colouring of the entire melt pool and (b) magnification of the region identified in (a).

The EBSD data confirms the results speculated as a result of (i) the columnar structure observed in the arc melted buttons and (ii) the solidification conditions presented in Figure 6.16. The prior β reconstructions show that boron additions have no effect on the grain morphology or texture of EBM material and are ineffective as a grain refiner under EBM conditions.

6.3.5. *Potential EBM Ti-6Al-4V-xB Applications*

Although additions of boron to EBM Ti-6Al-4V did not result in grain refinement, the microstructures produced may be useful for other applications. Figure 6.19 – Figure 6.22 show the rather unique microstructure formed during solidification of the boron containing materials. The combination of Ti-6Al-4V with TiB and/or TiC particles has been referred to as a titanium metal-matrix composite (MMC) which have potential aerospace applications. Such applications include high strength, high stiffness, low density structural components [154]. Titanium MMCs have been shown to have increased yield strength, tensile strength and Young's Modulus, although their ductility is poor. Wear resistance of Ti-6Al-4V-*x*B materials are also significantly better than Ti-6Al-4V alone [155].

In comparison to TiB containing MMCs, the structure of the EBM material is somewhat unique and thus may exhibit some unique properties. Further work studying bulk EBM components, produced from pre-alloyed powder, may provide some interesting results.

6.4. Summary

- Two methods were used to investigate the response of Ti-6Al-4V-*x*B alloys to EBM.
    - Direct melting of a Ti-6Al-4V and elemental boron powder mixture was generally unsuccessful owing to the highly exothermic reaction between Ti and B.
    - Production of solid, pre-alloyed, arc melted material resulted in grain refinement of the columnar structure with boron additions.
- The utilisation of an empirical model to compare results from this work with that of a previous author reveals boron potency in Ti-6Al-4V to be in the region of 1430 μmK.
    - Physical interpretation of the value *a* in the empirical model seems questionable because of the decreasing amount grain refinement with boron concentrations > 0.1 wt%.
- JMatPro was used to determine the effect of boron on the freezing range of Ti-B binary alloys. Using this data, plus curve fitting of Kobryn and Semiatin's solidification map [71], the affect of boron additions on grain morphology was established.
    - All concentrations of boron investigated caused an upward shift of the equiaxed and columnar grains boundaries i.e. a larger range of conditions are available to form equiaxed grains.
    - In spite of this, EBM solidification still begins in the columnar region and boron does not drive a columnar to equiaxed transition.
- The exposure of solid Ti-6Al-4V-*x*B alloys to an electron beam produced melt tracks in which the TiB morphology was significantly different from that of the substrate.
- The interconnected TiB network within melt pools is though to result from the rapid solidification during EBM.
- EBSD reveals that the presence of boron does not influence the prior β grain structure or texture within a melt pool.

It is thus concluded that, although clearly effective in cast material, boron is not capable of promoting a change in grain: (i) size, (ii) morphology or (iii) texture in EBM processed material. The EBM process occupies the range of solidification conditions that are growth rather than nucleation dominated and as such, it has been observed that a chemical change alone is not enough to produce a refinement in grain morphology. A change in thermal conditions during the EBM process is required to exploit the influence of boron on the solidification conditions.

7. CONCLUSIONS

The investigations carried out in this work are best summarised into three sections. Firstly, characterisation and numerical modelling of the electron beam, discussed in Chapter 4, gave an insight into material solidification conditions and influence of the power source. Resulting microstructures, textures and mechanical properties were discussed in Chapter 5 prior to investigating the potential to refine the as-built grain structure in Chapter 6. The conclusions from these chapters are summarised here.

7.1. Electron Beam Characterisation and Numerical Modelling (Chapter 4)

- The use of a preheated, solid substrate (stainless steel or Ti-6Al-4V) is an effective means of determining the extent of the Arcam S12 electron beam and monitoring how its form varies with process parameters.
- The electron beam is asymmetrical about the focal point; the beam is more focussed at positive focus offset values compared with equivalent negative values.
- Under standard operating conditions, the extent of the melt pool is well described by the Rosenthal solution using a fitting parameter of $\eta = 0.6$. The fitting parameter incorporates the effects of beam efficiency and *focus offset* under standard hatch conditions.
- Calculation of solidification conditions shows that solidification begins in the fully columnar regime; this is confirmed by the observed microstructures. Although the progression of solidification conditions indicates that grain morphology will change during solidification, a columnar structure remains. The location of the first point on the solidification map for EBM solidification is therefore the most descriptive; under standard operating conditions the predicted mixed morphologies are not observed.
- When speed-current combinations are decoupled i.e. speed and current are not linked by the *speed function*, it is possible to use the electron beam to produce a mixed morphology. However, the conditions required to do so are far removed from those acceptable to produce an EBM component and predictions of the extent of such a melt pool were not accurate.

7.2. Microstructural Characterisation (Chapter 5)

- The EBM Ti-6Al-4V microstructure typically consists of a transformed colony/Widmanstätten $\alpha + \beta$ microstructure with α_{GB} delineating prior β grain boundaries.

- Prior β grains are highly columnar and arise from epitaxial growth during deposition. In this work prior β grains that extend through tens of layers have been observed.
- The standard practice of melting onto a stainless steel base plate results in a β-stabilised brittle region, contaminated with stainless steel. This region extends approximately 800 μm into a component.
- At the top of small samples, martensite has been observed as a result of high cooling rates. Cooling rates, determined from predicted solidification conditions in Chapter 4 and measurement of secondary dendrite arm spacing in Chapter 5, are $\geq 10^3$ Ks^{-1}.
- It was not possible to decompose a fully martensitic microstructure to a fully transformed α + β microstructure after isothermal treatment at 650 °C for 17.5 hours. Facchini *et al.* [68] suggest that the transformation of martensite results purely from holding at the *build temperature*; it is suggested here that this alone is not sufficient. It is proposed that the *build temperature* and energy supplied by thermal cycling results in the transformation of martensite.
- A *build temperature* of 700 °C is detrimental to mechanical properties. In comparison to lower *build temperatures* (≤678 °C); components manufactured at 700 °C exhibit reduced mechanical properties as a consequence of microstructural coarsening (α_{GB}, α lath width and α colony scale factor).
- Hot isostatic pressing of EBM material results in a microstructure that is independent of build temperature (in the range of 650 – 700 °C). Compared to as-built material HIP EBM material is lower in strength but shows a slight increase in elongation.
- Ti-6Al-4V powder used in the EBM process may change chemistry over time, specifically the oxygen content, as a result of moisture in the vacuum chamber reacting with hot powder. Constant monitoring of powder composition is necessary to ensure that the composition remains within specification.
- EBM Ti-6Al-4V exhibits a 10 × random preference of the <001> pole of the β phase to align itself with the *z*-axis. Both cube and fibre-like textures have been observed. Upon transformation, this textured microstructure is refined and transformed α laths have not been observed to undergo any variant selection.
- Reconstruction of prior β grains reveals a significant number of low angle grain boundaries which appear to be more prevalent in β grains in which the [001] pole is most closely aligned with the *z*-axis.
- Although billed as a near-net manufacturing process, EBM components have an as-built surface roughness with an $R_a > 25$ μm. This is highly detrimental to

static mechanical properties and is likely to be even more deleterious in dynamic conditions. The removal of ~ 500 μm of material from each component surface results in a material with mechanical properties that meet the wrought specification.

7.3. Boron Additions to EBM Ti-6Al-4V (Chapter 6)

- The addition of elemental boron to Ti-6Al-4V powder is not an effective means of producing TiB during EBM because of the exothermic (thermite) reaction between Ti and B. An excessive increase in temperature makes the EBM process very difficult to control.
- In Ti-6Al-4V-*x*B ingots produced by argon arc melting, boron has a marked refining effect on the columnar prior β grain structure. TiB can be seen in interdendritic regions as a result of solute partitioning (rejection of solute into the liquid) during solidification.
- Using an empirical relationship developed by Bermingham *et al.* [149], the potency of boron in arc melted Ti-6Al-4V was determined to be in the region of 1430 μmK – this value is also applicable to cast material produced by Tamirisakandala *et al.* [27].
- Exposure of solid Ti-6Al-4V-*x*B substrates to an S12 electron beam produces a TiB morphology, within the melt pool, that is significantly different to the that found in the arc melted, substrate material. TiB forms an '*interconnected network*' at boron concentrations ≥ 0.10 wt% B.
- Both arc melted and EBM Ti-6Al-4V-*x*B material consisted of columnar prior β grains.
- Using Hunt's equations [100], the effect of boron additions to the Ti-6Al-4V solidification map was predicted. In spite of increasing the size of the equiaxed morphology region, EBM solidification was still predicted to begin in the columnar region.
- Electron microscopy and reconstruction of EBSD data reveal that under EBM conditions, and as predicted, the columnar morphology remains and boron fails to refine prior β grain size or influence the as-built texture.

8. FURTHER WORK

As an emerging technology, there is plenty of work still to be done to investigate and understand EBM as a means of manufacturing near-net shape components. The scope of work is wide when one considers the number of alloy systems that it may be possible to investigate. However, concentrating on Ti-6Al-4V, this chapter will discuss potential avenues for further investigation identified during this work.

5.6. Hardware Improvements

- In all of the experiments conducted in this work, the electron beam quality of the EBM system was assumed to remain constant; the same parameter set was assumed to give the same material response. However, it is likely that the quality of the electron beam degrades with time and an interesting investigation would involve assessing how significant filament age is on its appearance and melting ability.
- As already mentioned several times through this work, a necessary investigation involves determining the temperature of material at the deposition surface rather than at the lower base plate surface. This would provide key information for process control and microstructural interpretation.
- From a processing perspective, a significant issue in EBM is the inability to restart a build after a fault that causes a delay of greater than approximately 20 minutes. A problem may occur in the final few layers of a component that may result in the entirety of the *build* being scrapped. Given the cost of the process and the material, such an event occurs at great expense. Producing a recoverable process would be a significant step forward.

5.7. Processing

- It has been suggested that thermal cycling of deposited material provides energy to allow full transformation of a martensitic microstructure. Experiments investigating the effect of thermal cycling on microstructure would help gain a better understanding of the material response. A potential means of doing this is to use an induction coil to hold samples at elevated temperature and rapidly cycle them to higher temperatures. The effect of number of cycles, hold temperature, cycle temperature and their influence on microstructure could then be determined. If successful, such experiments could be used to simulate how other materials would behave in the EBM process.

- An increase in oxygen content of the feedstock powder was identified in Chapter 5, however, the number of times the powder was used before the oxygen content was above the specification limit is unknown. A long term but useful investigation would be to frequently monitor the oxygen content of the powder to determine its usable life before looking at ways to extend its usage.
- The appearance and localisation of low-angle grain boundaries in the EBSD samples is puzzling in terms of both their origin and the reason for their localisation. TEM on such material would be useful to investigate further the observed substructure and perhaps shed some light on their formation.
- As illustrated in Chapter 5, the surface finish of EBM Ti-6Al-4V has room for improvement. Currently, the as-deposited surface is likely to restrict components used in the as-built state to a non-structural capacity. Any improvements to this surface finish or ideas for a novel means of removing it from complex shapes would expand the scope for EBM component use.
- The modest variation of microstructure with z-height for a tall sample has been reported here, however, the mechanical property variation with z-position, if any, has not been determined. Determining any variation in properties, as a function of 3 dimensional position within the build chamber, would be a useful exercise.
- Microstructural assessment of geometries that undergo large section changes, rather than the relatively uniform sections investigated here, would give an insight into the effect of varying the amount of heat input per layer. Geometries with large section changes are generally quite difficult to manufacture because of the change in energy input during melting – this may have an influence on microstructure.
- Although boron has been found to have no effect on either texture or grain refinement in EBM material, the TiB morphology in the melt pool may posses some interesting properties. It is suggested that some mechanical test specimens are produced from a pre-alloyed Ti-6Al-4V-0.1B alloy powder to assess the effect of the TiB network on properties.

9. REFERENCES

[1] Sir A. Russell, *The Rev. William Gregor (1791 – 1817), discoverer of titanium*, The Mineralogical Magazine and Journal of the Mineralogical Society, **229**, 1955, p617 – 624.

[2] McQuillan and McQuillan, *Titanium*, Butterworths Scientific Publications, 1956, Great Britain.

[3] A. D. Hartman, S. J. Gerdemann, J. S. Hansen, *Producing lower-cost titanium for automotive applications*, JOM, 2007, **50**, no. 9, p 16 – 19.

[4] G. Z. Chen, D. J. Fray, T. W. Farthing, *Direct electrochemical reduction of titanium dioxide to titanium in molten calcium chloride*, Nature, 2000, **407**, p361 – 364.

[5] I. J. Polmear, *Light Alloys – Metallurgy of the Light Alloys*, 2nd Edition, Chapman & Hall, UK, 1989.

[6] G. Lütjering, J. C. Williams, *Titanium*, Springer, Germany, 2003.

[7] M. Donachie Jr., *Titanium, A Technical Guide*, ASM International, USA, 1988.

[8] C. Leyens & M. Peters, *Titanium and Titanium Alloys, Fundamentals and Applications*, Wiley-VCH, 2003.

[9] H. M. Flower, *Microstructural development in relation to hot working of titanium alloys*, Materials Science and Technology, **6**, Nov. 1990, p1082 – 1092.

[10] G. Welsch, R. Boyer, E. W. Collings, *Materials Properties Handbook: Titanium Alloys*, ASM International, Ohio, 1994.

[11] W. G. Burgers, *On the process of transition of the cubic-body-centred modification into the hexagonal-close-packed modification of zirconium*, Physica, **I**, 1934, p561 – 586.

[12] Z. Nishiyama, *Martensitic Transformation*, Academic Press, USA, 1978, , edited by M. Fine, M. Meshii, C. Wayman.

[13] J. Burke, *The Kinetics of Phase Transformations in Metals*, Pergamon Press, Great Britain, 1965.

[14] G. A. Chadwick, *Metallography of Phase Transformations*, Butterworths, Great Britain, 1972.

[15] H. K. D. H. Bhadeshia, *Metallurgy of titanium and its alloys*, www.msm.cam.ac.uk/phase-trans/2004/titanium/titanium.html, accessed on 12/01/2009.

[16] E. Tal-Gutelmacher, D. Eliezer, D. Eylon, *The effects of low fugacity hydrogen in duplex- and beta- annealed Ti-6Al-4V alloy*, Materials Science and Engineering A, **381**, 2004, p230 – 236.

[17] G. Lütjering, *Influence of processing on microstructure and mechanical properties of (α + β) titanium alloys*, Materials Science and Engineering **A243**, 1998, p32 – 45.

[18] J. H. Zuo, Z. G. Wang, E. H. Han, *Effect of microstructure on ultra-high cycle fatigue behaviour of Ti-6Al-4V*, Materials Science and Engineering A, Article in press 2007.

[19] J. I. Qazi, H. J. Rack, *Effects of thermal treatment on the mechanical properties of biomedical titanium alloys*, ASM International Conference, Anahein CA, 8th September, 2003.

[20] T. Ahmed, H. J. Rack, *Phase transformations during cooling in α + β titanium alloys*, Materials Science and Engineering **A243**, 1998, p206 – 211.

[21] G. F. VanderVoort (editor), *Atlas of Time-Temperature Diagrams for Non-Ferrous Alloys*, ASM International, Materials Park, OH, 1991.

[22] S. D. Henry, K. S. Dragolich, N. D. DiMatteo, *Fatigue Data Book : Light Structural Alloys*, ASM International, Materials Park, OH, 1995.

[23] R. Filip, K. Kubiak, W. Ziaja, J. Sieniawski, *The effect on the mechanical properties of two-phase titanium alloys*, Journal of Materials Processing Technology, **133**, 2003, p84 – 89.

[24] S. Neelakantan, P.E.J. Rivera-Díaz-del-Castillo, Sybrand van der Zwaag, *Prediction of martensite start temperature for β titanium alloys as a function of composition*, Scripta Materilia, **60**, 2009, p611 – 614.

[25] D. A. Porter, K. E. Easterling, *Phase Transformations in Metals and Alloys*, Second Edition, Chapman & Hall, Great Britain, 1993.

[26] Jun Zhu, Akira Kamiya, Takahiko Yamada, Wen Shi, Katsuyoshi Naganuma, *Influence of boron addition on microstructure and mechanical properties of dental cast titanium alloys*, Materials Science and Engineering, **A339**, 2003, p53 – 62.

[27] S. Tamirisakandala, R. B. Bhat, J. S. Tiley, D. B. Miracle, *Grain refinement of cast titanium alloys via trace boron addition*, Scripta Materialia, **53**, 2005, p1421 – 1426.

[28] M. J. Bermingham, S. D. McDonald, K. Nogita, D. H. St. John, M. S. Dargusch, *Effects of boron on microstructure in cast titanium alloys*, Scripta Materialia, **59**, 2008, p538 – 541.

[29] I. Sen, S. Tamirisakandala, D. B. Miracle, U. Ramamurty, *Microstructural effects on the mechanical behaviour of B-modified Ti-6Al-4V alloys*, Acta Materialia, 55, 2007, p4983 – 4993.

[30] W. Chen, C. J. Boehlert, *The elevated-temperature fatigue behaviour of boron-modified Ti-6Al-4V(wt%) castings*, Materials Science and Engineering A, **494**, 2008, p132 – 138.

[31] D. Hill, R. Banerjee, D. Huber, J. Tiley, H. L. Fraser, *Formation of equiaxed alpha in TiB reinforced Ti alloy composites*, Scripta Materialia, **52**, 2008, p387 – 392.

[32] S. Tamirisakandala, R. B. Bhat, D. B. Miracle, S. Boddapati, R. Bordia, R. Vanover, V. K. Vasudevan, *Effect of boron on the beta transus of Ti-6Al-4V alloy*, Scripta Materialia, **53**, 2005, p217 – 222.

[33] U. F. Kocks, C. N. Tomé, H. R. Wenk, *Texture and Anisotropy*, Cambridge, Cambridge University Press, 1998.

[34] V. A. Randle, O. Engler, *Introduction to Texture Analysis: Macrotexture, Microtexture and Orientation Mapping*, Amsterdam, Gordon & Breach, 2000.

[35] H. R. Wenk, P. Van Houte, *Texture and anisotropy*, Reports on Process in Physics, 67, 2004, p1367 – 1428.

[36] M. Hatherly, W. B. Hutchinson, *An Introduction to Textures in Metals*, Chameleon Press, London, 1979.

[37] N. Hopkinson, R. J. M. Hague, P. M. Dickens, *Rapid manufacturing an industrial revolution for the digital age*, John Wiley & Sons, UK, 2006.

[38] C. Hull, M. Feygin, Y. Baron, R. Sanders, E. Sachs, A. Lightman, T. Wohlers, *Rapid prototyping: current technology and future potential*, Rapid Prototyping Journal, **1**, 1995, p11 – 19.

[39] L-E. Rännar, A. Glad, C-G. Gustafson, *Efficient cooling with tool inserts manufactured by electron beam melting*, Rapid Prototyping Journal, **13**, 2007, p128 – 135.

[40] K. M. B. Taminger, R. A. Hafley, *Electron beam freeform fabrication: a rapid metal deposition process*, Proceedings of the 3rd Annual Automotive Composites Conference, September 9-10, 2003, Troy , MI.

[41] R. Hauge, S. Mansour, N. Saleb, *Design opportunities with rapid manufacture*, Assembly Automation, **23**, 2003, p346 – 356.

[42] G. P. Dinda, L. Song, J. Mazumder, *Fabrication of Ti-6Al-4V scaffolds by direct metal deposition*, Metallurgical and Materials Transactions A, **39**, 2008, p2914 – 2922.

[43] http://www.arcam.com/customers/case-studies.aspx, accessed on 06/01/2010.

[44] http://fabathome.org/wiki/index.php?title=Main_Page, accessed on 06/01/2010.

[45] J.-Y. Jeng, S.-C. Peng, C.-J. Chou, *Metal rapid prototype fabrication using selective laser cladding*, International Journal of Advanced manufacturing Technology, **16**, 2000, p681 – 687.

[46] M. Agarwala, D. Bourell, J. Beaman, H. Marcus, J. Barlow, *Direct selective laser sintering of metals*, Rapid Prototyping Journal, **1**, no. 1, 1995, p26 – 36.

[47] J. Dück, F. Niebling, T. Neeβe, A. Otto, *Infiltration as post-processing of laser sintered metal parts*, Powder Technology, **145**, 2004, p62 – 68.

[48] D. Gu, Y. Sehn, *Effects of dispersion technique and component ratio on densification and microstructure of multi-component Cu-based metal powder in direct laser sintering*, Journal of Materials Processing Technology, **182**, 2007, p564 – 573.

[49] D. Clark, M. R. Bache, M. T. Whittaker, *Shaped metal deposition of a nickel alloy for aero engine applications*, Journal of Materials Processing Technology, **203**, 2008, p439 – 448.

[50] H. J. Niu, I. T. H. Chang, *Selective laser sintering of gas atomized high speed steel powders*, Scripta Materialia, **41**, 1999, p25 – 30.

[51] I.-H. Oh, N. Nomura, N. Masahashi, S. Hanada, *Mechanical properties of porous titanium compacts prepared by powder sintering*, Scripta Materialia, **49**, 2003, p1197 – 1202.

[52] S. P. Mates, G. S. Settles, *A study of liquid metal atomization using close-coupled nozzles, Part 1 : Gas dynamic behaviour*, Atomization and Sprays, **15**, 2005, p19 – 40.

[53] L. V. M. Antony, R. G. Reddy, *Processes for production of high-purity metal powders*, JOM, **55**, 2003, p14 – 18.

[54] R. H. Bricknell, *The structure and properties of a nickel-base superalloy produced by osprey atomization-deposition*, Metallurgical and Materials Transactions A, **17**, 1986, p583 – 591.

[55] H. H. Zhu, J. Y. H. Fuh, L. Lu, *The influence of powder apparent density on the density in direct laser-sintered metallic parts*, International Journal of Machine Tools & Manufacture, **47**, 2007, p294 – 298.

[56] N. Taniguchi, M. Ikeda, I. Miyamoto, T. Miyazaki, *Energy-Beam Processing of Materials*, Oxford University Press, UK, 1989.

[57] R. Bakish, *Introduction to Electron Beam Technology*, John Wiley & Sons, USA, 1962.

[58] J. E. Matz, T. W. Eagar, *Carbide formation in alloy 718 during electron-beam solid freeform fabrication*, Metallurgical and Materials Transactions A, **33A**, 2002, p2559 – 2567.

[59] D. Cormier, O. Harrysson, H. West, *Characterization of H13 steel produced via electron beam melting, Rapid Prototyping Journal*, **10**, 2004, p35 – 41.

[60] K. W. Dalgarno, R. D. Goodridge, *Compression testing of layer manufactured metal parts: the RAPTIA compression benchmark*, Rapid Prototyping Journal, **10**, 2004, p261 – 264.

[61] O. L. A. Harryson, O. Cansizoglu, D. J. Marcellin-Little, D. R. Cormier, H. A. West II, *Direct metal fabrication of titanium implants with tailored materials and mechanical properties using electron beam melting technology*, Materials Science and Engineering C, 2008, **28**, p366 – 373.

[62] S. Ponader, E Vairaktaris, P. Heinl, C. v. Wilmowsky, A. Rottmair, C. Körner, R. F. Singer, S. Holst, K. A. Schlegel, F. W. Neukam, E. Nkenke, *Effects of topographical surface modifications of electron beam melted Ti-6Al-4V titanium on human foetal osteoblasts*, Journal of Biomedical Materials Research, 2008, **84A**, p1111 – 1119.

[63] L-E Rännar, A. Glad, C-G. Gustafson, *Efficient cooling with tool inserts manufactured by electron beam melting*, Rapid Prototyping Journal, **13**, 2007, p128 – 135.

[64] L. E. Murr, S. A. Quinones, S. M. Gaytan, M. I. Lopez, A. Rodela, E. Y. Martinez, D. H. Hernandez, E. Martinez, F. Medina, R. B. Wicker, *Microstructure and mechanical behaviour of Ti-6Al-4V produced by rapid-layer manufacturing, for biomedical applications*, Journal of the Mechanical Behaviour of Biomedical Materials, 2009, **2**, p20 – 32.

[65] O. Cansizoglu, O. Harryson, D. Cormier, H. West, T. Mahale, *Properties of Ti-6Al-4V non-stochastic lattice structures fabricated via electron beam melting*, Materials Science and Engineering A, **492**, 2008, p468 – 474.

[66] L. E. Murr, S. M. Gaytan, F. Medina, E. Martinez , J. L. Martinez, J, D. H. Hernandez, B. I. Machado, D. A. Ramirez, R. B. Wicker, *Characterization of Ti-6Al-4V open cellular foams fabricated by additive manufacturing using electron beam melting*, Materials Science and Engineering A, article in press 2010.

[67] X. Li, C. Wang, W. Zhang, Y. Li, *Fabrication and characterization of porous Ti6Al4V parts for biomedical applications using electron beam melting process*, Materials Letters, **63**, 2009, p403 – 405.

[68] L. Facchini, E. Magalini, P. Robotti, *Microstructure and mechanical properties of Ti-6Al-4V produced by electron beam melting of pre-alloyed powders*, Rapid Prototyping Journal, **153**, 2009, p171 – 178.

[69] L. Qian, J. Mei, J. Liang, X. Wu, *Influence of position and laser power on thermal history and microstructure of direct laser fabricated Ti-6Al-4V*, Materials Science and Technology, **21**, 2005, p597 – 605.

[70] J. Mazumder, A. Schifferer, J. Choi, *Direct materials deposition: designed macro and microstructure*, Materials Research Innovations, **3**, 1999, p118 – 131.

[71] P. A. Kobryn, S. L. Semiatin, *The laser additive manufacture of Ti-6Al-4V*, JOM, **53**, 2001, p40 – 42.

[72] G. P. Dinda, L. Song, J. Mazumder, Fabrication of Ti-6Al-4V scaffolds by direct metal deposition, Metallurgical and Materials Transactions A, **39**, 2008, p2914 – 2922.

[73] R.J. Moat, A.J. Pinkerton, L. Li, P.J. Withers and M. Preuss, *Crystallographic texture and microstructure of pulsed diode laser deposited Waspaloy*, Acta Materialia, 2009, **57**, p1220-1229.

[74] S. M. Kelly, S. L. Kampe, *Microstructural evolution in Laser-deposited multilayer Ti-6Al04V builds: Part I. Microstructural characterization*, Metallurgical and Materials Transactions A, **35**, 2004, p1861 – 1867.

[75] R. Rai, J. W. Elmer, T. A. Palmer, T. DebRoy, *Heat transfer and fluid flow during keyhole mode laser welding of tantalum, Ti-6Al-4V, 304L stainless steel and vanadium*, Journal of Applied Physics D, **40**, 2007, p5753 – 5766

[76] D. A. Porter, K. E. Easterling, Phase Transformations in Metals and Alloys, 2nd ed., Chapman & Hall, London, 1993.

[77] Gäumann, C. Bezençon, P. Canalis and W. Kurz, *Single-crystal laser deposition of superalloys: processing-microstructure maps*, Acta Materialia, 2001, **49**, p1051-1062.

[78] P. A. Kobryn, S. L. Semiatin, *Microstructure and texture evolution during solidification processing of Ti-6Al-4V*, Journal of Materials Processing Technology, **135**, 2003, p330 – 339.

[79] L. E. Murr, E. V. Esquivel, S. A. Quinones, S. M. Gaytan, M. I. Lopez, E. Y. Martinez, F. Medina, D. H. Hernandez, E. Martinez, J. L. Martinez, S. W. Stafford, D. K. Brown, T. Hoppe, W. Meyers, U. Lindhe, R. B. Wicker, *Microstructures and mechanical properties of electron beam-rapid manufactured Ti-6Al-4V biomedical prototypes compared to wrought Ti-6Al-4V*, Materials Characterization, 60, 2009, p96 – 105.

[80] A. Christensen, A. Lippincott, R. Kircher, *Qualification of electron beam melted (EBM) Ti6Al4V-ELI for orthopaedic implant applications*, White paper available from www.medicalmodeling.com/ebm/, accessed on 18/12/2007.

[81] D. Rosenthal, *The theory of moving sources of heat and its application to metal treatments*, Transactions of the A.S.M.E., **11**, 1946, p849 – 866.

[82] S. Bontha, N. W. Klingbeil, P. A. Kobryn, H. L. Fraser, *Thermal process maps for predicting solidification microstructure in laser fabrication of thin-wall structures*, Journal of Materials Processing Technology, **178**, 2006, p135 – 142.

[83] D. Couëdel, P. Rogeon, P. Lemasson, M. Carin, J. C. Parpillon, R. Berthet, *2D heat transfer modelling within limited regions using moving sources : application to electron beam welding*, International Journal of Heat and Mass Transfer, **46**, 2003, p4553 – 4559.

[84] N. T. Nguyen, A. Ohta, K. Matsuoka, N. Suzuki, Y. Maeda, *Analytical solutions for transient temperature of semi-infinite body subjected to 3-D moving heat sources*, Welding Research Supplement, American Welding Society, August 1999, p265-s – 274-s.

[85] Arcam EBM A2 and S12 User's Manual, Arcam AB, Gothenburg, September 2007.

[86] Arcam level 2 training, Arcam AB, Gothenburg, 07/04/2008.

[87] D. J. Whitehouse, *Handbook of Surface Metrology*, Institute of Physics Publishing, Bristol, 1994.

[88] T. V. Vorburger, J. A. Dagata, G. Wilkening, K. Iizuka, *Characterisation of Surface Topography*, in *Beam effects, surface topography, and depth profiling in surface analysis*, Eds. A. Warren Czanderna, T. E. Madey, C. J. Powell, Plenum, New York, 1998.

[89] J. Tiley, T. Searles, E. Lee, S. Kar, R. Banjeree, J. C. Russ, H. L. Fraser, *Quantification of microstructural features in α/β titanium alloys*, Materials Science and Engineering A, **372**, 2004, p191 – 198.

[90] H. Jones, *Rapid Solidification of Metals and Alloys*, The Institution of Metallurgists, Chameleon Press, London, 1982.

[91] R. L. Higginson, C. M. Sellars, *Worked Examples in Quantitative Metallography*, Maney, London, 2003.

[92] http://www.matter.org.uk/diffraction/electron/kikuchi_lines_2.htm, accessed on 30/11/2009.

[93] P. S. Davies, PhD Thesis, *An Investigation of Microstructure and Texture Evolution in the Near-α Titanium Alloy Timetal® 834*, The University of Sheffield, March 2009.

[94] N. Gey, M. Humbert, *Specific analysis of EBSD data to study the texture inheritance due to the β → α phase transformation*, Journal of Materials Science, **38**, 2003, p1289 – 1294.

[95] M. Humbert, F. Wagner, H. Moustahfid, C. Esling, *Determination of the orientation of a parent β grain from the orientations of the inherited α plates in the phase transformation from body-centred cubic to hexagonal close packed*, Journal of Applied Crystallography, **28**, 1995, p 571 – 576.

[96] www.eos.info/fileadmin/download/literature/EOSINT_M_270_E.pdf, accessed 12/07/2010.

[97] http://www.timet.com/tables/6-4t-2.html, accessed 10/11/2008.

[98] http://asm.matweb.com/search/SpecificMaterial.asp?bassnum=MTP641, accessed 10/11/2008.

[99] Discussions with Dr Ulric Ljungblad of Arcam AB, September 2009.

[100] J. D. Hunt, *Steady state columnar and equiaxed growth of dendrites and eutectic*, Materials Science and Engineering, 65, 1984, p75 – 83.

[101] S. Lampmann, *Weld integrity and performance*, ASM International, Materials Park, Ohio, 1997.

[102] W. Kurz, D. J. Fisher, *Fundamentals of solidification*, 4th Edition, Trans Tech Publications, UK, 1998.

[103] M. McLean, *Directionally solidified materials for high temperature service*, TMS, London, 1983.

[104] S. Bontha, *The effect of process variables on microstructure in laser-deposited materials*, PhD Thesis, Wright State University, 2002.

[105] G. R. Hadley, *Thermal conductivity of packed metal powders*, International Journal of Heat and Mass Transfer, **6**, 1996, p909 – 920.

[106] K. Bala, P. R. Pradhan, N. S. Saxena M. P. Saksena, *Effective thermal conductivity of copper powders*, Journal of Physics D: Applied Physics, **22**, 1989, p1068 – 1072.

[107] K. Bala, P. R. Pradhan, N. S. Saxena M. P. Saksena, *Effect of medium on the effective thermal conductivity of a macroporous solid*, Journal of Physics D: Applied Physics, **23**, 1990, p748 – 750.

[108] S. Lagutkin, L. Achelis, S. Sheikhaliev, V. Uhlenwinkel, V. Srivastava, *Atomization process for metal powder*, Materials Science and Engineering A, **383**, 2004, p1 – 6.

[109] C. Andrès, P. Réginault, M. H. Rochat, B. Chaillot, Y. Pourcelot, *Particle-size distribution of a powder: comparison of three analytical techniques*, International Journal of Pharmaceutics, **144**, 1996, p141 – 146.

[110] http://www.outokumpu.com/42328.epibrw, 29/05/10.

[111] J. W. Elmer, T. A. Palmer, S. S. Babu, W. Zhang, T. DebRoy, *Phase transformation dynamics during welding of Ti-6Al-4V*, Journal of Applied Physics, **95**, 2004, p8327 – 8339.

[112] Y. Fan, P. Cheng, Y. L. Yao, Z. Yang, K. Egland, *Effect of phase transformations on laser forming of Ti-6Al-4V alloy*, Journal of Applied Physics, **98**, 2005, p013518-0 – 013518-10.

[113] S. Malinov, P. Markovsky, W. Sha, Z. Guo, *Resistivity study and computer modeling of the isothermal transformation kinetics of Ti-6Al-4V and Ti-6Al-2Sn-4Zr-2Mo-0.08Si alloys*, Journal of Alloys and Compounds, **314**, 2001, p181 – 192.

[114] http :// www. arcam.com/ CommonResources /Files /www.arcam.com /Documents /EBM % 20 Materials /Arcam- Ti6Al4V -Titanium-Alloy.pdf.

[115] L. Facchini, E. Magalini, P. Robotti, A. Molinari, *Microstructure and mechanical properties of Ti-6Al-4V produced by electron beam melting of pre-alloyed powders*, Rapid Prototyping Journal, **15**, 2009, p171 – 178.

[116] B. Baufeld, O. Van der Biest, S. Dillien, *Texture and crystal orientation in Ti-6Al-4V builds fabricated by shaped metal deposition*, Metallurgical and Materials Transactions A, 41A, 2010, p1917 – 1927.

[117] M. J. Bermingham, S. D. McDonald, M. S. Dargusch, D. H. StJohn, *Microstructure of cast titanium alloys*, Materials Forum, **31**, 2007, p84 – 89.

[118] F. X. Gil Mur, D. Rodriguez, J. A. Planell, *Influence of tempering temperature and time on the α'-Ti-6Al-4V martensite*, Journal of Alloys and Compounds, **234**, 1996, p287 – 289.

[119] http://www.3trpd.co.uk/pdf/ti64-titanium-alloy-eos-ti64.pdf, accessed 06/06/2010.

[120] T. Searles, J. Tiley, A. Tanner, R. Williams, B. Rollins, E. Lee, S. Kar, R. Banjeree, H. L. Fraser, *Rapid characterisation of titanium microstructural features for specific modelling of mechanical properties*, Measurement Science and Technology, **16**, 2005, p60 – 60.

[121] J. W. Brooks, M. D. Griffiths, A. J. Storton, R. Waddingham, *Modelling Microstructural Development – Measurement and Validation*, Proceedings Materials Science and Technology, Cincinnati, Ohio, 2006.

[122] W. Chen, C.J. Boehlert, E.A. Payzant, J.Y. Howe, *The effect of processing on the 455 °C tensile and fatigue behaviour of boron-modified Ti–6Al–4V*, International Journal of Fatigue, **32**, 2010, p627 – 638.

[123] M. R. Bache, W. J. Evans, B. Suddell, F. R. M. Herrouin, *The effect of temperature in titanium alloys for engineering components under fatigue*, International Journal of Fatigue, **23**, 2001, p153 – 159.

[124] X. Wu, R. Sharman, J. Mei, W. Voice, *Direct laser fabrication of a burn-resistant Ti alloy*, Materials and Design, **23**, 2002, p239 – 247.

[125] X. Wu, J. Liang, J. Mei, C. Mitchell, P. S. Goodwin, W. Voice, *Microstructures of laser-deposited Ti-6Al-4V*, Materials and Design, **25**, 2004, p137 – 144.

[126] M. Humbert and N. Gey, The calculation of a parent grain orientation from inherited variants for approximate orientation relations, Journal of Applied Crystallography, **35**, 2002, p401 – 405.

[127] M. C. Flemings, *Solidification Processing*, McGraw-Hill, New York, 1974.

[128] J. Fukai and T. Ando, *Microstructure development in alloy splats during rapid solidification*, Materials Science and Engineering A, **383**, 2004, p175 – 183.

[129] S.A. David, S.S. Babu, J.M. Vitek, *Welding: Solidification and Microstructure*, JOM, **55**, 2003, p14 – 21.

[130] K. E. Easterling, *Introduction to the Physical Metallurgy of Welding*, Butterworths, UK, 1992.

[131] N. Stanford, P. S. Bate, Crystallographic variant selection in Ti-6Al-4V, Acta Materialia, **52**, 2004, p5215 – 5224.

[132] S. L. Semiatin, P. N. Fagin, M. G. Glavicic, I. M. Sukonnik, O. M. Ivasishin, Materials Science and Engineering A, **299**, 2001, p 225 – 234.

[133] M. G. Glavicic, P. A. Kobryn, T. R. Bieler, S. L. Semiatin, *A method to determine the orientation of the high-temperature beta phase from measured EBSD data for the low-temperature alpha phase in Ti-6Al-4V*, Materials Science and Engineering A, **346**, 2003, p50 – 59.

[134] G. W. Greenwood, R. H. Johnson, *The deformation of metals under small stresses during phase transformations*, Proceedings of the Royal Society A, **283**, 1965, p403 – 422.

[135] D. J. Whitehouse, *Handbook of Surface Metrology*, Bristol, Institute of Physics Publishing, 1994.

[136] A. Crespo, R. Vilar, *Finite element analysis of the rapid manufacturing of Ti-6Al-4V parts by laser powder deposition*, Scripta Materialia, **63**, 2010, p140 – 143.

[137] S. de Waziers, S. Roy, S. Suwas, S. Tamirisakandala, R. Srinivasan, D. B. Miracle, *Solidification microstructure and texture in grain-refined titanium alloys*, in: Texture in Grain-Refined Titanium Alloys, Springer, London, 2009.

[138] H-y. Zhao, X. Wang, X-c. Wang, Y-p. Lei, *Reduction of residual stress and deformation in electron beam welding using multiple beam technique*, Frontiers of Materials Science in China, **2**, 2008, p66 – 71.

[139] G. L. Zhunkovskii, T. M. Evtushok, V. A. Kotenko, P. V. Mazur, S. P. Gordienko, *Reaction of boron-containing materials with titanium during self-propagating high-temperature synthesis*, Powder Metallurgy and Metal Ceramics, **45**, 2006, p163 – 167.

[140] Nicola Harrison, *Magnetic properties and microstructure of intermediate and low rare earth content $Nd_2Fe_{14}B$-based nanocomposite magnets*, PhD Thesis, The University of Sheffield, 2007.

[141] S. H. Whang, *Review: Rapidly solidified titanium alloys for high-temperature applications*, Journal of Materials Science, 21, 1986, p2224 – 2238.

[142] C. J. Boehlert, S. Tamirisakandala, W. A. Curtin, D. B. Miracle, *Assessment of in situ TiB whisker tensile strength and optimization of TiB-reinforced titanium alloy design,* Scripta Materialia, **61**, 2009, p245 – 248.

[143] S. Tamirisakandala, R.B. Bhat, D.J. McEldowney, D.B. Miracle, in: *Affordable metal matrix composites for high performance applications II*, TMS, Warrendale, PA, 2003, p. 185.

[144] M. J. Bermingham, S. D. McDonald, K. Nogita, D. H. StJohn, M. S. Dargusch, *Effects of boron on microstructure in cast titanium alloys*, Scripta Materialia, **59**, 2008, p538 – 541.

[145] A. L. Greer, P. S. Cooper, M. W. Meredith, W. Schneider, P. Schumacher, J. A. Spittle, A. Tronche, *Grain refinement of aluminium alloys by inoculation*, Advanced Engineering Materials, **5**, 2003, p81 – 91.

[146] I. Maxwell, A. Hellawell, *A simple model for grain refinement during solidification*, Acta Metallurgica, **23**, 1975, p229 – 237.

[147] T. E. Quested, A. T. Dinsdale, A. L. Greer, *Thermodynamic modelling of growth-restriction effects in aluminium alloys*, Acta Materialia, **53**, 2005, p1323 – 1334.

[148] M. J. Bermingham, S. D. McDonald, M. S. Dargusch, D. H. StJohn, *Grain-refinement mechanisms in titanium alloys*, Journal of Materials Research, **23**, 2008, p97 – 104.

[149] M. J. Bermingham, S. D. McDonald, M. S. Dargusch, D. H. StJohn, *The mechanism of grain refinement of titanium by silicon*, Scripta Materialia, **58**, 2008, p1050 – 1053.

[150] M. Easton, D. StJohn, *An analysis of the relationship between grain size, solute content, and potency number density of nucleant particles*, Metallurgical and Materials Transactions A, **36**, 2005, p1911 – 1920.

[151] O. K-Von Glodbeck, *Atomic Energy Review Special*, Issue No. 8, *Ti : Physiochemical Properties of its Compounds and Alloys*, Futemat, AEA, 1983, Vienna.

[152] Z. Fan, A.P. Miodowink, L. Chandrasekaran, C.M. Ward-Close, *Microstructural investigation of a rapidly solidified Ti-6Al-4V-1B-0.5Y alloy*, Journal of Material Science, **30**, 1995, p1653 – 1660.

[153] W. Kurz, C. Bezençon, M. Gäumann, *Columnar to equiaxed transition in solidification processing*, Science and Technology of Advanced Materials, **2**, 2001, p185 – 191.

[154] C. F. Yolton, *The pre-alloyed powder metallurgy of titanium with boron and carbon additions*, JOM, **56**, 2004, p56 – 59.

[155] F. Wang, J. Mei, X. Wu, *Direct laser fabrication of Ti6Al4V/TiB*, Journal of Materials Processing Technology, **195**, 2008, p321 – 326.